Development of ultra-stable characterization techniques for ultrashort laser beams

Miguel López Ripa

Departamento de Física Aplicada. Área de Óptica
Grupo de Investigación de Aplicaciones del Láser y Fotónica (ALF)
Universidad de Salamanca

A thesis submitted for the degree of
Doctor in Physics at Universidad de Salamanca
supervised by Dr. Íñigo Juan Sola Larrañaga
and Dr. Benjamín Alonso Fernández

Salamanca, April 2023

D. ÍÑIGO JUAN SOLA LARRAÑAGA y D. BENJAMÍN ALONSO FERNÁNDEZ, ambos Profesores Titulares del Área de Óptica en el Departamento de Física Aplicada de la Universidad de Salamanca, en calidad de codirectores CERTIFICAN:

Que la presente Memoria, “Development of ultra-stable characterization techniques for ultrashort laser beams/Desarrollo de técnicas ultraestables para la caracterización de haces láser ultracortos” ha sido realizada bajo su dirección en el Área de Óptica del Departamento de Física Aplicada de la Universidad de Salamanca por D. MIGUEL LÓPEZ RIPA y constituye su Tesis Doctoral para optar al grado de Doctor en Física con Mención Internacional.

Salamanca, abril de 2023.

Fdo. Íñigo Juan Sola Larrañaga

Fdo. Benjamín Alonso Fernández

Agradecimientos/ acknowledgments

Si cuando entré a la carrera me hubieran dicho que en un futuro iba a ser Doctor en Física, no me lo hubiese creído. Cada pequeño detalle me ha ido guiando en este largo viaje y, aunque esta última etapa ha sido larga y dura, puedo decir con orgullo que todo el esfuerzo y dedicación han merecido la pena. Llegados a este punto, quisiera agradecer a todo el que ha aportado su granito de arena para que llegue hasta aquí.

En primer lugar, me gustaría agradecer a Íñigo y Benja por su gran labor como directores a lo largo de estos años. Gracias por dedicarme todo vuestro tiempo, vuestra paciencia y transmitirme vuestro conocimiento y pasión por la ciencia, pero, sobre todo, gracias por apoyarme a lo largo de este periodo. También me gustaría agradecer a todos los miembros del Grupo de Aplicaciones del Láser y Fotónica (ALF) por acogerme y hacerme sentir uno más de esta gran familia. En especial quisiera dar las gracias a Nacho y Warein por sus consejos en el laboratorio en mi etapa más temprana del doctorado. Además, no puedo olvidarme de las personas con las que he compartido tantos buenos momentos fuera de la universidad durante estos años (Elena, Alba, Ana, Javi, Laura, Aurora, Víctor, Rodrigo...).

Desde el plano personal, agradezco a toda mi familia por su apoyo incondicional siempre que me he enfrentado a los diferentes retos que me he propuesto en la vida, nunca me cansaré de celebrar cada éxito con vosotros. En especial a mis padres, a mi hermana y a Olatz por hacerme sentir que todo es posible y animarme a seguir adelante, sin vosotros esto no hubiera sido posible. Gracias por estar ahí siempre que os he necesitado.

Además, quisiera agradecer a Andreas Döpp por abrirme las puertas de su grupo para realizar mi estancia internacional, y a todos los miembros de la LMU con los que he colaborado, en especial a Jannik y Nils. También quiero dar las gracias a Rosa Weigand y Óscar Pérez de la UCM por brindarnos la oportunidad de colaborar con ellos y realizar experimentos en sus instalaciones.

Por último, también quiero agradecer a Miguel Miranda y Cord Arnold por aceptar ser los revisores externos de esta tesis, además de a la Universidad de Salamanca por el contrato predoctoral.

Abstract

The dramatic evolution that the laser science has undergone in the last six decades, and particularly in the field of ultrashort pulses, has been accompanied by breakthrough advances in the development of techniques for their characterization. Despite the large number of characterization techniques developed in the last two decades, it is still necessary to implement simpler and more robust techniques that can also operate in multiple spectral ranges.

This Thesis is devoted to the study and development of temporal and spatiotemporal characterization techniques with compact and stable configurations, which are versatile, e.g., to analyze ultrashort laser beams with different temporal durations and in various spectral regions.

The structure of this Thesis is made up of four main blocks. Firstly, a brief introduction to ultrafast optical metrology and the state of the art of spatial, temporal and spatiotemporal characterization techniques is presented in Part I. Then, Part II is focused on the review and extension of the capabilities of the amplitude swing temporal characterization technique, demonstrating three key advances: operation in different spectral regions from visible to near-infrared, with a tunability range spanning of more than one octave; characterization of ultrashort pulses in the few-cycle regime; or study of the implementation with different amplitude modulation schemes. In addition, a new retrieval algorithm is developed to analyze the amplitude swing traces based on differential evolution strategies. Thirdly, the fundamentals, operation range and experimental demonstration of a spatiotemporal characterization technique based on bulk lateral shearing interferometry are depicted in Part III. Furthermore, the technique is applied to characterize complex spatiotemporal couplings, like constant and time-varying optical

vortices or the aberrations when focusing with astigmatic lenses. Finally, the main conclusions of the work and future perspectives are discussed in Part IV.

Resumen

La drástica evolución que ha experimentado la ciencia láser en las últimas seis décadas, y en particular en el campo de los pulsos ultracortos, ha ido acompañada de grandes avances en el desarrollo de técnicas para su caracterización. A pesar de la gran cantidad de métodos de caracterización desarrollados en las últimas dos décadas, aún es necesario implementar sistemas más simples y robustos que también puedan operar en múltiples rangos espectrales.

Esta Tesis está dedicada al estudio y desarrollo de técnicas de caracterización temporal y espaciotemporal con configuraciones compactas y estables, que sean versátiles para, por ejemplo, analizar haces láser ultracortos con diferentes duraciones temporales y en diversas regiones espectrales.

La estructura de la Tesis está dividida en cuatro bloques principales. En primer lugar, en la Parte I se presenta una breve introducción a la metrología óptica ultrarrápida y los avances de las técnicas de caracterización espacial, temporal y espaciotemporal a lo largo de los últimos años. Después, la Parte II se enfoca en la revisión y extensión de las capacidades de la técnica de caracterización temporal *amplitude swing*, demostrando tres avances clave: operación en diferentes regiones espectrales desde visible hasta infrarrojo cercano, con un rango de sintonizabilidad que abarca más de una octava; caracterización de pulsos ultracortos en régimen de pocos ciclos; o estudio de diferentes esquemas de modulación de amplitud. Además, se implementa un nuevo algoritmo de reconstrucción para analizar las trazas del sistema *amplitude swing* basado en las estrategias *Differential Evolution*. En tercer lugar, en la Parte III se describen los fundamentos, el rango de operación y la demostración experimental de una técnica de caracterización espaciotemporal

basada en la interferometría lateral compacta (*bulk lateral shearing interferometry*). Además, la técnica se emplea para caracterizar acoplamientos espaciotemporales complejos, como son los vórtices ópticos constantes y variables en el tiempo o las aberraciones introducidas al focalizar haces láser con lentes astigmáticas. Finalmente, en la Parte IV se resumen las principales conclusiones y futuras líneas de trabajo.

Acronyms

BBO	Beta-Barium Borate [$\beta - BaB_2O_4$]
CPA	Chirped Pulse Amplification
DE	Differential Evolution
DFG	Difference-Frequency Generation
d-scan	dispersion-scan
DOEs	diffractive optical elements
FFT	Fast Fourier Transform
FROG	Frequency Resolved Optical Gating
FT	Fourier Transform
FTL	Fourier Transform Limit
FTS	Fourier Transform Spectroscopy
FTSI	Fourier Transform Spectral Interferometry
FWHM	Full-Width at Half Maximum
GDD	Group Delay Dispersion
GRENOUILLE	GRating-Eliminated No-nonsense Observation of Ultrafast Incident Laser Light E-fields
GVD	Group Velocity Dispersion

HAMSTER	Hartmann–Shack-assisted, Multidimensional, Shaper-based Technique for Electric-field Reconstruction
HHG	High-order Harmonic Generation
HWP	half-waveplate
IFT	Inverse Fourier Transform
IR	infrared
KTP	Potassium Titanyl Phosphate
LCP	left-circular polarization
MIIPS	Multiphoton Intrapulse Interference Phase Scan
MWP	multi-order waveplate
NA	Numerical Aperture
O.A.	optical axis
OAM	Orbital Angular Momentum
PCGPA	Principal Components Generalized Projections Algorithm
PG	Polarization gating
PPLN	Periodically Poled Lithium Niobate
RCP	right-circular polarization
rms	root-mean-square
QWP	quarter-waveplate
SEA SPIDER	Spatially Encoded Arrangement Spectral Phase Interferometry for Direct Electric-field Reconstruction

SEA TADPOLE	Spatially Encoded Arrangement for Temporal Analysis by Dispersing a Pair Of Light E-fields
SFG	Sum-Frequency Generation
SHG	Second Harmonic Generation
SI	Spectral Interferometry
SPIDER	Spectral Phase Interferometry for Direct Electric-field Reconstruction
SRSI	Self-Referenced Spectral Interferometry
STARFISH	Spatio-Temporal Amplitude-and-phase Reconstruction by Fourier-transform of Interference Spectra of Highly-complex-beams
STC	SpatioTemporal Coupling
STRIPED FISH	Spatially and Temporally Resolved Intensity and Phase Evaluation Device: Full Information from a Single Hologram
SVEA	slowly varying envelope approximation
TERMITES	Total E-field Reconstruction using a Michelson Interferometer TEmporal Scan
THG	Third Harmonic Generation
TiO_2	Rutile
TOD	Third Order Dispersion
XPW	Cross-polarized wave generation
YVO_4	Yttrium orthovanadate
ZDW	zero-dispersion wavelength
ZWP	zero-order waveplate

Contents

Part I

INTRODUCTION

Chapter 1

History of ultrafast lasers

Laser science has drastically evolved since its first experimental demonstration in 1960 [1]. Over these six decades of continuous development, new laser sources have been implemented and laser science has been consolidated as a relevant topic with multiple applications in various fields such as telecommunications [2], material processing [3], biomedicine [4], spectroscopy [5], nonlinear optics [6] or strong field physics [7] , among many others [8–11].

The importance of laser sources increased considerably with the discovery of efficient approaches of pulsed emission, which consist on concentrating the energy of the laser beam in a short period of time, thus considerably increasing the achievable peak power and hence the intensity. One of the first successful strategies was the Q-switching method, firstly demonstrated in [12]. This method is based on the introduction of a variable attenuator inside the laser cavity to periodically control the losses, hence the quality factor (Q) of the resonator. First, it introduces high losses to prevent feedback of light inside the active medium and increase the stored pump energy. Then, it drastically reduces the losses, thus enabling the feedback and the stimulation of the emission process, generating an intense laser pulse. The Q-switching approach produces short pulses, typically in the ns range (1 ns= 10^{-9} s), but it could achieve shorter durations at the 100 ps range (1 ps= 10^{-12} s) [13].

On the other hand, in 1964 the mode-locking method was introduced [14], which enables the generation of laser pulses in the sub-picosecond temporal range. This method generates extremely short pulses by achieving a fixed phase relationship between the longitudinal modes of the laser cavity, making them interfere constructively.

In particular, mode-locking lasers were the cornerstone of the drastic increment of interest because their ultrashort laser pulses of tens of femtoseconds (1 fs= 10^{-15} s) opened the access to the so-called ultrafast regime. These lasers are very interesting because their short duration allows extremely short processes to be studied (e.g., processes in molecules or atoms [15]). Also, the significant increment in the peak intensity enables the induction of many nonlinear processes [16, 17]. Another interesting application of ultrafast lasers is material processing, because it can be done without significant thermal effects, since heat transfers are done in nanosecond or longer temporal scales [18].

Among all the advances experienced by ultrafast laser science in its history, we want to highlight the invention of the Chirped Pulse Amplification (CPA) technology [19]. A typical CPA system, as the one shown in Fig. 1.1, consists of three different elements: stretcher, amplifier and compressor.

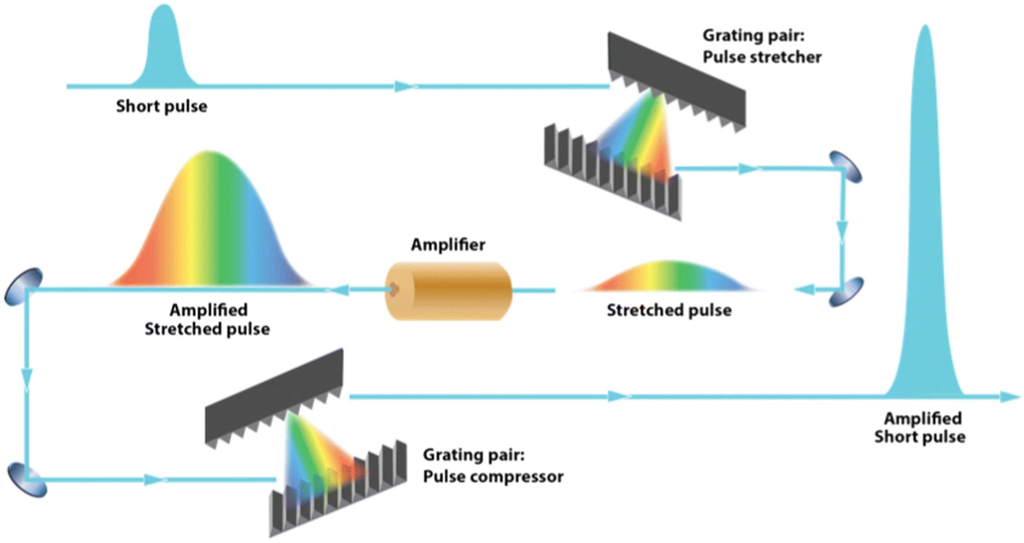

Fig. 1.1. *Scheme of a CPA system obtained from [20].*

First, the ultrashort laser pulse that is going to be amplified goes through the stretcher. This system introduces a significant chromatic dispersion (different optical path depending on the optical frequency), thus temporally stretching the pulse typically into hundreds of picoseconds. Therefore, the stretched pulse presents a time dependent spectrum, what is called chirp. A common configuration of the stretcher is composed by diffraction gratings, separating the different spectral components and driving them by different length paths before recombining them. Another possibility is to use prisms instead of diffraction gratings or directly introduce high dispersion materials. After the stretcher, it is obtained a lower peak power and longer pulse that can be amplified in an active medium (amplifier) without risk of damage due to its much longer temporal duration. Finally, the chromatic chirp introduced by the stretcher, and any other that eventually could have been acquired due to propagation, are compensated using a compressor, thus obtaining a high energy ultrashort pulse. The compressor typically is a system similar to the stretcher but introducing dispersion of the opposite sign.

Before the invention of CPA, ultrafast lasers were only able to be amplified up to megawatt or gigawatt levels without damaging the amplification medium. After the CPA, ultrafast laser power can be easily risen several orders of magnitude into the terawatt or even petawatt level. Its discoverers, Donna Strickland and Gérard Mourou, were awarded with the 2018 Physics Nobel Prize.

A CPA system can be relatively compact, so it can be used to generate terawatt table-top lasers like the ones used in this Thesis.

The continuous development of ultrafast lasers has given access to new fields of science like micro-machining [21, 22], High-order Harmonic Generation (HHG) [23, 24], attoscience [25, 26], laser-plasma interaction [27, 28] or electron/ion acceleration [29, 30], among many others.

Motivation of the Thesis

The development and optimization of new laser sources and their correct use in different applications is sustained in the exhaustive knowledge of the laser emission. For this purpose, since the development of the first laser, many characterization techniques (e.g., polarization, temporal, spatial and spatiotemporal) have been proposed to analyze them. In particular, this

Thesis is devoted to the temporal and spatiotemporal analysis.

Despite the broad variety of temporal and spatiotemporal characterization techniques that have been developed in the last decades, which will be mentioned later in Section 2.2, there is still a necessity of simpler and more robust techniques that can be reliable even in less controlled conditions, as in noisy environments or outside laboratory conditions.

In addition, there is an emerging need for characterization techniques capable to operate in different spectral regions due to the development of new laser sources in the visible and infrared (IR) spectral regions, which present interesting applications in various fields like spectroscopy, biomedicine, metrology, micro-welding or telecommunications, among many others.

Taking into account the current needs of ultrafast characterization, this Thesis is focused on the development, study and application of new prototypes of simple, compact and ultra-stable characterization techniques. In particular, we are going to characterize linearly polarized laser beams, so we can assume the electric field is a scalar magnitude. Nevertheless, we will take advantage of how materials interact with light at different states of polarization in order to generate certain special beams to be studied or to implement our characterization techniques.

On one hand, Part II extends the studies of a recently published temporal characterization technique, the amplitude swing [31], demonstrating that it is able to operate in diverse spectral regions in the visible and IR (Chapter 5), characterize ultrashort pulses in the few-cycle regime (Chapter 6) and to be implemented with different configurations of the set-up (Chapter 7). Moreover, we implement a new retrieval algorithm based on genetic algorithms (Chapter 4).

On the other hand, Part III presents a new compact and ultra-stable spatiotemporal characterization technique, which solves the high complexity and low stability problems of previous spatiotemporal techniques, enabling even the possibility to operate in different spectral regions without modification of the set-up. First, in Chapters 8-10 are settled the foundations of the technique, including the analysis of its operability range. Then, in Chapter 11, the capabilities of the technique characterizing spectrally and temporally beams with different types of spatiotemporal/spatiospectral distortions are shown.

Finally, conclusions of the work and future perspectives are discussed in Part IV.

Chapter 2

Ultrafast characterization

As laser systems evolved, so did the techniques to characterize them. This continuous evolution of the characterization techniques is essential to optimize the laser performance and to correctly use them in their corresponding applications.

The main challenge associated with the study and control of ultrafast lasers is the difficulty to observe such brief events (femtosecond range), since they are much shorter than the temporal response of the fastest electronic devices (usually in the nanosecond-picosecond range). Thus, different methods need to be used, in particular optical methods are very extended [32–34].

2.1 Basic concepts of ultrashort laser beams

This Section is focused on establishing the basic concepts of ultrafast lasers that underlie the present Thesis.

2.1.1 Electric field: temporal and spectral domains

Ultrafast optical metrology is focused on the study of the electric field of ultrashort laser pulses and their interaction with matter. It is well known that the light electric field can be expressed, using complex number notation, as the combination of an amplitude (A) and a phase term (Ω), being the electric field $E = A \cdot \exp(i\Omega)$.

In general, the electric field can be expressed as a function that depends on the three spatial coordinates (x, y, z) and the time (t), so $E = E(x, y, z, t)$. Furthermore, by choosing the reference axis, z represents the propagation direction and usually the electric field is characterized at a certain propagation plane (z_0), so $E(x, y, z = z_0, t) = E(x, y, t)$.

As a first approach, in order to understand the underlying physics, for the moment we are going to assume that the electric field does not vary spatially. In this case, the electric field in the temporal domain can be expressed as:

$$E(t) = A(t) \exp\left[i\left(\varphi(t) - \omega_0 t\right)\right] \qquad \mathbf{(2.1)}$$

where the amplitude of the electric field is its modulus $(A(t) = |E(t)|)$, ω_0 represents the central or carrier frequency and $\varphi(t)$ corresponds to phase term varying in time (i.e., temporal phase relative to the carrier frequency phase term).

From Eq. **2.1**, it can be defined the temporal intensity, $I(t)$, as the square of the modulus of the electric field, $I(t) = |E(t)|^2 = [A(t)]^2$. Moreover, from the temporal intensity it can be defined the temporal pulse duration, which is usually done following the criterion of Full-Width at Half Maximum (FWHM).

In addition to the temporal representation, the electric field can equivalently be expressed in the spectral domain as:

$$\widetilde{E}(\omega) = \sqrt{S(\omega)} \exp\left[i\varphi(\omega)\right] \qquad \mathbf{(2.2)}$$

where $S(\omega) = |\widetilde{E}(\omega)|^2$ is the spectral power density (hereafter spectrum) and $\varphi(\omega)$ the spectral phase term.

Furthermore, the temporal and spectral domains are related by the direct/inverse Fourier Transform. Thus, if the electric field is known in one domain, it can be calculated in the analogous just by:

$$\begin{aligned} E(t) &= \mathscr{F}\left\{\widetilde{E}(\omega)\right\} = \int_{-\infty}^{+\infty} \widetilde{E}(\omega) \exp\left[-i\omega t\right] d\omega \\ \widetilde{E}(\omega) &= \mathscr{F}^{-1}\left\{E(t)\right\} = \int_{-\infty}^{+\infty} E(t) \exp\left[i\omega t\right] dt \end{aligned} \qquad \mathbf{(2.3)}$$

being, $\mathscr{F}$ the direct Fourier Transform (FT) and $\mathscr{F}^{-1}$ the Inverse Fourier Transform (IFT).

Sometimes the spectral representation is done in wavelengths (λ) instead of the angular frequencies (ω), but the change of variable from ω to λ (or vice versa) is not only an axis change. In fact, it is also a reshape of the spectrum because of the density conservation rule:

$$\int_0^\infty S_\omega(\omega)d\omega = \int_0^\infty S_\lambda(\lambda)d\lambda \qquad \textbf{(2.4)}$$

Thus, since they are inversely proportionals ($\omega = 2\pi c/\lambda$, being c the speed of light) the relation between the spectrum of each parameterization is given by Eq. **2.5**. In addition, this reshape is specially relevant in few-cycle regime due to the ultra-broadband spectra of these pulses.

$$S_\omega(\omega) = \frac{\lambda^2}{2\pi c} S_\lambda(\lambda) \qquad \textbf{(2.5)}$$

Moreover, since temporal and spectral domains are equivalent, the electric field can be represented indistinctly in each domain. However, from an experimental point of view, it is useful to represent the electric field in the spectral domain due to two main reasons. Firstly, the dispersion of materials and optical elements will be manifested as different phases depending on the frequency. Secondly, the spectral characterization is the easiest one because under linear processes the spectrum is not modified due to propagation through a medium (apart from attenuation or some particular distortions), whereas the temporal intensity and temporal phase are affected if the spectral phase (or amplitude) changes. This idea is shown in Fig. 2.1, where the temporal intensity has been calculated for a fixed spectrum with different spectral phases.

In the examples of Fig. 2.1, the spectral phase has been parameterized using a Taylor expansion series, like the one in Eq. **2.6**, and the spectrum corresponds to a Gaussian profile.

$$\varphi(\omega) = \phi_0 + \phi_1(\omega - \omega_0) + \frac{1}{2!}\mathrm{GDD}(\omega - \omega_0)^2 + \frac{1}{3!}\mathrm{TOD}(\omega - \omega_0)^3 + ... \qquad \textbf{(2.6)}$$

where ϕ_0 corresponds to a constant term, ϕ_1 is the coefficient of the linear contribution and the GDD and TOD terms are the second and third spectral derivatives of the phase, respectively $\left(\mathrm{GDD} = \frac{\partial^2\varphi(\omega)}{\partial\omega^2}\Big|_{\omega_0} \text{ and } \mathrm{TOD} = \frac{\partial^3\varphi(\omega)}{\partial\omega^3}\Big|_{\omega_0}\right)$.

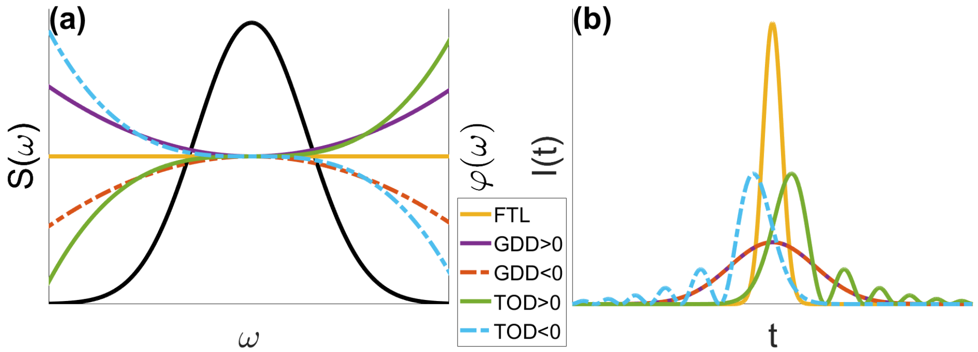

Fig. 2.1. *Representation of the effect of the spectral phase in the temporal intensity for the same Gaussian spectrum. (a) Spectrum (black line) and spectral phases. (b) Temporal intensities.*

In this representation, the quadratic phase term is called Group Delay Dispersion (GDD) and, when accounting for material dispersion, it is generated due to the accumulation of Group Velocity Dispersion (GVD) during the propagation through a medium of a certain length (L), $\mathrm{GDD} = \mathrm{GVD} \cdot L$. The GDD is translated into the temporal domain as an increment of the temporal duration and, also, a reorganization of the frequencies. If $\mathrm{GDD} > 0$, it is said that the pulse has positive chirp and the redder frequencies arrive before the bluer frequencies (the opposite if $\mathrm{GDD} < 0$). Please notice that both GDD signs depicted in Fig. 2.1(b) present the same temporal intensity profile, but actually they have opposite chirp. This can be verified by looking at the oscillations of the electric field shown in Fig. 2.2.

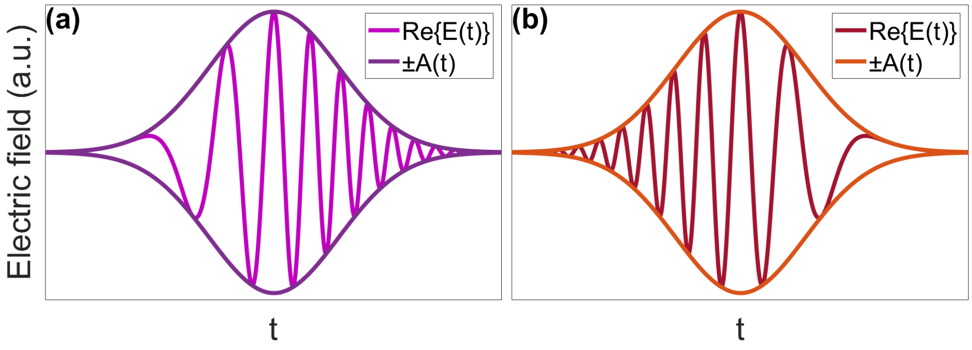

Fig. 2.2. *Representation of the electric field temporal oscillations for a pulse with (a) GDD>0 and (b) GDD<0.*

On the other hand, the Third Order Dispersion (TOD) generates satellites arriving before (pre-pulses) or after (post-pulses) the main pulse, if TOD < 0 or TOD > 0 respectively.

Furthermore, if $\varphi(\omega)$ is constant or linear dependent, in the temporal domain it corresponds to the shortest pulse obtainable with that spectrum and it is called Fourier Transform Limit (FTL) pulse.

Previously, it has been explained that spectral and temporal domains are linked by Fourier Transform (Eq. **2.3**), so the time-bandwidth product is fixed (i.e., the product of the temporal duration and spectral bandwidth of the pulse is constant). Therefore, to achieve shorter FTL pulses it is needed a broader spectra.

2.1.2 Spatiotemporal couplings

As mentioned before, in general the electric field at a certain propagation plane can be expressed as a function that depends on the transverse spatial coordinates and the temporal or spectral variables ($E(x, y, t)$ or $E(x, y, \omega)$).

From this parameterization two concepts widely used in spatiotemporal characterization can be defined. Firstly, in the spatiotemporal domain, the surface containing the maxima of the temporal intensity for different spatial positions is called pulse-front. Secondly, in the spatiospectral domain, the spatial surface of constant phase is called wavefront and, in a general case, it can be different for each wavelength.

In some situations, it is assumed that the spatial and temporal/spectral properties are separable ($E(x, y, t) = E_{xy}(x, y) \cdot E_t(t)$). If this assumption is fulfilled, the spatial term could be studied using a spatial characterization technique and the temporal term using a temporal characterization technique. Thus, combining both characterizations, the complete electric field would be obtained.

However, in a general case, the temporal or spectral properties may vary spatially, hence the beam presents the so-called SpatioTemporal Coupling (STC). In those cases, the electric field dependences are not separable, $E(x, y, t) \neq E_{xy}(x, y) \cdot E_t(t)$, and a new kind of techniques, called spatiotemporal characterization techniques, are required.

Some examples of STCs are the pulse-front tilt (i.e., the arrival time of the pulse depends on the spatial location within the beam profile, varying linearly in a direction perpendicular to the beam propagation direction), pulse-front curvature (e.g., the arrival time of the pulse varies quadratic in the spatial dimension), spatial chirp (i.e., spatial dependence of the spectrum) or chromatic aberrations, among many others [33, 34].

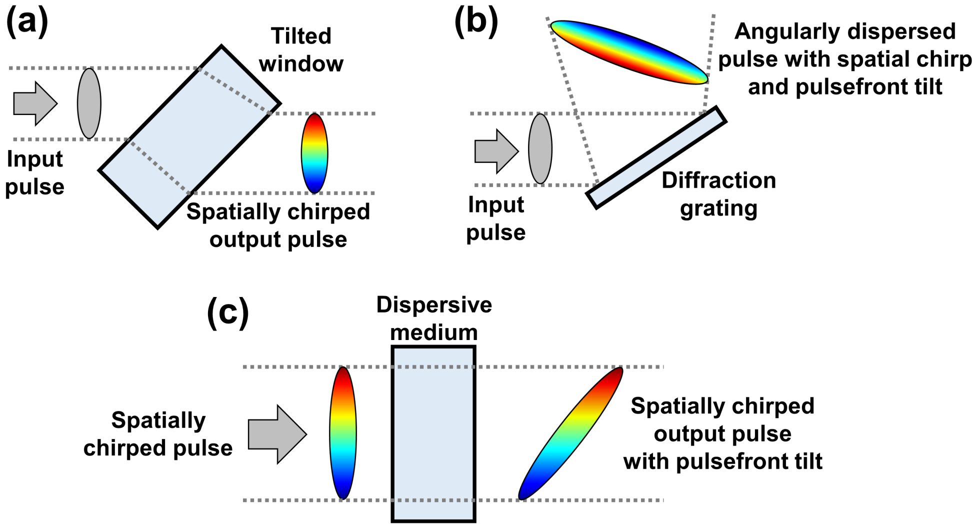

Fig. 2.3. *Representation of different common cases of STCs. Images adapted from the tutorials of [35].*

Furthermore, the presence of STCs is not rare since it can be observed in multiple common situations like the represented in Fig. 2.3. Firstly, Fig. 2.3(a) shows the spatial chirp introduced due to traveling through a tilted window. Secondly, Fig. 2.3(b) represents the spatial chirp and pulse-front tilt introduced after diffraction on a grating. Then, Fig. 2.3(c) shows the pulse-front tilt due to propagation of a spatially chirped pulse through a dispersive medium.

These are just some examples, but there are many other typical STCs such as the frequency dependent focal length in chromatic lenses, spatial chirp after propagation through a prism pair or complex STCs induced due to nonlinear effects or diffractive optical elements (DOEs), among many others

[33, 36]. One example of complex STCs are the optical vortices that will be analyzed in Chapter 11.

It is crucial to characterize and control these spatiotemporal dependences. On one hand, non-desired spatiotemporal couplings can introduce significant changes in the laser beam characteristics (e.g., temporal lengthening or beam aberrations), implying a critical reduction of the peak intensity and non-optimal operation in the corresponding application. On the other hand, their controlled manipulation can be used to generate beams with specific distributions that can be interesting for certain applications [36, 37].

2.1.3 Spatial and spectral interference

Considering the coherence of laser emission, two superimposed electric fields interfere depending on their relative phase. There are different ways of interference and here we are going to explore two types of interest for this Thesis: spectral and spatial interference.

On one hand, from the spectral point of view, the resulting spectrum of the combination of two collinear ultrashort laser pulses (E_1 and E_2) with the same polarization and a certain delay (τ) between them is given by:

$$\begin{gathered} S_{SI}(\omega) = |\mathscr{F}\{E_1(t) + E_2(t-\tau)\}|^2 = \\ = |\widetilde{E}_1(\omega)|^2 + |\widetilde{E}_2(\omega)|^2 + 2\sqrt{|\widetilde{E}_1(\omega)|^2|\widetilde{E}_2(\omega)|^2} \cdot \cos\left(\varphi_1(\omega) - \varphi_2(\omega) - \omega\tau\right) \end{gathered} \tag{2.7}$$

An example using this type of interference with ultrashort pulses is shown in Fig. 2.4(a). Indeed, Eq. **2.7** is used in Spectral Interferometry (SI) [38, 39] to obtain the relative phase between the interfering pulses. Thus, knowing one of them, the phase of the other can be characterized.

On the other hand, from the spatial point of view, there are different possibilities. Firstly, if two beams with different wavefronts are superimposed, the resulting combination will lead to a spatial interference pattern due to the phase difference.

Secondly, there are some configurations that enable the combination of a beam with a replica of itself encoding its information. For example, if two beams are combined with a certain tilt angle, the combination will create a spatial interference pattern. Another interesting case is the shearing interferometry, in which a beam interferes with a laterally sheared replica of itself, generating a spatial interference pattern that contains the spatial phase gradient. An example of a commercial system based on the shearing interferometry with the resulting patterns for flat and convergent wavefronts for a continuous wave laser is shown in Fig. 2.4(b).

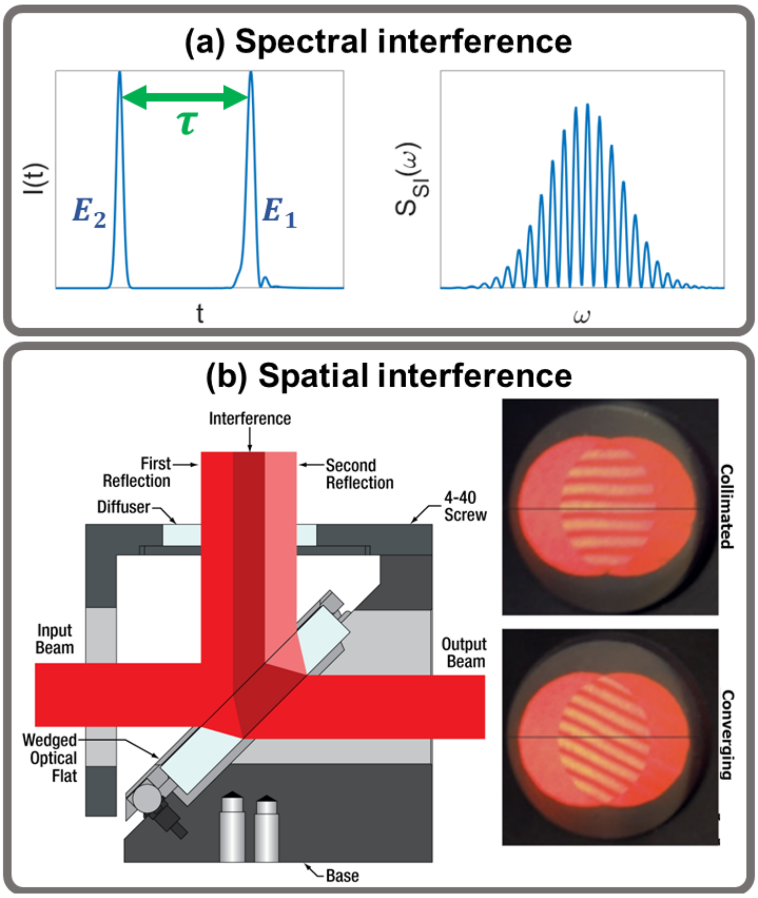

Fig. 2.4. *(a) Simulated example of spectral interferometry. (b) Scheme of a commercial lateral shearing interferometer from Thorlabs (image from [40]).*

Notice that, when using ultrashort pulsed beams, and depending on the wavefront spectral dependence, these spatial patterns can be different for each frequency of the beam. From the spectral point of view, the spectral interference pattern can be different for each spatial position.

In this Thesis, we will combine the concepts of SI and lateral shearing interferometry to create a spatiotemporal characterization technique, which will be explained in Part III.

2.1.4 Nonlinear effects: second harmonic generation

In general, characterization techniques based on linear processes can only give information about the spectrum and the phase difference. It is true that, provided a known reference pulse, a laser beam can be characterized using linear processes like SI. However, that reference usually has been previously calibrated with a technique based on nonlinear optics, as it will be shown in Subsection 2.2.2.

Nonlinear processes are generated due to a nonlinear response of the medium. As long as the pulse intensity is high enough, any medium can present them, but there are some materials, called nonlinear materials, which more likely present this type of processes [41]. Usually, anisotropic crystals with nonlinear response of the refractive index are used as nonlinear media, and they are called nonlinear crystals.

The main point of using nonlinear effects is that they are sensitive to changes in the phase, so they can be used to codify all the information of the electric field. There are many nonlinear processes that can be used in ultrafast characterization like Sum-Frequency Generation (SFG), Difference-Frequency Generation (DFG), Third Harmonic Generation (THG), Cross-polarized wave generation (XPW) or Polarization gating (PG) [32, 41]. Despite the diversity of nonlinear processes, the majority of ultrafast characterization techniques are based on Second Harmonic Generation (SHG) because it requires less intensity.

The SHG is a special case of SFG in which two photons of the same fundamental frequency, ω, are *'combined'* to produce one photon of double frequency 2ω. This process was observed experimentally for the first time in [42] and nowadays is widely used in many ultrafast characterization techniques. As seen in [41], it is usually studied from a monochromatic point of view using the following equation:

$$I_2(L) = \frac{8\omega_1^2 d_{eff}^2 I_1^2}{n_1^2 n_2 \varepsilon_0 c^2} L^2 \operatorname{sinc}\left(\Delta k L/2\right) \tag{2.8}$$

where d_{eff} corresponds to the effective efficiency of the SHG process, L is the nonlinear medium thickness, c the light velocity and ε_0 the vacuum permittivity. The subindices '1' and '2' refer to the fundamental and SHG variables like the frequency (ω), the refractive index (n) and the intensity (I). The term $\Delta k = k_2 - 2k_1$ is called phase-matching (between the wavevectors) and it must be close to zero to have an efficient SHG. Furthermore, it can be expressed as a function of the refractive indices difference:

$$\Delta k = \frac{2\omega_1}{c}(n_2 - n_1) \tag{2.9}$$

However, in ultrafast metrology the beams are broadband and, in general, the problem cannot be directly solve studying independently each wavelength.

In fact, when using ultrashort beams, the easiest way is to calculate the SHG (actually, SFG) electric field in the temporal domain because, assuming instantaneous response, it is directly the product of both fundamental electric fields. Then, the spectral electric field can be calculated by simply using the Fourier Transform:

$$\begin{aligned} E_{SHG}(t) &= E(t)^2 \\ \widetilde{E}_{SHG}(\omega) &= \mathscr{F}^{-1}\{E(t)^2\} \end{aligned} \tag{2.10}$$

To calculate the electric field directly in the spectral domain, the spectral convolution of both fundamental fields has to be done.

Moreover, the SHG for a certain material is efficient if the phase-matching condition is satisfied ($\Delta k = 0$), but that condition depends on the wavelength and the angle of incidence with respect to the crystal axis. In the experiments it is highly important to verify that the phase-matching is good along all the spectrum to avoid distortions that can introduce artifacts in the pulse characterization.

Furthermore, an anisotropic crystal is usually cut with the optical axis at a certain angle so the phase-matching for the desired wavelength is perfect under normal incidence. Thus, if the same nonlinear crystal is used in a different spectral range, it should be rotated to have the correct phase-matching angle.

Notice that larger values of L in Eq. **2.8** increase the SHG intensity, at the expense of reducing the spectral bandwidth due to vanishing faster the ‘sinc’ term. Therefore, in ultrafast metrology thin nonlinear crystals are commonly used, so the phase-matching condition for different frequencies is less restrictive. However, there are some situations, specially with ultra-broadband pulses, in which it is not possible to have perfectly flat phase-matching for all the spectrum, even for very thin nonlinear media. In those cases, it can be used a SHG response function (R_{SHG}) in the retrieval algorithms to take into account this spectral dependence of SHG expressing the SHG spectrum as:

$$S_{SHG}(\omega) = R_{SHG}(\omega) \cdot I_{SHG}(\omega) = R_{SHG}(\omega)|\mathscr{F}^{-1}\{E(t)^2\}|^2 \qquad \mathbf{(2.11)}$$

There are different ways of obtaining this SHG response, like experimental calibration using a known broadband source, iteratively as a free parameter in the retrieval algorithm, taking into account the frequency marginal of the trace or theoretically considering the SHG equations and the material parameters [43].

2.2 State of the art of ultrafast characterization techniques

Ultrafast characterization techniques of scalar electric fields can be divided in three groups taking into account the dependences that are studied. Firstly, the spatial characterization techniques, which only pay attention to the spatial dependences. Secondly, the temporal characterization techniques, which assume the beam is spatially homogeneous (or characterize it at a certain spatial position) and only pay attention to the temporal/spectral properties. Finally, the spatiotemporal characterization techniques that fully characterize the spatial and temporal/spectral properties, taking into account the possible couplings.

2.2.1 Spatial characterization

The spatial characterization techniques are focused on the measurement of the spatial dependence of the intensity and phase, disregarding the temporal/spectral dependences.

The characterization of the spatial intensity, $I(x, y)$, can be easily done using a camera. On the contrary, the spatial phase, $\varphi(x, y)$, characterization requires a wavefront sensor. There are different types of wavefront sensors, for example, common-path interferometers [44], shearing interferometers [45], multiwave interferometers [46], wavefront curvature sensors [47] or Shack-Hartmann sensors [48].

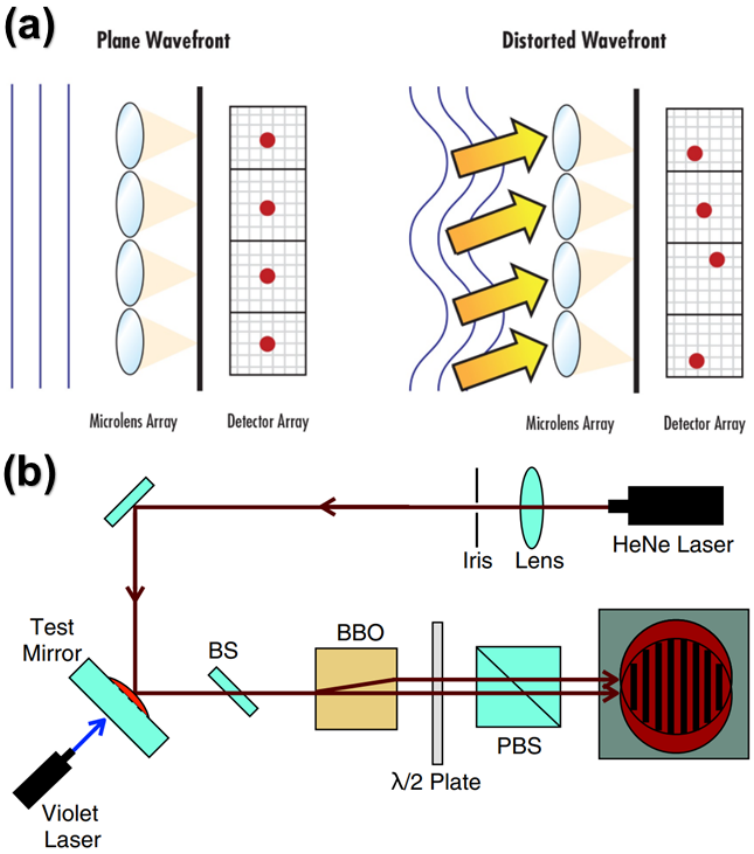

Fig. 2.5. *(a) Representation of the Shack-Hartmann characterization for plane and distorted wavefront (image from [49]) (b) Scheme of a technique based on spatial shearing interferometry from [45].*

On one hand, Shack-Hartmann is one of the most extended wavefront sensors. This device focus over a camera the beam under test using a matrix of micro-lenses obtaining a dot pattern, like in Fig. 2.5(a). Knowing the reference pattern for a flat wavefront, the deviation of each dot in the measured pattern contains the information of the phase spatial derivative in that area and, from it, it can be extracted the spatial phase profile.

On the other hand, we also want to highlight the shearing interferometers, since the spatiotemporal technique proposed in Part III shares part of their principles. They measure the interference pattern of two spatially sheared replicas of the beam under test to extract information like the spatial gradient. In particular, we are interested in a type of shearing interferometer called polarization interferometry [50], because it uses uniaxial birefringent elements to generate laterally sheared replicas. Fig. 2.5(b) shows an example of this technique characterizing the wavefront of a continuous wave laser [45].

2.2.2 Temporal characterization

In its beginnings, the characterization of ultrafast lasers was quite rudimentary and temporal techniques only gave partial information of the pulse. One example of these techniques are the intensity autocorrelators [51], whose scheme is shown in Fig. 2.6(a). This technique combines the pulse under test with a delayed replica of itself inside a SHG medium and measures the temporally integrated intensity for different delays.

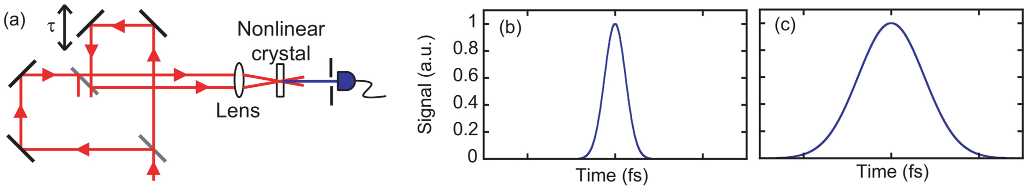

Fig. 2.6. *Representation of the set-up of intensity autocorrelation (a) with the measurement of a Gaussian FTL pulse (b) and a Gaussian pulse with GDD (c). Image extracted from [32].*

Figs. 2.6(b,c) represent the intensity autocorrelator trace for a Gaussian FTL pulse and for a Gaussian pulse with GDD, respectively. This technique only gives partial information of the pulse, like a FWHM estimation, assuming that the shape of the pulse is known. This assumption is necessary because the pulse duration (FWHM) directly given by an autocorrelation trace needs to be corrected by a shape factor. Despite its limitations, it is still in use nowadays, specially at situations where there is no need of knowing the actual shape of the pulse, but it is required only an estimate of the pulse duration or an optimization of it.

The previously mentioned technique is not able to fully measure the amplitude and phase of the electric field, but in the last three decades many temporal techniques able to fulfill this necessity have been proposed, as we mentioned below. Nevertheless, these temporal characterization techniques, except those specifically designed to measure it, are insensitive to zero-th order and the first order phase changes.

One of the most consolidated temporal characterization techniques is also based on the autocorrelation schemes, but spectrally resolved. This technique was introduced in 1993 and it is called Frequency Resolved Optical Gating (FROG) [52]. There are different types of FROG systems but essentially they are based on the scan of the pulse with a short optical gate (gate pulse) and the generation of a nonlinear trace spectrally resolved given by Eq. **2.12**, which is analyzed with an iterative algorithm to obtain the electric field (amplitude and phase).

$$S_{FROG}(\omega,\tau) = \left| \int_{-\infty}^{+\infty} P(t)G(t-\tau)e^{i\omega t}dt \right|^2 \qquad \textbf{(2.12)}$$

In this equation, $P(t)$ is the probe pulse under study and $G(t-\tau)$ the gate pulse that scans it. Moreover, τ is the scanned variable and corresponds to the temporal delay between both pulses.

The most common set-up is the SHG FROG [52], represented in Fig. 2.7. In this case, the gate pulse is a delayed replica of the pulse under test and the combination is produced with a non-collinear configuration inside a SHG medium. Thus, the FROG trace for this configuration will be:

$$S_{FROG}^{SHG}(\omega,\tau) = \left| \int_{-\infty}^{+\infty} E(t)E(t-\tau)e^{i\omega t}dt \right|^2 \qquad \textbf{(2.13)}$$

being, $E(t)$ the electric field of the pulse under test and $E(t-\tau)$ the delayed replica.

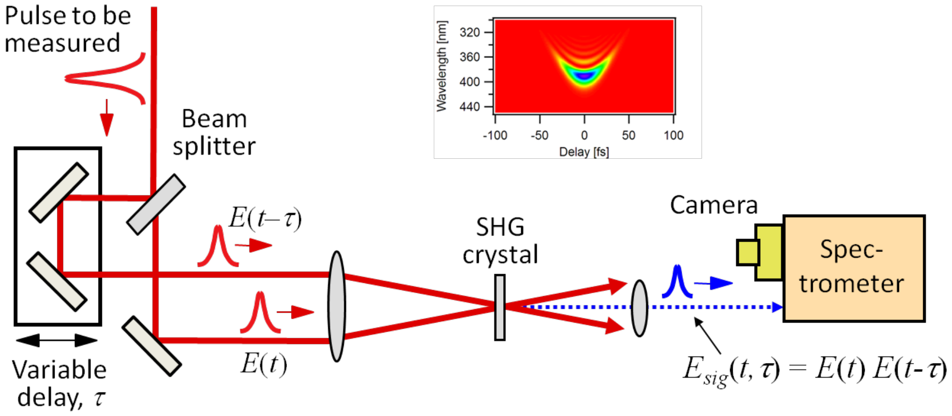

Fig. 2.7. *Representation of the SHG FROG technique with an inset of a FROG measurement. Image from [35].*

Although SHG FROG is the most extended version, there are many other FROG systems based on other nonlinear processes or configurations like Polarization gating [52], Third Harmonic Generation [53], Self-diffraction [54] or Transient Grating [55].

The FROG technique is, in principle, a multi-shot technique, since it needs to scan different delays between the pulse and the gate. Nevertheless, it was implemented a single-shot version substituting the beamsplitter and the delay line by a Fresnel biprism, and the thin nonlinear medium by a thick one with narrow and angular dependent spectral phase-matching to spatially resolve the frequencies. That single-shot version was called GRating-Eliminated No-nonsense Observation of Ultrafast Incident Laser Light E-fields (GRENOUILLE) [56].

Previously we have mentioned that the SI can be used to characterize pulses provided a known reference pulse. Taking into account this idea, the Self-Referenced Spectral Interferometry (SRSI) [57] uses the XPW nonlinear process to generate a FTL replica to be used as a reference in the SI with the pulse under test. Thus, the difference of phases extracted from the spectral interference is actually the phase of the pulse under test.

Another interferometric technique, and one of the most consolidated temporal characterization techniques, is called Spectral Phase Interferometry for Direct Electric-field Reconstruction (SPIDER), Fig. 2.8. This technique is based on the interference of two delayed and spectrally sheared replicas. The most usual configuration, firstly introduced in 1998 [58], uses a nonlinear process (generally SFG) to combine two delayed replicas with an extremely chirped pulse, so each replica observes a slightly different frequency of the chirped pulse (ω_0 and $\omega_0 + \Omega$). Therefore, the spectral interference of the replicas after the nonlinear process contains the spectral phase derivative ($\partial\varphi/\partial\omega$) and, by integration, the spectral phase can be extracted.

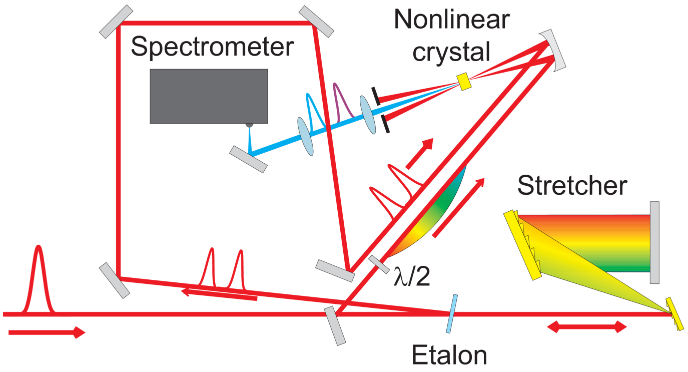

Fig. 2.8. *Representation of the SPIDER technique from [32].*

A well known technique is Multiphoton Intrapulse Interference Phase Scan (MIIPS) [59], which is based on the insertion of known GDD phase amounts while generating a SHG trace. By scanning the maximum of the trace, it measures the second derivative of the spectral phase and, integrating it, extracts the phase without the zero-th and first order terms of the Taylor expansion series.

Another temporal characterization technique is the dispersion-scan (d-scan) [60], which has strongly risen to establish itself as a consolidated technique in the characterization of few-cycle pulses (i.e., extremely short pulses with durations close to a single oscillation of the electric field) and other pulse ranges.

The d-scan technique, shown in Fig. 2.9, is based on adding different dispersion values to a pulse under test and, thus, generating a nonlinear signal and measuring its spectrum. As a result, a trace of the nonlinear spectrum for different added dispersion values is obtained. The pulse spectral phase is extracted from the trace by using an iterative algorithm. Usually the dispersion in a d-scan is simply introduced using two wedges over a translation stage [60], slightly tuning a grating or prism compressor [61] or even using an acousto-optic programmable dispersive filter [62].

In the simplest case, when the dispersion is introduced by two glass wedges over a translation stage and SHG as nonlinear process (Fig. 2.9), the d-scan trace can be expressed as:

$$S(\omega, z) = \left| \int_{-\infty}^{+\infty} \left(\int_{-\infty}^{+\infty} E(\omega) e^{ik(\omega)z} e^{-i\omega t} d\omega \right) e^{i\omega t} dt \right|^2 \qquad \textbf{(2.14)}$$

being z the material insertion, $k(\omega)$ the frequency dependent wavenumber in the dispersive medium, $k(\omega)z$ the dispersion phase term added and $E(\omega)$ the electric field of the pulse under test.

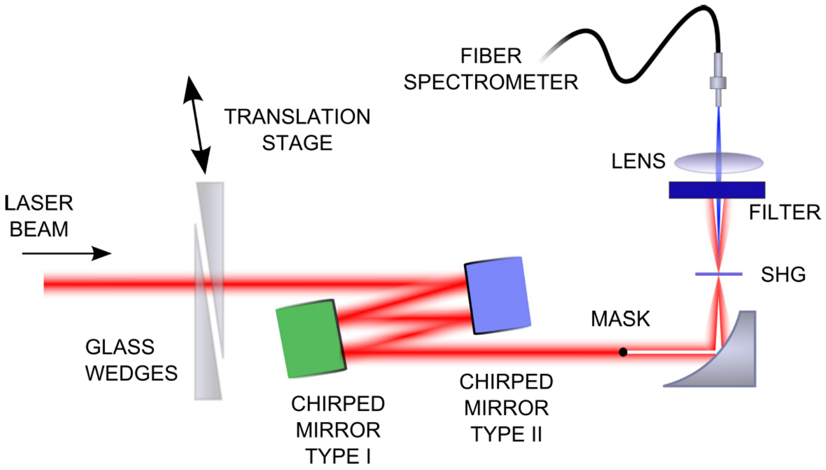

Fig. 2.9. *Representation of the d-scan technique from [60].*

Furthermore, the d-scan technique adds positive and negative dispersion to the pulse around the spectral phase compensation, so that it is naturally designed to measure almost compressed pulses. In particular, it is interesting for the analysis of few-cycle pulses because, if the dispersion scan is large enough (scanning a full trace), the frequency marginal of the trace (i.e., integral in the material insertion, z) does not depend on the pulse phase [63].

Thus, knowing the spectrum, the marginal for the FTL pulse trace can be simulated to calibrate the SHG signal. If the scan is not large enough, other strategies such as optimization during the retrieval can be used, like in other temporal techniques.

These are just some examples of temporal characterization techniques, but there are many more due to the continuous evolution of the field. Some recent techniques are time-domain ptychography [64], time-domain observation of an electric field (TIPTOE) [65], phase-matching-free pulse retrieval based on transient absorption in solids [66] or amplitude swing [31]. From this list of novel techniques we want to highlight the amplitude swing, which will be used in this Thesis and deeply studied in Part II, due to its compactness and robustness.

During the last decade, some strategies have been shown to identify some pulse trains instabilities in conventional temporal characterization techniques such as FROG [67, 68], MIIPS [69, 70] or d-scan [71, 72]. Nevertheless, in this Thesis we will always assume that the pulse trains are stable and do not change shot-to-shot.

2.2.3 Spatiotemporal characterization

During the last two decades, the importance given to spatiotemporal characterization has increased considerably and, with it, multiple spatiotemporal characterization techniques have emerged.

The main reason for the change in the approach towards the development of spatiotemporal techniques is due to the continuous advances in the laser field (e.g., new applications and possibility to have a greater control of the laser emission) and the desire to correctly measure the laser beams, avoiding distortions generated by the STCs or introducing them in a controlled manner [33, 34, 36, 37].

One could think that any STC can be studied by simply performing the temporal characterization, using one of the techniques mentioned in the previous Subsection in multiple spatial positions. However, these temporal techniques usually are insensitive to the zero-th and first orders of the spectral phase, so they are not sensitive to STCs as simple as pulse-front tilt or pulse-front curvature. Although there are some exceptions like GRENOUILLE, which has been proved to be sensitive to pulse-front tilt [73] and spatial chirp [74], in general the commented techniques cannot measure any other STC.

Therefore, for a complete and correct study of a beam with STCs it is necessary to use a spatiotemporal characterization technique and, nowadays, there are many different configurations. Anyway, the spatiotemporal characterization techniques usually measure relative phases and they need a temporal characterization of a reference pulse to obtain the absolute profile, so both types of techniques coexist.

One type of spatiotemporal characterization technique consists on modifying temporal techniques encoding the phase information in a 1D spectral trace, while measuring it with a 2D-imaging spectrometer in order to obtain the spatiotemporal characterization in a 1D spatial dimension. This is the case of Spatially Encoded Arrangement Spectral Phase Interferometry for Direct Electric-field Reconstruction (SEA SPIDER) [75], which uses the spatial fringes of the spectrally sheared replicas to obtain in one direction the phase spectral gradient ($\partial\varphi/\partial\omega$) and, in the other direction, the phase spatial gradient ($\partial\varphi/\partial x$).

Another type of spatiotemporal characterization technique uses the spectral interferometry and monomode optical fibers to obtain the spatiospectral phase. On one hand, Spatially Encoded Arrangement for Temporal Analysis by Dispersing a Pair Of Light E-fields (SEA TADPOLE) [76] scans with one fiber the beam under test, whereas another static fiber collects the reference beam. Then, both signals go out the fibers collimated in free space propagation, spectrally angularly dispersed using a diffraction grating and collimated with a tilt among them over a camera, so the camera records the spatial interference among both pulses, reference and test, at a given spatial position, spectrally resolved, Fig. 2.10(a).

On the other hand, Spatio-Temporal Amplitude-and-phase Reconstruction by Fourier-transform of Interference Spectra of Highly-complex-beams (STARFISH) [77] introduces a certain delay between the reference and test arms, and uses a special monomode optical fiber coupler to measure the spectral interference of each spatial position in a common spectrometer, Fig. 2.10(b). Both techniques give the relative phase with respect to the reference, so they need a temporal technique to measure the reference phase and obtain the absolute spatiotemporal characterization.

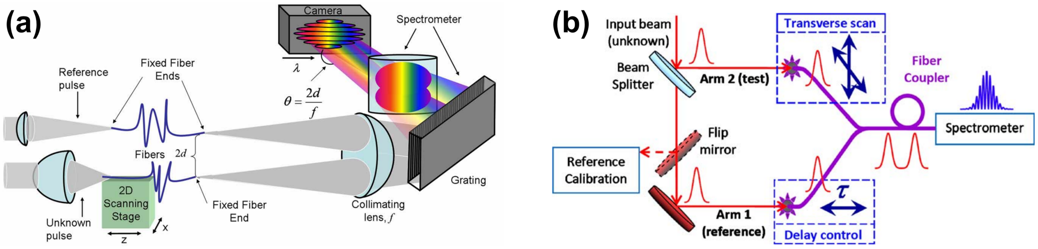

Fig. 2.10. *Representation of (a) SEA TADPOLE technique from [78] and (b) STARFISH from [77].*

There is another group of spatiotemporal techniques that is based on the Fourier Transform Spectroscopy (FTS) method, changing slightly the implementation. Essentially, FTS enables measuring the spectrally-resolved relative phase between two interfering beams using a time-integrating detector, provided that the delay between both beams is scanned with sub-cycle resolution. Mathematically the signal measured by the time-integrating detector ($\widetilde{I}(\vec{r},\tau)$) can be expressed as:

$$\widetilde{I}(\vec{r},\tau) = \int_{-\infty}^{+\infty} |E_T(\vec{r},t) + E_R(\vec{r},t-\tau)|^2 dt \qquad \textbf{(2.15)}$$

where E_T and E_R correspond to the electric fields of the beam under test and the reference beam, respectively. Moreover, $\vec{r}$, t and ω represent the space, time and frequency coordinates, respectively, whereas τ indicates the delay introduced among them. Then:

$$\varphi_T(\vec{r},\omega) - \varphi_R(\vec{r},\omega) = Arg\left\{\widetilde{I}(\vec{r},\omega)\right\} = Arg\left\{\mathscr{F}^{-1}\left\{\widetilde{I}(\vec{r},\tau)\right\}\right\} \qquad \textbf{(2.16)}$$

being $\varphi_T(\vec{r},\omega)$ and $\varphi_R(\vec{r},\omega)$ the spectral phase of the beam under test and the reference beam respectively, and Arg a function to obtain the argument of the complex number. Moreover, if $|\widetilde{I}(\vec{r},\omega)|^2$ is measured, it is equivalent to measuring the product of both pulses spectra.

The main difference between the two principal spatiotemporal techniques based on FTS is the reference beam. On one hand, in [79] a spherical beam generated by spatially filtering a replica of the beam under test with a pinhole is used as a reference, Fig. 2.11(a).

On the other hand, in the Total E-field Reconstruction using a Michelson Interferometer TEmporal Scan (TERMITES) technique [80], it is used a curved mirror in the reference arm of the interferometer, Fig. 2.11(b). Thus, the beam under test is interfering with a diverging tiny part of itself, which can be extracted within the algorithm, obtaining the spatiospectral phase of the beam under test.

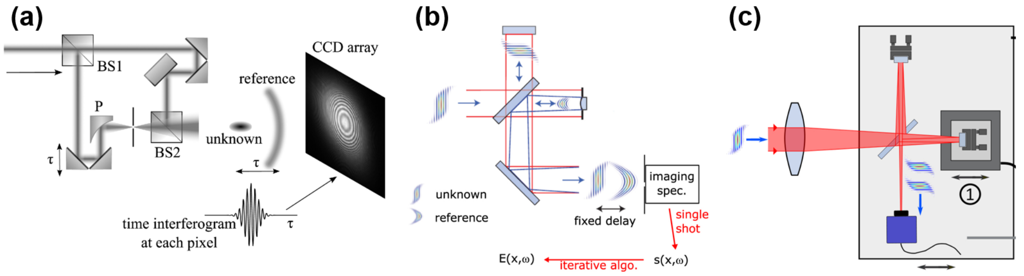

Fig. 2.11. *Representation of the FTS based spatiotemporal techniques: (a) pinhole filtering of reference from [79], (b) TERMITES from [80] and (c) INSIGHT from [81].*

Furthermore, there is another widespread technique, INSIGHT [81], which focuses the beam before the interferometer and measures the FTS at three different propagation planes around the focal plane, Fig. 2.11(c). This technique uses a Gerchberg-Saxton algorithm [82] to obtain the spatiotemporal characterization of the beam under test.

A fourth approach for the spatiotemporal characterization consists on combining a wavefront sensor with a temporal characterization technique to link the frequencies at a certain spatial point, as it is done in Shackled-FROG [83], combining a Shack-Hartmann wavefront sensor with a FROG system. Other possibilities are to use the Shack-Hartmann with programmable spectral filters like is done in Hartmann–Shack-assisted, Multidimensional, Shaper-based Technique for Electric-field Reconstruction (HAMSTER) [84] or narrow bandpass filters as done in [85].

Finally, in another different group it is included Spatially and Temporally Resolved Intensity and Phase Evaluation Device: Full Information from a Single Hologram (STRIPED FISH) [86], Fig. 2.12. It uses a 2D tilted diffraction grating and an angle dependent spectral filter to generate over a camera a spatial interference pattern for each frequency, encoding the spatiospectral phase difference between the beam under test and a reference beam.

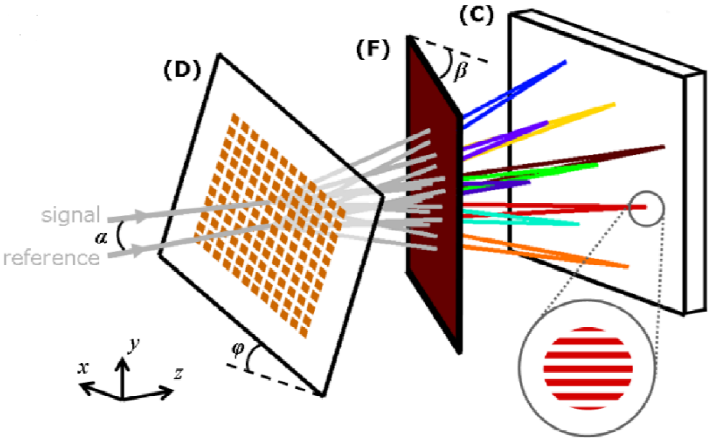

Fig. 2.12. *Representation of the STRIPED FISH technique from [86] .*

It is clear that there are multiple spatiotemporal techniques, but usually they require complex set-ups or present high dependence to external perturbations. Consequently, there is still a necessity of developing new spatiotemporal techniques that can be more robust and simple. Taking this into account, in Part III of this Thesis we will focus on the development of a compact, simple and ultra-stable spatiotemporal technique.

Part II

TEMPORAL CHARACTERIZATION WITH AMPLITUDE SWING

Chapter 3

Amplitude swing technique

In the last decade, interest in developing more compact and simpler ultrashort characterization techniques has aroused, which can also analyze a large range of temporal durations with the same system. Moreover, the scientific community is seeking for robust techniques that can operate in less controlled conditions.

Following these motivations, few years ago it was developed the amplitude swing technique [31] as a simple, compact and robust temporal characterization technique that can be implemented with common and relatively inexpensive optical elements (e.g., optical polarizers, retarder plates).

3.1 Fundamentals of amplitude swing

Amplitude swing is an in-line temporal characterization technique based on the generation of two replicas, shifted by a given temporal delay, whose relative amplitude is varied before a nonlinear process. The resulting interference pattern created by the relative amplitude changes depends not only on the amplitude of the initial pulse, but also on its phase. Thus, a nonlinear process, like SHG, can be used to encode this information in a spectrally resolved nonlinear trace that can be obtained by measuring SHG spectra while scanning different relative amplitudes.

One simple and robust implementation of this technique [31] relies on using a rotating birefringent element with a given thickness and its optical axis contained in the surface, also known as multi-order waveplate (MWP), followed by a linear polarizer to generate the interference pattern in an in-line configuration. This combination produces two replicas of the initial pulse with a fixed temporal delay whose relative amplitude changes depending on the MWP axes orientation.

3.1.1 Amplitude swing trace

Consider a horizontally polarized input pulse with normal incidence on the MWP. Assuming that the MWP has its fast axis forming an angle θ with the horizontal (x-) axis, after going through it, as seen in [31], the electric field will be given by:

$$\begin{cases} E_x(\omega) = E_0(\omega)\left(e^{i\rho_f(\omega)}\cos^2\theta + e^{i\rho_s(\omega)}\sin^2\theta\right) \\ E_y(\omega) = E_0(\omega)\left(e^{i\rho_f(\omega)} - e^{i\rho_s(\omega)}\right)\cos\theta\sin\theta \end{cases} \tag{3.1}$$

being ρ_f and ρ_s the phases introduced by the fast and slow axes of the MWP, respectively, and $E_0(\omega)$ the electric field of the initial pulse.

If the horizontal projection is selected using a linear polarizer, and propagated through a SHG crystal for different rotation angles of the MWP, it will be obtained:

$$\begin{gathered} S_x^{SHG}(\omega,\theta) = \left|E_x^{SHG}(\omega,\theta)\right|^2 = \left|\int (E_x(t,\theta))^2 e^{i\omega t}dt\right|^2 = \\ = \left|\int \left(\int E_x(\omega',\theta)e^{-i\omega' t}d\omega'\right)^2 e^{i\omega t}dt\right|^2 \Longrightarrow \\ S_x^{SHG}(\omega,\theta) = \left|\int \left(\int E_0(\omega')\left[e^{i\rho_f(\omega')}\cos^2\theta + e^{i\rho_s(\omega')}\sin^2\theta\right]e^{-i\omega' t}d\omega'\right)^2 e^{i\omega t}dt\right|^2 \end{gathered} \tag{3.2}$$

where $S_x^{SHG}(\omega,\theta)$ is the spectrally resolved SHG trace for different angles of the MWP.

Before presenting the analytical model for a specific case, we can simulate the interference term (Eq. **3.1**) and the corresponding SHG signal (Eq. **3.2**) for some MWP rotation angles and different spectral phases to have an idea of the amplitude swing concept. Fig. 3.1 shows the simulation of the interference pattern (first row) and SHG signal (second row) for a given spectrum centered in 800 nm with a spectral phase with opposite GDD sign: Figs. 3.1(a,c) and Figs. 3.1(b,d) correspond to GDD<0 and GDD>0, respectively.

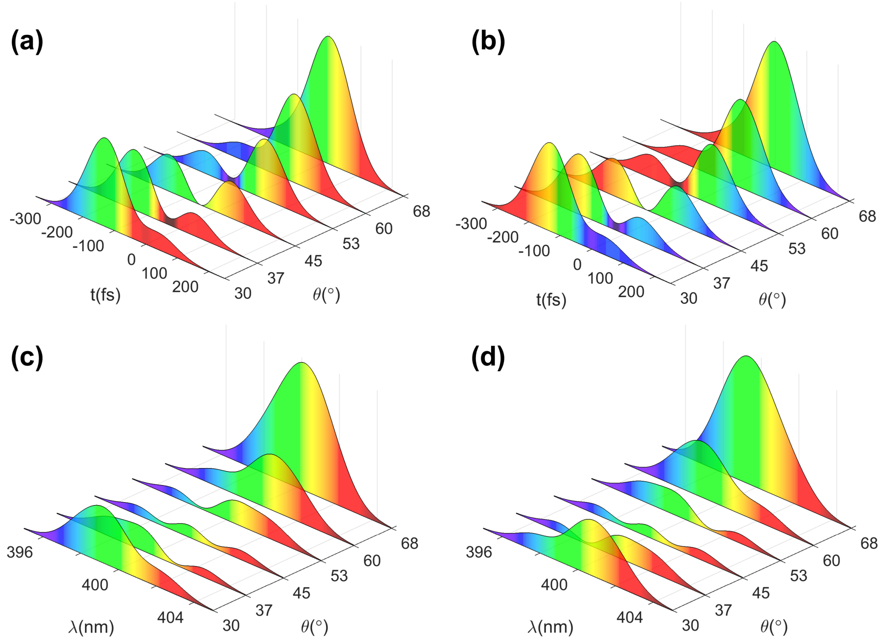

Fig. 3.1. *Simulation of amplitude swing fundamental temporal intensity interference term (a,b) and SHG spectrum (c,d) for some rotation angles of the MWP considering a pulse under test with the same spectrum but opposite chirp sign: (a,c) GDD<0 and (b,d) GDD>0. The temporal intensities of (a,b) are colored with the instantaneous wavelength. Images from [87].*

Please notice that we only represent some angles of an amplitude swing scan to understand the process. From Figs. 3.1, it can be extracted that the SHG signal produced with amplitude swing is sensitive to the phase.

Analytical model

A first look at Eq. **3.2** indicates that the amplitude swing traces depend on the electric field of the pulse under test ($E_0(\omega)$). In [31], it was presented an analytical development to verify that amplitude swing traces depend on the phase of the pulse under study. In that model [31], it was considered a Gaussian pulse with a given quadratic phase (b=GDD/2), whose electric field is given by:

$$E_0(\omega) = A_0 e^{-i\cdot b(\omega-\omega_0)^2} e^{-(\omega-\omega_0)^2/\Gamma^2} \tag{3.3}$$

where A_0 corresponds to the amplitude, Γ is the Gaussian spectral bandwidth and ω_0 the central frequency.

In that study, it was shown that the horizontal projection of the electric field in temporal domain after going through the MWP is given by Eq. **3.4**. Notice that, for simplicity, it was considered that the phase terms associated to the fast and slow axes are constant along the bandwidth and they expressed them as a certain optical path difference $\delta = (n_y - n_x) \cdot d$, being d the thickness and n_x and n_y the refractive indices of the two orthogonal projections of the MWP.

$$E_x(t) = \frac{A_0}{\sqrt{2\left(\Gamma^{-2} + ib\right)}} \left(e^{-i\omega_0 t - \frac{1}{1+ib\Gamma^2}\left(\frac{t\Gamma}{2}\right)^2} \cos^2\theta + e^{-i\omega_0\left(t-\frac{\delta}{c}\right) - \frac{1}{1+ib\Gamma^2}\left(\left(t-\frac{\delta}{c}\right)\frac{\Gamma}{2}\right)^2} \sin^2\theta \right) \tag{3.4}$$

From the interfering electric field of Eq. **3.4**, in [31] the following expression for the amplitude swing trace of this pulse under study was obtained:

$$\begin{gathered} S_x^{SHG}(\omega,\theta) = \frac{A_0^4 e^{-2\frac{(\omega-2\omega_0)^2}{2\Gamma^2}}}{4\sqrt{\Gamma^{-4}+b^2}} \cdot \left[\cos^8\theta + \right. \\ +4e^{-\frac{1}{2(1+b^2\Gamma^4)}\left(\frac{\Gamma\delta}{2c}\right)^2} \cos\left(\frac{\omega\delta}{2c} + \frac{b\Gamma^4}{8(1+b^2\Gamma^4)}\left(\frac{\delta}{c}\right)^2\right) \cos^6\theta\sin^2\theta + \\ +2\cos\left(\omega\frac{\delta}{c}\right)\cos^4\theta\sin^4\theta + 4e^{-\frac{1}{(1+b^2\Gamma^4)}\left(\frac{\Gamma\delta}{2c}\right)^2}\cos^4\theta\sin^4\theta + \\ \left. +4e^{-\frac{1}{2(1+b^2\Gamma^4)}\left(\frac{\Gamma\delta}{2c}\right)^2} \cos\left(\frac{\omega\delta}{2c} - \frac{b\Gamma^4}{8(1+b^2\Gamma^4)}\left(\frac{\delta}{c}\right)^2\right) \cos^2\theta\sin^6\theta + \sin^8\theta \right] \end{gathered} \tag{3.5}$$

Therefore, as hinted in [31], the SHG signal contains the information of the spectral phase (b in this simplified demonstration with quadratic dependence). Moreover, all terms that contain b are linked with the optical path difference (δ) of the MWP. On one hand, high values of δ imply a considerable reduction of the terms depending on b, even vanishing, due to the negative exponentials. On the other hand, extremely low values of δ make the cosine terms tend to zero, decreasing or even fading the terms depending on b. Moreover, in those dependences, δ is linked with the spectral bandwidth (Γ). Thus, if Γ is getting smaller, it is required bigger δ values to conserve the terms that depend on b.

In conclusion, the MWP thickness and material must be selected to introduce a temporal delay (δ/c, being c the speed of light) that balances all the terms, efficiently encoding the phase information. From the analysis of this simplified case, it can be extracted that the temporal delay of the MWP ($\tau = \delta/c$, with c the speed of light) must be of the order of the FTL pulse duration. Later in Section 3.3 we will explore the flexibility of this constraint. Indeed, provided a MWP delay suitable for the FTL duration, chirped pulses with temporal durations much longer than the delay introduced can be analyzed, as it will be shown later.

The phase dependence of the amplitude swing traces can also be observed by simulating traces with different spectral dependences using Eq. **3.2**, as done in Fig. 3.2.

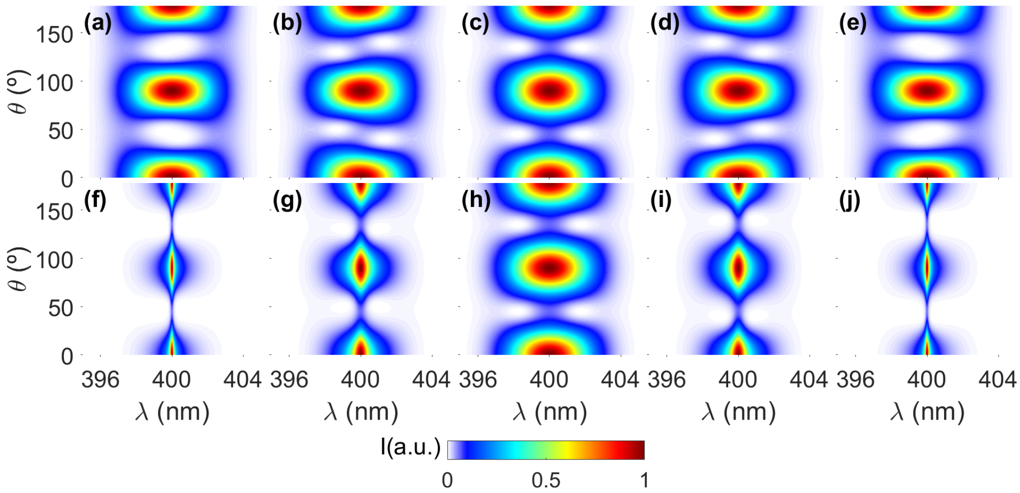

Fig. 3.2. *Simulation of amplitude swing traces for a Gaussian spectrum centered at 800 nm with a FTL duration of 100 fs and a MWP acting as HWP and introducing a delay equal to the FTL duration for different values of GDD and TOD added. GDD cases: (a) -40000 fs*^{2}*, (b) -5000 fs*^{2}*, (c) 0 fs*^{2}*, (d) 5000 fs*^{2} *and (e) 40000 fs*^{2}*. TOD cases: (f) -4* $\cdot\, 10^6$ *fs*^{3}*, (g) -*10^6 *fs*^{3}*, (h) 0 fs*^{3}*, (i)* 10^6 *fs*^{3} *and (j)* $4 \cdot 10^6$ *fs*^{3}*.*

In these examples we have considered a Gaussian spectrum centered at 800 nm with a FTL pulse duration of 100 fs to which is added a certain dispersion value. Moreover, we have assumed a MWP acting as a half-waveplate (HWP) at 800 nm and introducing a 100-fs delay (equal to the FTL duration).

Figs. 3.2(a-e) show the amplitude swing SHG traces when adding different values of GDD to the pulse under test. On the other hand, Figs. 3.2(f-j) depict the simulations using the same spectrum but adding TOD instead of GDD.

From these simulations it can be extracted that the presence of GDD introduces lobes, whereas the TOD produces a spectral narrowing in the traces. Moreover, opposite signs of GDD and TOD are manifested differently in the SHG traces. The change in the TOD sign is harder to see, but easily retrieved with a comparative algorithm. Thus, amplitude swing is sensitive to chirp sign, as expected from the analytical model.

The particular features of the traces will change depending on the incident pulse and the used MWP, but it is clear that the trace will contain the electric field information. Therefore, a retrieval algorithm can be used to obtain it, as it will be discussed in Section 3.2.

Furthermore, analyzing the trace dependence with the rotation angle of the MWP (examples of Fig. 3.2 and Eq. **3.2**), it can be extracted that the amplitude swing traces from 90°-180° are a mirror of the scan from 0°-90°. In addition, the traces are repeated with a period of 180°. Therefore, amplitude swing traces from 0°-180° contain all the information.

3.1.2 Experimental set-up

In Fig. 3.3 it is represented the scheme of the experimental implementation of the amplitude swing technique for the characterization of horizontally polarized pulses.

In this scheme, it can be observed the rotating MWP, whose fast axis forms an angle θ with the horizontal axis, and the linear polarizer (LP) that selects the horizontal projection. Sometimes, if the laser beam power is too low, it could be necessary to use a lens (L) to focus the beam on the nonlinear medium (NL) in order to increase the SHG signal, thus improving the signal

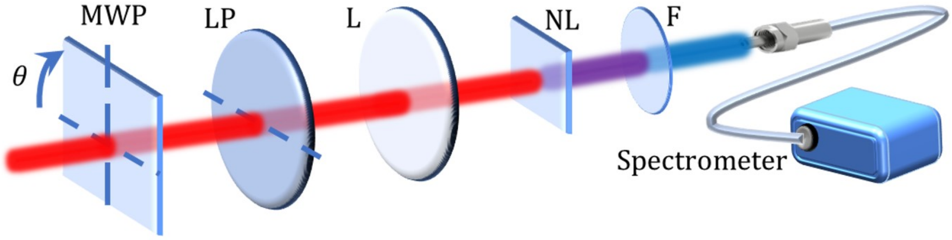

Fig. 3.3. *Scheme of the amplitude swing technique working with the input pulses with horizontal polarization. Image from [31].*

to noise ratio. After the nonlinear medium, it can be introduced a filter (F) to select the SHG signal (removing the fundamental signal). This filter can be either a color filter or, e.g., if the nonlinear medium presents Type-I phase-matching, a linear polarizer (in that case, fundamental and SHG signal will have orthogonal polarizations). This last option is specially interesting if the fundamental and SHG signals spectrally overlap (e.g., the case of few cycle pulses, exhibiting ultra-broadband spectra). Finally, the SHG signal is measured with a spectrometer for different orientations of the MWP.

3.2 Retrieval algorithm

In Subsection 3.1.1, it has been mentioned some features of the pulse that can be extracted from an amplitude swing trace (e.g., presence and sign of GDD or TOD). However, these features are not general and depend on the pulse under test and the MWP used. Nonetheless, the electric field information of an arbitrary pulse is codified in the amplitude swing trace, so the full spectral phase can be extracted using a retrieval algorithm to analyze them.

Expressing the electric field of the pulse under test as $E_0(\omega) = A(\omega)e^{i\varphi(\omega)}$, the amplitude swing trace for a horizontally polarized pulse of Eq. **3.2** will be:

$$S_x^{SHG}(\omega,\theta) = \left| \int \left(\int A(\omega')e^{i\varphi(\omega')} \left[e^{i\rho_f(\omega')} \cos^2\theta + e^{i\rho_s(\omega')} \sin^2\theta \right] e^{-i\omega' t} d\omega' \right)^2 e^{i\omega t} dt \right|^2 \tag{3.6}$$

As previously mentioned, $\rho_f(\omega)$ and $\rho_s(\omega)$ are the phases added by the fast and slow axes, respectively. These phase terms can be calculated from the refractive indices and thickness of the MWP, knowing the phase retardation (i.e., zero-th order phase between fast and slow axes) at any certain wavelength (e.g., the central wavelength). On one hand, the refractive indices can be obtained using the Sellmeier equations. On the other hand, the phase retardation can be given by the manufacturer or experimentally calibrated (e.g., using the technique presented in [88]).

If the pulse spectrum is experimentally measured, what can be easily done using a spectrometer, the only unknown variable in Eq. **3.6** will be the spectral phase of the pulse. Thus, an iterative algorithm can be used to obtain it.

Regarding the spectral phase function, there are different ways to parameterize it. Some examples are: Taylor expansion, Fourier expansion and spectral phase or phase derivative discretized at certain frequencies, or combinations of them. Indeed, provided a phase parameterization, different algorithms can be used to retrieve it [89, 90].

In particular, the amplitude swing works previous to this Thesis [31, 91] used a gradient-based algorithm, Levenberg-Marquardt nonlinear optimization algorithm. Knowing the fundamental spectrum it can retrieve the phase that minimizes the differences between the experimental and the retrieved traces.

Moreover, in its application to amplitude swing [31, 91] the authors used the algorithm in two steps. The first one parameterized the phase as a combination of second (GDD) and third (TOD) order terms of the Taylor expansion to obtain a first approximation to the solution. The second one optimized the first derivative of the discretized phase, using the first step solution as a guess, to obtain the final optimized solution.

Despite the amplitude swing traces from 90° to 180° is a mirror of the 0° to 90°, the scans were done from 0° to 180° to have data redundancy. Furthermore, the presence of any asymmetry of the pattern in the 0°-180° scan will hint that something is not working correctly.

The Levenberg-Marquardt retrieval algorithm was tested with different pulses showing good convergence even with high GDD and TOD values. Fig. 3.4 shows some examples of retrievals presented in [31], which correspond to the amplitude swing traces simulated in Fig. 3.2(a-e).

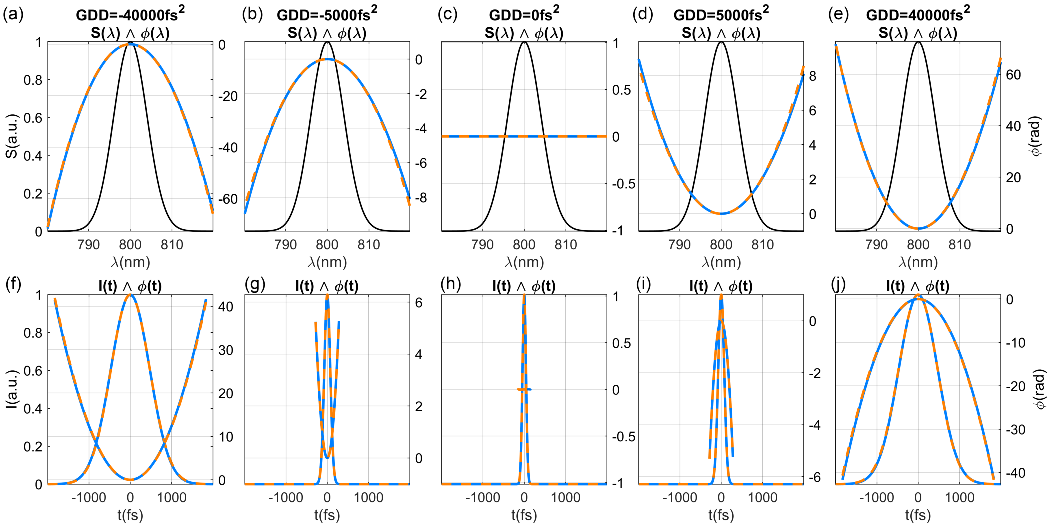

Fig. 3.4. *Comparison of the electric fields retrieved from the amplitude swing traces with GDD shown in Fig. 3.2 using the Levenberg-Marquardt algorithm and the theoretical fields. (a-e) Spectrum (black) and spectral phases. (f-j) Temporal intensity and phase. Simulated (solid blue) and retrieved (dashed orange). Image from [31].*

Apart from the GDD and TOD studies, the algorithm was numerically tested with more complex structures, like a sinusoidal phase term, obtaining good results. In addition, in its first work it was experimentally verified with the well stablished techique self-calibrating d-scan [61].

3.3 Capabilities of the technique

The main advantages of amplitude swing over other conventional temporal characterization techniques, such as FROG [52] or SPIDER [58], lie in its capacity to characterize pulses with different temporal durations in various spectral regions with a compact in-line system, which presents high stability and direct alignment. In addition, in a recent work [91] it has been demonstrated that, due to the data redundancy in the trace, amplitude swing is also robust under less controlled situations (e.g., noise or clipping in the trace).

In [31] it was observed that, provided an appropriate delay respect to the FTL pulse duration, amplitude swing can characterize pulses much longer than their FTL durations. This is shown in the limit cases of Fig. 3.4, in which structures around 1-2 ps were measured for a FTL duration of 100 fs and also in the TOD cases shown in [31].

To study other capabilities of the amplitude swing technique, in [91] several simulations under different conditions were performed and it was used the Levenberg-Marquardt algorithm previously mentioned to analyze the traces, thus verifying a correct phase codification. The simulations of that study were done for a theoretical pulse with a Gaussian spectrum (centered at 800 nm with FTL duration of 50 fs FWHM) and a spectral phase combining a GDD of -8000 fs^2 and a TOD of 20000 fs^3, but the conclusions obtained can be extended to a general case, as detailed below.

Previously, it has been mentioned that the delay introduced by the plate should be of the order of the FTL pulse duration to efficiently codify the phase information. In [91] the authors simulated amplitude swing traces for different delays relative to the FTL pulse durations (τ/τ_{FL}) to see the range of possible values that can be used. Fig. 3.5 shows some simulations of the amplitude swing traces and the retrievals obtained for relative delays going from one fifth to 4 times the FTL duration.

From this analysis, the authors concluded that, being conservative, a MWP with a certain delay (τ) can characterize pulses with a FTL duration up to three times bigger or smaller than τ.

Furthermore, the authors studied the effects of the phase retardation observing that the trace patterns change considerably depending on its value, but always encoding efficiently the phase information. Thus, any value of phase retardation can be chosen. In Fig. 3.6 there are shown some of the simulations for different values of phase retardation used in [91] to demonstrate this idea.

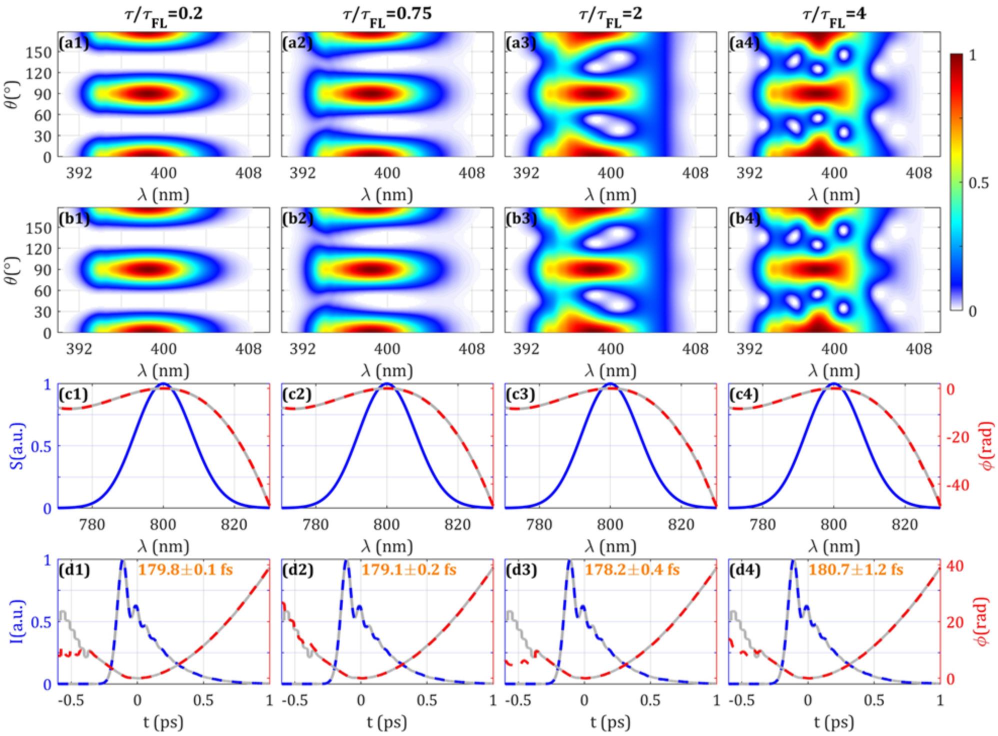

Fig. 3.5. *Simulation for different relative delay of the MWP compared to the FTL duration (τ/τ_{FL}). (a) Simulated and (b) retrieved amplitude swing traces. For each case it is shown the (c) spectral and (d) temporal comparison between the simulations (gray) and retrievals (dashed blue and red). Image from [91].*

Apart from studying the influence of the MWP parameters (delay and phase retardation), in [91] they also analyzed the possibility to study noisy or incomplete traces. On one hand, the authors observed that the information redundancy in the trace is enough to correctly retrieved the pulse information even with relatively noisy traces. In the cases presented in [91] the convergence is acceptable for noise up to 5% root-mean-square (rms) of the noise to signal.

On the other hand, different ways of spectral clipping were studied due to their interest, since they can occur, for example, if part of the SHG signal is absorbed by the optical elements or cannot be measured with the spectrometer. In [91], they observed that the retrievals can be done successfully for moderate lateral (high or low frequencies) or central spectral clipping.

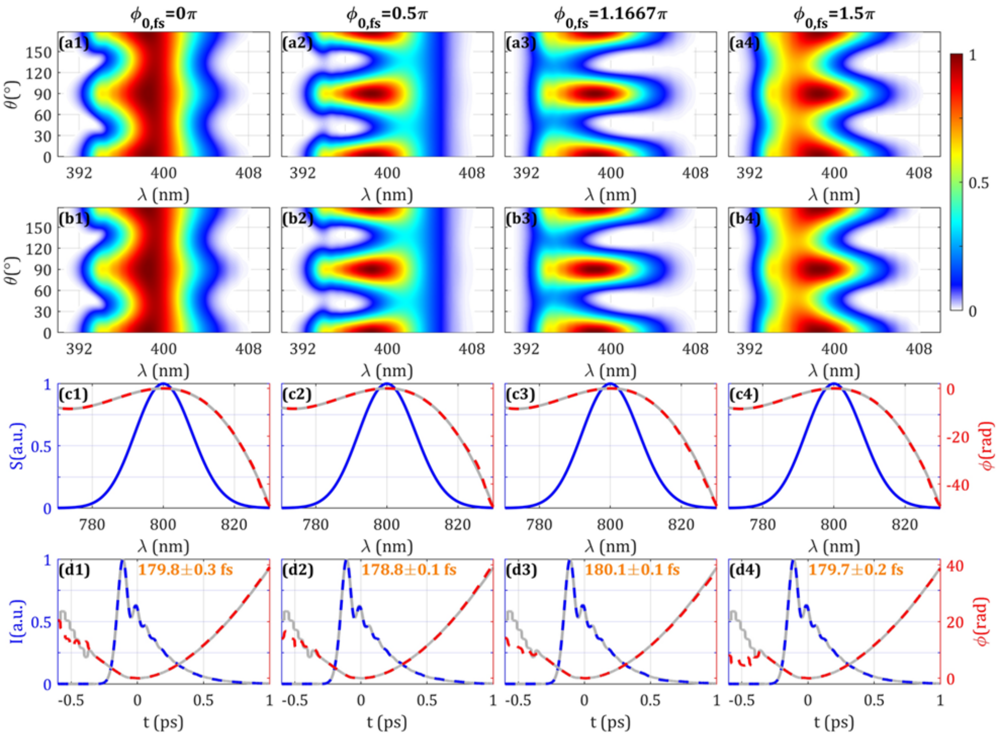

Fig. 3.6. *Simulation for different phase retardation of the MWP. (a) Simulated and (b) retrieved amplitude swing traces. Moreover, for each case is shown the (c) spectral and (d) temporal comparison between the simulations (gray) and retrievals (dashed blue and red). Image from [91].*

Related to the idea of spectral clipping, it can also happen that the phase-matching can be incomplete or non-flat for all the spectral bandwidth. In that case, it is necessary to calibrate the SHG response either experimentally, theoretically or iteratively in the algorithm. In the study of [91], it was analyzed the frequency marginal (i.e., integral of the amplitude swing trace in the angular dimension), to see if it is phase invariant, but it was observed that, in amplitude swing, that marginal depends on the initial pulse phase.

Despite the complete analysis of the operability of amplitude swing previously performed [91], further studies can be done in order to exploit all the advantages of this technique. Taking this into account, in this Thesis we have analyzed the possibility to operate in different spectral regions (Chapter 5), with pulses in the few-cycle regime (Chapter 6) and using different configurations of rotating and fixed plates (Chapter 7). Moreover, in order to explore new ways to analyze amplitude swing data, we have implemented a different kind of algorithm based on genetic algorithms, which will be explained in Chapter 4 and used in the retrievals of Chapter 5.

Chapter 4

Differential evolution amplitude swing algorithm

In Chapter 2, it has been explained that temporal characterization techniques usually encode the pulse information in nonlinear traces, which have to be analyzed using retrieval algorithms. Since the first characterization technique was implemented, many different retrieval algorithms have been proposed.

For example, the analysis of FROG traces is usually done with a Generalized Projections (GP) algorithm [92] or its advanced version, Principal Components Generalized Projections Algorithm (PCGPA) [93]. In the case of d-scan, nonlinear optimization algorithms such as Nelder-Mead (NM), Broyden-Fletcher-Goldfarb-Shanno (BFGS) or Levenberg-Marquardt (LM) [61, 94, 95] are widely used. Other strategies used to analyze the nonlinear traces of these techniques have been Differential Evolution (DE) [96], Ptychographic reconstruction [97] or, more recently, deep neural networks [98, 99].

Regarding the amplitude swing, as mentioned before, the works previous to this Thesis [31, 91] were done based on a Levenberg-Marquard nonlinear optimization algorithm, but different approaches can be taken into account. A quite interesting possibility are genetic algorithms and, in particular, the DE algorithms, due to their low probability to stagnation in a local minima, as shown using d-scan in [89].

4.1 Fundamentals of differential evolution algorithms

Differential evolution algorithms are a popular class of evolutionary algorithm that were firstly introduced by Storn and Price at the end of the 20^{th} century [100]. These algorithms are based on Darwin's theory of evolution and they mimic the biological selection process to obtain the optimal solution mixing a set of possible solutions, each called chromosome.

Since their introduction, various strategies have been proposed [96, 100, 101], but all of them are based on the same four processes: initialization, mutation, crossover and selection. The initialization is done one time at the beginning of the algorithm, whereas the other three processes are repeated iteratively until a given convergence criterion (e.g., certain merit function value or maximum number of iterations) is reached, Fig. 4.1.

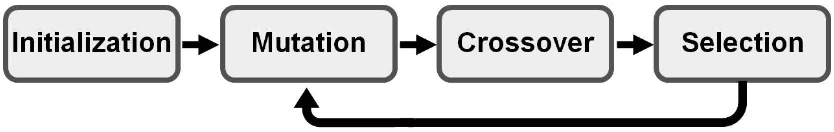

Fig. 4.1. *Flux scheme of a DE algorithm.*

Usually the initialization consists on the creation of a starting population of N possible solutions, each with D elements, generated by random selection between some boundaries. Each possible solution is called target vector (x) and can be expressed as:

$$x_i^j = rand(Bounds) \quad \text{being} \quad j = 1, ..., N \text{ and } i = 1, ..., D$$

The mutation process corresponds to the perturbation applied to each target vector to generate a new offspring. The target vector after mutation is called donor vector (v) and, during the last decades, many strategies have been proposed for this mixing process. For simplicity, the different strategies are called *'DE/∗/n'*, being *'∗'* the target vector considered during mutation and *'n'* the number of difference vectors involved in the change (i.e., number of target vectors differences taken into account to generate the perturbation).

Some examples of mutation strategies are summarized in Table 4.1, where F represents the scaling factor that weights the combination in the mutation, which is typically in the range $F \in (0, 2]$.

Strategy	**Mutation expression**
DE/rand/1	$v_i = x_{r_1} + F\,(x_{r_2} - x_{r_3})$
DE/rand/2	$v_i = x_{r_1} + F\,(x_{r_2} - x_{r_3}) + F\,(x_{r_4} - x_{r_5})$
DE/best/1	$v_i = x_{best} + F\,(x_{r_1} - x_{r_2})$
DE/best/2	$v_i = x_{best} + F\,(x_{r_1} - x_{r_2}) + F\,(x_{r_3} - x_{r_4})$

Table 4.1: Examples of mutation strategies used in DE algorithms that can be used to generate a new donor vector (v_i) by combining different target vectors (x_{r_l}) using the scaling factor (F) to weight the mutation process.

In all the mutation strategies the mixing indices r_l are selected randomly from the D elements of the target vector verifying that $r_1 \neq r_2 \neq r_3 \neq r_4 \neq r_5 \neq i$. Moreover, there are some strategies, referred as *'DE/best'*, in which the modification is applied to the target vector with the lowest merit function value, x_{best} (i.e., all modifications are applied to the best solution of the population).

Once the donor vector is generated, it can be done the crossover process in order to obtain the new offspring, which is called trial vector (u). Also there are different strategies of crossover. One of the most common strategies is called binomial crossover (*'bin'*), which updates the element of the solution if a random number in the range $[0, 1]$ is lower than the crossover probability (p_c) and/or if the element index is equal to an integer δ randomly selected from the set $\{1, 2, ..., D\}$:

$$u_i^j = \begin{cases} v_i^j & \text{if } r \leq p_c \text{ or } j = \delta \\ x_i^j & \text{if } r > p_c \text{ or } j \neq \delta \end{cases} \qquad \textbf{(4.1)}$$

where $\delta = rand\{1, ..., D\}$, $r = rand(0, 1)$ and $p_c \in (0, 1)$.

Another strategy is called exponential crossover. In this case, the recombination starts at a randomly selected element index $i = rand\{1, ..., D\}$ and, in cyclical order, for each element is calculated a random number in the range $(0, 1)$, so:

- If $rand(0, 1) \leq p_c$, that element of the trial vector is equal to the corresponding donor vector element.
- If $rand(0, 1) > p_c$, the recombination is stopped and all the remaining elements of the trial vector are equal to the target vector.

After the crossover, the merit function is evaluated for each trial vector (offspring) and compared to the value of the target vector (parent), selecting for each index $j = 1, ..., N$ the solution with the lowest merit value. There are different possible definitions of merit functions depending on the problem under study and later, in Section 4.2, it will be explained the one used for amplitude swing.

Finally, the mutation, crossover and selection processes are repeated iteratively until the desired convergence criterion is reached. After convergence, the solution with the lowest merit function is selected as the optimal solution to the optimization problem under study.

Notice that the most important parameters that control the DE algorithm are the scaling factor (F) and the crossover probability (p_c), and it is crucial to select them appropriately to correctly converge. Regarding the scaling factor, extremely low values of F will allow only small changes, thus slowing down the convergence and even implying stagnation into a local minima. On the other hand, too large values of F may prevent an optimal convergence in a reasonable time, since moderate changes are required when the solution is close to the optimal value. Regarding the crossover probability, very low values of p_c may inhibit meaningful modifications in the new offspring, slowing down the convergence significantly. Moreover, extremely high values of p_c may introduce strong changes at each iteration, hindering the convergence into the optimal when the solution is close to it.

4.2 Differential evolution applied to amplitude swing

The information known in an amplitude swing measurement is the SHG trace, the system parameters and the fundamental spectrum, so the unknown term that must be retrieved is the spectral phase of the pulse under test. In a DE algorithm it is required to parameterize that phase function as a chromosome with D elements and there are many ways of doing it. Some examples are:

- **Taylor expansion**

  In this case, the phase is parameterized as a Taylor expansion series, being each element of the D length chromosome the coefficient of the Taylor series. Moreover, since the amplitude swing is insensitive to the phase offset and the linear term, we can express the phase starting the Taylor series at the second order:

  $$\varphi(\omega) = x_1 \cdot \frac{(\omega-\omega_0)^2}{2!} + x_2 \cdot \frac{(\omega-\omega_0)^3}{3!} + ... + x_D \cdot \frac{(\omega-\omega_0)^{D+1}}{(D+1)!} \quad \mathbf{(4.2)}$$

  where ω_0 corresponds to the central frequency of the fundamental spectrum and x_i to the element i of the target vector, being $i \in [1, ..., D]$.

- **Fourier expansion**

  In this case, the phase is parameterized as a Fourier series, being the elements of the D length chromosome the coefficients of the expansion:

  $$\varphi(\omega) = \sum_{m=1}^{D/2} x_{(2m-1)} \cos\left(\frac{2\pi m\omega}{\omega_{max}-\omega_{min}}\right) + x_{(2m)} \sin\left(\frac{2\pi m\omega}{\omega_{max}-\omega_{min}}\right) \quad \mathbf{(4.3)}$$

  where ω_{max} and ω_{min} are the maximum and minimum frequencies of the spectral bandwidth of adjustment, respectively. Moreover, x_i corresponds to the element i of the target vector being $i = (2m-1)$ and $i = (2m) \in [1, ..., D]$. Notice that the length of each chromosome (D) has to be an even number to use this parameterization, since each order of the series has two coefficients.

  This strategy is interesting for pulses close to FTL, but it may present convergence problems with pulses far from compression.

- **Discretized phase**

  This parameterization consists of discretizing the fundamental spectral range in D points, being each point the phase between 0 and 2π. It is very interesting for pulses close to FTL, but it can present convergence problems if the phase changes quickly.

- **Phase 1st derivative** (DPhase)
  This parameterization consists of discretizing the fundamental spectral range in D points, where each point represents the first derivative of the spectral phase. This is more robust than using the discretized phase directly because bigger changes are easily retrieved.

The differential evolution retrieval algorithm for amplitude swing developed in this Thesis is based on two of the basic strategies mentioned before, in particular the *DE/rand/1/bin* and the *DE/best/1/bin*. The merit function to be minimized in the selection process is the rms, also called sometimes G-error, between the normalized experimental and retrieved traces.

This merit function for the 2D traces is calculated as:

$$\text{Merit function} = \frac{1}{\sqrt{N_\omega N_\theta}} \sqrt{\sum_\theta \sum_\omega \left(S_{exp}^{SHG}(\omega, \theta) - S_{retr}^{SHG}(\omega, \theta) \right)^2} \qquad \textbf{(4.4)}$$

being S_{exp}^{SHG} and S_{retr}^{SHG} the experimental and retrieved amplitude swing traces, respectively. Moreover, N_ω and N_θ are the lengths of each dimension of the amplitude swing traces: frequencies (ω) and orientation of the MWP (θ), respectively. This merit function can be modified to pay more attention to the minimum signal area, for example, computing the traces in logarithmic scale up to a certain order or other strategies.

The algorithm can be used selecting one of the above mentioned parameterizations and the preferred strategy between *DE/rand/1/bin* or *DE/best/1/bin*. Although this is possible for simple structures, we decided to develop a 2-steps algorithm, mixing strategies and parameterizations to be able to retrieve complex phase structures, as shown in Fig. 4.2.

The first step (blue box in Fig. 4.2), is a *DE/rand/1/bin* using the Taylor expansion parameterization with a set of $N_{1st} = 12$ solutions, each with 2 elements ($D_{1st} = 2$). These two elements represent the GDD and TOD of the Taylor series, respectively. This first step enables a coarse retrieval of the main aspects of the amplitude swing trace.

After optimization, the best solution of the first step is used as guess for the second step, in which the finest structure is retrieved. This second step is a *DE/best/1/bin* using the phase derivative (DPhase) parameterization

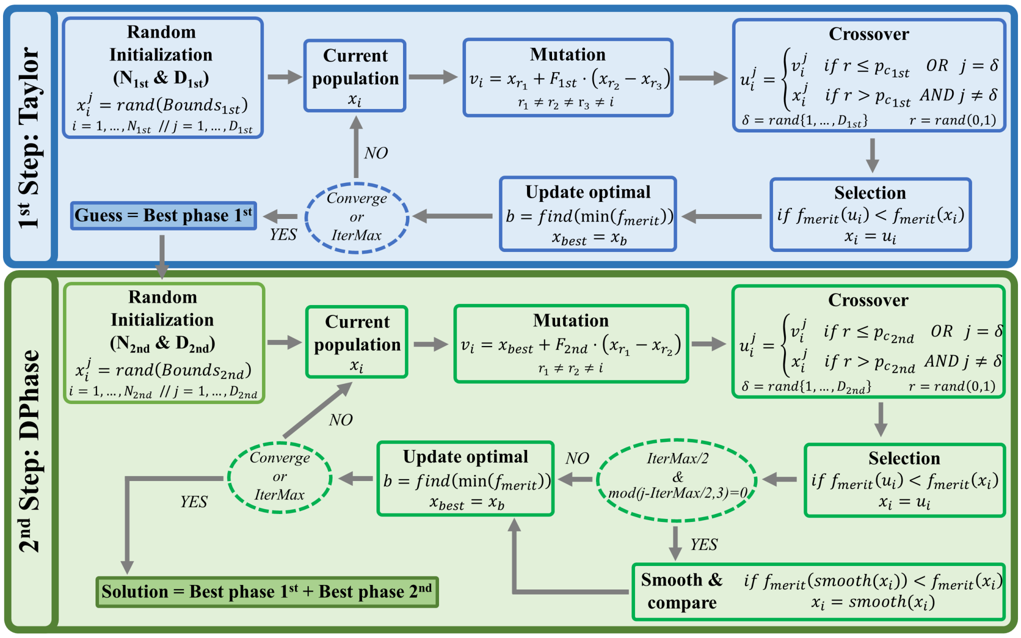

Fig. 4.2. *Flowchart of the 2-steps DE algorithm adapted to retrieve amplitude swing measurements.*

done with a set of $N_{2nd} = 25$ solutions, each with 19 elements ($D_{2nd} = 19$). Finally, the retrieved solution is the combination of the phase obtained at each step.

As previously mentioned, in this type of algorithms it is crucial to choose appropriated values for the scaling factor (F) and the crossover probability (p_c). For the retrievals with the algorithm shown in this Thesis, we used an F of 0.8 for the first step and 0.4 for the second step, and p_c of 0.7 in both cases. Notice that we use a bigger scaling factor in the first than in the second step because the latest step is a finer adjustment and it is closer to the optimal value, so small changes are better for an optimal convergence.

4.3 Numerical testing of the algorithm

This new algorithm was theoretically tested with different examples of ultrashort pulses, obtaining satisfactory results.

For example, Fig. 4.3 shows the simulations and retrievals obtained for a

50-fs FTL Gaussian spectrum centered at 800 nm with different combinations of GDD and TOD contributions. In this case, we have simulated the traces generated with a MWP that introduces a delay equal to the FTL pulse duration and a phase retardation of π rad for the central wavelength.

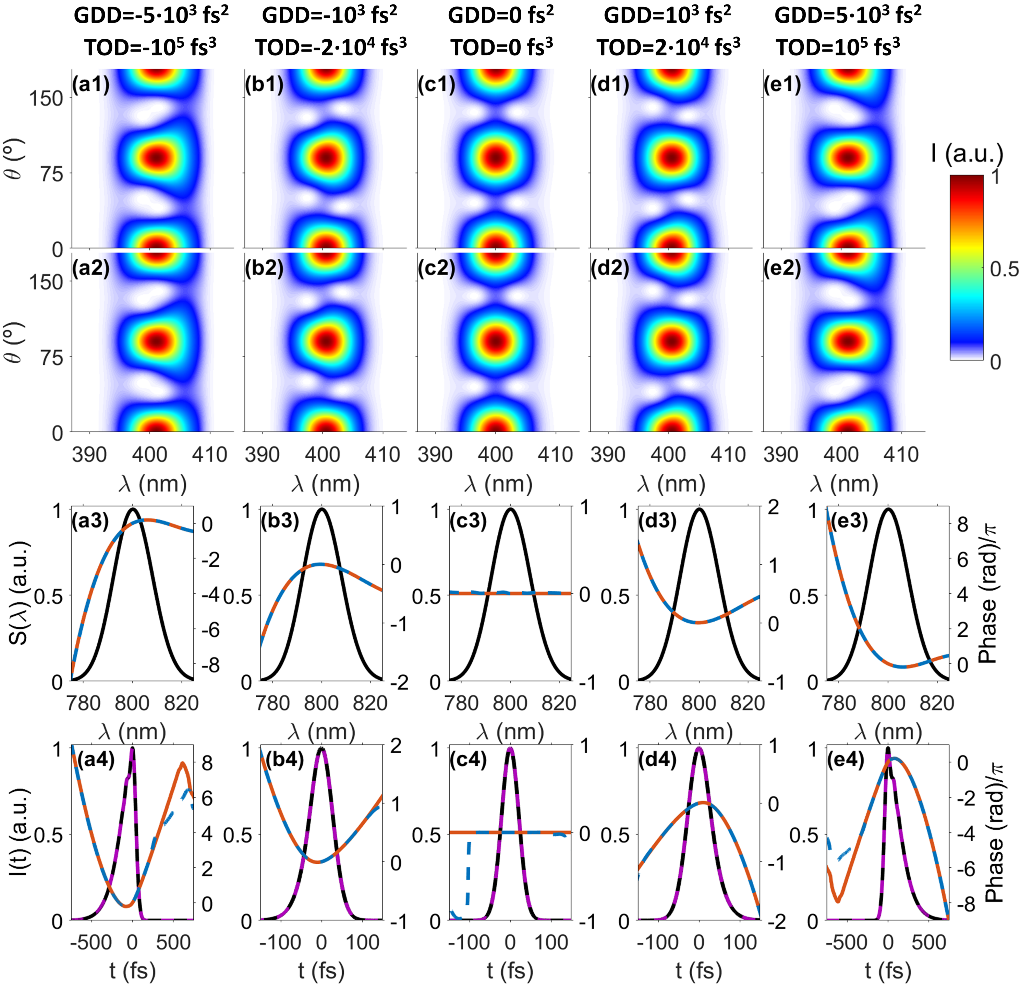

Fig. 4.3. *Simulation for different combinations of GDD and TOD. (Row 1) simulated and (row 2) retrieved amplitude swing traces. (Row 3) Spectrum (black) and spectral phase comparison: simulated (orange) and retrieved (blue). (Row 4) Temporal intensity (black, purple) and phase (orange,blue) comparison: simulated (black, orange) and retrieved (purple, blue).*

First and second rows of Fig. 4.3 correspond to the simulated and retrieved traces, which show good agreement (biggest rms below $6 \cdot 10^{-4}$). In addition, when compared, the retrieved and simulated electric fields in spectral and temporal domains (third and fourth rows, respectively) are almost indistinguishable.

Apart from GDD and TOD values, we also tested the algorithm with other complex structures, like a moderate oscillatory spectral phase. Figs. 4.4(a,c) depict the simulated and retrieved amplitude swing traces for the same FTL Gaussian spectrum centered at 800 nm, but with an oscillatory phase of amplitude 0.3π rad, and using a MWP with 50-fs delay and 0.4π rad phase retardation.

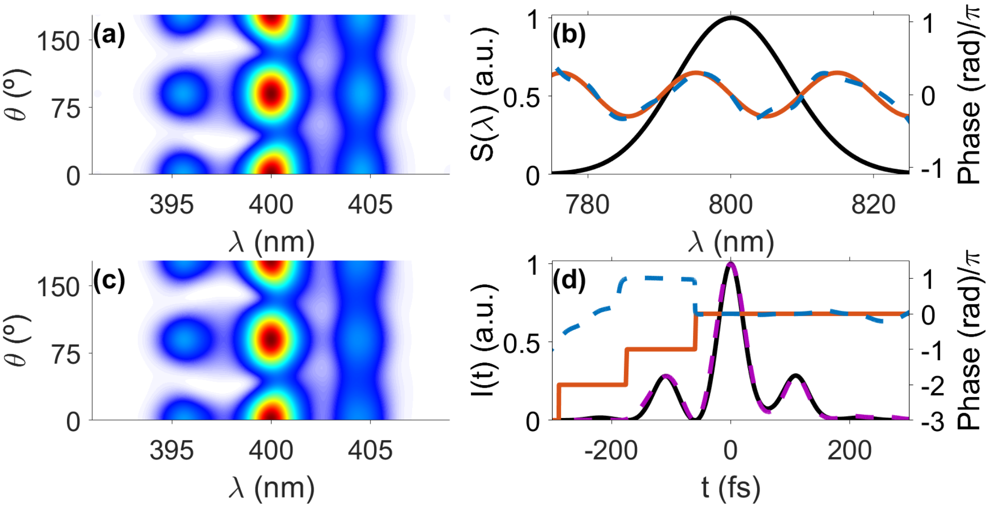

Fig. 4.4. *Simulation of a moderate oscillatory spectral phase. (a) Simulated and (c) retrieved amplitude swing traces. (b) Spectrum (black) and spectral phase comparison: simulated (orange) and retrieved (blue). (d) Temporal intensity (black, purple) and phase (orange,blue) comparison: simulated (black, orange) and retrieved (purple, blue).*

The retrieval presents good convergence with a G-error of $5.9 \cdot 10^{-3}$. In this case, the G-error is one order of magnitude bigger than the simulation of GDD and TOD, but the retrieval is still very good. This good convergence is also observed in the spectral and temporal comparison of Figs. 4.4(b,d), respectively.

Notice that the differences observed in the temporal phase are associated to π rad phase discontinuities introduced when the pulse intensity is null, but the same phase is retrieved shifted 2π rad.

In conclusion, the DE algorithm designed for the analysis of amplitude swing traces is able to retrieve the pulse information even in complex cases. This algorithm will be used in the experiment of Chapter 5 to retrieve the spectral phase of amplitude swing traces at different spectral regions.

Chapter 5

Amplitude swing across visible to near-infrared

In the past few decades, the development of optical parametric oscillators and amplifiers has derived into the creation of tunable ultrafast laser sources with multiple applications in different spectral regions [102, 103]. However, most of the temporal techniques mentioned in Subsection 2.2.2 are usually applied to certain typical spectral regions (e.g., emission range of Ti:sapphire lasers around 800 nm) and, sometimes, it is not trivial to adapt them to operate in multiple spectral regions.

As seen before, amplitude swing produces the pulse replicas with a rotating MWP to implement a compact and robust temporal technique. In addition, the lack of spectral limitations associated to elements like beam-splitters, stretchers or chirped mirrors, enables the possibility to operate in different spectral ranges without significant modifications in the system. This is possible because, in principle, the amplitude swing only depends on the transparency window and the birefringence of its elements to generate the amplitude varying replicas before the nonlinear medium and the detection.

Taking this into account, in this Chapter we use amplitude swing to characterize ultrashort pulses tuned within a spectral range of more than an octave across visible to near-infrared regions [104].

5.1 Materials and Methods

The ultrashort laser source used in this experiment was a tunable system. In particular, a CPA laser (Spitfire ACE from Spectra-Physics) and an optical parametric amplifier (TOPAS-Prime from Light Conversion).

The TOPAS system is a two-stage parametric amplifier, which uses the amplified output from the Spitfire ACE system (centered at 798 nm with ∼64-fs FWHM FTL duration and a repetition rate of 5 kHz) as pump. This system relies on parametric amplification processes to generate two pulsed beams called Signal and Idler. The central wavelength of these beams can be tuned adjusting the angle of the nonlinear crystals and the arriving time of each beam in the parametric processes. In the case of the Signal, it can be efficiently tuned from 1160 nm up to 1600 nm, while the Idler can emit from 1600 nm to 2600 nm.

Once the Signal and Idler are generated, the second stage of the TOPAS system has a set of wavelength separators/combiners and nonlinear crystals in which either the Signal, the Idler or the remnant pump beams are combined to generate the ultrashort pulse in the desired spectral range. Table 5.1 summarizes the main processes used to produce the emission in the different spectral regions of the system, and Fig. 5.1 shows the approximately pulse energy at each spectral region.

Range (nm)	**Process**
1600-2600	Idler
1160-1600	Signal
800-1160	Second harmonic Idler (SHI)
580-800	Second harmonic Signal (SHS)
533-580	Idler and pump sum-frequency (SFI)
470-533	Signal and pump sum-frequency (SFS)
400-470	Fourth harmonic Idler (FHI)
290-400	Fourth harmonic Signal (FHS)
267-290	Second harmonic of (Idler and pump sum-frequency) (SHSFI)
240-267	Second harmonic of (Signal and pump sum-frequency) (SHSFS)

Table 5.1: Spectral emission ranges and main processes of the TOPAS system pumped with a pulse centered around 800 nm.

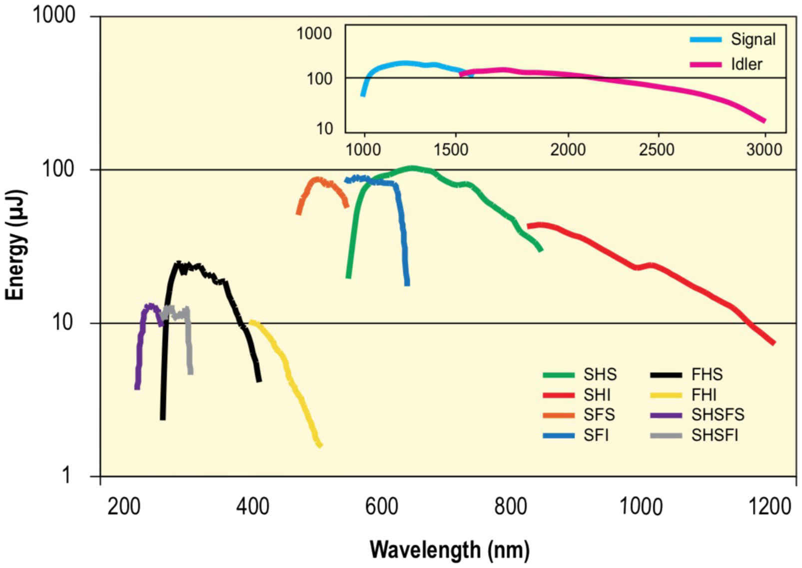

Fig. 5.1. *Specifications of the TOPAS-Prime approximate pulse energy at each spectral and process involved in the generation taken from the manufacturer's manual. Acronyms of the parametric processes are summarized in Table 5.1.*

The amplitude swing system used to characterize those pulses consisted of a 2.1-mm-thick quartz MWP placed between two linear polarizers, and a 10-μm Type I Beta-Barium Borate [$\beta - BaB_2O_4$] (BBO) cut at 29.2° as nonlinear medium. The delay introduced by the MWP in the different spectral regions studied in this Chapter goes from 64.8 fs up to 68.5 fs.

Moreover, at each spectral region we implemented a SHG FROG system in non-collinear configuration with the same nonlinear medium in order to validate the amplitude swing retrievals. This FROG system uses a Michelson interferometer, conformed by a beamsplitter, a moving mirror and a roof-mirror. After the interferometer, both delayed replicas of the pulse under test are focused using an off-axis parabola over the BBO (same crystal as the amplitude swing). The delay scan is done displacing the moving mirror in steps of 1 μm, thus the temporal resolution of the scan is 6.7 fs.

Since the BBO is designed for optimal phase-matching under normal incidence at 800 nm, at each spectral range it is necessary to orientate it searching the optimal phase-matching for those wavelengths.

Furthermore, we have used various spectrometers, whose specifications are summarized in Table 5.2, for the characterization of the fundamental and the SHG spectra in the different spectral ranges.

Spectrometer model	λ_{min} **(nm)**	λ_{max} **(nm)**	$\langle\Delta\lambda\rangle$ **(nm)**
Ocean Optics HR4000	240	450	0.06
Avantes AvaSpec-2048	300	1100	0.56
StellarNet Dwarf-Star	1000	1700	1.50

Table 5.2: Summary of the specifications of the spectrometers used to measure the SHG and fundamental spectra in this experiment. Minimum (λ_{min}) and maximum (λ_{max}) wavelengths of operation and average spectral numerical resolution along the spectral range ($\langle\Delta\lambda\rangle$).

In addition, the amplitude swing retrievals were obtained using the two step DE algorithm explained in Chapter 4 (*DE/rand/1/bin* and *DE/best/1/bin* parameterizing the phase as Taylor series and discretized spectral phase derivative), whereas the FROG measurements were analyzed using a Principal Components Generalized Projections Algorithm (PCGPA) [93, 105]. Notice that we had to measure the fundamental spectrum for the amplitude swing algorithm, but the FROG algorithm does not required it to operate. Nevertheless, we can use the experimental spectrum to correct the measured FROG traces as will be explained later.

Moreover, we decided to both, calibrate the MWP phase retardation (zero-th order phase), using the technique described in [88], and calculate the spectral phase using the Sellmeier equations. This can be done with the calibration of the phase-retardation at a certain wavelength (e.g., λ =800 nm) and, then, extrapolating with Sellmeier equations, but small errors in the parameterization of the MWP (e.g., tiny error in the thickness) can introduce significant errors in the phase retardation. Therefore, we decided to calibrate the phase retardation at each spectral region analyzed.

Second harmonic response

In the experiments of this Chapter we used the same nonlinear crystal for various spectral regions adjusting the phase-matching by rotating the crystal.

However, this phase-matching tunability is limited and there can be situations in which the SHG response is not perfectly flat due to the dispersion changes in different spectral regions, as it will happen in the extreme spectral regions of Section 5.2. In order to deal with these non-ideal cases, we modified the retrieval algorithms to calculate the SHG responses of the systems for both techniques, FROG and amplitude swing. Moreover, in order to improve the FROG convergence and reduce the noise effect of the traces, we took into account the second harmonic response correction for all the FROG measurements.

Regarding the FROG measurement, we integrated the approach explained in Chapter 10 of [106]. In that study of FROG, it is demonstrated that the frequency marginal (i.e., integral of the FROG trace in the delay dimension) can be theoretically calculated as the convolution of the fundamental spectrum $S(\omega)$:

$$M_{FROG}^{theo} = S(\omega) * S(\omega) = \int_{-\infty}^{\infty} S(\Omega) S(\omega - \Omega) d\Omega \qquad \mathbf{(5.1)}$$

Since we are measuring the fundamental spectrum, we can obtain the SHG response of the FROG system as the ratio between the theoretical and experimental frequency marginals:

$$R_{FROG}(\omega) = \frac{M_{FROG}^{theo}(\omega)}{M_{FROG}^{exp}(\omega)} \qquad \mathbf{(5.2)}$$

being $M_{FROG}^{exp}(\omega)$ the experimental marginal obtained by integrating the measured FROG trace in the delay dimension.

Regarding the amplitude swing, as mentioned in Chapter 3, in [91] it was shown that the frequency marginal (i.e., integral of amplitude swing trace in angular dimension) depends on the phase of the pulse under study. Despite this, it can be computed a SHG response comparing the experimental and retrieved frequency marginals at each iteration of the retrieval algorithm. Moreover, to avoid introducing artifacts with the SHG response, the ratio is strongly smoothed. Thus the amplitude swing SHG response ($R_{aswing}(\omega)$) at each iteration of the algorithm will be given by:

$$R_{aswing}(\omega) = \text{Smooth}\left\{ \frac{M_{aswing}^{exp}(\omega)}{M_{aswing}^{retr}(\omega)} \right\} \qquad \mathbf{(5.3)}$$

where $M^{exp}_{aswing}(\omega)$ and $M^{retr}_{aswing}(\omega)$ denoted the frequency marginals of the experimental and retrieved amplitude swing traces.

5.2 Results and Discussion

As previously mentioned, there is a necessity to develop compact and simple characterization techniques able to operate in different spectral regions. In this Chapter we have studied various spectral regions of high interest as it is explained below.

Fig. 5.2 shows the experimental (row 1 and 3) and retrieved (row 2 and 4) SHG traces of amplitude swing (row 1 and 2) and FROG (row 3 and 4) for five different interesting spectral regions:

- Visible spectral region, Fig. 5.2(a) (carrier wavelength obtained as the spectrum gravity center, $\lambda_c = 619$ nm): interesting applications in biomedicine, micro-processing or telecommunications. [107–109].
- Ti:sapphire spectral range, Fig. 5.2(b) ($\lambda_c = 821$ nm): widely studied during the last decades and multiple applications in micro-processing, high-intensity, high-harmonic generation or microscopy, among others [110–112].
- Ytterbium doped lasers, Nd:YAG and some semiconductor lasers emission spectral region, Fig. 5.2(c) ($\lambda_c = 1063$ nm): presents potential biomedical and marking applications [113, 114].
- Spectral region of zero-dispersion wavelength (ZDW) of fused silica and triplet to singlet molecular oxygen transition, Fig. 5.2(d) ($\lambda_c = 1316$ nm): interesting in different fields such as spectroscopy, biomedicine and metrology [115–117].
- Spectral emission region of Erbium-doped lasers, Fig. 5.2(e) ($\lambda_c = 1540$ nm): specially interesting because it is a spectral region used in telecommunication, but also due to applications in micro-welding or optical coherence tomography [118, 119].

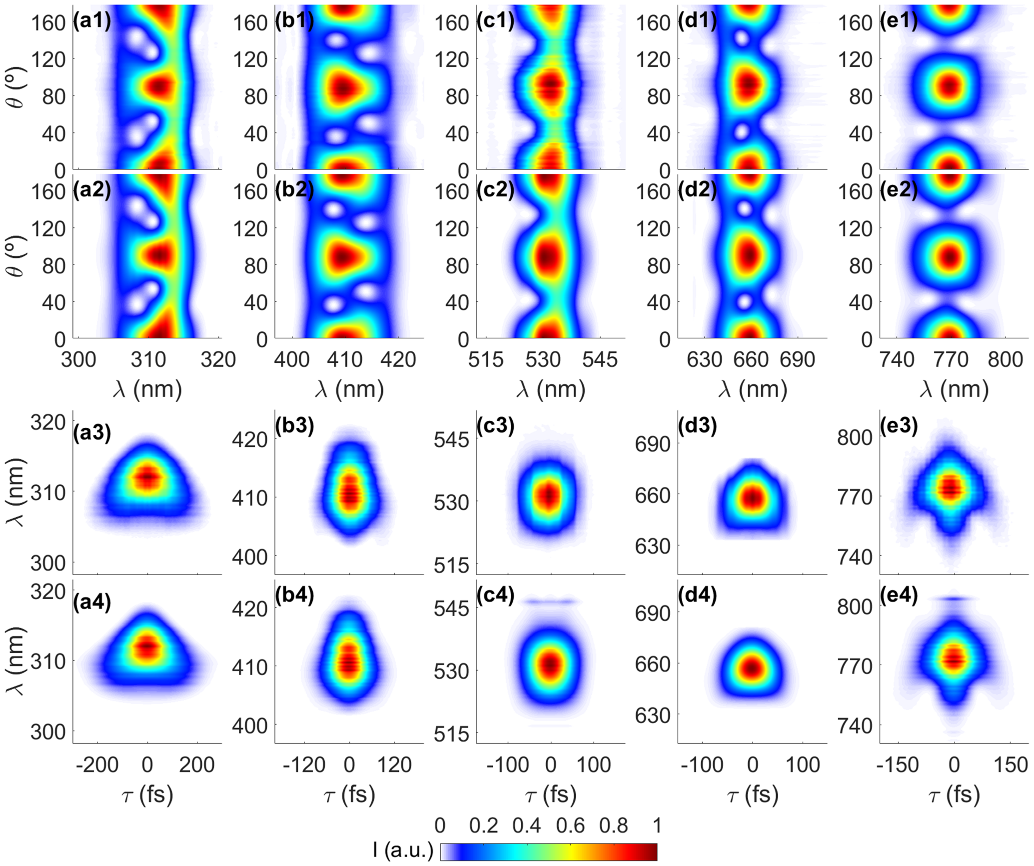

Fig. 5.2. *Experimental (rows 1 and 3) and retrieved (rows 2 and 4) SHG traces of amplitude swing (rows 1 and 2) and FROG (rows 3 and 4) for five different interesting spectral regions with carrier wavelengths around: (a)* λ_c *=619 nm, (b)* λ_c *=821 nm, (c)* λ_c *=1063 nm, (d)* λ_c *=1316 nm and (e)* λ_c *=1540 nm. Notice that the experimental FROG traces (row 3) have been corrected with the marginal strategy, Eq.* **5.2**.

All the retrievals have good convergence with low G-errors (i.e., rms difference between experimental and retrieved traces), being the biggest value in these retrievals 0.04. As said in the previous Section, in order to have a good convergence at the amplitude swing measurements in the extreme spectral range (λ_c equal to 619 nm and 1540 nm), we have to take into account the SHG response due to non-perfect phase-matching. In the case of the FROG, we have applied the SHG response to correct all the measured traces, thus improving the convergence and dealing with the noisy data.

The spectral (row 1) and temporal (row 2) intensity and phase comparison of the retrievals are shown in Fig. 5.3. Moreover, the FTL pulse intensity of the measured spectrum have been included in the second row of Fig. 5.3.

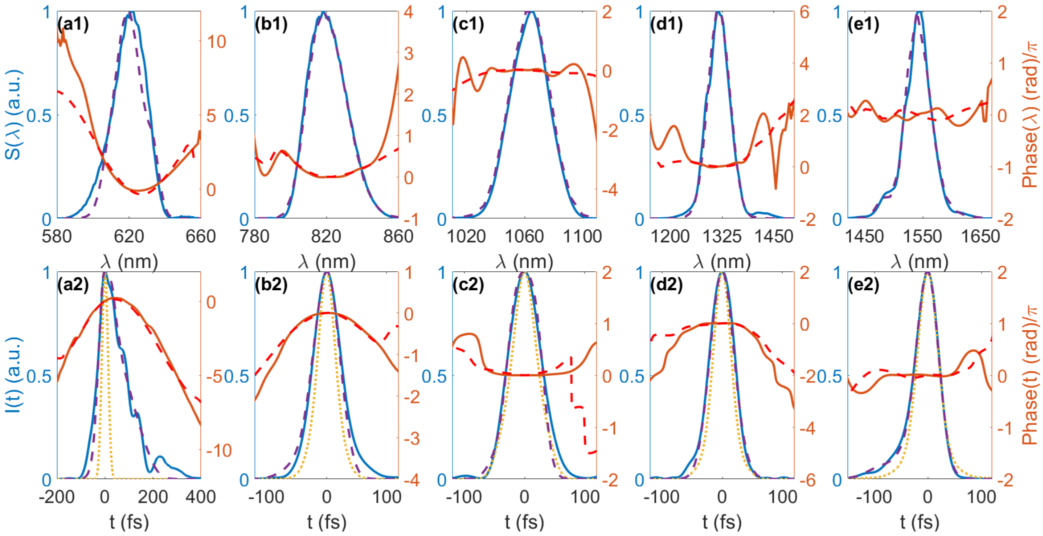

Fig. 5.3. *Spectral (row 1) and temporal (row 2) retrievals for the amplitude swing (solid blue and orange lines) and FROG (dashed purple and red lines) measurements shown in Fig. 5.2 for five different spectral regions of interest with carrier wavelengths: (a) λ_c =619 nm, (b) λ_c =821 nm, (c) λ_c =1063 nm, (d) λ_c =1316 nm and (e) λ_c =1540 nm. Second row also includes a comparison with the temporal intensity of the FTL pulse (dotted yellow lines).*

Observing the experimental retrievals of Fig. 5.3, there is a good agreement between FROG and amplitude swing measurements, specially in the phase terms. The small discrepancies in the extreme cases, Figs. 5.3(a,e), may be originated from experimental error in the amplitude swing retrieval, as well as small differences in the spectrum retrieved by FROG and the experimentally measured by the spectrometer, being this one the considered in the amplitude swing measurement. Furthermore, the accuracy of FROG is limited due to the smallest delay that can be introduced with our set-up (6.7 fs), which may also affect the retrieval.

Notice that the dispersion of the pump was not optimized changing the grating compressor of the CPA laser to obtain the maximum emission. Nevertheless, it seems that the dispersion introduced after the generation is higher for shorter wavelengths than for higher wavelengths, suggesting this is due to the material and optics dispersion.

In this experiment we can observe the high flexibility of amplitude swing because with the same MWP, polarizer and BBO we are studying pulses with FWHM in the range 29.8-49.4 fs for the FTL and 46.5-125.5 fs for the pulse retrieval in spectral regions over more than an octave, as shown in Fig. 5.4 for each case.

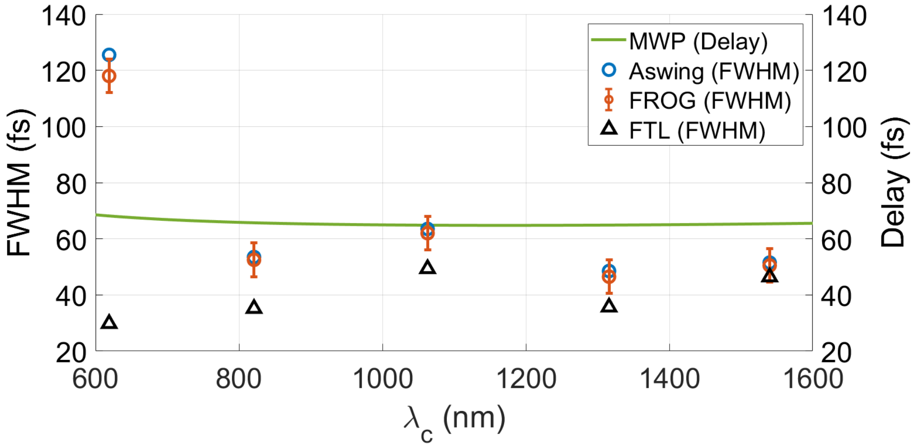

Fig. 5.4. *Spectral dependence of the MWP delay (green) and temporal FWHM duration comparison of the FTL (black), amplitude swing (blue) and FROG (orange) retrievals of the measurements shown in Fig. 5.3.*

In Fig. 5.4 it has been included the FROG scale uncertainty, which in our system is significant due to the minimum temporal step that our system can introduce (6.7 fs). It is important to highlight that, for a complete comparison between both techniques, FROG and amplitude swing retrievals, we must pay attention to the full pulse intensity and phase comparison shown in Fig. 5.3, because considering only one parameter, like the FWHM (as done in Fig. 5.4), can lead to wrong conclusions about the retrievals similarity.

Please notice that comparing the spectral dependence of the MWP delay with the FTL durations, shown in Fig. 5.4, all the measurement are in the confidence range (MWP delay between 3 times bigger or smaller than the FTL duration).

In principle, the spectral operation range of amplitude swing can be extended to all the transparency range of its elements (the pulse replicas management), provided the nonlinear process and the detection reach that range. In this experiment, the threshold was due to phase-matching limitations with our nonlinear crystal. We think that this can be solved using different nonlinear media, such as BBO with a different cut angle, Potassium Titanyl Phosphate (KTP) crystal or a crystal in quasi phase matching condition like Periodically Poled Lithium Niobate (PPLN) [120] or poly-crystalline zinc selenide [121].

Another specially interesting option is to use commercially available SHG nanoparticles as nonlinear medium in the amplitude swing system. As shown with the d-scan technique in [122], it is not required a specific phase-matching angle, hence the amplitude swing system could operate at different spectral ranges without any modifications. Moreover, if required, another option could be to use a different nonlinear process like XPW or PG, which are automatically phase-matched.

In conclusion, amplitude swing is a robust temporal technique that can retrieve ultrashort pulses in various spectral regions with different temporal durations without significant modifications in the system. Therefore, it can be used in diverse applications of ultrashort lasers. Moreover, it is foreseeable that the spectral region of application may be extended to the entire visible and mid-IR by adapting the SHG medium.

Chapter 6

Amplitude swing in the few-cycle pulse regime

A regime of high interest of ultrashort laser beams is the few-cycle regime, which presents applications in various fields like attoscience [123–126], high field physics [127, 128] or extreme nonlinear effects [129], among others.

This regime includes pulses with a temporal duration no longer than a small multiple of a single cycle of the electric field in the corresponding spectral range (e.g., 2.67 fs at 800 nm). Characterizing these pulses is challenging because extremely short temporal durations are associated with ultra-broadband spectra, which can be troublesome due to the spectral dependence of some elements of the characterization techniques.

Furthermore, the pulse characterization of few-cycle is highly important for its applications due to its delicate handling (e.g., relatively small added dispersion can stretch the pulses to much longer pulses).

During the last decades, some temporal techniques have been adapted to operate in this regime (e.g., SPIDER [130], FROG [131] and more recently SRSI [132]). Despite this, among all temporal techniques, there is one that was developed in the scope of few-cycle pulses and presents some features that make it particularly appropriate to characterize pulses in that range: the d-scan technique explained in Subsection 2.2.2. No matter whether it is the conventional d-scan technique [60] or one of its variants [61, 122, 133], all of them can deal with few-cycle pulses. For example, in [134] the authors characterized a 2.2-fs FWHM pulse, which corresponds to a 1.04 cycles, using d-scan.

Regarding the amplitude swing, its application in this regime would enable the characterization with a compact set-up without common interferometers or elements that could limit the bandwidth. In [91], a simulation to theoretically demonstrate that, in principle, this technique is able to characterize few-cycle pulses was shown. However, that work presented a simulated situation and, since it is a complex regime, a complete study is required to experimentally validate it. In the current Chapter, we will show this capability experimentally and, in order to verify the retrievals, we are going to compare the results with the d-scan technique. Moreover, we will show that amplitude swing is able to characterized non-compressed pulses.

The results presented here were obtained during an experimental campaign at the Universidad Complutense de Madrid (UCM), in collaboration with Prof. Rosa Weigand and Óscar Pérez.

6.1 Materials and Methods

The few-cycle laser source was a home-made Ti:sapphire oscillator pumped with a Verdi-V6 laser. During the experimental campaign, its spectral bandwidth was optimized searching the widest spectrum, while remaining stable, in order to generate few-cycle pulses with the shortest temporal durations.

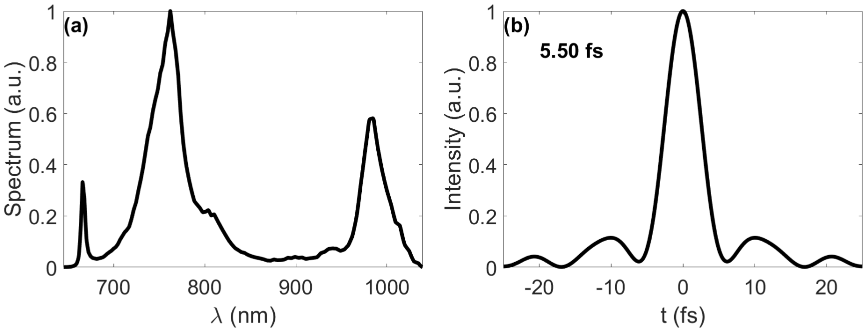

Fig. 6.1. *(a) Spectrum of the few-cycle Ti:sapphire laser used in the experiments. (b) FTL pulse of the laser spectrum with an inset of its duration (FWHM).*

The obtained spectrum is shown in Fig. 6.1(a) and has a FTL pulse duration with FWHM of 5.50 fs, represented in Fig. 6.1(b). All the results exhibited in this Chapter were done with this optimized situation.

The scheme of the experimental set-up used to characterize the few-cycle laser combining both temporal characterization techniques, amplitude swing and d-scan, is represented in Fig. 6.2.

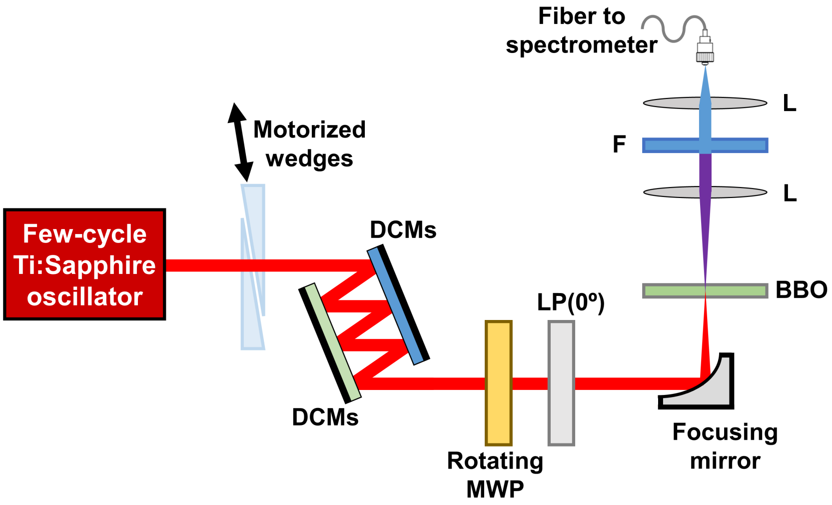

Fig. 6.2. *Scheme of the experimental set-up combining the d-scan and the amplitude swing characterization techniques.*

Firstly, the laser beam goes through two motorized BK7 wedges with an angle of 8°, which are used for the d-scan measurement and to control the pulse chirp to be measured with amplitude swing. Then, the dispersion is compensated bouncing three times over each mirror of a pair of chirped mirrors (DCMs, model DCM7 from Venteon), which introduce negative dispersion (-120 fs^2 per reflection pair at 800 nm). After that, it is placed a rotating 200-μm quartz plate (MWP), which introduces a 6.58-fs delay at 800 nm, that is used as MWP for the amplitude swing scan. After the MWP a wire grid linear polarizer (LP) is placed, set at 0° to select the horizontal projection. Then, the beam is focused using an off-axis parabolic mirror (1-inch focal length) over a 10-μm Type-I BBO in order to produce SHG. Finally, the SHG signal is filtered (F) using a neutral density filter and two color filters (FGB37 from Thorlabs and BG12 from Schott), and collected with an UV-Grade Fused Silica lens (L) into an optical fiber connected to an Ocean Optics spectrometer (model HR4000 from Ocean Optics Inc.), operating from 196 nm up to 660 nm.

Moreover, the fundamental spectrum can be measured introducing a diffuser medium before the BBO crystal and collecting the diffused signal into an Avantes spectrometer.

Since we use a hybrid set-up to validate the amplitude swing results against the d-scan reconstructions, during the d-scan measurement the SHG spectrum is recorded for different insertions of the motorized wedges, whereas the MWP is fixed with its fast axis at 0°. During the amplitude swing measurement, the wedges are fixed at a desired position and the SHG spectrum is measured for different angles of the MWP. Furthermore, to compare both retrievals it should be taken into account the phase introduced by the MWP, which is typically withdrawn in the amplitude swing retrievals, but in this configuration it will be kept because the d-scan measurement in this configuration takes it into account, since it measures the pulse after it. Anyway, it could also be subtracted here if needed.

The amplitude swing retrievals were done using the Levenberg-Marquardt algorithm [31] with two optimization steps. The first step optimizes the GDD and TOD terms of a Taylor expansion and the second step performs a finer adjustment fitting the combination of GDD, TOD and phase first derivative at 22 spectral points. On the contrary, the d-scan retrievals were done using a Quasi Newton Broyden–Fletcher–Goldfarb–Shanno (BFGS) algorithm, as in [122], characterizing the phase as a Fourier series with 15 sine and 15 cosine terms.

Notice that, since the few-cycle regime is related with ultra-broadband pulses, the delay introduced by the MWP varies along the spectrum, as shown in Fig. 6.3. Despite this spectral dependence, the delay is always close to the FTL duration (delay $\sim$1.1-1.2 times the FTL pulse duration) and its dispersion is taken into account in the algorithm. Therefore, the delay introduced by amplitude swing can be non-constant, in contrast with the delay of a common interferometer.

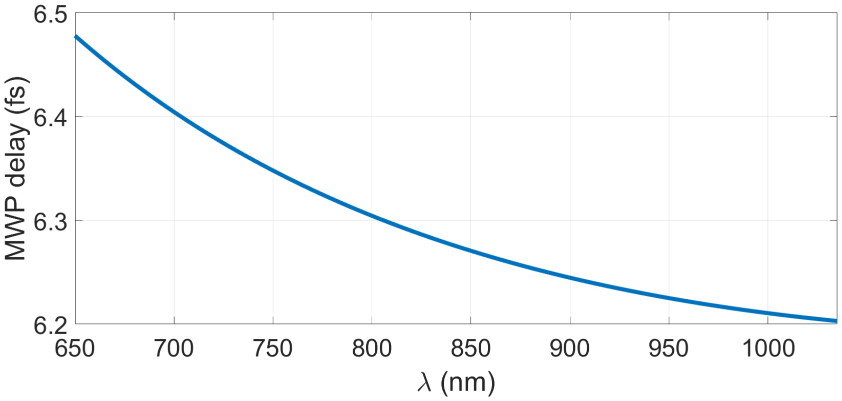

Fig. 6.3. *Spectral dependence of the delay introduced by the 200-μm-thick quartz MWP used in amplitude swing.*

Second harmonic response

Notice that, due to the large spectral bandwidth of the laser, the SHG response must be properly calibrated for a correct characterization.

In the case of d-scan, the SHG response is directly obtained during the iterative retrieval algorithm by comparison of the experimental and simulated traces using the following equation:

$$R_{dscan}(\omega) = \frac{\sum_{k} I_{meas}(\omega, z_k) \cdot I_{sim}(\omega, z_k)}{\sum_{k} I_{sim}^2(\omega, z_k)} \tag{6.1}$$

where $I_{meas}(\omega, z_k)$ and $I_{sim}(\omega, z_k)$ are the experimentally measured and simulated d-scan traces, respectively.

Regarding the amplitude swing, the SHG response can be obtained in the retrieval algorithm as explained in Section 5.1 and used in the experiment shown in Section 5.2. This strategy can be used in few-cycle regime for pulses relatively close to compression (dispersion compensation). However, this approach, while working properly near FTL pulse conditions, can be troublesome for highly chirped pulses with ultra-broadband spectra, as the most chirped situations that will be studied in Subsection 6.2.2. This limitation appears because the frequency marginals of the SHG traces present huge null signal areas. To solve this issue, we decided to simulate the theoretical SHG response of the system and consider it in the amplitude swing algorithm.

The theoretical SHG response of the system can be obtained, following the ideas presented in [43], combining the detection and the nonlinear medium spectral dependence. On one hand, the detection response can be expressed as the combination of the color and neutral filters used to select the SHG signal (R_{Filters}) and the spectrometer (R_{HR4000}) responses, orange and yellow curves of Fig. 6.4(a). In this case, the filters response was given by the manufacturer and the spectrometer response was experimentally calibrated measuring the emission spectrum of a known white lamp. On the other hand, the theoretical nonlinear medium response, green curve of Fig. 6.4(a), includes the phase-matching efficiency ('sinc' term) dependence weighted with the second order susceptibility of the refractive index ($\chi^{(2)}$). Therefore, the theoretical SHG response of the system, as seen in [43], will be given by:

$$R_{Total}(2\omega) \propto \frac{\omega^3}{n_e(2\omega)} \cdot R_{Filters}(2\omega) \cdot R_{\mathrm{HR4000}}(2\omega) \cdot |\chi^{(2)}(2\omega)|^2 \,\mathrm{sinc}^2\left[\Delta k(2\omega) L/2\right] \qquad \mathbf{(6.2)}$$

where $\chi^{(2)} \propto [n_e(2\omega)^2 - 1] \cdot [n_o(2\omega)^2 - 1]^2$ and $\Delta k = \omega L/2\,[n_e(2\omega) - n_o(\omega)]$ is the phase-mismatch, being n_o and n_e the ordinary and extraordinary refractive indices of the BBO, which can be calculated using Sellmeier equations [135] and knowing the crystal cut angle ($\theta = 29.2°$), and L its thickness (10 μm in our case).

The resulting theoretical SHG response is compared with the obtained using the d-scan technique in Fig. 6.4(b), showing good agreement but with some differences. On one hand, the d-scan SHG response is represented for a shorter spectral range because it is the optimization range of the d-scan retrieval. On the other hand, the d-scan SHG response is lower around 425 nm, while this is not observed in the theoretical response. This difference may be a small and non-significant artifact of the d-scan retrieval because this area matches with the lowest fundamental signal region. In addition, the theoretical response is based on the slowly varying envelope approximation (SVEA) and considering monochromatic plane wave, thus the SHG response can be slightly different. Anyway, the retrieval tolerates this kind of deviation in the SHG response calibration, as shown in Subsection 6.2.1 by comparing

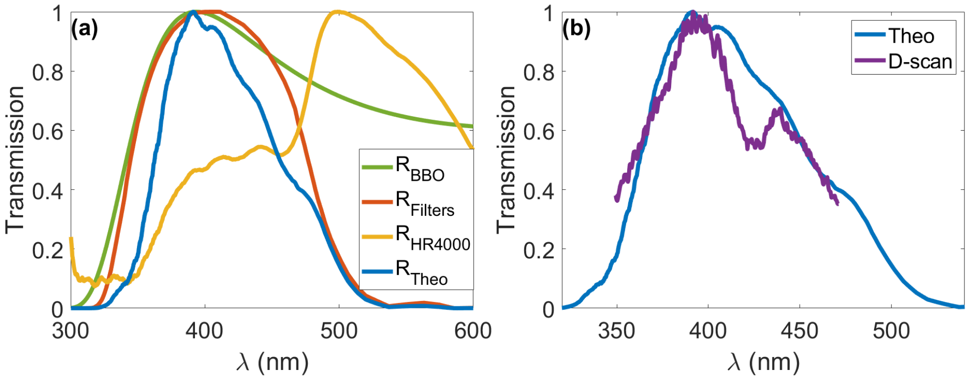

Fig. 6.4. *(a) Theoretical simulation of the system SHG response (blue), obtained from the combination of the BBO theoretical response (green) and the spectral dependence of the filters used to select the signal (orange) and spectrometer (yellow). (b) Comparison of the theoretical SHG response (blue) and the experimentally obtained in the d-scan retrieval (purple).*

the amplitude swing retrieval using both responses, obtaining similar pulse reconstructions.

In the amplitude swing retrievals, we used the theoretical SHG response and optimized them in the spectral range with significant signal (322.5-520.0 nm) avoiding areas with low signal where the theoretical response can differ from the experiment. By doing so, the amplitude swing reconstructions are self-consistent and do not depend on the response obtained from the d-scan measurement, which is used here just to validate the amplitude swing results. Indeed, it is easy to estimate it, since the phase-matching curve of a BBO crystal is well known and the spectral response of the filters is usually given by the manufacturer. Nevertheless, other strategies can be used to obtain the SHG response. For example, it can be experimentally calibrated using a known reference pulse with equal or bigger bandwidth. Another possibility is to directly use the response obtained from other temporal charactererization technique like the d-scan. This last approach will be demonstrated at the end of Subsection 6.2.1 as a verification that different SHG responses can be used.

6.2 Results and Discussion

The versatility of amplitude swing, as explained in Chapter 3, enables to characterize pulses with different bandwidths. In addition, provided that the MWP delay is appropriate for the FTL temporal duration, amplitude swing can characterize highly chirped pulses. Taking this into account, firstly we will characterize the beam for the insertion of the wedges that gives the most compensated dispersion (the best pulse compression position), Subsection 6.2.1, and then for different wedge insertion positions, Subsection 6.2.2.

6.2.1 Compressed pulse

In this Subsection, the electric field is measured at the position of the wedges that produces the shortest possible pulse (closest to the FTL pulse conditions). As shown later, at this position the pulse is not a FTL pulse due to the residual phase that cannot be compensated by the dispersion of the wedges.

Fig. 6.5 shows the characterization obtained with both techniques, being the amplitude swing measurement done at the compensated dispersion position of the wedges.

Firstly, Figs. 6.5(a1,a2) show the experimental and retrieved amplitude swing traces taking into account the theoretical SHG response. Secondly, Figs. 6.5(b1,b2) correspond to the experimental and retrieved d-scan traces using the SHG response obtained by the d-scan measurement. The glass insertion axis is shown with respect to the compressed position (i.e., the best compensation dispersion position is 0 mm). Logically, positive insertion of material correspond to positively chirped pulses, and vice versa. Finally, Figs. 6.5(c1,c2) correspond to the spectral and temporal comparison of both retrievals for the compensation dispersion position.

There is very good agreement between both retrievals, which is also manifested in the similar temporal FWHM, 5.98 fs and 5.99 fs for the amplitude swing and d-scan, respectively. Regarding the temporal duration of a single cycle for the carrier wavelength of the spectrum, calculated as the gravity

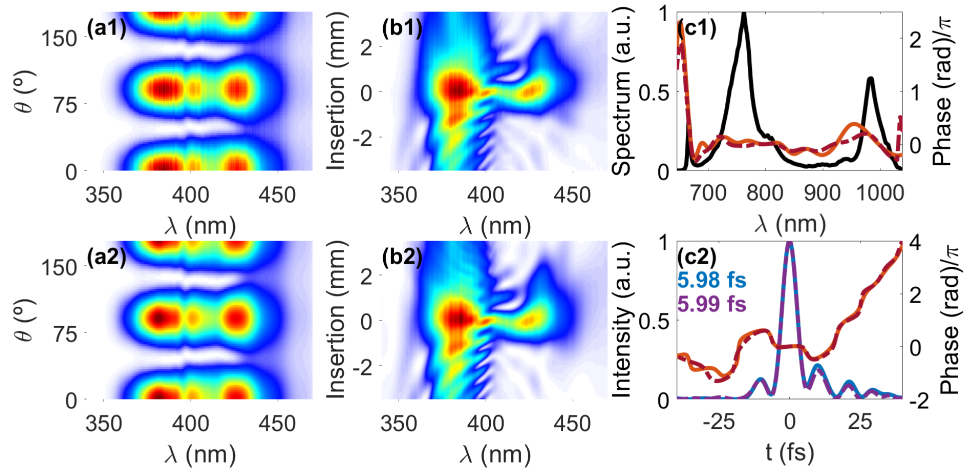

Fig. 6.5. *Experimental (a1,b1), retrieved (a2,b2) amplitude swing (a1,a2) and d-scan (b1,b2) traces and electric field at insertion 0 comparison in spectral (c1) and temporal (c2) domains, being the solid lines the amplitude swing and the dashed lines the d-scan retrieval. An inset of the temporal intensity FWHM of amplitude swing (blue) and d-scan (purple) is included in (c2).*

center of the spectrum (2.71 fs at 817 nm), the retrieved pulse corresponds to a 2.2-cycles pulse. Furthermore, these FWHM values are close to the FTL temporal FWHM, which in this case is 5.50 fs.

The previous amplitude swing retrieval has been done using the theoretical SHG response, but, as previously suggested, it can also be done using the d-scan response. Fig. 6.6 shows the amplitude swing retrieval for the same compensated dispersion position using the d-scan SHG response and compares it with the result obtained with the theoretical SHG response.

The convergence of the amplitude swing retrieval algorithm using the d-scan SHG response is also very good. The spectral and temporal retrievals of Figs. 6.6 present the same dependences as the ones obtained using the theoretical SHG response and the FWHM only differs in 0.02 fs.

Therefore, both strategies for obtaining the SHG response are valid. Taking this into account, we are going to retrieve the measurements of Subsection 6.2.2 using the theoretical SHG response, so that the amplitude swing reconstructions do not rely on any other technique.

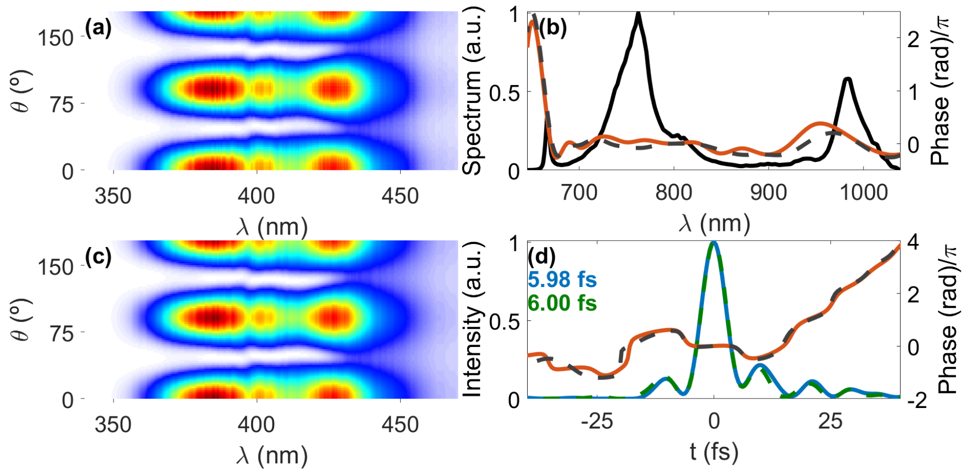

Fig. 6.6. *Experimental (a), retrieved (c) amplitude swing traces using the d-scan SHG response and electric field comparison in spectral (b) and temporal (d) domains, being the solid lines and dashed lines the amplitude swing retrievals obtained with the theoretical SHG response and the d-scan SHG response, respectively. An inset of the temporal FWHM obtained using the theoretical response (blue) and the d-scan response (green) is included in (d).*

6.2.2 Non-compensated dispersion cases

In addition to characterizing the pulse at the compensated dispersion position of the wedges, the versatility of amplitude swing enables to measure the pulse with different dispersion values. To demonstrate this, in this Subsection the pulse is characterized for different insertion of the wedges.

For the validation of amplitude swing results out of compression, it can be obtained the d-scan retrieval for each glass insertion by adding to the compensated spectral phase the corresponding dispersion phase, which can be calculated taking into account the material thickness and the Sellmeier coefficients of the refractive index of the BK7 wedges. Please notice that, in the case of d-scan, it is necessary to scan the dispersion around compression position of the pulse and then, from the full trace, it can be extracted the pulse at different insertions. On the contrary, with amplitude swing no compression is required because it can directly measure the pulse at the corresponding insertion.

In Fig. 6.7 there are shown the experimental (first and third rows) and retrieved (second and fourth rows) amplitude swing traces, obtained introducing a dispersion with respect to the material insertion position for the compensated dispersion in steps of 40 fs^2 from -160 fs^2 (Fig. 6.7(a)) up to +160 fs^2 (Fig. 6.7(h)). Actually, we refer each material insertion position (i.e., material thickness relative to the compensate dispersion position) with the added GDD, but the glass dispersion is not a pure GDD and it also includes higher order phase terms.

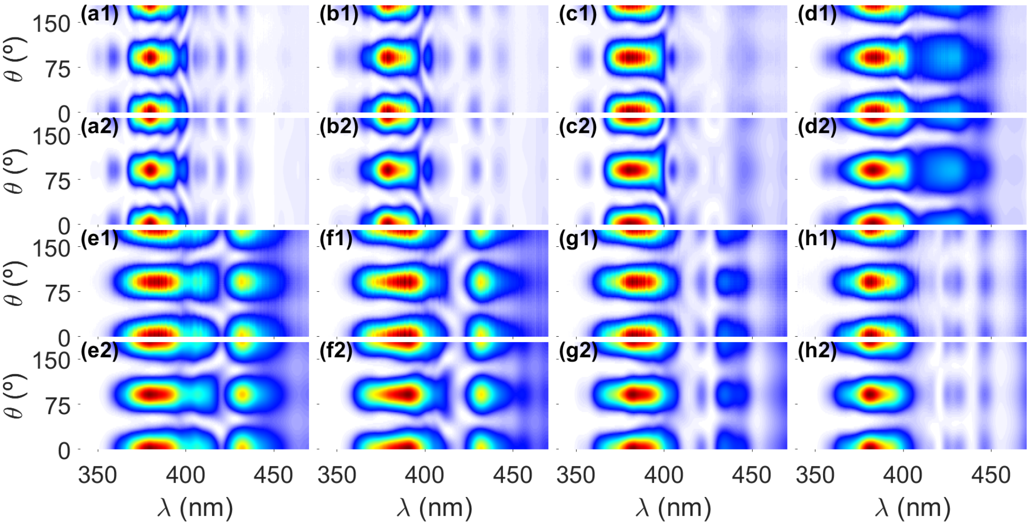

Fig. 6.7. *Experimental (first and third rows) and retrieved (second and fourth rows) amplitude swing traces for different insertion of the wedges corresponding to a relative added dispersion respect to the compensated position of (a) -160 fs^2, (b) -120 fs^2, (c) -80 fs^2, (d) -40 fs^2, (e) +40 fs^2, (f) +80 fs^2, (g) +120 fs^2 and (h) +160 fs^2.*

All the amplitude swing traces have been retrieved using the theoretical SHG response of the system shown in Fig. 6.4.

On one hand, Figs. 6.8(a1-h1) depict the spectral phase comparison between the amplitude swing and d-scan retrievals for each added dispersion case. On the other hand, the temporal electric field comparison is shown in Figs. 6.8(a2-h2). Moreover, for each case an inset of the FWHM temporal duration is added to easily compare each insertion observing the very good agreement.

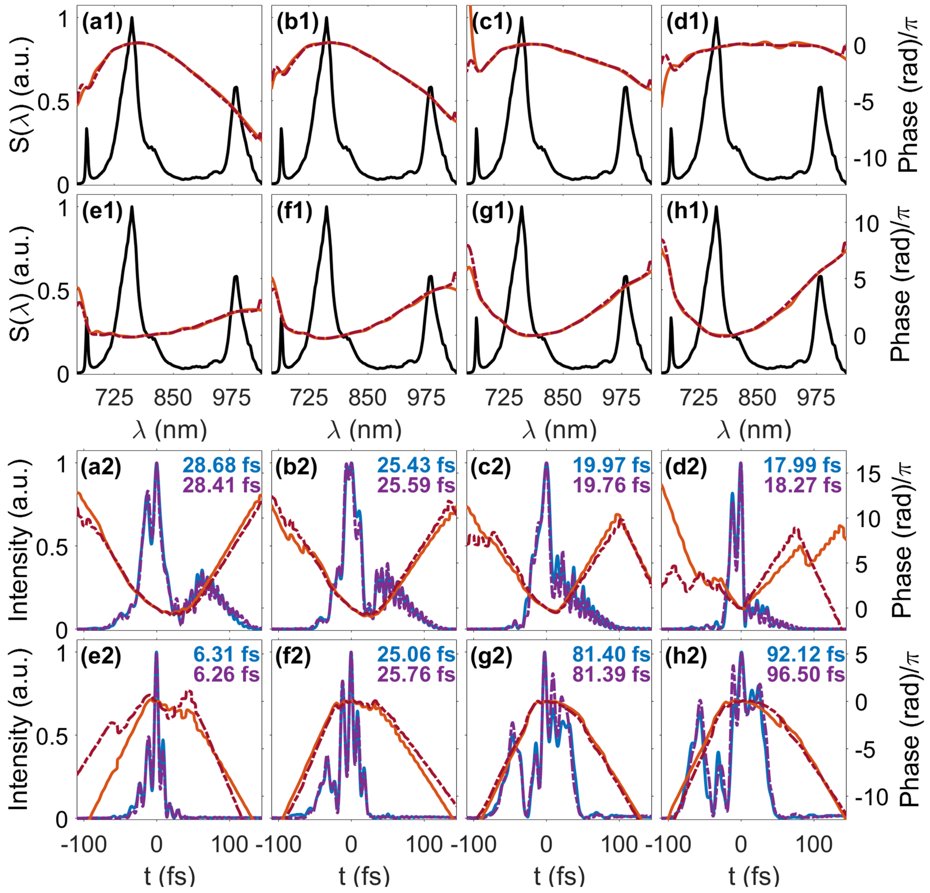

Fig. 6.8. *Spectral (first and second rows) and temporal (third and fourth rows) electric field comparison obtained with amplitude swing (solid lines) and d-scan (dashed lines) for the relative added dispersion values of (a) -160 fs^2, (b) -120 fs^2, (c) -80 fs^2, (d) -40 fs^2, (e) +40 fs^2, (f) +80 fs^2, (g) +120 fs^2 and (h) +160 fs^2. Moreover, for each temporal retrieval is shown an inset of the FWHM temporal duration of amplitude swing (blue) and d-scan (purple).*

Both, spectral and temporal electric field comparisons, present excellent agreement for each dispersion value, even far from compensated dispersion. Notice that the pulse is stretched up to ~15-20 times its FTL pulse duration (FWHM).

In conclusion, amplitude swing is able to characterize few-cycle laser pulses without modifying the original scheme, and the only points to take into account are to use a MWP introducing a delay of the order of the pulse

FTL and a good calibration (either experimental or theoretical) of the SHG response. In addition, its versatility enables the possibility to characterize the ultra-broadband pulses even if the dispersion is not perfectly compensated, as shown with the pulse reconstructions far from compression.

Chapter 7

Generalizing amplitude swing

Previously, in Chapter 3, the fundamentals of the amplitude swing technique have been discussed, and a compact implementation has been presented, based on a rotating MWP and a linear polarizer, to generate two delayed replicas of the pulse under test with varying amplitude [31].

The current Chapter is focused on the generalization of the amplitude swing concept to other configurations that could be implemented, modulating the amplitude with different evolutions and ratios between the relative amplitude of the pulse replicas. In fact, it is also possible to use modulations with complex amplitudes, as it will be shown later, including the case of relative phase variation introduced in addition to the amplitude variation.

In particular, here it is studied the possibility of using a rotating zero-order waveplate (ZWP) before a static MWP and a linear polarizer. This configuration is interesting because it enables different ways to introduce the varying amplitude and, depending on the phase retardation of the ZWP, also a varying phase term, thus presenting various strategies to apply the amplitude swing concept.

Moreover, in Chapter 3 and previous works [31, 91], it has been demonstrated that the amplitude swing needs to introduce a delay of the order of the FTL duration (less than 3 times greater or smaller) to efficiently codify the spectral phase. For this reason, sometimes it may be necessary to combine multiple MWP to have the appropriate delay. Another interesting possibility is to use a pair of birefringent wedges, so the delay can be tuned modifying the optical path length. In this sense, rotating these systems (set of MWP or wedges) can be complex or awkward. Therefore, the configuration with rotating ZWP and fixed MWP could also be useful in these situations.

7.1 Theoretical analysis

The original amplitude swing implementation, explained in Chapter 3 and represented in Fig. 7.1(a), is based on a rotating MWP followed by a horizontal linear polarizer (LP) and a SHG crystal. Previously, it has been shown that, for a horizontal linearly polarized electric field, its SHG trace with this conventional configuration is:

$$\begin{aligned} S_M^{SHG}(\omega,\theta_M) = \Bigg| \int \Bigg(\int A(\omega')e^{i\varphi(\omega')} \Big[e^{i\Phi_f(\omega')} G_{fM}(\theta_M) + \\ + e^{i\Phi_s(\omega')} G_{sM}(\theta_M) \Big] e^{-i\omega' t} d\omega' \Bigg)^2 e^{i\omega t} dt \Bigg|^2 \end{aligned} \tag{7.1}$$

where $A(\omega)$ and $\varphi(\omega)$ are the spectral amplitude and phase of the pulse under test, respectively, and Φ_f and Φ_s correspond to the phase terms acquired by the fast and slow components after propagation through the MWP, respectively. In this representation, $G_{fM}(\theta_M)$ and $G_{sM}(\theta_M)$ are the modulation factors of the fast and slow components due to the rotating MWP and the linear polarizer:

$$\begin{cases} G_{fM}(\theta_M) = \cos^2\theta_M \\ G_{sM}(\theta_M) = \sin^2\theta_M \end{cases} \tag{7.2}$$

being θ_M the azimuthal angle of the fast axis of the MWP with the horizontal axis.

The alternative configuration studied in this Chapter, and represented in Fig. 7.1(b), consists on a rotating ZWP followed by a fixed MWP with its fast axis at 45°, a horizontal linear polarizer (LP) and a SHG crystal. Firstly, in Subsection 7.1.1 we will present the general formalism and, after that, we will focus on two cases of particular interest of ZWP: half-waveplate (HWP) and quarter-waveplate (QWP) in Subsections 7.1.2 and 7.1.3, respectively.

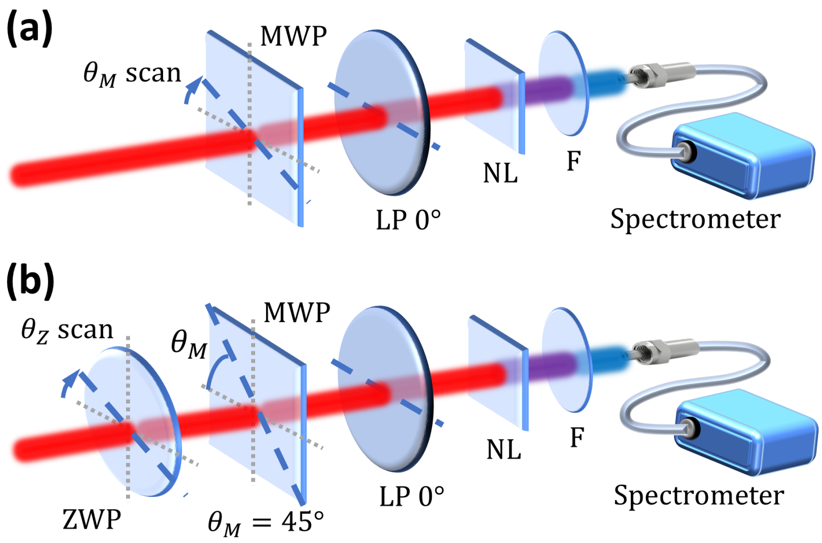

Fig. 7.1. *(a) Original amplitude swing based on a rotating MWP and (b) proposed configuration based on a rotating ZWP with a fixed MWP.*

7.1.1 General formalism

Let's consider a initial pulse horizontally polarized given by $E(\omega) = A(\omega)e^{i\varphi(\omega)}$, being $A(\omega)$ and $\varphi(\omega)$ the spectral amplitude and phase, respectively. Using the Jones calculus matricial formalism, this field can be expressed in the laboratory system (XY) as:

$$\vec{E}_{ini}^{(\mathrm{XY})}(\omega) = E(\omega)\begin{pmatrix}1\\0\end{pmatrix} \tag{7.3}$$

This input pulse can be expressed in the system of coordinates of the ZWP axes (fast and slow, respectively), by rotating the coordinates the azimuthal angle between the fast axis of the ZWP and the horizontal axis (θ_Z):

$$\begin{cases}\vec{E}_{ini}^{(\mathrm{ZWP})}(\omega) = R(\theta_Z)\cdot\vec{E}_{ini}^{(\mathrm{XY})}(\omega)\\ R(\theta_Z) = \begin{pmatrix}\cos\theta_Z & \sin\theta_Z\\ -\sin\theta_Z & \cos\theta_Z\end{pmatrix}\end{cases} \Longrightarrow$$

$$\vec{E}_{ini}^{(\mathrm{ZWP})}(\omega) = E(\omega)\begin{pmatrix}\cos\theta_Z\\ -\sin\theta_Z\end{pmatrix} \tag{7.4}$$

During the propagation through the ZWP, this element introduces a phase retardation, Φ_r, between the fast and slow components. Thus, the electric field after it will be:

$$\begin{cases} \vec{E}^{(\mathrm{ZWP})}_{\mathrm{ZWP}}(\omega) = M^{(\mathrm{ZWP})}_{\mathrm{ZWP}} \cdot \vec{E}^{(\mathrm{ZWP})}_{\mathrm{ZWP}}(\omega) \\ M^{(\mathrm{ZWP})}_{\mathrm{ZWP}} = \begin{pmatrix} 1 & 0 \\ 0 & e^{i\Phi_r} \end{pmatrix} \end{cases} \Longrightarrow$$

$$\vec{E}^{(\mathrm{ZWP})}_{\mathrm{ZWP}}(\omega) = E(\omega) \begin{pmatrix} \cos\theta_Z \\ -e^{i\Phi_r}\sin\theta_Z \end{pmatrix} \tag{7.5}$$

being, $M^{(\mathrm{ZWP})}_{\mathrm{ZWP}}$ the matrix of the ZWP in its coordinate system.

After the ZWP, the electric field will go through a fixed MWP whose fast axis forms an azimuthal angle $\theta_M = 45°$ with respect to the horizontal axis. Before applying the MWP matrix, for simplicity, we project the electric field of Eq. **7.5** onto the MWP axes:

$$\begin{cases} \vec{E}^{(\mathrm{MWP})}_{\mathrm{ZWP}}(\omega) = R(\theta_{ZM}) \cdot \vec{E}^{(\mathrm{ZWP})}_{\mathrm{ZWP}}(\omega) \\ R(\theta_{ZM}) = \begin{pmatrix} \cos\theta_{ZM} & \sin\theta_{ZM} \\ -\sin\theta_{ZM} & \cos\theta_{ZM} \end{pmatrix} \end{cases} \Longrightarrow$$

$$\vec{E}^{(\mathrm{MWP})}_{\mathrm{ZWP}}(\omega) = E(\omega) \begin{pmatrix} \cos\theta_Z\cos\theta_{ZM} - e^{i\Phi_r}\sin\theta_Z\sin\theta_{ZM} \\ -\cos\theta_Z\sin\theta_{ZM} - e^{i\Phi_r}\sin\theta_Z\cos\theta_{ZM} \end{pmatrix} \tag{7.6}$$

being, $\theta_{ZM} = (\theta_M - \theta_Z)$ the relative azimuthal angle between the fast axes of both retarder plates (please remember that along the present discussion $\theta_M = 45°$ is considered to be constant).

Now that the electric field is expressed in the MWP axes system, we can directly apply the MWP matrix obtaining:

$$\begin{cases} \vec{E}^{(\mathrm{MWP})}_{\mathrm{MWP}}(\omega) = M^{(\mathrm{MWP})}_{\mathrm{MWP}} \cdot \vec{E}^{(\mathrm{MWP})}_{\mathrm{ZWP}}(\omega) \\ M^{(\mathrm{MWP})}_{\mathrm{MWP}} = \begin{pmatrix} e^{i\Phi_f(\omega)} & 0 \\ 0 & e^{i\Phi_s(\omega)} \end{pmatrix} \end{cases} \Longrightarrow$$

$$\vec{E}^{(\mathrm{MWP})}_{\mathrm{MWP}}(\omega) = E(\omega) \begin{pmatrix} \left[\cos\theta_Z\cos\theta_{ZM} - e^{i\Phi_r}\sin\theta_Z\sin\theta_{ZM}\right] e^{i\Phi_f(\omega)} \\ \left[-\cos\theta_Z\sin\theta_{ZM} - e^{i\Phi_r}\sin\theta_Z\cos\theta_{ZM}\right] e^{i\Phi_s(\omega)} \end{pmatrix} \tag{7.7}$$

where, Φ_f and Φ_s are the phase terms added to the fast and slow components due to the propagation through the MWP, respectively, and $M_{\mathrm{MWP}}^{(\mathrm{MWP})}$ is the matrix of the MWP in its coordinate system.

This electric field in the MWP system can be expressed in the laboratory system (XY) rotating $-\theta_M$. Since in this case $\theta_M = 45°$, the electric will be:

$$\begin{cases} \vec{E}_{\mathrm{MWP}}^{(\mathrm{XY})}(\omega) = R(-45°) \cdot \vec{E}_{\mathrm{MWP}}^{(\mathrm{MWP})}(\omega) \\ R(-45°) = \frac{1}{\sqrt{2}} \begin{pmatrix} 1 & -1 \\ 1 & 1 \end{pmatrix} \end{cases} \implies$$

$$\vec{E}_{\mathrm{MWP}}^{(\mathrm{XY})}(\omega) = E(\omega) \begin{pmatrix} G_f(\theta_Z, \varphi_r) e^{i\Phi_f(\omega)} + G_s(\theta_Z, \varphi_r) e^{i\Phi_s(\omega)} \\ G_f(\theta_Z, \varphi_r) e^{i\Phi_f(\omega)} - G_s(\theta_Z, \varphi_r) e^{i\Phi_s(\omega)} \end{pmatrix} \tag{7.8}$$

where, $G_f(\theta_Z, \varphi_r)$ and $G_s(\theta_Z, \varphi_r)$ are the modulation factors of the fast and slow components defined as:

$$\begin{cases} G_f(\theta_Z, \varphi_r) = \frac{1}{\sqrt{2}} \left[\cos\theta_Z \cos\theta_{ZM} - e^{i\Phi_r} \sin\theta_Z \sin\theta_{ZM}\right] \\ G_s(\theta_Z, \varphi_r) = \frac{1}{\sqrt{2}} \left[\cos\theta_Z \sin\theta_{ZM} + e^{i\Phi_r} \sin\theta_Z \cos\theta_{ZM}\right] \end{cases} \tag{7.9}$$

Therefore, if the horizontal projection is selected with a linear polarizer, the amplitude swing fundamental electric field will be:

$$\begin{aligned} E_f(\omega) = \frac{E(\omega)}{\sqrt{2}} \Bigg(& \left[\cos\theta_Z \cos\theta_{ZM} - e^{i\Phi_r} \sin\theta_Z \sin\theta_{ZM}\right] e^{i\Phi_f(\omega)} + \\ & + \left[\cos\theta_Z \sin\theta_{ZM} + e^{i\Phi_r} \sin\theta_Z \cos\theta_{ZM}\right] e^{i\Phi_s(\omega)} \Bigg) \end{aligned} \tag{7.10}$$

From this analysis it can be observed that the initial pulse, $E(\omega)$, is divided into two replicas, corresponding to the fast and slow components in the MWP. The replicas are delayed due to an appropriate choice of birefringence and thickness in the MWP, as happens in the original amplitude swing configuration. In addition, these replicas are modulated as a function of the ZWP orientation, θ_Z, (please remember $\theta_{ZM} = \theta_M - \theta_Z$ and $\theta_M = 45°$) and the phase retardation of the ZWP, Φ_r.

Finally, using this electric field to produce SHG signal, the amplitude swing trace for the horizontal projection will be:

$$S_Z^{SHG}(\omega,\theta_Z) = \left| \int \left(\int A(\omega')e^{i\varphi(\omega')} \Big[e^{i\Phi_f(\omega')} G_f(\theta_Z,\Phi_r) + \right.\right. \\ \left.\left. + e^{i\Phi_s(\omega')} G_s(\theta_Z,\Phi_r) \Big] e^{-i\omega' t} d\omega' \right)^2 e^{i\omega t} dt \right|^2 \tag{7.11}$$

where, the modulation factors, $G_f(\theta_Z,\varphi_r)$ and $G_s(\theta_Z,\varphi_r)$, can be simplified taking into account $\theta_M = 45°$:

$$\begin{cases} G_f(\theta_Z,\Phi_r) = \frac{1}{4}(1+\cos 2\theta_Z + \sin 2\theta_Z) + \frac{1}{4}(1-\cos 2\theta_Z - \sin 2\theta_Z)e^{i\Phi_r} \\ G_s(\theta_Z,\Phi_r) = \frac{1}{4}(1+\cos 2\theta_Z - \sin 2\theta_Z) + \frac{1}{4}(1-\cos 2\theta_Z + \sin 2\theta_Z)e^{i\Phi_r} \end{cases} \tag{7.12}$$

We find that the modulation factors are complex but, in our case, a global phase term can be disregarded. Thus, to analyze the dependence of the amplitude swing trace with these factors, we focus our attention on their amplitudes and their relative phase, being the last one defined as:

$$\Phi_{G_s-G_f}(\theta_Z,\Phi_r) = Arg\Big\{ \big(1+\cos(4\theta_Z) + 2\cos\Phi_r \sin^2(2\theta_Z)\big) + i\left(4\cos\theta_Z \sin\theta_Z \sin\Phi_r\right) \Big\} \tag{7.13}$$

where *Arg* is a function to obtain the argument of the complex number.

The modulation introduced in a scan of θ_Z for different Φ_r values of the ZWP is shown in Fig. 7.2. In particular, Figs. 7.2(a,b) correspond to the amplitudes of G_f and G_s, respectively, whereas Fig. 7.2(c) represents the relative phase introduced between the slow and fast replicas. Please notice that the maximum possible amplitude value for each modulation factor is $1/\sqrt{2}$. In addition, Fig. 7.2(d) depicts the contrast between the modulation factors for each θ_Z and Φ_r, defined as the difference between maximum and minimum amplitude value of the modulation factors divided by the maximum value (i.e., $(M_G - m_G)/M_G$, being M_G and m_G the maximum and minimum value between the amplitude of the modulation factors at the corresponding θ_Z and Φ_r).

Regarding the amplitudes, Figs. 7.2(a,b), the fast and slow modulation factors exhibit alternate maxima and minima, thus presenting maximum

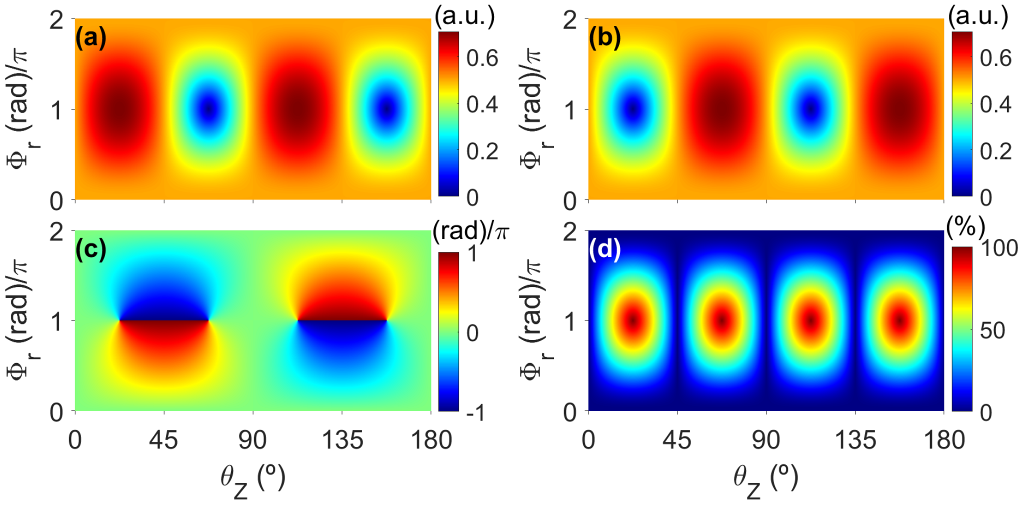

Fig. 7.2. Simulation of modulation factors dependences with the ZWP orientation (θ_Z) for different retardation phases (Φ_r). (a,b) Amplitude of the fast (G_f) and slow (G_s) modulation factors, respectively. (c) Relative phase between the fast and slow components due to the ZWP ($\Phi_{G_s-G_f}$). (d) Contrast between the amplitude of the modulation factors.

contrast at some particular θ_Z scan angles ($22.5° + m \cdot 45°$, being m an integer). In contrast, there are some θ_Z positions (multiples of 45°) that present equal amplitude of G_f and G_s, thus having null contrast. In the case of HWP ($\Phi_r = \pi$ rad), the contrast goes from 0% to 100%, whereas for a ZWP with $\Phi_r = 0$ or 2π rad the contrast is always null and there is no amplitude modulation.

Regarding the relative phase between the fast and slow replicas, Fig. 7.2(c), it varies along the ZWP scan and it also changes depending on the value Φ_r of the ZWP. Indeed, there are some ZWP azimuthal angles (θ_Z multiples of 90°) where $\Phi_{G_s-G_f} = 0$ regardless the value of Φ_r. The maximum ($+\pi$ rad) and minimum ($-\pi$ rad) relative phases are observed for a phase retardation of $\Phi_r = \pi$ rad (i.e., HWP) and the relative phase introduced tends to zero when approaching to $\Phi_r = 0$ or 2π rad.

To identify suitable phase retardations of the ZWP, it can be calculated the maximum contrast between the modulation factors and the maximum dephase excursion (i.e., difference between maximum and minimum relative phase among the fast and slow components) along a θ_Z scan as a function of Φ_r, Figs. 7.3(a,b) respectively. From this representation, it can be easily observed that using Φ_r close to 0 or 2π rad will hardly introduce any amplitude or phase modulation. The best contrast situation corresponds to $\Phi_r = \pi$ rad (i.e., HWP). Regarding $\Phi_r = \pm\pi/2$ rad (i.e. QWP), which will be studied later, it presents a maximum contrast of 42% (i.e., none replica reaches zero amplitude) and the maximum dephase excursion is π rad.

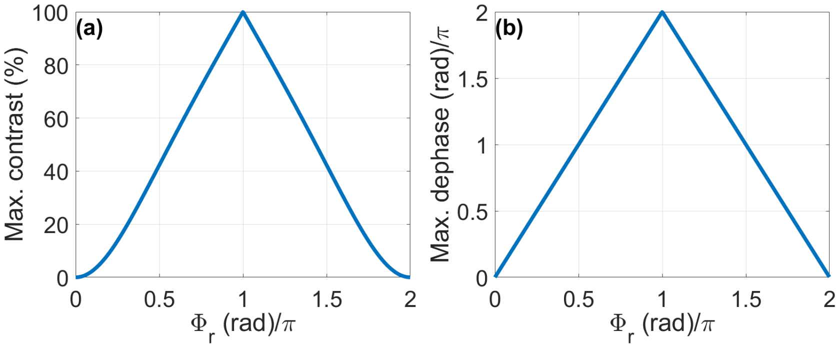

Fig. 7.3. *Representation of the maximum amplitude contrast (a) and dephase excursion (b) of G_f and G_s for a scan of the ZWP as a function of the ZWP phase retardation (Φ_r).*

Therefore, the modulation of amplitude swing traces will change depending on the phase retardation of the ZWP. Fig. 7.4 depicts some examples of amplitude swing traces obtained with different configurations for a 50-fs FTL Gaussian spectrum pulse centered at 800 nm with a spectral phase of GDD=40000 fs^2 and TOD= $2 \cdot 10^5$ fs^3. In this example, we have assumed a 2-mm-thick quartz MWP with a phase retardation of π rad for the central wavelength, which introduces a ~60-fs delay. Fig. 7.4(a) corresponds to the original amplitude swing configuration rotating the MWP, whereas Figs. 7.4(b-j) show the here proposed configuration (rotating ZWP and fixed MWP at 45°) for different values of Φ_r from 0 to 2π rad in steps of 0.25π rad.

The new configuration with $\Phi_r = 0$ or 2π rad, Figs. 7.4(b,j), does not present any modulation, as previously discussed. Moreover, for this specific case, the configuration with rotating ZWP with $\Phi_r \neq 0$ or 2π rad presents a more intricate structure of interference compared to the rotating MWP.

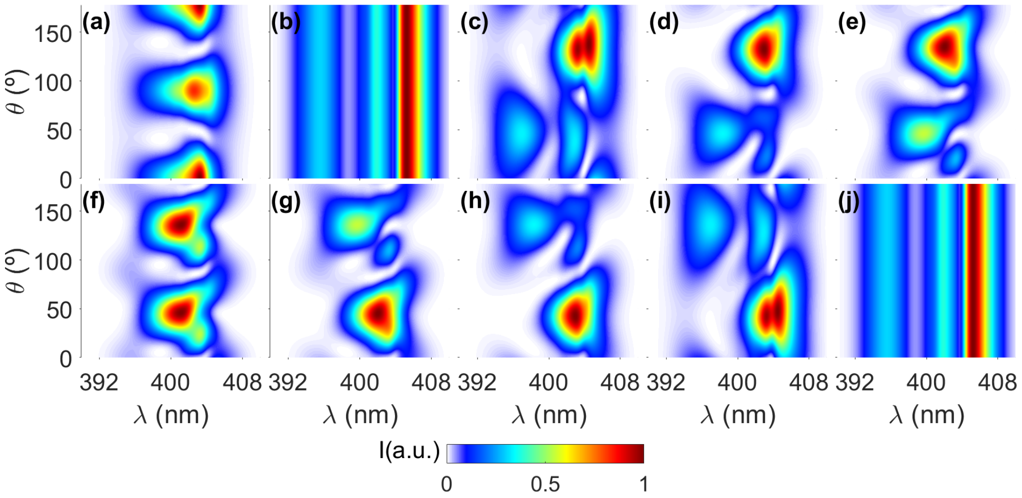

Fig. 7.4. *Example of amplitude swing for (a) rotating MWP and (b-j) rotating ZWP with fixed MWP at 45° for different phase retardations of the ZWP: (b) 0 rad, (c) 0.25π rad, (d) 0.50π rad, (e) 0.75π rad, (f) 1π rad, (g) 1.25π rad, (h) 1.50π rad, (i) 1.75π rad and (j) 2π rad.*

7.1.2 Rotating HWP

In previous Subsection, the amplitude swing formalism has been explained for a general case, but here we will focus on what happens if the ZWP is a HWP (i.e., $\Phi_r = \pi$ rad). As mentioned before, this case is interesting because it corresponds to the best contrast situation of the modulation factors.

For this particular situation, the modulation factors can be expressed as:

$$\begin{cases} G_f(\theta_Z, \pi) = \frac{1}{\sqrt{2}} \cos\left(2\theta_Z - \pi/4\right) \\ G_s(\theta_Z, \pi) = -\frac{1}{\sqrt{2}} \sin\left(2\theta_Z - \pi/4\right) \end{cases} \tag{7.14}$$

being θ_Z the angle of the HWP with the horizontal axis. In this case, the ZWP rotates the orientation of the initial linear polarization that is decomposed on the MWP axes.

Comparing the amplitude of the modulation factors for the rotating HWP, Eqs. **7.14** and solid lines (blue and orange for the fast and slow components) of Fig. 7.5, with the ones of the original configuration, Eq. **7.2** and dashed lines of Fig. 7.5, they are similar but now the cosine and sine are non-squared and they vary with θ_Z (instead of θ_M). In addition, a 22.5° shift appears in the amplitude modulation of trace. From these dependences it can be extracted that, in this configuration, the trace is repeated twice during a 180° scan in θ_Z, whereas for the original amplitude swing the trace is symmetrical with respect to 90°. Please notice that we have normalized the modulation factors of the original amplitude swing in Fig. 7.5 to have the same maximum amplitude as the rotating HWP, easing the visualization.

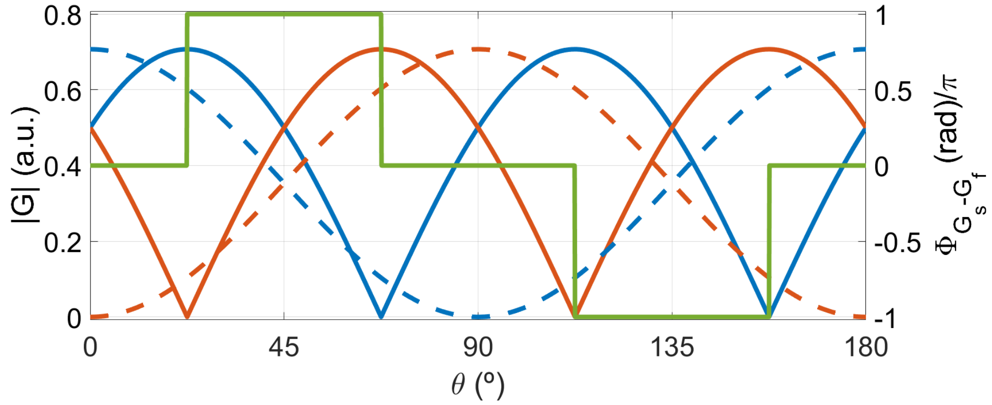

Fig. 7.5. *Amplitude (blue and orange for the fast and slow components) and relative phase (green) of the modulation factors for a rotating HWP (solid lines) and rotating MWP (dashed lines). Please notice that the relative phase with rotating MWP is always zero and it is not represented to clarify the comparison.*

Furthermore, paying attention to the relative phase difference for the HWP, green line of Fig. 7.5, there is a 0 or π rad phase difference between the fast and slow replicas depending on θ_Z. The 0 dephase corresponds to positions where both modulation factors are positive or negative, whereas the π rad dephase is associated to positions where they have opposite sign.

One interesting feature of the rotating HWP configuration is that, as happens with the conventional amplitude swing, along an azimuthal angle scan the amplitude evolves from having only one replica to present only the other one. The main differences between configurations are the rate of the change, the phase shift and the 0 or π rad dephase in the rotating HWP.

Paying attention to the positions with 0 dephase, $\theta_Z \in (0° - 22.5°,\ 62.5° - 112.5°,\ 157.5° - 180°)$, it can be found that this area of a rotating HWP trace contains the equivalent information to the rotating MWP trace (if the scan were performed instead rotating the same MWP from 0° to 180°). This is due to, as said before, the amplitude modulation is similar in both cases (from 0 to 100% contrast), but at a different rate. In order to obtain conversion to the corresponding MWP trace, we first impose the condition that the amplitude ratio of the replicas is the same:

$$\frac{|G_s(\theta_Z,\pi)|}{|G_f(\theta_Z,\pi)|}=\frac{|G_{sM}(\theta_M)|}{|G_{fM}(\theta_M)|}\Rightarrow \tan(2\theta_Z-\pi/4)=-\tan^2(\theta_M) \qquad \textbf{(7.15)}$$

From this, it can be extracted the following reshaping function, which has been represented with a blue line in Fig. 7.6(a), taking into account that the chosen scan ranges are from 0° to 180°:

$$\theta_Z=\begin{cases}\text{mod}\left\{\frac{\pi}{8}+\frac{\arctan\left(-\tan^2(\theta_M)\right)}{2},\pi\right\} & \text{for } \theta_M\in[0,\pi/2)\text{ rad}\\ \text{mod}\left\{\frac{\pi}{8}+\frac{\arctan\left(-\tan^2(\theta_M)\right)+\pi}{2},\pi\right\} & \text{for } \theta_M\in[\pi/2,\pi)\text{ rad}\end{cases} \qquad \textbf{(7.16)}$$

being mod$\{a,b\}$ a function that returns the remainder after division of a and b. Notice that a π rad term is added to the result of the arctan function in the second equation in order to correctly resolve the arctan ambiguity according to our problem (considering that the arctan function gives the result between $-\pi/2$ rad and $+\pi/2$ rad).

To complete the transformation and obtain the corresponding rotating MWP trace, in addition to the pulse replica ratio equality at the given position, the pulse intensity modulation rate should be the same too. Since the replica amplitude ratio has been fixed, it is enough to adjust now the amplitude of one replica. We select here the fast replica, but choosing the slow one would also give the same condition. Thus, for each angle θ_M, we apply the following rescaling function, which has been represented with a blue line in Fig. 7.6(b):

$$\left[\frac{G_{fM}(\theta_M)}{G_f(\theta_Z,\pi)}\right]^4=\left[\frac{\cos^2(\theta_M)}{\cos(2\theta_Z-\pi/4)}\right]^4 \qquad \textbf{(7.17)}$$

where θ_Z is given by Eq. **7.16**. Please notice that the 4^{th} power comes from considering the spectrum (squared complex modulus) of the SHG of the interfering replicas.

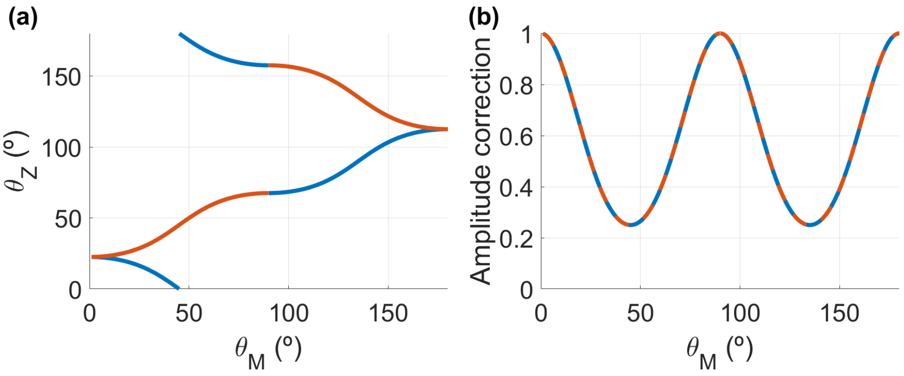

Fig. 7.6. *(a) Reshaping and (b) rescaling functions to transform a rotating HWP amplitude swing trace into a rotating MWP trace with phase retardation* Φ_M *(blue lines) or* $\Phi_M + \pi$ *(orange and dashed orange lines).*

Notice that for this transformation we have only used the areas of the rotating HWP with 0 dephase. The rest of the HWP trace, which presents π rad dephase, is equivalent to a rotating MWP trace but with an additional phase retardation term of π rad ($\Phi_M \longrightarrow \Phi_M + \pi$, being Φ_M the phase retardation of the employed MWP). Using an analogous study, taking into account the sign change in the reshaping condition, it can be obtained the reshaping function for this case, which is collected in Eq. **7.18** and represented with orange line in Fig. 7.6(a).

$$\theta_Z = \begin{cases} \text{mod}\left\{\frac{\pi}{8} + \frac{\arctan\left(+\tan^2(\theta_M)\right)}{2}, \pi\right\} & \text{for } \theta_M \in [0, \pi/2) \\ \text{mod}\left\{\frac{\pi}{8} + \frac{\arctan\left(+\tan^2(\theta_M)\right)+\pi}{2}, \pi\right\} & \text{for } \theta_M \in [\pi/2, \pi) \end{cases} \qquad \textbf{(7.18)}$$

The rescaling function for this case, represented with dashed orange line in Fig. 7.6(b), is the same as the 0 dephase situation.

From Fig. 7.6(b) it can be concluded that the rescaling function evolves from 1, for HWP angles where there is only one replica, to 0.25, for positions where the replicas have the same amplitude. Therefore, the signal to noise ratio can be up to 4 times better in the region of the trace where the interfering replicas have similar amplitudes.

To show an example of this transformation, we have used a 50-fs FTL Gaussian spectrum pulse centered at 800 nm with a spectral phase of GDD=

40000 fs^2 and TOD$= 2 \cdot 10^5$ fs^3. In this example we have assumed a 2-mm-thick quartz MWP, which introduces a ~60-fs delay with a phase retardation of $\Phi_M = 0.8\pi$ rad for the central wavelength.

On one hand, Figs. 7.7(a,b) represent the original amplitude swing traces calculated with the rotating MWP configuration using as phase retardation Φ_M and $\Phi_M + \pi$, respectively. Fig. 7.7(c) corresponds to the amplitude swing trace simulated with a rotating HWP, considered achromatic in all the spectral range.

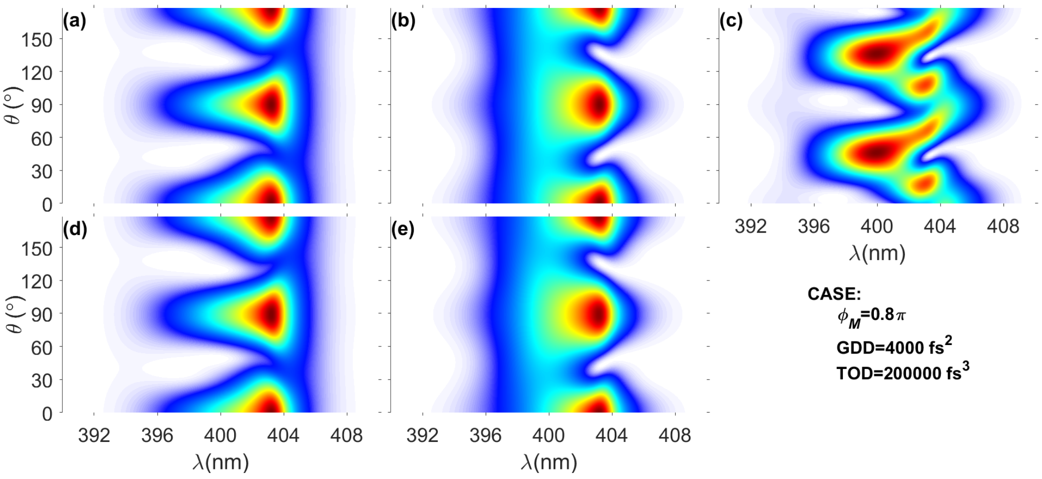

Fig. 7.7. *Amplitude swing traces for 50-fs FTL Gaussian spectrum pulse centered at 800 nm with GDD=4000 fs^2 and TOD=$2{\cdot}10^5$ fs^3. (a,b) Simulated rotating MWP traces for a retardation phase Φ_M of (a) 0.8π rad and (b) 1.8π rad. (c) Simulated rotating HWP trace with a fixed MWP of $\Phi_M = 0.8\pi$ rad. (d,e) Calculated rotating MWP traces for retardation phase Φ_M (d) 0.8π rad and (e) 1.8π rad, using the reshaping and rescaling of the rotating HWP trace shown in (c).*

On the other hand, Figs. 7.7(d,e) correspond to the rotating MWP traces obtained applying the reshaping and rescaling factors to the rotating HWP trace of Fig. 7.7(c). In particular, Fig. 7.7(d) is obtained from the 0 dephase information using Eqs. **7.16-7.17**, whereas Fig. 7.7(e) is calculated with the π rad dephase area using Eqs. **7.17-7.18**.

There is very good agreement between the rotating MWP simulated and reshaped amplitude swing traces. Therefore, the transformation is possible and a single rotating HWP trace contains the information of two conventional amplitude swing traces.

7.1.3 Rotating QWP

Another interesting case of rotating ZWP is when it is a QWP (i.e., $\Phi_r = \pi/2$ rad). In this situation, the modulation factors can be expressed as:

$$\begin{cases} G_f(\theta_Z, \pi/2) = \frac{1}{4}\left(1 + \cos(2\theta_Z) + \sin(2\theta_Z)\right) + \frac{1}{4}\left(1 - \cos(2\theta_Z) - \sin(2\theta_Z)\right) i \\ G_s(\theta_Z, \pi/2) = \frac{1}{4}\left(1 + \cos(2\theta_Z) - \sin(2\theta_Z)\right) + \frac{1}{4}\left(1 - \cos(2\theta_Z) + \sin(2\theta_Z)\right) i \end{cases} \tag{7.19}$$

being θ_Z the angle of the QWP with the horizontal axis. The dependence of the amplitudes and the relative phase of the modulation factors for this case are represented in Fig. 7.5 as a function of θ_Z.

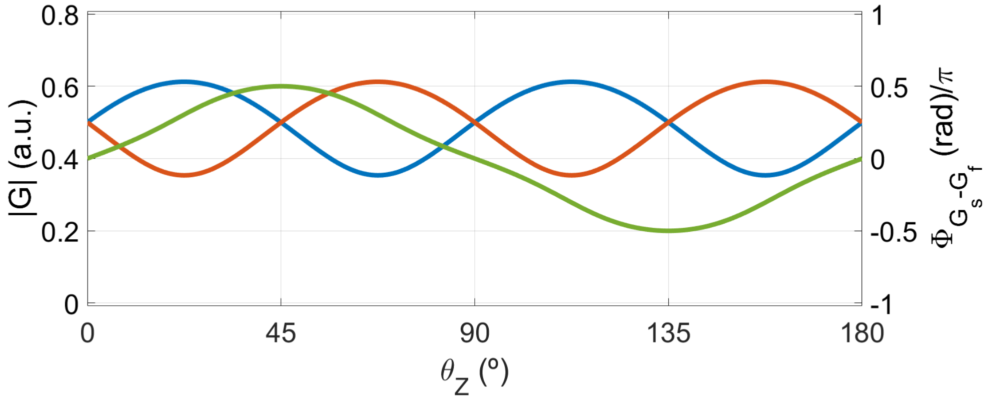

Fig. 7.8. *Amplitude (blue and orange for the fast and slow components, respectively) and relative phase (green) of the modulation factors for a rotating QWP.*

In this case, the contrast between the pulsed replicas evolves from null contrast, for those positions where the QWP preserves the input linear polarization or converts it into circular polarization (having the same relative amplitude), to a maximum of 42% in the intermediate elliptical polarization positions.

Moreover, in contrast to the conventional amplitude swing or the rotating HWP configurations, both replicas are always interfering during a scan (i.e., there is not a position of θ_Z where there is only one replica).

Regarding the relative phase added by the rotating QWP, it varies in the range $-\pi/2$ to $\pi/2$ rad depending on the QWP orientation. This implies that, in addition to the varying amplitude modulus, it is also introduced a continuously varying dephase. Thus, the trace in this configuration could be interpreted as several portions of conventional amplitude swing traces with different phase retardations. Furthermore, the periodicity of the scans with this configuration is 180°.

7.2 Numerical simulation

In the previous Section, we have presented the analytical study of new configurations of amplitude swing based on a rotating ZWP before a fixed MWP, and we have compared some features with the original amplitude swing configuration (rotating MWP).

The current Section compares the robustness against noise of various configurations simulating and reconstructing different amplitude swing traces for four set-ups: rotating MWP, rotating HWP with fixed MWP, rotating QWP with fixed MWP and rotating ZWP of $\Phi_r = 0.75\pi$ rad with fixed MWP, being the fixed MWP always at $\theta_M = 45°$.

In particular, we are going to study each retrieval with the Levenberg-Marquardt retrieval algorithm used in [31], upgraded to include the shaping elements that perform the amplitude swing modulation presented in this work (e.g., fixed or rotating MWP and rotating ZWP). The dispersion of the different elements of each amplitude swing configuration is considered within the reconstruction algorithm, so that the input pulse is retrieved and the results from each configuration can be directly compared.

All configurations presented in this Section use the same MWP (either rotating or static), 2-mm-thick quartz with π rad phase retardation, which introduces a ∼60-fs delay around 800 nm. Regarding the HWP, QWP and ZWP, without lack of generality, we will assume that all of them can be considered achromatic and non-dispersive in the bandwidth of the pulses under test.

Here we present the analysis of a pulse with Gaussian spectrum centered at 800 nm with 50-fs FTL duration FWHM and a spectral phase that combines GDD=1000 fs^2, TOD=2000 fs^3 and an oscillatory term $(0.3\pi\cdot\cos[50(\omega-\omega_0)+0.25\pi])$. To study the behavior of the different configurations against various noise level, the ideal amplitude swing traces for each configuration have been simulated and different white Gaussian noise levels (defined as the rms of the noise with respect to the normalized trace) from 0 to ∼15% have been added to them.

An example with a noise level of 4.3% rms is shown in Fig. 7.9 and the complete study for different levels of noise is depicted in Appendix A.

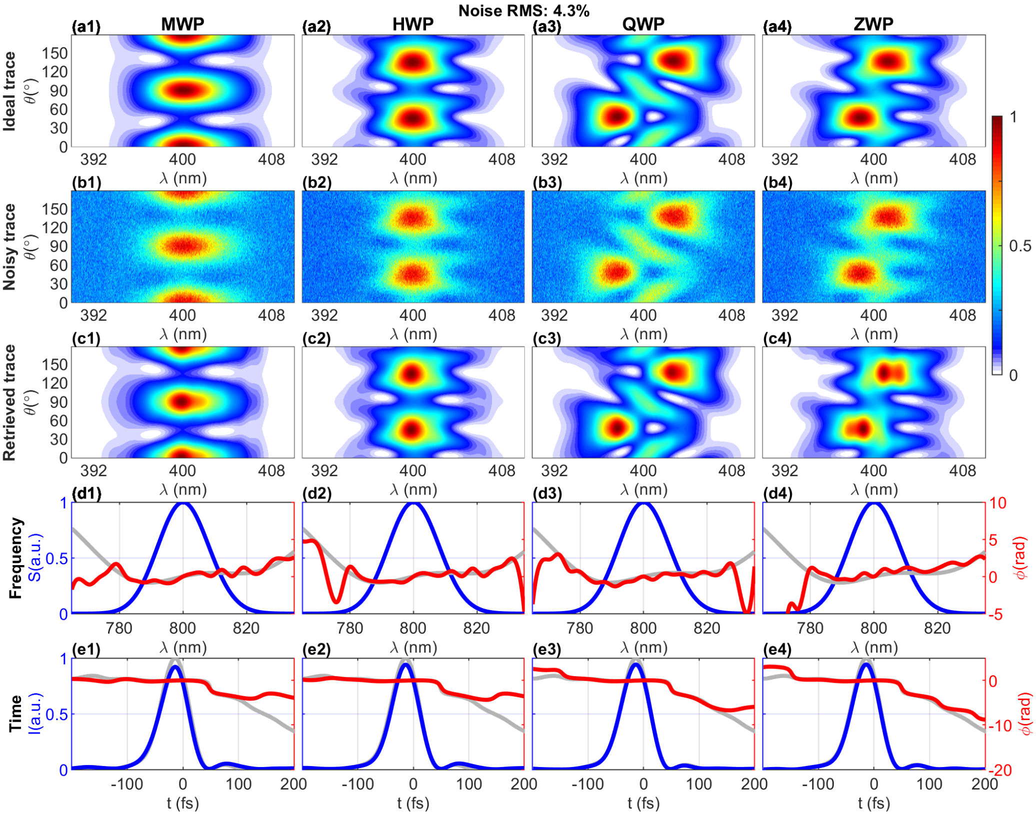

Fig. 7.9. Comparison of amplitude swing configurations analyzing traces with 4.3% rms noise added. (a) Ideal, (b) noisy and (c) retrieved amplitude swing traces. (d) Spectral and (e) temporal comparison of the retrieved (blue and red) and theoretical (gray) pulses. The configurations studied are: (column 1) rotating MWP, (column 2) rotating HWP, (column 3) rotating QWP, and (column 4) rotating ZWP with $\Phi_r = 0.75\pi$ rad.

Figs. 7.9(a-c) correspond to the ideal, noisy and retrieved amplitude swing traces, respectively. From this representation, it can be observed that the agreement of the retrieved and ideal traces is good, even with the high noise level of the simulated traces analyzed with the algorithm, Fig. 7.9(b). The good agreement is also observed in the spectral and temporal intensity and phase comparison depicted in Figs. 7.9(d,e), respectively, where the theoretical dependences are shown in gray lines.

Some parameters that can be taken into account to compare the robustness for different noise levels are depicted Fig. 7.10. On one hand, Fig. 7.10(a) represents the rms between the ideal and retrieved traces (solid lines) for different noise levels using the four configurations. Notice that we compare the retrieved trace with the ideal one, instead of the noisy trace, because it gives a better quantification of the quality of the retrieval. In addition, Fig. 7.10(a) also includes the rms between the temporal intensities of the ideal pulse used to simulate the traces and the retrieved from the noisy trace (dashed lines). On the other hand, the retrieved temporal pulse duration (FWHM) of each case is compared with the theoretical value (dashed gray line) in Fig. 7.10(b).

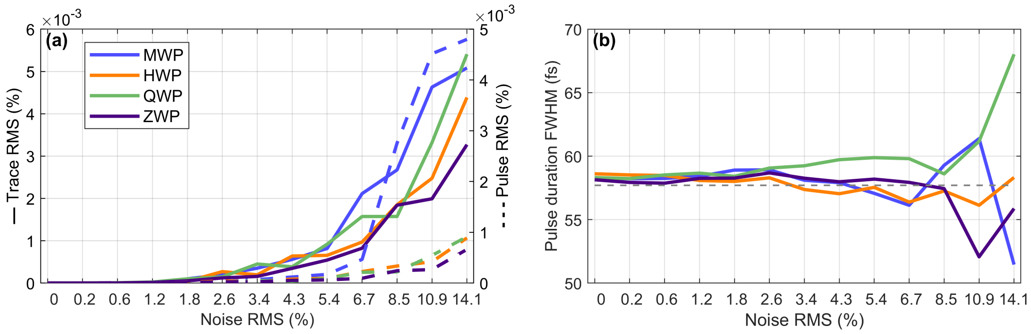

Fig. 7.10. *Comparison of (a) rms between the ideal and retrieved amplitude swing traces (solid lines) and temporal intensities (dashed lines), and (b) pulse duration (FWHM) for different noise levels. The amplitude swing configurations are: (blue) rotating MWP, (orange) rotating HWP, (green) rotating QWP, and (purple) rotating ZWP with* $\Phi_r = 0.75\pi$ *rad. The theoretical FWHM (dashed gray line) is depicted in (b).*

From the analysis of this specific case, it seems that, with high noise values, all the new configurations are slightly better than the original amplitude swing, highlighting the rotating ZWP with $\Phi_r = 0.75\pi$ rad. Nevertheless, the behavior may change depending on the pulse under study, the phase retardation of the MWP, the merit function used for the optimizations and the retrieval algorithm itself. Thus, depending on the specific situation one configuration may be better than the others.

One general feature that we have observed simulating different situations is that, for low and moderate noise levels, all the configurations present good convergence. Indeed, the noise levels in which some differences can be observed are very high and, if seen in experiments, are usually considered as too high and some other experimental strategies to improve the signal to noise ratio are seeked.

7.3 Experimental demonstration

In this Section we present the experimental demonstration of different amplitude swing configurations.

The laser system used in this experiment was a Titanium:sapphire CPA laser (Spectra-Physics, model Spitfire ACE) that provides pulses centered at 798 nm with a FTL of ∼56-fs FWHM and a repetition rate of 5 kHz. The compressor of this system allows to modify the output pulse GDD, thus generating compressed or chirped pulses. We used it to study an almost compressed pulse and a chirped pulse with different amplitude swing configurations.

In particular, the pulses were characterized using three different configurations of amplitude swing. All of them were implemented using a 2-mm-thick quartz MWP, which introduces a delay between replicas of ∼60 fs and has a phase retardation of 0.34π rad at 800 nm. One configuration was the original amplitude swing based on a rotating MWP, firstly presented in [31] and explained in Chapter 3. The other two configurations were based on a rotating ZWP before a fixed MWP at 45°. In particular, we have used a HWP and a QWP (from Eksma Optics), which can be considered achromatic in the bandwidth of the laser system. The SHG medium was a 20-μm Type-I BBO with perfect phase-matching for the pulse bandwidth. Moreover, the SHG signal was measured with a spectrometer (HR4000 from Ocean Optics Inc.) for different positions of the retarder plates and the fundamental spectrum was measured before the amplitude swing system using another spectrometer (AvaSpec 2048-USB1 from Avantes Inc.).

The traces were analyzed with the upgraded Levenberg-Marquardt retrieval algorithm used in Section 7.2. As done before, the dispersion of the different elements is taken into account within the retrieval algorithm in order to directly obtain the input pulse with each configuration.

Fig. 7.11 depicts the amplitude swing experimental (columns 1 and 3) and retrieved (columns 2 and 4) traces for the characterization of a compressed (columns 1 and 2) and a chirped (columns 3 and 4) pulse.

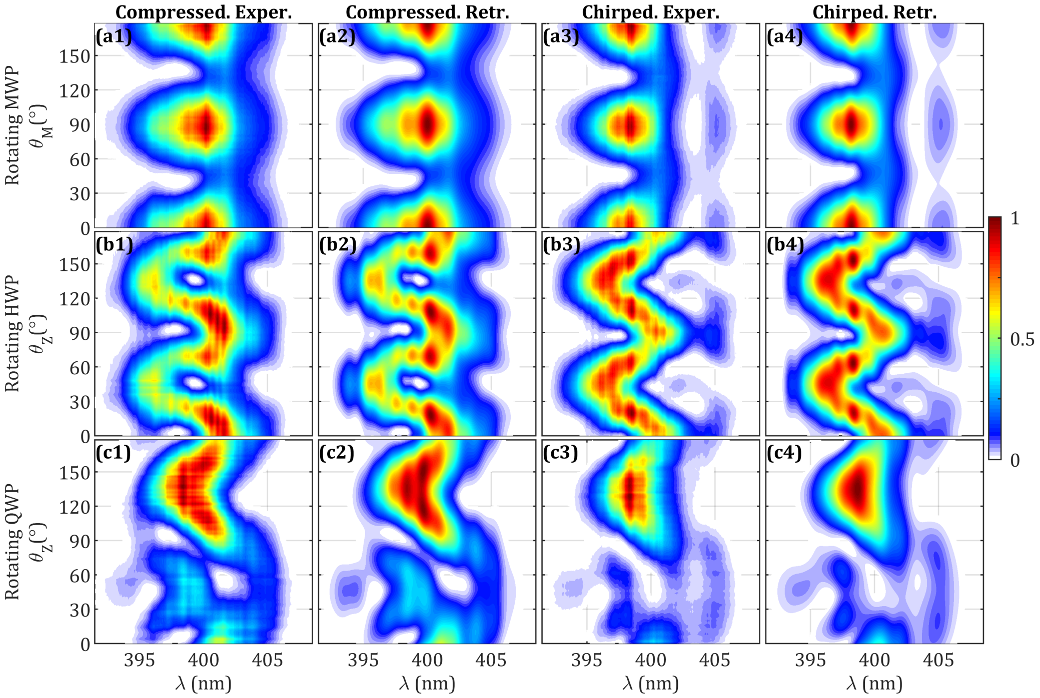

Fig. 7.11. *Amplitude swing experimental (columns 1 and 3) and retrieved (columns 2 and 4) traces for a compressed (columns 1 and 2) and a chirped (columns 3 and 4) pulses using three different configurations of the technique: (a) conventional amplitude swing rotating MWP, (b) rotating HWP with fixed MWP and (c) rotating QWP with fixed MWP.*

Fig. 7.11(row a) shows the traces for the conventional amplitude swing configuration, whereas Figs. 7.11(rows b,c) depict the traces for the rotating HWP and QWP, respectively.

Notice that the convergence is good for all the strategies showing rms differences between the experimental and retrieved traces lower than $1.2{\cdot}10^{-3}$.

The retrieved pulses with the different amplitude swing configurations are shown in Figs. 7.12(a,c) for the compressed pulse and Figs. 7.12(b,d) for the chirped pulse. The gray shaded areas in the retrievals correspond to the standard deviation from the mean phase of each retrieval with the 3 configurations in the spectral and temporal domains.

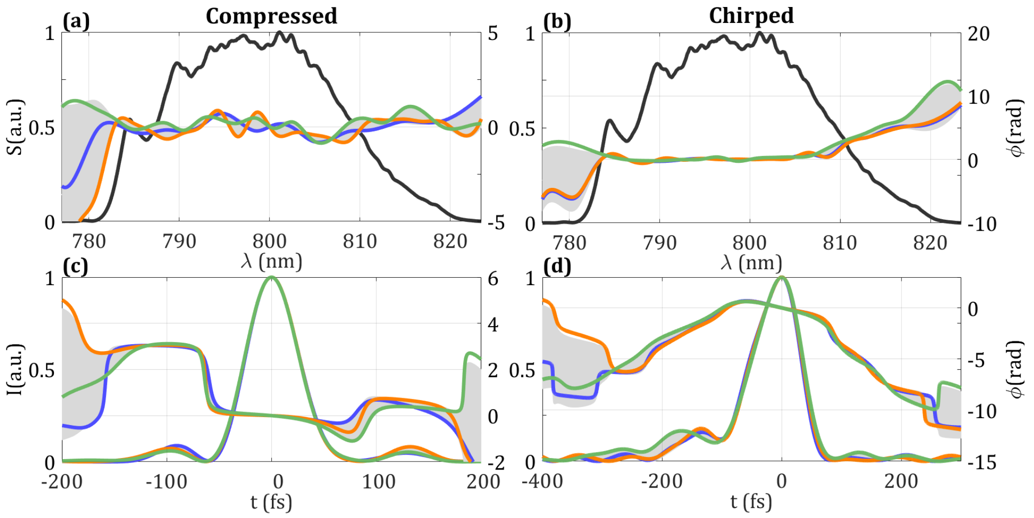

Fig. 7.12. *(a,b) Experimental spectrum (black) and retrieved spectral phases and (c,d) retrieved temporal intensities and phases for the compressed (a,c) and chirped (b,d) pulses of Fig. 7.11. Retrievals obtained for amplitude swing trace with rotating MWP (blue), rotating HWP with fixed MWP (orange) and rotating QWP with fixed MWP (green). The gray shaded areas represent the standard deviation from the mean of each retrieval with the 3 configurations.*

Regarding the spectral comparison, Figs. 7.12(a,b), the retrievals present the same spectral phases in each situations (compressed and chirped pulse), regardless the amplitude swing configurations. This good agreement is also observed in the temporal intensity and phase, Figs. 7.12(c,d), and the temporal FWHM for each pulse. The retrieved FWHM for the compressed pulse are: 57.0 fs with the rotating MWP, 57.4 fs the rotating HWP and 57.3 fs the rotating QWP. The retrieved temporal FWHM durations for the chirped pulse also agree between them: 93.4 fs with the rotating MWP, 93.2 fs the rotating HWP and 93.0 fs the rotating QWP.

We can also use the experimental traces with the rotating HWP and MWP to verify the reshaping strategy explained in Subsection 7.1.2. Fig. 7.13 demonstrates this process comparing the rotating MWP trace experimentally measured, Figs. 7.13(a,b), and the calculated, Figs. 7.13(c,d), for the compressed and chirped pulses, respectively, using Eqs. **7.16-7.17** with the information of 0 dephase of the rotating HWP trace of Fig. 7.11(b).

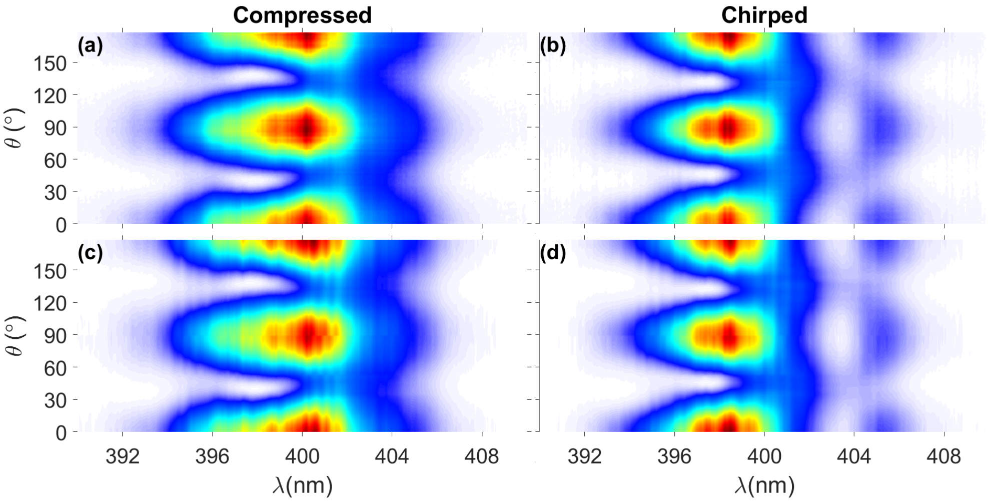

Fig. 7.13. *(a,b) Experimental rotating MWP (orange) and (c,d) calculated rotating MWP from the analysis reshape of the rotating HWP with fixed MWP traces shown in Fig. 7.11. (a,c) Compressed pulse and (b,d) chirped pulse.*

In conclusion, we have demonstrated that, based on the amplitude swing concept, different strategies to modulate the amplitude can be implemented in order to characterize ultrashort laser pulses.

Part III

SPATIOTEMPORAL CHARACTERIZATION WITH BULK LATERAL SHEARING INTERFEROMETRY

Chapter 8

Bulk lateral shearing interferometry technique

In Section 2.2, we have mentioned many spatiotemporal techniques that have been implemented during the last decades. However, these techniques are usually based on complex set-ups to be implemented in the laboratory and/or present low stability due to their high sensitivity to external perturbations. In this Chapter, we present the compact, simple and ultra-stable spatiotemporal technique developed during this Thesis [136], whose high stability enables to retrieve the spectrally and temporally resolved wavefronts of complex ultrashort laser beams. The compact implementation of the developed technique was firstly hinted as a possible optimization in [137], but it was not demonstrated.

8.1 Concept and fundamental ideas

The spatiotemporal technique proposed in this Thesis is based on the combination of spectral and lateral interferometry. In particular, it relies on the properties of uniaxial birefringent crystals to implement this combination in a compact and ultra-stable system.

Specifically, the technique takes advantage of two particular properties of uniaxial birefringent media, the delay and the walk-off among polarization components, to obtain two temporally delayed and laterally sheared replicas of the beam, whose interference encodes the spatiospectral information. The properties of these media, which will be explained in Chapter 9, depend on the medium thickness, the optical axis orientation, the birefringent refractive indices and the angle of incidence. In a first approach, to understand the concept, we will assume that we are working with collimated beams under normal incidence conditions. Thus, the properties of the uniaxial birefringent crystals will follow the simplified model that will be explained in Subsection 9.2.3. Moreover, later in Section 10.2 we will study what happens with non-collimated beams with a given numerical aperture using the general model that will be explained in Section 9.2.

Under normal incidence conditions, we can distinguish two types of uniaxial birefringent crystals according to the optical axis orientation. On one hand, if the optical axis (O.A.) is not contained in the crystal interface, as considered in Fig. 8.1(a), the incident beam is split into two temporally delayed and laterally sheared replicas (ordinary and extraordinary beams, being the last one the laterally displaced beam) through its propagation in the medium. Crystals with this configuration will be called walk-off crystals and constitute the pillar of the spatiotemporal technique proposed in this Thesis.

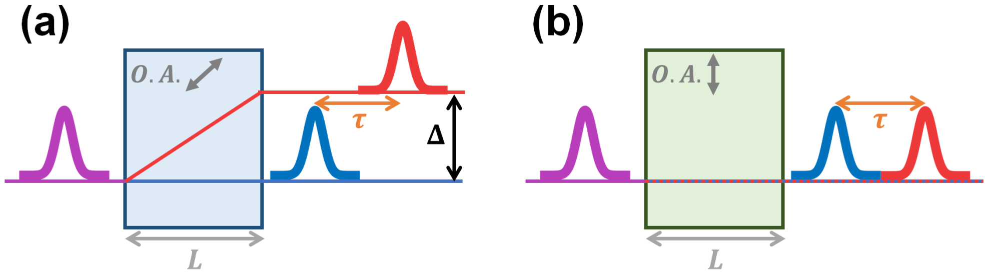

Fig. 8.1. *Representation of the delay (τ) and walk-off (Δ) properties experienced by an incident pulsed beam (purple) due to traveling through an uniaxial birefringent medium in (a) walk-off crystal and (b) retarder plate configuration. The blue and red lines represent the ordinary and extraordinary beams, respectively. Notation: L corresponds to the crystal thickness and the arrow indicates the orientation of the optical axis (O.A.).*

On the other hand, if the optical axis is contained in the crystal interface, Fig. 8.1(b), the original beam will split into two temporally delayed replicas (ordinary and extraordinary beams) without lateral shearing. The crystals with this configuration will be called retarder plates and, in the spatiotemporal technique, they can be used to adjust the delay between the replicas.

In both cases, the ordinary and extraordinary beams will be linearly polarized in orthogonal directions. In addition, since we are considering normal incidence and plane-parallel crystals, in both configurations the output beams will be parallel to the input beam.

Taking into account the above mentioned properties, uniaxial media can be used to combine the spectral and lateral interferometry by generating two delayed and laterally sheared replicas of the beam under test. Thus, as we will demonstrate in this Section, the spectral interference pattern, obtained from the projection of both replicas into a common direction by using a linear polarizer, encodes the spatiospectral phase gradient.

The technique can retrieve 1D or 2D structures but, for simplicity, we will explain the fundamentals with a 1D approach and later extend it to 2D.

Since more than one uniaxial birefringent crystals can be simultaneously used to implement the technique (e.g., to adjust the walk-off and delay values), whose ordinary and extraordinary components can be different, we will always refer to the laterally sheared replica as walk-off beam (WB) and the non-sheared replica as ordinary beam (OB), regardless of whether the WB or OB play the opposite role on the additional retarder plate. Moreover, we have chosen the criterion that the first component to arrive to the detection is the walk-off beam for the SI. If the ordinary beam arrives before the walk-off beam, the same formalism of this Section can be used, but conjugating the extracted relative phase or filtering the $-\tau$ satellite peak in the Fourier Transform Spectral Interferometry (FTSI) algorithm that will be explained below.

Taking into account the notation and criterion above mentioned, if the two linearly polarized replicas are projected onto a common polarization projection, the spectrum of the spectral interferometry (S_{SI}) at the detection stage will be:

$$\begin{aligned} S_{SI}(r_j,\omega) = S_{OB}(r_j,\omega) + S_{WB}(r_j,\omega) + 2\sqrt{S_{OB}(r_j,\omega)S_{WB}(r_j,\omega)}\cdot \\ \cdot \cos\left[(\varphi_{OB}(r_j,\omega) - \varphi_{WB}(r_j,\omega))_{meas}\right] \end{aligned} \tag{8.1}$$

where, S and φ are the spectrum and spectral phase at the spatial point r_j with the subindices 'OB' and 'WB' referring to the ordinary or walk-off beam, respectively. Moreover, ω and r_j represent the angular frequency of the light and the spatial position of the measurement.

The $(\varphi_{OB}(r_j,\omega) - \varphi_{WB}(r_j,\omega))_{meas}$ term corresponds to the relative phase between the walk-off and ordinary beams, which is a combination of the relative phase of the beams itself (*beam*) and the phase acquired due to traveling through the birefringent crystal (*crys*):

$$\begin{aligned} (\varphi_{OB}(r_j,\omega) - \varphi_{WB}(r_j,\omega))_{meas} = \\ = (\varphi_{OB}(r_j,\omega) - \varphi_{WB}(r_j,\omega))_{beam} + (\varphi_{OB}(\omega) - \varphi_{WB}(\omega))_{crys} \end{aligned} \tag{8.2}$$

presenting $(\varphi_{OB}(\omega) - \varphi_{WB}(\omega))_{crys}$ only spectral dependence, not spatial, because the birefringent crystals used in the technique are plane-parallels (i.e., the relative phase introduced by the crystal is the same regardless the position). This relative phase term must be known from the crystal specifications or experimentally calibrated. In our case we choose the latter option because a theoretical estimation requires a highly accurate calibration of the system parameters, in particular the thickness.

The key point of the technique is that the ordinary and walk-off beams are two delayed and laterally sheared replicas of the same initial beam, so Eq. **8.1** can be expressed in terms of the initial beam spectrum ($S(r,\omega)$) and phase ($\varphi(r,\omega)$). Assuming that the lateral shear is introduced in the positive direction, and the incident and final polarizations are linearly polarized at an intermediate direction between both replicas (45° with respect to the projection of the O.A. onto the crystal interface), Eq. **8.1** is equivalent to:

$$\begin{aligned} S_{SI}(r_j,\omega) = \frac{1}{2}S(r_j,\omega) + \frac{1}{2}S(r_{j-1},\omega) + \sqrt{S(r_j,\omega)S(r_{j-1},\omega)}\cdot \\ \cdot \cos\left[(\varphi(r_j,\omega) - \varphi(r_{j-1},\omega))_{meas}\right] \end{aligned} \tag{8.3}$$

Notice that the incident and the final polarizations presents the best contrast in the SI because each beam has the same energy, but any linear polarization state oriented in a common direction between both replicas is possible.

If we measure in steps equal to the walk-off, the phase term of Eq. **8.3** represents the spatiospectral phase gradient in the walk-off direction: $\nabla_{\varphi}^{meas} = (\varphi(r_j,\omega) - \varphi(r_{j-1},\omega))_{meas}$. Please notice that the phase gradient array ∇_{φ}^{meas} also includes the phase introduced by the birefringent elements of the system, as explained in Eq. **8.2**. Thus, it must be calibrated to extract the phase gradient information of the beam under test: $\nabla_{\varphi}^{beam} = \nabla_{\varphi}^{meas} - \nabla_{\varphi}^{crys}$. The calibration can be done using an average flat wavefront (pulsed) beam. We have observed that it is useful to average the calibration at different spatial points, so small fluctuations in the wavefront are compensated and the calibration is less restrictive in terms of quality of the calibration plane beam. Despite we have used this strategy, it can be accomplished alternatively, for example, using a conventional wavefront sensor to calibrate certain wavelengths and then extrapolating the result for the whole pulse bandwidth or theoretically from the manufacturer specifications.

Once ∇_{φ}^{beam} is known, the relative spatiospectral phase can be obtained (i.e., spectrally resolved wavefronts without linking between wavelengths). Nevertheless, in order to obtain the absolute spatiospectral or spatiotemporal phase, it is necessary to know the spectral or temporal phase at a given spatial point (r_{j_0}), which can be measured with any temporal technique, for example one of those shown in Subsection 2.2.2. In our case, we find interesting to use amplitude swing for measuring the reference, since it is also a simple, compact and ultra-stable technique, as shown in Chapter 3. Therefore, the absolute spatiospectral phase of the pulse under study can be obtained integrating from the known point using the following equation (the spectral dependence is omitted and the spatial position r_j is referred as a subindex j in order to clarify the expressions, i.e., $\varphi(r_j,\omega) \equiv \varphi_j$):

$$\begin{aligned} \varphi_{j+1} &= \varphi_j + \{\nabla\varphi_{j+1}\}^{beam} \qquad &\text{if } r_j > r_{j_0} \\ \varphi_{j-1} &= \varphi_j - \{\nabla\varphi_j\}^{beam} \qquad &\text{if } r_j < r_{j_0} \end{aligned} \tag{8.4}$$

In case the walk-off is introduced in the negative direction, it can be done an analogous extraction, but taking into account that the spatiospectral phase gradient will be defined as: $\nabla_{\varphi} = [\varphi(r_j,\omega) - \varphi(r_{j+1},\omega)]$.

When the spatiospectral phase profile is extracted, it is necessary to know the spatiospectral amplitude to have the complete spatiospectral or spatiotemporal characterization. On one hand, this spatiospectral amplitude can be obtained by measuring the spectrum at different spatial positions using a linear polarizer to select only the ordinary beam. Notice that the walk-off beam can also be measured, but it should be taken into account that it is laterally displaced. On the order hand, the spatiospectral amplitude can also be extracted by filtering the $\tau = 0$ peak in the FTSI, if the condition of slowly spatially varying spectrum ($S(r_j, \omega) \sim S(r_{j\pm1}, \omega)$) is satisfied.

The 1D retrieval process analytically explained above can be summarized in the diagram shown in Fig. 8.2, in which a simulated divergent beam is analyzed.

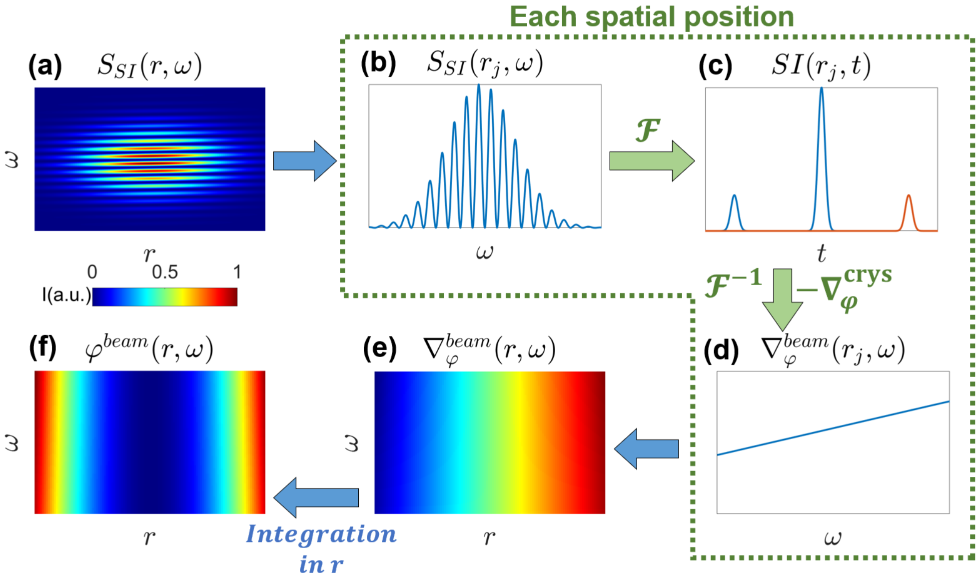

Fig. 8.2. *Scheme of the retrieval process of 1D measurements using the spatiotemporal technique.*

Firstly, in Fig. 8.2(a) it is shown an example of the spectral interferometry pattern along the spatial dimension. Secondly, Figs. 8.2(b-d) show the process done at each spatial point in order to obtain the spatiospectral gradient of the beam. In Fig. 8.2(b), the SI in the spectral domain is represented for the corresponding spatial point. Then, in Fig. 8.2(c) it is shown the SI in the temporal domain (blue line) and the filtered satellite (orange line). Once the satellite is filtered, the algorithm goes back to the spectral domain and obtains the phase gradient of the beam extracting the calibrated term, Fig. 8.2(d). The spatiospectral gradient along the spatial position is represented in Fig. 8.2(e). Finally, the full spatiospectral phase profile, Fig. 8.2(f), is obtained from the integration in the spatial dimension (r) of the spatiospectral gradient, knowing the phase at a reference point (in this example, we have chosen a flat phase at the center of the beam, for simplicity), following Eq. **8.4**.

Retrieval process of 2D structures

Now that we know how the technique works in a 1D approach, we can extend it to a 2D approach. The main difference is that, in the 2D approach, it is necessary to obtain the spatiospectral phase gradient in two non-collinear directions. We usually use the X and Y directions, and the change in the walk-off direction is done by azimuthally rotating the walk-off crystal around the longitudinal direction. Notice that the second measurement is necessary to link the different 1D slices.

In addition, during the Thesis we have implemented different ways of integrating the 2D measurements and we select the most appropriate depending on the beam structure.

On one hand, the simplest way consists in a matrix scan in one walk-off direction and a 1D array in the orthogonal direction to connect different 1D sections/slices. Depending on which direction is introduced the walk-off for the 2D scan, we call the approach *2DMx* or *2DMy* for the 2D scan done with walk-off in the X or Y directions, respectively. An example of this strategy is shown in Fig. 8.3, where a convergent wavefront is retrieved using the *2DMx* approach.

Firstly, the spatial grid of measurement with the reference point (purple star) at position (x_0, y_0) is represented in Fig. 8.3(a). The horizontal blue lines represent the slices that will give the phase gradient in the horizontal direction, whereas the green line represents the 1D vertical array used to link

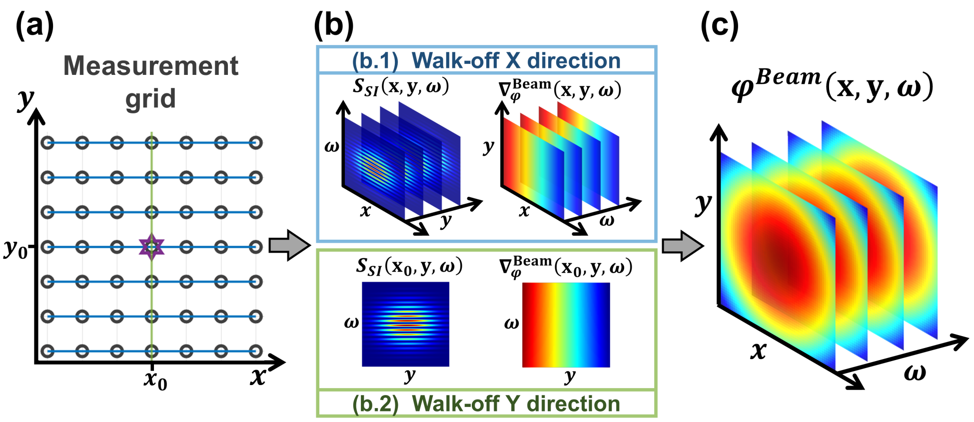

Fig. 8.3. *Example of the phase retrieval of a simulated convergent wavefront using the 2DMx approach measuring the 1D array to link all the heights at* x_0 *and knowing the spectral phase at* (x_0, y_0).

all the x-scans performed for different y values (in this case it is measured at x_0). Secondly, Fig. 8.3(b) depicts the measured SI spectra and the retrieved phase gradients with the walk-off introduced in the horizontal, Fig. 8.3(b.1), and vertical, Fig. 8.3(b.2), directions. Finally, the complete spatiospectral phase profiles obtained from the integration of both spatiospectral gradients are shown in Fig. 8.3(c).

On the other hand, more complex approaches can be done to avoid null signal points, which can introduce noise, by measuring the 2D matrix in both walk-off directions and changing the integration path.

For example, in Fig. 8.4 we show a strategy called *2D4Quad*, which retrieves the spatial phase combining the retrieval of 4 quadrants using *2DMx* or *2DMy* and knowing that in the spatial overlapping points (diagonal lines of the final scheme of Fig. 8.4) the phase must be the same. This strategy retrieves each quadrant separately imposing FTL phase reference at different points (triangles in Fig. 8.4). Then, the relative phase between quadrants is fixed, imposing that the phase of each retrieval must be the same at a certain position of the diagonals called '*phase set point*' (red stars in Fig. 8.4). The other spatial positions of the diagonal, which are not '*phase set point*', are obtained by averaging the two adjacent quadrants and, in the central position of the grid, by averaging the four quadrants. Finally, it is corrected the offset of the whole spatiospectral phase profile knowing the spectral phase at a reference point, thus obtaining the complete spatiospectral characterization.

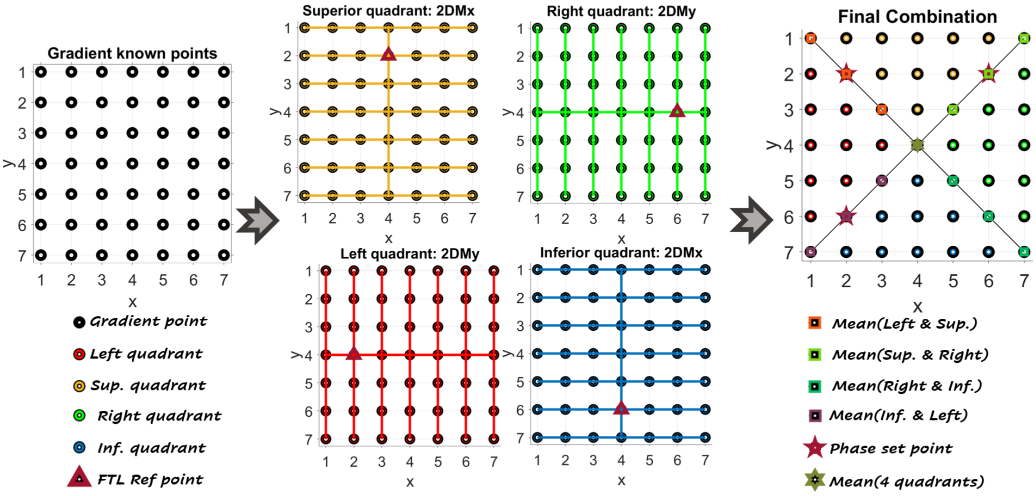

Fig. 8.4. *Scheme of the 2D retrieval approach called 2D4Quad.*

Another possibility is to perform the retrieval combining two quadrants instead of four, what we call it *2D2Quad*. These strategies are interesting to avoid null signal points at the center of the spatial profile, as it will happen in some examples studied in Chapter 11.

Besides these strategies, any other integration path can be used to avoid null signal points (e.g., integrating following a specific path to avoid some null signal areas) or somehow improve the reconstruction.

8.2 Spatial scan prototype

Once the fundamental concepts of the spatiotemporal technique have been introduced, we can focus on the experimental set-up. In Fig. 8.5, we show the scheme of the technique for 2D measurements introducing the walk-off in the X and Y directions.

In this scheme, the axis of the birefringent media (walk-off crystal and retarder plate) are in the horizontal and vertical directions, rotating 90° from Fig. 8.5(a) to Fig. 8.5(b). Thus, the walk-off is introduced in the vertical direction, while the delay remains constant. Notice that it can be done by

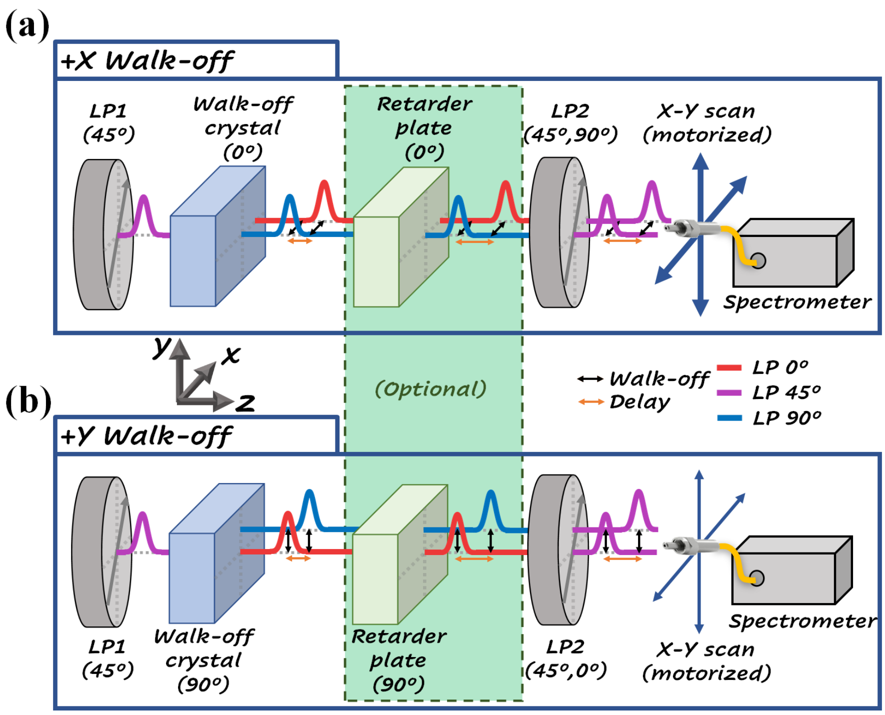

Fig. 8.5. *Scheme of the technique for 2D measurement with the walk-off introduced in: (a)X-direction and (b)Y-direction.*

rotating only the walk-off crystal and taking into account the corresponding delay for the FTSI algorithm at each situation.

Firstly, a linear polarizer selects the light 45° projection in order to have the same energy in the X and Y polarization projections. Then, a walk-off crystal delays and laterally shears both projections, obtaining after it the ordinary and walk-off beams with orthogonal polarizations (vertical and horizontal). If the delay is not suitable for the spectrometer resolution, it can be adapted using a retarder plate with the appropriate orientation and thickness. Afterwards, it is placed another polarizer that selects the interference pattern, if the transmission axis is set at 45°, or the ordinary/walk-off beam (depending on the optical axis direction), if it is set at 0° or 90°. Finally, an optical fiber, which collects the signal into a spectrometer, is placed in a 2D motorized stage to scan the beam.

The prototype implemented in the laboratory is shown in Fig. 8.6. In this prototype, we are using two linear polarizers (LP1 and LP2, black and gray boxes respectively), a walk-off crystal (blue box), a retarder plate (green box) and a XY motorized stage with an optical fiber connected to a spectrometer (AvaSpec 2048-USB1, from Avantes Inc.). In this case the XY-stage is controlled by two Kinesis K-cubes (Thorlabs).

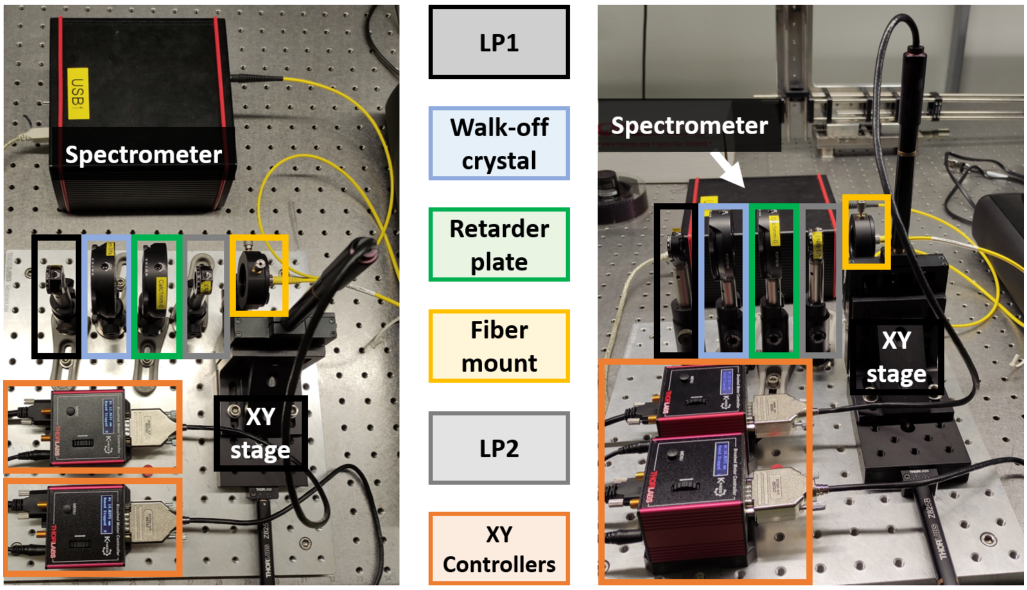

Fig. 8.6. *Two different views of the laboratory prototype for 2D measurements implemented with a XY-motorized stage and a fiber spectrometer.*

Other configurations can be implemented just by changing the detection stage. For example, it can be used an imaging spectrometer over a 1D motorized stage instead of the 2D motorized stage with the fiber connected to a spectrometer.

Chapter 9

Uniaxial birefringent crystals

The spatiotemporal characterization technique developed in this Thesis, which has been explained in Chapter 8, is based on the properties of uniaxial birefringent crystals in order to obtain a compact and ultra-stable set-up.

Previously, we have briefly introduced the main properties of the uniaxial birefringent media used by our spatiotemporal technique (delay and walk-off). In the current Chapter, we are going to focus on developing different theoretical models to deeply study these media. These models have been the key to understand the behavior of the principal elements used in our characterization technique, and they are based on the theoretical developments reported in [138, 139].

Firstly, in Section 9.1, we will study the propagation of monochromatic plane waves inside an uniaxial birefringent crystal. Then, in Section 9.2, we will analyze how the propagation changes if the uniaxial birefringent crystal is immersed in an isotropic medium. After that, in Section 9.3, we will generalize the application of the model to non-plane waves. Finally, in Section 9.4, we will explain the strategy that we have used to calibrate the uniaxial birefringent crystals.

9.1 Plane wave propagation inside uniaxial medium

Let's consider that we have a monochromatic plane wave with a wavevector $\vec{k}$ traveling inside an uniaxial birefringent medium that is non-magnetic, non-conductor and non-absorbent. Then, the constitutive relations between the displacement ($\vec{D}$) and electric field ($\vec{E}$) vectors and the magnetic induction ($\vec{B}$) and magnetic field ($\vec{H}$) vectors are:

$$\vec{D} = \overline{\overline{\varepsilon}}\vec{E} \tag{9.1}$$

$$\vec{B} = \mu_0 \vec{H} \tag{9.2}$$

where $\overline{\overline{\varepsilon}}$ and μ_0 correspond to the medium electric permittivity tensor and the vacuum magnetic permeability, respectively.

Since we are in an uniaxial birefringent medium, the $\overline{\overline{\varepsilon}}$ can be expressed in the crystal principal axes basis, $(\widehat{z_1}, \widehat{z_2}, \widehat{z_3})$, in which the electric permittivity tensor is diagonalized. Considering the optical axis is in the direction $\widehat{z_3}$, then:

$$\overline{\overline{\varepsilon}} = \begin{pmatrix} \varepsilon_o & 0 & 0 \\ 0 & \varepsilon_o & 0 \\ 0 & 0 & \varepsilon_z \end{pmatrix} \tag{9.3}$$

Taking into account the relation between the velocity in the medium and the permittivity and permeability, it is possible to define the following phase velocities associated with the two different values of the medium electric permittivity tensor:

$$u_o^2 = \frac{1}{\mu_0 \varepsilon_o} \tag{9.4}$$

$$u_z^2 = \frac{1}{\mu_0 \varepsilon_z} \tag{9.5}$$

Thus, if the relation between $\vec{D}$ and $\vec{E}$ shown in Eq. **9.1** is expressed in the crystal principal axes basis, it is equivalent to:

$$\begin{cases} E_1 = \mu_0 u_o^2 D_1 \\ E_2 = \mu_0 u_o^2 D_2 \\ E_3 = \mu_0 u_z^2 D_3 \end{cases} \tag{9.6}$$

where $\vec{E} = (E_1, E_2, E_3)$ and $\vec{D} = (D_1, D_2, D_3)$ are the electric field and displacement vectors in the basis $(\widehat{z_1}, \widehat{z_2}, \widehat{z_3})$.

The Maxwell's equations in the MKS system (i.e., physical system of measurement that uses the meter, kilogram, and second as base units) for this non-magnetic, non-conductor and non-absorbent medium can be expressed as:

$$\begin{cases} \nabla \times \vec{H} = \frac{\partial \vec{D}}{\partial t} \\ \nabla \times \vec{E} = -\mu_0 \frac{\partial \vec{H}}{\partial t} \\ \nabla \cdot \vec{D} = 0 \\ \nabla \cdot \vec{H} = 0 \end{cases} \qquad \mathbf{(9.7)}$$

As we have previously mentioned, we want to study the propagation of plane waves, so the following solutions for the Maxwell's equations can be proposed:

$$\vec{E} = \vec{E}_* e^{i\phi} \qquad \vec{D} = \vec{D}_* e^{i\phi} \qquad \vec{H} = \vec{H}_* e^{i\phi} \qquad \mathbf{(9.8)}$$

with

$$\phi = \frac{2\pi}{\lambda} n \left[\hat{s} \cdot \vec{r} - ut\right] + \phi_0 \qquad \mathbf{(9.9)}$$

being $\hat{s} = \frac{\vec{k}}{\|k\|}$ the unitary wavevector, $\vec{r}$ the vector from the input in the crystal to the output of the crystal where the field is calculated, λ the wavelength in vacuum, n the refractive index of the medium and u the phase velocity. The amplitude term of each variable is denoted as $\vec{E}_*$, $\vec{D}_*$ and $\vec{H}_*$.

Introducing the solution indicated in Eq. **9.8** in the Maxwell's equation system **9.7**, we obtain:

$$\begin{cases} \hat{s} \times \vec{H} = -u\vec{D} \\ \hat{s} \times \vec{E} = \mu_0 u \vec{H} \\ \hat{s} \cdot \vec{D} = 0 \\ \hat{s} \cdot \vec{H} = 0 \end{cases} \qquad \mathbf{(9.10)}$$

Substituting the second equation into the first equation of the system **9.10**, we obtain the following relation:

$$\mu_0 u^2 \vec{D} = \vec{E} - (\hat{s} \cdot \vec{E})\hat{s} \qquad \mathbf{(9.11)}$$

From the relation between components of $\vec{D}$ and $\vec{E}$ shown in the equation system **9.6**, we can express the relation **9.11** as:

$$\begin{cases} \left[u^2 + u_o^2\left(s_1^2 - 1\right)\right] D_1 + u_o^2 s_2 s_1 D_2 + u_z^2 s_3 s_1 D_3 = 0 \\ u_o^2 s_1 s_2 D_1 + \left[u^2 + u_o^2\left(s_2^2 - 1\right)\right] D_2 + u_z^2 s_3 s_2 D_3 = 0 \\ u_o^2 s_1 s_3 D_1 + u_o^2 s_2 s_3 D_2 + \left[u^2 + u_z^2\left(s_3^2 - 1\right)\right] D_3 = 0 \end{cases} \qquad \textbf{(9.12)}$$

being s_1, s_2 and s_3 the components of $\hat{s}$ in the crystal principal axes basis.

There are two possible solutions of the phase velocity, u, for the system **9.12**:

$$u' = u_o \qquad \textbf{(9.13)}$$

$$u'' = \sqrt{u_z^2 + (u_o^2 - u_z^2) s_3^2} \qquad \textbf{(9.14)}$$

These phase velocities are associated with two plane waves, the ordinary wave and the extraordinary wave, which travel with u' and u'' velocities, respectively. Moreover, as explained in [139], the propagation of each plane wave has to be studied separately and, since they are infinite, we can focus on the study of the propagation of one individual plane wave to later see how they propagate.

9.1.1 Ordinary ray

The ordinary ray travels with a phase velocity of $u = u_o$. Knowing this, we can extract the components of $\vec{D}$ substituting the phase velocity in the system **9.12**:

$$\vec{D_o} = (D_{o1}, D_{o2}, D_{o3}) = \left(-\frac{s_2}{s_1}, 1, 0\right) D_{o2} \qquad \textbf{(9.15)}$$

Now, we can obtain the electric field using the relation **9.6**:

$$\vec{E_o} = (E_{o1}, E_{o2}, E_{o3}) = \left(-\frac{s_2}{s_1}, 1, 0\right) E_{o2} \qquad \textbf{(9.16)}$$

Finally, using the second equation of the system **9.10** we obtain that:

$$\vec{H_o} = (H_{o1}, H_{o2}, H_{o3}) = \left(\frac{s_1}{s_2}, 1, \frac{s_3^2 - 1}{s_2 s_3}\right) H_{o2} \qquad \textbf{(9.17)}$$

Moreover, we can calculate the Poynting vector ($\vec{S}$), which corresponds to the propagation vector of the energy, and proof that for the ordinary wave is parallel to the unitary wavevector ($\hat{s}$).

$$\vec{S}_o = \vec{E}_o \times \vec{H}_o = \frac{H_{o2} E_{o2} (s_3^2 - 1)}{s_1 s_2 s_3} \hat{s} \qquad \mathbf{(9.18)}$$

9.1.2 Extraordinary ray

The extraordinary ray travels with a phase velocity of $u'' = \sqrt{u_z^2 + (u_o^2 - u_z^2) s_3^2}$, which is between u_o and u_z.

As done before, we can calculate $\vec{D}$ substituting the phase velocity in the system **9.12** and we also obtain the relations for $\vec{E}$ and $\vec{H}$ substituting in **9.6** and the second equation of **9.10**:

$$\vec{D}_e = (D_{e1}, D_{e2}, D_{e3}) = \left(\frac{s_1}{s_2}, 1, \frac{s_3^2 - 1}{s_2 s_3} \right) D_{e2} \qquad \mathbf{(9.19)}$$

$$\vec{E}_e = (E_{e1}, E_{e2}, E_{e3}) = \left(\frac{s_1}{s_2}, 1, \frac{u_z^2 (s_3^2 - 1)}{u_o^2 s_2 s_3} \right) E_{e2} \qquad \mathbf{(9.20)}$$

$$\vec{H}_e = (H_{e1}, H_{e2}, H_{e3}) = \left(-\frac{s_2}{s_1}, 1, 0 \right) H_{e2} \qquad \mathbf{(9.21)}$$

In this case, if we calculate the Poynting vector, Eq. **9.22**, we observe that it will be not parallel to the unitary wavevector, except for $s_1 = s_2 = 0$ (i.e., propagation along s_3) or $s_3 = 0$ (i.e., propagation in the perpendicular plane to s_3). Thus, the energy and the phase of the extraordinary wave can follow different trajectories.

$$\vec{S}_e = \vec{E}_e \times \vec{H}_e = \frac{H_{e2} E_{e2} (1 - s_3^2)}{s_1 s_2 s_3} \frac{u_z^2}{u_o^2} \left(s_1, s_2, s_3 \frac{u_o^2}{u_z^2} \right) \qquad \mathbf{(9.22)}$$

This non-parallelism of $\vec{S}_e$ and $\hat{s}$ produces the spatial displacement, called walk-off, between the ordinary and extraordinary rays. This displacement can also be null if $u_o = u_z$, which corresponds to the previously mentioned situation where the plane wave is propagating along the O.A. of the uniaxial birefringent crystal (i.e., $\hat{s} = (0, 0, \pm 1)$).

9.2 Plane wave propagation through uniaxial medium immersed in isotropic medium

In the case of Section 9.1, the initial plane wave is split into two plane waves, both having the same unitary wavevector ($\hat{s}$) but different Poynting vectors ($\vec{S_o}$ and $\vec{S_e}$). In the current Section, we are going to see how this propagation is modified if the uniaxial birefringent crystal is immersed in an isotropic medium of refractive index 'n' from which the wave impinges.

Now, the plane wave will be refracted, when going from the isotropic medium to the birefringent medium and, from it, again to the isotropic medium, and the phase direction of the refracted wave will be given by Snell's Law. The Snell's Law in the incidence plane (i.e., plane formed by the incident wavevector and the normal to the interface) can be expressed as:

$$n_1 \sin\theta_1 = n_2 \sin\theta_2 \tag{9.23}$$

where θ_1 and θ_2 are the incidence and refraction angles, respectively, and n_1 and n_2 correspond to the refractive indices of the incidence and transmitted media, respectively. Since the ordinary and extraordinary waves experience different refractive indices, n_o and n_e respectively, the unitary wavevectors inside the uniaxial medium will be different.

9.2.1 Notation and working coordinate systems

First of all, we will assume that the uniaxial birefringent medium is a plane-parallel crystal, while their interfaces are always parallel to the measurement plane of the spatiotemporal characterization technique proposed in this Thesis. In addition, for simplicity we will consider that the crystal can be azimuthally rotated but will not be tilted, as said before.

In this theoretical study we are going to work with three different coordinate systems (laboratory, incidence and crystal), being all of them in the Cartesian coordinates space and related by rotations. The selection of these specific systems significantly eases the study of the propagation. On one hand, the laboratory system is fixed regardless of the direction of the initial wavevector, and it is useful to visualize the global propagation. On the other hand, the incidence system enables to directly apply the Snell's Law (Eq. **9.23**) during the refraction without the necessity to use the vector Snell's Law [140]. Finally, the crystal system is the natural basis to calculate the propagation inside a birefringent medium, since the dielectric tensor is diagonalized in it (as seen in Section 9.1).

Laboratory system

Firstly, we define the laboratory system (lab or $\overline{xyz}$) as a fixed system with the unit vector $\hat{z}$ normal to the crystal and pointing to the measurement plane. Moreover, $\hat{x}$ and $\hat{y}$ correspond to the unit vectors of the laboratory system in the horizontal and vertical directions, respectively, and the crystal surface will be always parallel to the $\overline{xy}$ plane. This system is represented in Fig. 9.1.

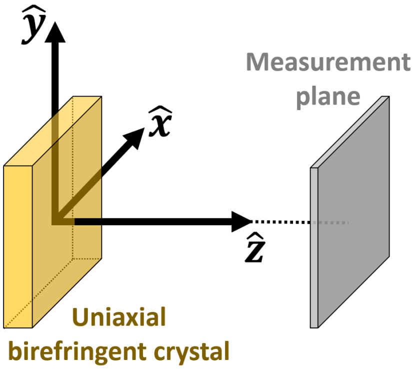

Fig. 9.1. *Representation of the laboratory coordinate system.*

A monochromatic plane wave will have a wavevector in the laboratory system, defined as $\overrightarrow{k^{\text{lab}}} = \|k\| \cdot \widehat{s^{\text{lab}}}$, being $\widehat{s^{\text{lab}}}$ the unitary wavevector in this system:

$$\widehat{s^{\text{lab}}} = (s_x, s_y, s_z) \tag{9.24}$$

Incidence system

Secondly, we designate the incidence system (inc or $\overline{x'y'z'}$) in such a way that the $\overline{x'z'}$ plane is the incidence plane of the wave traveling from the isotropic medium to the uniaxial crystal. This system, in contrast to the laboratory system, depends on the wavevector direction, so it is not fixed for different wavevectors. Moreover, we choose $z' = z$ because z is always in the incidence plane (notice that it is normal to the interface).

The incidence system is related to the laboratory system by the rotation of an angle Φ_i along the $\hat{z}$ axis, as shown in Fig. 9.2. This angle will be given by the initial wave.

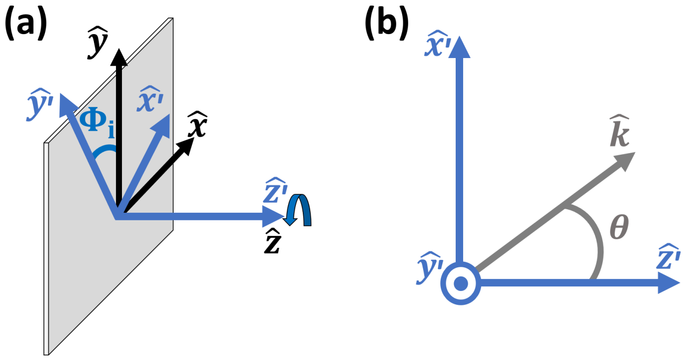

Fig. 9.2. *(a) Representation of the incidence coordinate system (blue) and azimuthal angle* (Φ_i) *with respect to the laboratory system (black). (b) Definition of the incidence angle* (θ) *of a plane wave with wavevector* ($\vec{k}$) *in the incidence plane* ($\overline{x'z'}$).

A wavevector in the incidence system can be expressed as $\overrightarrow{k^{\text{inc}}} = \|k\| \cdot \widehat{s^{\text{inc}}}$, being $\widehat{s^{\text{inc}}}$ the unitary wavevector in the incidence system:

$$\widehat{s^{\text{inc}}} = (\sin\theta, 0, \cos\theta) \tag{9.25}$$

where θ is an angle of incidence in the $\overline{x'z}$ plane respect to the $\hat{z}$ axis defined positive in counter-clockwise direction.

Moreover, since incidence and laboratory systems are related by a simple rotation about the $\hat{z}$ axis, a vector in one system can be easily transformed into the other system by applying a rotation matrix:

$$R(\beta) = \begin{pmatrix} \cos\beta & -\sin\beta & 0 \\ \sin\beta & \cos\beta & 0 \\ 0 & 0 & 1 \end{pmatrix} \tag{9.26}$$

where β corresponds to the rotation along the $\hat{z}$ axis and it is defined positive for counter-clockwise rotations, as indicated by the arrow in Fig. 9.2(a). Therefore, the unit wavevector in the incidence system variables (Φ_i and θ) can be expressed in the laboratory system as:

$$\widehat{s^{\mathrm{lab}}} = R(-\Phi_i) \cdot \widehat{s^{\mathrm{inc}}} = (\cos\Phi_i \sin\theta, -\sin\Phi_i \sin\theta, \cos\theta) \tag{\textbf{9.27}}$$

On the other hand, for a given wavevector in the laboratory system ($\overrightarrow{k^{\mathrm{lab}}} = (k_x, k_y, k_z)$), the angles of the incidence system can be calculated using Eqs. **9.28** and **9.29**.

$$\Phi_i = \arctan\left(-\frac{k_y}{k_x}\right) = \arctan\left(-\frac{s_y}{s_x}\right) \tag{\textbf{9.28}}$$

$$\theta = \arccos\left(\frac{k_z}{\|k\|}\right) = \arccos\left(s_z\right) \tag{\textbf{9.29}}$$

Crystal system

Thirdly, we define the crystal system (cry or $\overline{z_1 z_2 z_3}$) as the uniaxial crystal principal axes basis mentioned in Subsection 9.1.

The wavevector of a monochromatic plane wave in this system can be defined as $\overrightarrow{k^{\mathrm{cry}}} = \|k\| \cdot \widehat{s^{\mathrm{cry}}}$, being $\widehat{s^{\mathrm{cry}}}$ the unitary wavevector in the crystal system:

$$\widehat{s^{\mathrm{cry}}} = (s_1, s_2, s_3) \tag{\textbf{9.30}}$$

This system will be determined by the direction of the O.A. of the uniaxial birefringent medium. In particular, we can describe this direction as an azimuthal angle Φ_{OA}, which represents the rotation of the O.A. about the $\hat{z}$ axis, and an insertion angle θ_{OA}, which represents the rotation of the O.A. about the $\hat{y}$ axis. Fig. 9.3 represents these angles that are always defined positive for counter-clockwise rotations.

Therefore, as we have previously done with the incidence system, it can be determined the relation between the crystal and the laboratory systems, so a wavevector in one system can be expressed in the other. For this purpose, the basis $\overline{z_1 z_2 z_3}$ can be expressed in the laboratory system:

$$\overline{z_1 z_2 z_3} = \widehat{z_1^{\mathrm{cry}}} + \widehat{z_2^{\mathrm{cry}}} + \widehat{z_3^{\mathrm{cry}}} \equiv \widehat{z_1^{\mathrm{lab}}} + \widehat{z_2^{\mathrm{lab}}} + \widehat{z_3^{\mathrm{lab}}} \tag{\textbf{9.31}}$$

where each unitary vector of the crystal system in the laboratory system can be defined as:

$$\begin{cases} \widehat{z_1^{\text{lab}}} = (\cos\Phi_{OA}\cos\theta_{OA}, \sin\Phi_{OA}\cos\theta_{OA}, -\sin\theta_{OA}) \\ \widehat{z_2^{\text{lab}}} = (-\sin\Phi_{OA}, \cos\Phi_{OA}, 0) \\ \widehat{z_3^{\text{lab}}} = (\cos\Phi_{OA}\sin\theta_{OA}, \sin\Phi_{OA}\sin\theta_{OA}, \cos\theta_{OA}) \end{cases} \tag{9.32}$$

Please notice that the projection of each unit vector of the $\overline{z_1 z_2 z_3}$ in the laboratory system is normalized and also they are all orthogonal between them.

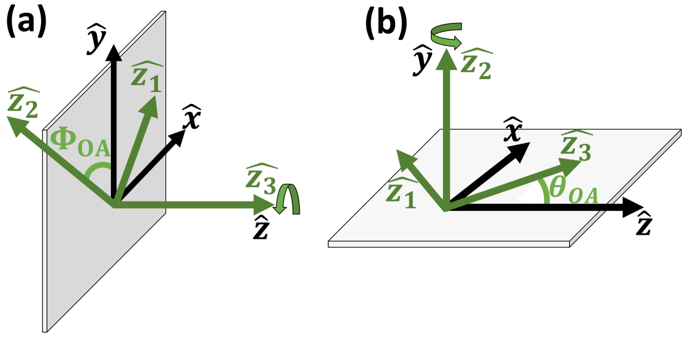

Fig. 9.3. *Representation of the crystal coordinate system (green) and rotation angles with respect to the laboratory system (black): (a) azimuthal angle (Φ_{OA}) and (b) insertion angle (θ_{OA}).*

Therefore, if the unitary wavevector is known in the laboratory system, it can be projected into the crystal system to obtain the expressions of s_1, s_2 and s_3 of Eq. **9.30** just by doing the scalar product:

$$\begin{cases} s_1 = \widehat{s^{\text{lab}}} \cdot \widehat{z_1^{\text{lab}}} \\ s_2 = \widehat{s^{\text{lab}}} \cdot \widehat{z_2^{\text{lab}}} \\ s_3 = \widehat{s^{\text{lab}}} \cdot \widehat{z_3^{\text{lab}}} \end{cases} \tag{9.33}$$

Then, substituting Eqs. **9.27** and **9.32** into the previous equation system, we obtain the components of the unitary wavevector in the crystal system as a function of the incidence and O.A. angles.

$$\begin{cases} s_1 = \cos\Phi_i \sin\theta \cos\Phi_{OA} \cos\theta_{OA} - \sin\Phi_i \sin\theta \sin\Phi_{OA} \cos\theta_{OA} - \cos\theta \sin\theta_{OA} \\ s_2 = -\cos\Phi_i \sin\theta \sin\Phi_{OA} - \sin\Phi_i \sin\theta \cos\Phi_{OA} \\ s_3 = \cos\Phi_i \sin\theta \cos\Phi_{OA} \sin\theta_{OA} - \sin\Phi_i \sin\theta \sin\Phi_{OA} \sin\theta_{OA} + \cos\theta \cos\theta_{OA} \end{cases} \tag{9.34}$$

In addition, it is interesting to express the unit vector of the O.A. ($\widehat{z_3}$) in the incidence system, because it will ease the calculation of the extraordinary refractive index (n_e) in the following Subsection. Taking into account the relation between systems:

$$\widehat{z_3^{\text{inc}}} = (\cos(\Phi_{OA} - \Phi_i)\sin\theta_{OA}, \sin(\Phi_{OA} - \Phi_i)\sin\theta_{OA}, \cos\theta_{OA}) \tag{9.35}$$

9.2.2 Propagation theory

Let's consider a monochromatic plane wave with a certain azimuthal incidence angle (Φ_i) and incidence angle (θ_i) in the interface of the isotropic-uniaxial media. The unitary wavevector of this initial wave in the laboratory system will be:

$$\widehat{s_i^{\text{lab}}} = (\cos\Phi_i \sin\theta_i, -\sin\Phi_i \sin\theta_i, \cos\theta_i) \tag{9.36}$$

Firstly, the wave will be refracted at the isotropic-uniaxial interface and this process will be governed by Snell's Law. Thus, it is necessary to express its initial unitary wavevector in the incidence system:

$$\widehat{s_i^{\text{inc}}} = (\sin\theta_i, 0, \cos\theta_i) \tag{9.37}$$

Since the initial wave will be split into two waves (ordinary and extraordinary), we are going to study them separately.

Ordinary wave

The ordinary wave will see a refractive index n_o that does not depend on the incidence angles. Thus, the application of Snell's Law is direct and the refraction angle of the ordinary wave inside the uniaxial medium will be given by:

$$\theta_o = \arcsin\left(\frac{n}{n_o}\sin\theta_i\right) \tag{9.38}$$

The refraction does not modify the azimuthal angle of the incidence plane (Φ_i), so after the isotropic-uniaxial interface the ordinary unitary wavevector in the laboratory system will be:

$$\widehat{s_o^{\text{lab}}} = (\cos\Phi_i\sin\theta_o, -\sin\Phi_i\sin\theta_o, \cos\theta_o) \tag{9.39}$$

In the case of the ordinary ray, the Poynting vector will be parallel to the unitary wavevector, Eq. **9.18**, so the energy and phase will follow the same trajectory. Furthermore, the ordinary ray will be laterally displaced on the exit interface of the crystal with respect to the entry face and it will strike at the second interface of the crystal at position (r_{ox}, r_{oy}, L), in the laboratory system, being L the thickness of the uniaxial medium.

Using trigonometric relations and knowing the refraction angles, we can calculate the lateral displacement that the ordinary ray will suffer:

- Displacement in X direction:

$$r_{ox} = L\cos\Phi_i\tan\theta_o = L\cos\Phi_i\tan\left[\arcsin\left(\frac{n}{n_o}\sin\theta_i\right)\right] \tag{9.40}$$

- Displacement in Y direction:

$$r_{oy} = -L\sin\Phi_i\tan\theta_o = -L\sin\Phi_i\tan\left[\arcsin\left(\frac{n}{n_o}\sin\theta_i\right)\right] \tag{9.41}$$

In addition, during the travel inside the uniaxial medium, the ordinary ray will acquire a phase term given by $\overrightarrow{k_o}\cdot\overrightarrow{r_o}$, being $\overrightarrow{k_o}$ the wavevector of the ordinary wave and $\overrightarrow{r_o}$ the vector from the input position of the ray at the first interface to the output position at the second interface of the crystal. These vectors in the laboratory system, assuming that the input position is at the coordinate origin $(0, 0, 0)$, can be expressed as:

$$\begin{cases} \overrightarrow{k_o^{\text{lab}}} = \frac{2\pi}{\lambda} n_o \widehat{s_o^{\text{lab}}} = \frac{2\pi}{\lambda} n_o (\cos\Phi_i\sin\theta_o, -\sin\Phi_i\sin\theta_o, \cos\theta_o) \\ \overrightarrow{r_o^{\text{lab}}} = (r_{ox}, r_{oy}, L) = L(\cos\Phi_i\tan\theta_o, -\sin\Phi_i\tan\theta_o, 1) \end{cases} \tag{9.42}$$

For simplicity and briefness, we indicate the expressions as a function of θ_o.

Thus, the phase acquired by the ordinary beam will be:

$$\varphi_o = \frac{2\pi}{\lambda} n_o \frac{L}{\cos\theta_o} \tag{9.43}$$

Finally, the ordinary ray will come out the uniaxial crystal going through the uniaxial-isotropic interface. This refraction is the opposite as the entrance, thus the output angle (θ_{out}) will be the same as the initial beam (θ_i), as expected:

$$n_o \sin\theta_o = n \sin\theta_{out} \longrightarrow \theta_{out} = \theta_i \tag{9.44}$$

Therefore, the ray that comes out the crystal is parallel to the incidence one, as expected since the crystal is plane-parallel.

Extraordinary ray

The extraordinary wave will experience an extraordinary refractive index n_e and Snell's Law will be expressed in the incidence system as:

$$n \sin\theta_i = n_e(\theta_e, \Phi_i) \sin\theta_e \tag{9.45}$$

being θ_e the refraction angle of the extraordinary beam inside the uniaxial medium. Thus, the unitary wavevector of the extraordinary ray in the incidence system can be expressed as:

$$\widehat{s_e^{\text{inc}}} = (\sin\theta_e, 0, \cos\theta_e) \tag{9.46}$$

However, Snell's Law cannot be analytically resolved to obtain θ_e in a general case due to the extraordinary refractive index dependence with the refracted angle:

$$n_e = \frac{n_z n_o}{\sqrt{n_o^2 + (n_z^2 - n_o^2)(\vec{s_e} \cdot \vec{z_3})^2}} \tag{9.47}$$

The scalar product ($\vec{s_e} \cdot \vec{z_3}$) can be easily calculated in the incidence system combining Eqs. **9.35** and **9.46**, thus obtaining:

$$n_e = \frac{n_z n_o}{\sqrt{n_o^2 + (n_z^2 - n_o^2)\left[\cos\left(\Phi_{OA} - \Phi_i\right) \sin\theta_{OA} \sin\theta_e + \cos\theta_{OA} \cos\theta_e\right]^2}} \tag{9.48}$$

If no simplification can be done, we recommend to obtain θ_e numerically solving the system of equations **9.45** and **9.48**, as we do in this Thesis. From this point, we continue the theoretical development assuming θ_e is known.

As explained before, the refraction does not modify the azimuthal angle Φ_i of the wavevector, so the extraordinary unitary wavevector inside the uniaxial crystal can be expressed in the laboratory system as:

$$\widehat{s_e^{\text{lab}}} = (\cos\Phi_i \sin\theta_e, -\sin\Phi_i \sin\theta_e, \cos\theta_e) \tag{9.49}$$

In contrast to the ordinary ray, as seen in Section 9.1, the extraordinary energy and phase do not follow the same trajectories inside an uniaxial medium because the Poynting vector and the unitary wavevector are not parallel. Therefore, we want to express the Poynting vector at the laboratory system and this can be done using Eq. **9.22** and expressing the unit vectors of the crystal system in the laboratory system using Eq. **9.32**:

$$\begin{gathered}\overrightarrow{S_e^{\text{lab}}} \propto s_{e1}\widehat{z_1^{\text{lab}}} + s_{e2}\widehat{z_2^{\text{lab}}} + \tfrac{n_z^2}{n_o^2} s_{e3}\widehat{z_3^{\text{lab}}} \Longrightarrow \\ \overrightarrow{S_e^{\text{lab}}} \propto \begin{pmatrix} s_{e1}\cos\Phi_{OA}\cos\theta_{OA} - s_{e2}\sin\Phi_{OA} + \frac{n_z^2}{n_o^2} s_{e3}\cos\Phi_{OA}\sin\theta_{OA} \\ s_{e1}\sin\Phi_{OA}\cos\theta_{OA} + s_{e2}\cos\Phi_{OA} + \frac{n_z^2}{n_o^2} s_{e3}\sin\Phi_{OA}\sin\theta_{OA} \\ -s_{e1}\sin\theta_{OA} + \frac{n_z^2}{n_o^2} s_{e3}\cos\theta_{OA} \end{pmatrix}\end{gathered} \tag{9.50}$$

where s_{e1}, s_{e2} and s_{e3} are the components of the extraordinary unitary wavevector in the crystal system, which using Eq. **9.34** can be expressed as a function of incidence, refraction and O.A. angles:

$$\begin{cases} s_{e1} = \cos\Phi_i \sin\theta_e \cos\Phi_{OA}\cos\theta_{OA} - \sin\Phi_i \sin\theta_e \sin\Phi_{OA}\cos\theta_{OA} - \cos\theta_e \sin\theta_{OA} \\ s_{e2} = -\cos\Phi_i \sin\theta_e \sin\Phi_{OA} - \sin\Phi_i \sin\theta_e \cos\Phi_{OA} \\ s_{e3} = \cos\Phi_i \sin\theta_e \cos\Phi_{OA}\sin\theta_{OA} - \sin\Phi_i \sin\theta_e \sin\Phi_{OA}\sin\theta_{OA} + \cos\theta_e \cos\theta_{OA} \end{cases} \tag{9.51}$$

Knowing the direction of the wavevector and the Poynting vector, we are going to calculate separately the spatial position where each of those vectors will go out through the second crystal interface in the laboratory system, $\left(r_{ex}^{\varphi}, r_{ey}^{\varphi}, L\right)$ and $\left(r_{ox}^{E}, r_{oy}^{E}, L\right)$, respectively.

- Displacement in X direction:
  - Phase:

$$r_{ex}^{\varphi} = L \cos\Phi_i \tan\theta_e \tag{9.52}$$

  - Energy:

$$r_{ex}^{E} = L \frac{s_{e1}\cos\Phi_{OA}\cos\theta_{OA} - s_{e2}\sin\Phi_{OA} + \frac{n_z^2}{n_o^2} s_{e3}\cos\Phi_{OA}\sin\theta_{OA}}{\frac{n_z^2}{n_o^2} s_{e3}\cos\theta_{OA} - s_{e1}\sin\theta_{OA}} \tag{9.53}$$

- Displacement in Y direction:
  - Phase:

$$r_{ey}^{\varphi} = -L \sin\Phi_i \tan\theta_e \tag{9.54}$$

  - Energy:

$$r_{ey}^{E} = L \frac{s_{e1}\sin\Phi_{OA}\cos\theta_{OA} + s_{e2}\cos\Phi_{OA} + \frac{n_z^2}{n_o^2} s_{e3}\sin\Phi_{OA}\sin\theta_{OA}}{\frac{n_z^2}{n_o^2} s_{e3}\cos\theta_{OA} - s_{e1}\sin\theta_{OA}} \tag{9.55}$$

The phase acquired by the extraordinary ray due to traveling inside the uniaxial medium has to be calculated at the position where the energy is. Thus the phase acquired will be given by $\overrightarrow{k_e} \cdot \overrightarrow{r_e}$, being $\overrightarrow{k_e}$ the wavevector of the extraordinary wave and $\overrightarrow{r_e}$ the vector from the input position of the ray at the first interface to the output position of the energy at the second interface of the crystal. As before, these vectors can be expressed in the laboratory system as:

$$\begin{cases} \overrightarrow{k_e^{\text{lab}}} = \frac{2\pi}{\lambda} n_e \widehat{s_e^{\text{lab}}} = \frac{2\pi}{\lambda} n_e \left(\cos\Phi_i \sin\theta_e, -\sin\Phi_i\sin\theta_e, \cos\theta_e\right) \\ \overrightarrow{r_e^{\text{lab}}} = \left(r_{ex}^E, r_{ey}^E, L\right) \end{cases}$$

Therefore, the acquired phase will be:

$$\varphi_e = \frac{2\pi}{\lambda} n_e \left[r_{ex}^E \cos\Phi_i \sin\theta_e - r_{ey}^E \sin\Phi_i \sin\theta_e + L\cos\theta_e\right] \tag{9.56}$$

After propagation, the extraordinary ray will go out the uniaxial crystal, going through the uniaxial-isotropic interface. This refraction, as happened before with the ordinary ray, is the opposite as the entrance, so the output/exit angle will be the same as the initial beam (θ_i).

9.2.3 Plane wave with normal incidence

In the previous Subsection, it was explained the general propagation model for an incident monochromatic plane wave. In this Subsection, we want to particularize it to a plane wave with normal incidence on the crystal (i.e., $\theta_i = 0$).

This specific situation is very useful to understand the physics of the spatiotemporal technique and enables the obtention of a simplified model, which can be used in the majority of situations, where collimated beams are characterized.

The first simplification that is observed with normal incidence is that, to fulfill Snell's Law, the ordinary and extraordinary refraction angles have to be null ($\theta_o = \theta_e = 0°$). This implies that the unitary wavevector of the ordinary (Eq. **9.39**) and extraordinary (Eq. **9.49**) rays in the laboratory system will be the same and parallel to the $\hat{z}$ axis.

$$\begin{cases} \widehat{s_o^{\text{lab}}} = (0,0,1) \\ \widehat{s_e^{\text{lab}}} = (0,0,1) \end{cases} \tag{9.57}$$

Moreover, in this situation the lateral displacement in the laboratory system of the extraordinary phase (r_{ex}^{φ} and r_{ey}^{φ}) and the ordinary phase and energy (r_{ox} and r_{oy}) due to traveling inside the uniaxial medium will be null. Although the extraordinary phase is not displaced, the extraordinary energy ray will be laterally sheared (except if the O.A. is contained in the interface plane or parallel to the interface normal). The simplified expressions of the extraordinary energy ray lateral displacement for this case, after some calculations imposing $\theta_e = 0°$ at Eqs. **9.51**, **9.53** and **9.55**, are:

- Displacement in X direction:

$$r_{ex}^{E} = \frac{L}{2} \cos\Phi_{OA} \sin(2\theta_{OA}) \frac{n_z^2 - n_o^2}{n_z^2 \cos^2\theta_{OA} + n_o^2 \sin^2\theta_{OA}} \tag{9.58}$$

- Displacement in Y direction:

$$r_{ey}^{E} = \frac{L}{2} \sin\Phi_{OA} \sin(2\theta_{OA}) \frac{n_z^2 - n_o^2}{n_z^2 \cos^2\theta_{OA} + n_o^2 \sin^2\theta_{OA}} \tag{9.59}$$

Finally the expression of the phase acquired by each wave, Eqs. **9.43** and **9.56**, in this simplified case will be:

$$\begin{cases} \varphi_o = \frac{2\pi}{\lambda} n_o L = \frac{\omega}{c} n_o L \\ \varphi_e = \frac{2\pi}{\lambda} n_e L = \frac{\omega}{c} n_e L \end{cases} \tag{9.60}$$

Two examples of the propagation under normal incidence, assuming that the O.A. is in the horizontal plane ($\Phi_{OA} = 0°$), are shown in Fig. 9.4. On one hand, Fig. 9.4(a) represents the propagation for $\theta_{OA} \neq 0°$ or $90°$, showing the walk-off property. As previously mentioned in Chapter 8, we call the uniaxial crystals with this configuration walk-off crystals. On the other hand, Fig. 9.4(b) shows the case for $\theta_{OA} = 90°$ (i.e., O.A. contained in the crystal surface). Following the notation of Chapter 8, the crystal in this configuration corresponds to a retarder plate.

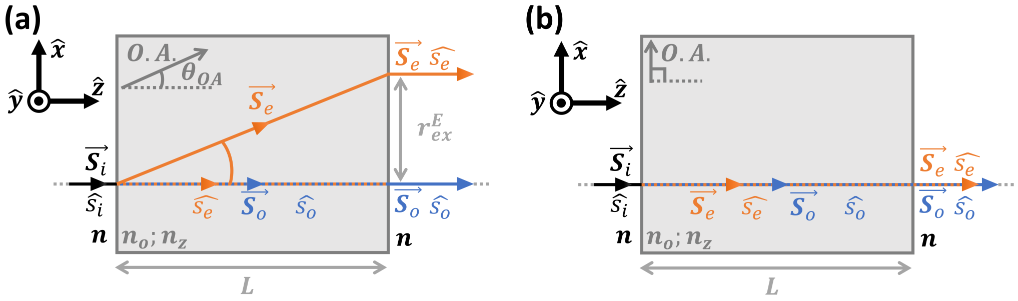

Fig. 9.4. *Representation of the ordinary and extraordinary ray propagation under normal incidence on an uniaxial birefringent medium with* $\Phi_{OA} = 0$ *and different configurations of* θ_{OA}*, which is immersed in an isotropic medium. (a)* $\theta_{OA} \neq 0°$ *or* $90°$ *and (b)* $\theta_{OA} = 90°$*.*

From the analysis of this simplified case, it can be extracted that the lateral displacement will be larger for materials with higher birefringence. Looking at Eqs. **9.58** and **9.59** it is also observed that for $\theta_{OA} = 90°$ (i.e., O.A. contained in the crystal surface) the lateral displacement is null, as seen in Fig. 9.4(b), but the propagation through the birefringent medium introduces a phase difference between the ordinary and extraordinary waves.

Furthermore, since the relative phase between extraordinary and ordinary waves depends on the frequency, they will be delayed:

$$\tau(\omega) = \frac{\partial}{\partial\omega}(\varphi_e - \varphi_o) \tag{9.61}$$

being $\tau(\omega)$ the delay introduced. Notice that, when using pulses, the beams will be composed by multiple frequencies and the refractive indices (n_o and n_e) will also depend on them.

9.3 General propagation theory of non-plane waves

So far, we have seen how monochromatic plane waves propagate through an isotropic medium with an uniaxial birefringent crystal inside it (Section 9.2). The current Section is focused on the generalization of the model to non-plane waves, and it will lay the foundations for the walk-off angular dependence study of Section 10.2.

Here, we will present the principles of the propagation model and how to implement it numerically (Subsection 9.3.1) and, after that, we will verify it with a known case (Subsection 9.3.2).

9.3.1 Principles of the propagation model

Firstly, it is well known that every beam in the spatial domain can be decomposed in a set of plane waves in the spatial Fourier space. Thus, a beam in the laboratory coordinate system (x, y, z) will correspond to a distribution of (k_x, k_y, k_z), corresponding each combination of (k_x, k_y, k_z) to a plane wave with the corresponding amplitude and phase obtained by Fourier Transform:

$$\begin{aligned} E(k_x, k_y, k_z) &= \mathscr{F}\Big\{E(x, y, z)\Big\} \\ E(x, y, z) &= \mathscr{F}^{-1}\Big\{E(k_x, k_y, k_z)\Big\} \end{aligned} \tag{9.62}$$

being $k_z = \sqrt{\|k\|^2 - k_x^2 - k_y^2}$ and $\|k\| = 2\pi/\lambda$. Notice that the components k_x, k_y and k_z used in the model are defined in the vacuum.

In particular, in this propagation model we are going to decompose the beam in a set of plane waves at a certain propagation distance ($z = z_i$) using the 2D spatial Fourier Transform:

$$\begin{cases} k_x = 2\pi/x \\ k_y = 2\pi/y \end{cases} \tag{9.63}$$

An example of this decomposition for a Gaussian monochromatic convergent wave is shown in Fig. 9.5.

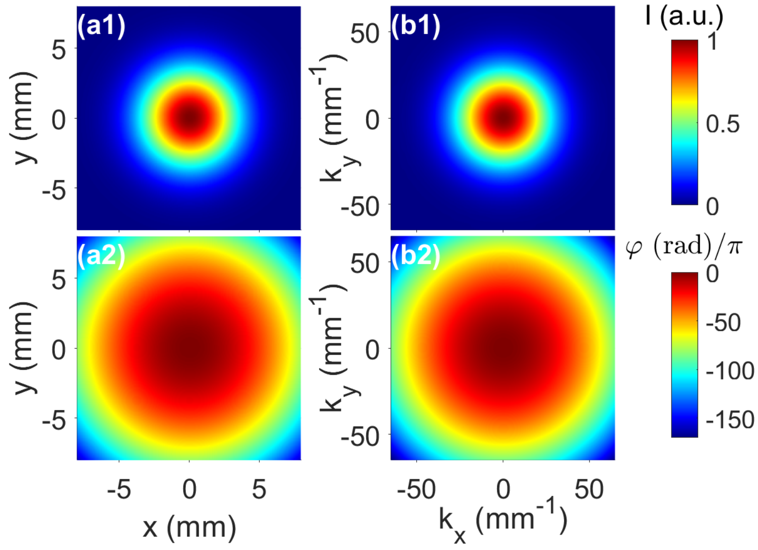

Fig. 9.5. *Example of decomposition of a Gaussian monochromatic convergent beam into plane waves. (a1) Intensity and (a2) phase profiles in XY coordinates. (b1) Intensity and (b2) phase in spatial frequencies coordinates.*

On one hand, the intensity and phase profiles in spatial domain $(x, y; z_i)$ are shown in Figs. 9.5(a1,a2), respectively. On the other hand, the intensity and phase distributions in the corresponding Fourier space $(k_x, k_y; z_i)$ are presented in Figs. 9.5(b1,b2), respectively.

Moreover, if the losses and the reflection are negligible, after traveling a certain distance in the spatial Fourier space, the amplitude of each plane wave does not vary and it only changes the phase. Thus, by calculating the phase acquired by each plane wave during the travel and inverting the

Fourier Transform, it can be obtained the beam in the Cartesian space after the propagation to $z = z_f$.

Please note that, depending on the incidence angle, the refractive index and applying the Fresnel laws, it could be some loses via reflection, different for each plane wave and the polarization components parallel and perpendicular to the incidence plane. In the sake of simplicity, we have not considered it. This approximation will be acceptable for low incidence angles, as the cases simulated in this Thesis (e.g., maximum transmission variation with the maximum Numerical Aperture (NA) analyzed is ∼±0.1%). Otherwise, the Fresnel laws should be added to the model.

Following the notation of Section 9.2, each plane wave can be associated with two incidence angles that, in our case, are the same before and after traveling through an uniaxial birefringent crystal:

$$\begin{cases} \Phi_i = \arctan\left(-\frac{k_y}{k_x}\right) \\ \theta_i = \arccos\left(\frac{k_z}{\|k\|}\right) \end{cases} \qquad \textbf{(9.64)}$$

On one hand, the phase acquired by each plane wave due to the travel in an isotropic medium of refractive index n and thickness $d_{isotrop}$ can be easily calculated using Eq. **9.65**. Notice that this phase term will be the same for the ordinary and extraordinary beams, since the medium is isotropic and outside the uniaxial crystal each beam presents the same Φ_i and θ_i (despite being laterally displaced).

$$\varphi_{isotrop} = \vec{k} \cdot \vec{r} = \frac{2\pi}{\lambda} n \frac{d_{isotrop}}{cos\theta_i} \qquad \textbf{(9.65)}$$

On the other hand, when going through an uniaxial birefringent crystal of thickness L, each ordinary and extraordinary plane wave will acquire different phases. In the case of the ordinary waves, the phase term gained by each plane wave (φ_o) will be given by Eq. **9.43**. In the case of the extraordinary wave, we know that each plane wave will acquire a phase term (φ_e) given by Eq. **9.56**, but also there is a change in the coordinate system from the phase to the energy due to the relative lateral displacement ($r^E - r^\varphi$). This last term, using the properties of Fourier Transform, can be expressed as a phase term in the Fourier space:

$$\varphi_{lat} = e^{i\left[k_x(r_x^E - r_x^{\varphi}) + k_y(r_y^E - r_y^{\varphi})\right]} \tag{9.66}$$

being k_x and k_y the horizontal and vertical components of the Fourier space variables in which the beam is decomposed. The lateral displacement of the energy (r_x^E and r_y^E) and the phase (r_x^{φ} and r_y^{φ}) can be calculated using Eqs. **9.52-9.55** for each pane wave.

Therefore, the phase acquired by each extraordinary plane wave due to propagation inside the uniaxial birefringent crystal will be computed as $(\varphi_e + \varphi_{lat})$. Moreover, this combination will encode also the lateral shearing introduced in case of using a walk-off crystal.

Please notice that φ_{lat} corresponds to a lateral displacement of each individual plane wave and it was not considered in Section 9.2 because it makes no difference for an individual infinite plane wave. Nevertheless, it is important in this model because the lateral displacement will be different for each plane wave and the relative change encodes information of the beam.

Numerical model

Taking all of this into account, we can develop a simple model based on Fast Fourier Transform (FFT), which, for a given beam electric field in an initial propagation position (z_{ini}), can simulate its propagation to a certain position (z_f). The numerical model is summarized in Fig. 9.6 and, in it, following the notation of the bulk lateral shearing interferometry technique, we will call the extraordinary beam walk-off beam. Therefore, OB and WB correspond to the ordinary and walk-off beams, respectively. Notice that in this case with only one birefringent crystal there is no confusion, but we want to maintain the notation and avoid misunderstandings.

To correctly propagate the beams it is necessary to have a good discretization in both spaces, spatial space and spatial frequencies space. This implies that the spatial resolution (Δ_r) and wavevector resolution (Δ_k) must be good enough. Moreover, the grid should be large enough to contain the beam without introducing edge artifacts during the FFT. In order to fulfill these requirements, the simulations of the study shown in this Section and

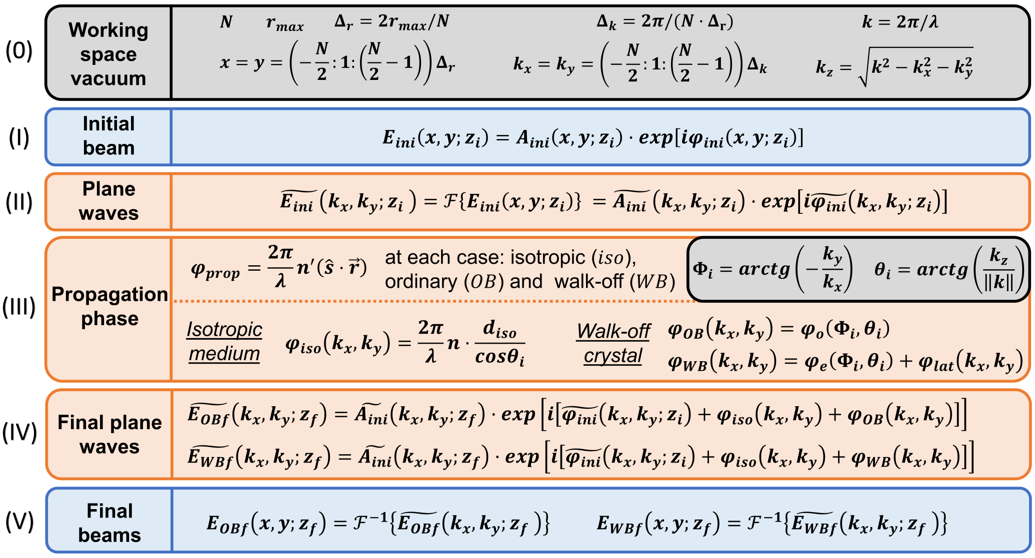

Fig. 9.6. *Summary of the propagation model conceptualization based on plane wave decomposition using spatial Fourier Transform. Notice that n' of φ_{prop} corresponds to n, n_o and n_e for the isotropic, ordinary and walk-off cases, respectively.*

in Section 10.2 were done with the working space parameters summarized in Table 9.1.

N	r_{max} (mm)	Δ_r (μm)	Δ_k (mm^{-1})
8192	9	2.2	0.3491

Table 9.1: Summary of space parameters used in the simulation.

Furthermore, if no action is taken, it could be a bottleneck in the simulations caused by calculation of the extraordinary angles inside the uniaxial crystal (i.e., numerical resolution of Eqs. **9.45** and **9.48**). This bottleneck is created because each position of the grid corresponds to one plane wave that has to be calculated, and in a 8192x8192 grid there are more than 67 million positions. In order to minimize the computational time making it affordable, we decided to obtain that extraordinary angles dependence in a grid with lower resolution (256x256) and then interpolate the solution in the desired one (8192x8192). This reduces considerably the problem since the 67 million numerical resolutions of Eqs. **9.45** and **9.48** are substituted by 65536 and a

2D interpolation. This can be done without introducing any artifact because the extraordinary angles vary slowly along our spatial grid and in a reduced range.

For example, for the incidence angles associated with space parameters mentioned in Table 9.1, a calcite ($CaCO_3$) crystal with $\theta_{OA} = 45°$ and $\Phi_{OA} = 180°$ presents extraordinary refraction angles from 0° to 9.6° for 800 nm. This case is represented in Fig. 9.7, where Figs. 9.7(a,b) correspond to the angles of each incident plane wave and Fig. 9.7(c) shows the extraordinary refraction angles.

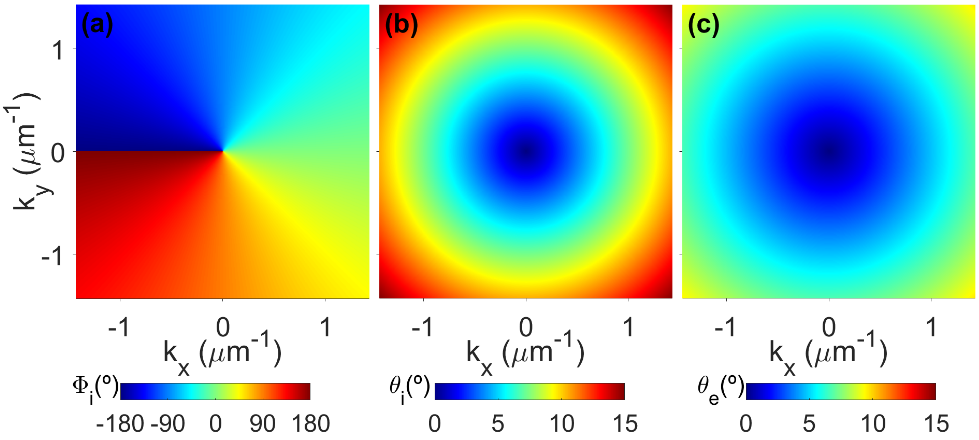

Fig. 9.7. *Incidence angles (a) Φ_i and (b) θ_i associated with the Fourier space of the numerical model using the parameters of Table 9.1 and (c) refraction angle of the extraordinary wave (θ_e) numerically resolved for a calcite crystal with $\theta_{OA} = 45°$ and $\Phi_{OA} = 180°$.*

9.3.2 Verification of the model

In this Subsection, we are going to test the numerical model studying the propagation of a finite monochromatic beam with Gaussian intensity profile and oblique incidence on a calcite crystal (uniaxial birefringent medium) immersed in air (isotropic medium). Moreover, the results are going to be compared with the propagation of a monochromatic plane wave with the same oblique incidence to verify the model.

The uniaxial medium in this simulation will be a 1-mm-thick calcite with

$\theta_{OA} = 45°$ and $\Phi_{OA} = 0°$, whose refractive indices for $\lambda = 800$ nm are $n_o = 1.6488$ and $n_e = 1.4819$ [141]. The isotropic medium will be air, so we can consider a refractive index of $n = 1$.

In this example, we are going to consider a finite incident electric field to the calcite crystal with a Gaussian intensity profile given at the a certain z by:

$$E(x,y) = A \cdot e^{-\frac{x^2+y^2}{w_0^2}} \cdot e^{-i\frac{2\pi}{\lambda}x\sin\Theta_i} \tag{9.67}$$

where A is the maximum amplitude, $w_0 = 1$ mm is the waist of the beam (defined as the spatial width over $1/e^2$ the maximum intensity) and $\Theta_i = 5°$ is the oblique horizontal incidence angle of the monochromatic beam. In addition, x and y correspond to the transverse spatial dependences and λ the wavelength of the monochromatic beam (in our case 800 nm).

This beam in the initial propagation distance will have the intensity profile shown in Fig. 9.8(a) at the laboratory Cartesian coordinate system and the decomposition in the spatial Fourier space shown in Fig. 9.8(b). Please notice that the set of plane waves of Fig. 9.8(b) is not centered at $k_x = 0$ because of the oblique incidence in the horizontal direction.

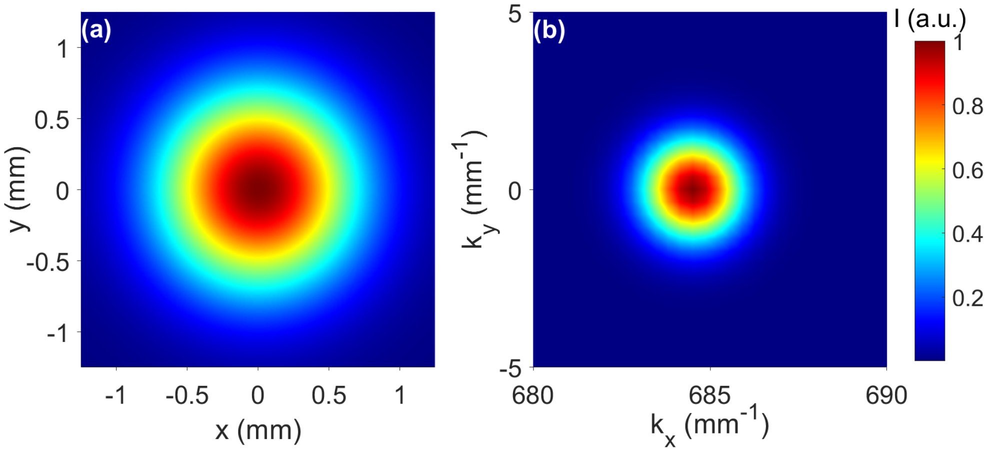

Fig. 9.8. *Intensity profiles of the initial beam used in the example of the propagation model in (a) laboratory Cartesian coordinate system and (b) Fourier coordinate system.*

Using the numerical model to propagate the beam to the other side of the crystal (i.e., $z_f = L_{crys} = 1$ mm), we obtain the corresponding ordinary and walk-off beams after propagation. Looking at the spatial intensity profile of the ordinary (Fig. 9.9(a)) and the walk-off (Fig. 9.9(b)) beams, it can be observed that they are laterally displaced. We have added the x and y axes (dotted white lines) in Fig. 9.9 to ease the visualization of the lateral displacement of each beam.

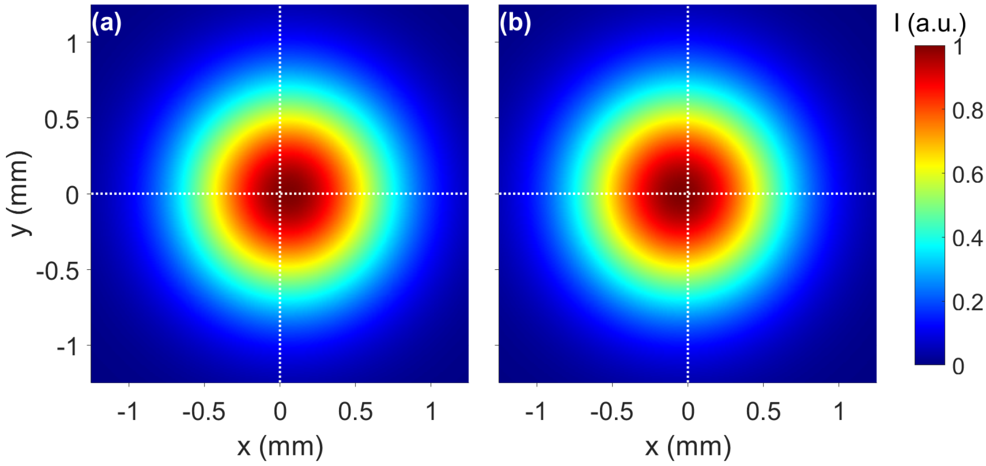

Fig. 9.9. *Intensity profile of the (a) ordinary and (b) walk-off beams in the laboratory Cartesian coordinates after being propagated through the 1-mm-thick calcite with* $\theta_{OA} = 45^\circ$ *and* $\Phi_{OA} = 0^\circ$ *using the numerical model.*

On one hand, the ordinary beam is centered at $(x_f, y_f) = (53, 0)$ μm with an uncertainty of ± 2.2 μm due to the spatial resolution of the numerical model. On the other hand, the center of the walk-off beam is displaced to $(x_f, y_f) = (-49.0, 0) \pm 2.2$ μm.

In order to verify the numerical model we can consider that, instead of the finite Gaussian beam, we have an infinite monochromatic plane wave with the same angles of incidence as the oblique beam, $\theta_i = \Theta_i = 5^\circ$ and $\Phi_i = 0^\circ$. In this case we can use the theoretical model of Section 9.2 to calculate the lateral displacement. Using Eqs. **9.40** and **9.41** we obtain that the ordinary plane wave presents a lateral displacement due to the oblique incidence of $(x_f, y_f) = (53, 0)$ μm, whereas the walk-off plane wave will be displaced $(x_f, y_f) = (-51, 0)$ μm, as given by Eqs. **9.53** and **9.55**.

Therefore, the lateral displacements for the infinite plane wave with the same oblique incidence fit with the results obtained with the finite beam using the numerical model. This comparison for verification is possible since the width of the wavevector distribution that compose the beam is small.

9.4 Calibration of uniaxial crystals

The uniaxial birefringent crystals are the principal element of the spatiotemporal technique implemented in this Thesis. Thus, it is crucial to correctly calibrate them in order to avoid high errors and artifacts during the beam characterizations.

It is very important to calibrate the crystal thickness with precision, because small changes in the manufacturer value can drastically change the crystal properties. In particular, it highly affects to the integration of the phase gradient explained in Section 8.1. Knowing the thickness and the other crystal parameters given by the manufacturer (material type and optical axis orientation angle, also called θ_{OA} in Subsection 9.2.3), we can calculate all the properties using the models shown in the previous Sections and the refractive indices (ordinary and extraordinary) given by Sellmeier equations.

Among all the possible ways of calibration, we decided to use an interference method based on SI using an ultrashort collimated flat wavefront laser beam under normal incidence. The calibration process used is the following:

i. **Calibration of optical axis azimuthal angle direction in laboratory system (Φ_{OA})**

   The uniaxial birefringent plate is azimuthally rotated between two crossed polarizers (e.g., horizontal and vertical) searching the azimuthal direction in which a minimum is observed. That direction corresponds to the projection of the O.A. onto the crystal surface parallel to one of the polarizers axes.

   Then, it is necessary to differentiate the direction of the O.A. between the two options (e.g., horizontal or vertical). One possibility is to use a external technique like STARFISH [77]. It can also be done rotating the initial and final polarizer 45° and comparing the SI of the uniaxial crystal and the SI of the combination of the uniaxial crystal and another one previously calibrated.

In case the manufacturer indicates the direction of the O.A., we recommend to do the calibration in order to improve the precision due to the importance of this parameter.

ii. **Calibration of crystal thickness**

Keeping the projection O.A. in the horizontal or vertical plane, the polarizers are rotated to +45°, so the spectral interferences due to the propagation through the fast and slow axis can be observed. Analyzing the SI using a FTSI algorithm, the delay introduced by the uniaxial medium under test can be extracted and, by comparing it with the theoretical delay given by Eq. **9.61**, the thickness can be estimated.

Note: if the delay introduced is not appropriate to observe the interferences with the spectrometer resolution or it is too low for the pulse spectral bandwidth, it can be introduced a known retarder plate between the polarizers to optimize it.

iii. **Walk-off direction**

In case we are calibrating a walk-off crystal, it is necessary to know whether the O.A. is oriented at $+\theta_{OA}$ or $-\theta_{OA}$. One way to do this, is to use a sharp object (e.g., a blade) to block part of the beam before the walk-off crystal and comparing the spatial profile for the horizontal and vertical projection of the last polarizer it can be observed the direction in which the walk-off beam (i.e., laterally displaced beam) is deviated.

The previously described process is one way to do it, but there are other possibilities, like using a technique such as STARFISH [77] or any standard interferometer to calibrate the material thickness.

Chapter 10

Operability range and limitations

This Chapter analyzes, from a theoretical point of view, the operability range of the spatiotemporal characterization technique proposed in this Thesis. Firstly, Sections 10.1 and 10.2 are focused on the study of the spectral and angular dependences of the walk-off property, respectively. Then, Section 10.3 mentions other general limitations that should be taken into account when using the technique.

10.1 Walk-off spectral dependence

As hinted before, the walk-off is one of the most important parameters in the bulk lateral shearing interferometry technique developed in this Thesis, and the uniaxial medium thickness must be calibrated in order to correctly characterize it. Nevertheless, when dealing with ultrashort pulsed beams, it is also important to take into account the spectral range of operation because the walk-off, like any other optical property of birefringent media, can spectrally vary due to the wavelength dependence of the ordinary and extraordinary refractive indices.

For simplicity, in this Section we are going to suppose that we are working under normal incidence conditions, so it can be used the simplified model of

Subsection 9.2.3.

As it will be shown later in Chapter 11, in the experiments performed during the Thesis we have used two different types of walk-off crystals with a thickness in the mm-scale: BBO with $\theta_{OA} = 29.2°$ and calcite with $\theta_{OA} = 45°$. Accordingly, we can use the theoretical model to calculate the walk-off spectral dependence for those walk-off crystals. The walk-off spectral dependence for a 1-mm-thick crystal of each material over more than an octave span, from 500 nm up to 1100 nm, is shown in Fig. 10.1.

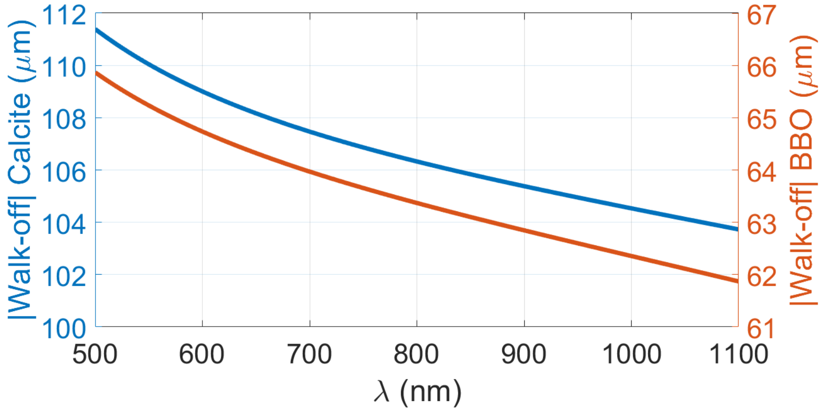

Fig. 10.1. *Walk-off spectral dependence under normal incidence for a 1-mm-thick calcite with $\theta_{OA} = 45°$ (blue) and for a 1-mm-thick BBO with $\theta_{OA} = 29.2°$ (orange) walk-off crystals. Notice that each crystal is represented in different scale.*

As it can be observed in Fig. 10.1, the walk-off along this large spectral range presents non-negligible variation in both cases, $[103.7 - 111.4]$ μm and $[61.9 - 65.9]$ μm for the 1-mm-thick calcite and BBO, respectively. This could be troublesome if the spatiotemporal technique is directly used to characterize an ultra-broadband beam (e.g., in the few-cycle regime), because the integration step would be significantly different for each frequency and the variation may be of the order of the resolution signal collection system size (e.g., in our case, 4 μm for the single mode fiber in the fiber spectrometer set-up of Section 8.2). Nonetheless, the spectral variation can be negligible for a multi-cycle laser in which the spectral bandwidth will be smaller.

For example, the spectral variation in the emission range of the ultrashort lasers used in Chapter 11 (from 785 nm up to 815 nm) is less than 0.1 μm for both crystals, which is much smaller than the walk-off introduced in these experiments (around 100 μm) and also smaller than the core of the fiber used to scan them (4 μm).

Therefore, at each experiment it must be ensured that the walk-off spectral variation is not significant compared with the walk-off mean value and the spatial resolution of the collection element.

Achromatization

During the experiments performed in this Thesis, it was not necessary to improve the spectral response of the spatiotemporal technique. Despite not being experimentally implemented yet, here we want to theoretically study how it could be addressed if it were necessary.

One possibility could be to implement an iterative retrieval algorithm, which takes into account the distortions introduced due to the spectral dependence. However, this would complicate the reconstruction algorithm, which is currently straightforward and simple, as it is only based on Fourier Transform analysis.

Another highly interesting possibility could be to implement an achromatic prototype or, at least, with a nearly flat spectral response. Here we are going to study this possibility since, in principle, it could be easily done following the ideas previously stated in polarization interferometry [142, 143]. Based on these previous works, one possibility could be to combine two different walk-off crystals in order to compensate the birefringence spectral dependence, while obtaining a certain desired walk-off value. Knowing the analytical expressions for the walk-off introduced by a uniaxial crystal (given for the normal incidence case by Eqs. **9.58** and **9.59**), we can simulate the combination of different uniaxial birefringent crystals in order to find what configurations optimize the spectral dependence.

In this study we are going to take into account four different commercially available walk-off crystals, also known as beam displacers: calcite ($CaCO_3$), BBO ($\beta-BaB_2O_4$), Yttrium orthovanadate (YVO_4) and Rutile (TiO_2). Despite being possible to select the angle θ_{OA} for custom crystals, in this simulation we are going to study the spectral dependence if all of them are cut with the optical axis at $|\theta_{OA}| = 45°$. This angle is commonly commercially available since the walk-off maximum value is generally close to it, as it is shown in Fig. 10.2, where the angular dependence of the walk-off introduced per mm of uniaxial crystal is shown for negative ($n_o > n_z$) and positive ($n_o < n_z$) uniaxial birefringent media. In the simulation of Fig. 10.2 we have assumed the refractive indices values of calcite for 800 nm in the case of the negative uniaxial ($n_o = 1.6488$ and $n_z = 1.4819$) and the same values exchanged for the positive uniaxial.

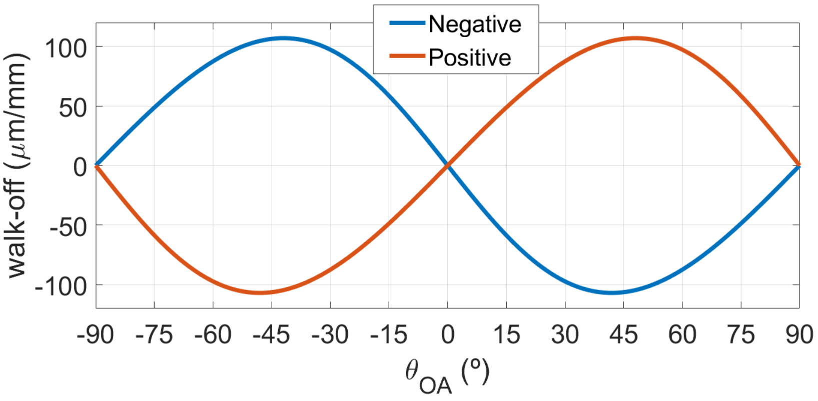

Fig. 10.2. *Angular dependence of the walk-off introduced per mm of uniaxial crystal under normal incidence conditions for negative ($n_o > n_z$) and positive ($n_o < n_z$) uniaxial birefringent media as a function of the optical axes insertion angle (θ_{OA}). The simulation takes into account the birefringent values of calcite at 800 nm for the negative case and the same values exchanged for the positive case.*

The implemented program searches for each pair of walk-off crystals (among all the possible combinations), the thicknesses and azimuthal angles that minimize the relative standard deviation of the walk-off dispersion and, after that, it calculates the optimal configuration to obtain a certain walk-off value. To simulate the different possible combinations, the program assumes that each crystal of the pair can vary its thickness from 0 to 2 cm. Regarding the azimuthal angle of the uniaxial media (Φ_{OA}), we consider two possibilities, Φ_{OA} and ($\Phi_{OA} + 180°$), because we want to introduce the walk-off in the same axis. Notice that this is the same as assuming a certain Φ_{OA}

and $+\theta_{OA}$ or $-\theta_{OA}$, respectively. In this simulations we are going to assume, without lack of generality, that $\Phi_{OA} = 0°$, so the walk-off will be given by Eq. **9.58**.

The walk-off spectral dependence for each individual walk-off crystal, as well as each optimal combination in order to obtain a walk-off mean value of 100 μm in the positive horizontal direction along more than an octave spanning spectrum (from 500 nm up to 1100 nm) are shown in Fig. 10.3.

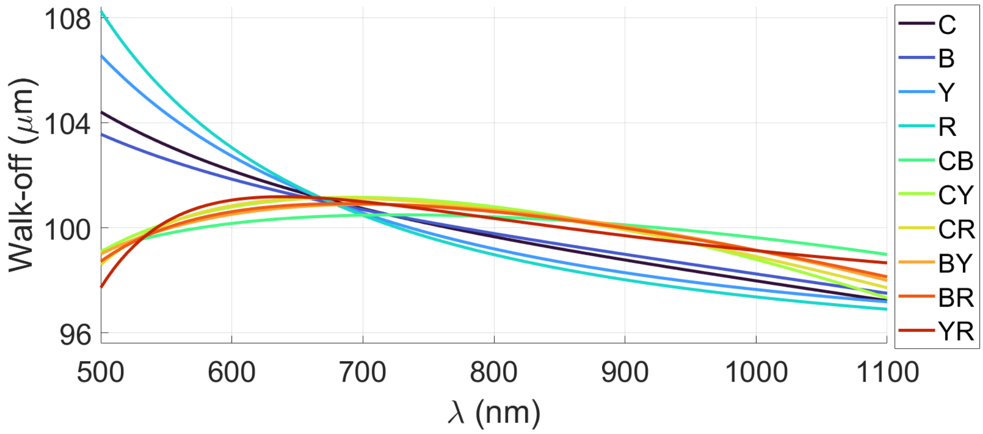

Fig. 10.3. *Walk-off spectral dependence for different combinations of walk-off crystals with $\theta_{OA} = \pm 45°$ that minimize the walk-off spectral variation, obtaining a walk-off mean value of $+100$ μm. Each individual crystal is referred by one reference letter and each combination is referred by the two crystal letters, being: calcite (C), BBO (B), YVO$_4$ (Y) and Rutile (R).*

The configurations, including materials, thicknesses (L) and O.A. angles (θ_{OA}), and the differences between minimum and maximum walk-off values (Diff.) within the considered spectral range of the simulations shown in Fig. 10.3 are summarized in Table 10.1.

From this simulation, it can be observed that the configurations with only one walk-off crystal present higher spectral variations with a maximum difference above 6.1 μm in the best situation. On the other hand, the spectral response can be considerably improved combining two walk-off crystals.

The calcite and BBO combination (CB) is quite interesting, since it has a maximum variation in the simulated spectral range of only 1.5 μm. Moreover, the other pairs of combinations are also interesting and, depending on

	CRYSTAL 1			**CRYSTAL 2**			
Name	**Material**	θ_{OA}(°)	**L(mm)**	**Material**	θ_{OA}(°)	**L(mm)**	**Diff.(μm)**
C	Calcite	-45	0.94	-	-	-	7.2
B	BBO	-45	1.40	-	-	-	6.1
Y	YVO_4	+45	0.96	-	-	-	9.4
R	Rutile	+45	0.97	-	-	-	11.3
CB	Calcite	+45	4.92	BBO	-45	8.70	1.5
CY	Calcite	-45	3.25	YVO_4	-45	2.38	3.8
CR	Calcite	-45	2.36	Rutile	-45	1.47	3.4
BY	BBO	-45	3.51	YVO_4	-45	1.46	2.9
BR	BBO	-45	2.83	Rutile	-45	1.00	2.8
YR	YVO_4	+45	5.99	Rutile	-45	5.07	3.5

Table 10.1: Summary of the configurations shown in Fig. 10.3 and difference between maximum and minimum walk-off value (Diff.) within the considered spectral range to obtain the best spectral response while having a 100-μm walk-off mean value.

the size of the signal collection element, they could be suitable. We want to highlight also the BBO and rutile combination (BR), which presents a maximum variation of 2.8 μm and requires relatively thin crystals implying a cost reduction.

In conclusion, the spectral dependence of the spatiotemporal technique can be considerably improved combining two different walk-off crystals. Although these crystals must be thicker than in the individual configuration, the dispersion will not be a problem since the SI measures the relative dispersion between each replica, and it will be calibrated when using the flat calibration beam.

10.2 Walk-off numerical aperture dependence

As we have seen before, when using collimated beams under normal incidence, the physics that rules our spatiotemporal technique, in particular the walk-off crystal, is quite simple and the main critical point is to pay attention to the walk-off spectral dependence. However, when using non-collimated beams (e.g., convergent or divergent beams), the complexity increases because the walk-off crystal properties can vary with the angle of incidence.

Taking this into account, in this Section we want to study how non-collimated beams are affected due to traveling a certain distance in an isotropic medium (e.g., air) with a walk-off crystal immersed in it. In particular, we will compare the ordinary and walk-off beam profiles after the propagation to see if there is any significant difference between them, which could lead to errors in the measurement of the spatiospectral gradient.

10.2.1 Methods: beam under study

We are going to use the model explained in Subsection 9.3.1 (with the same discretization parameters of Table 10.2) to study the propagation of focusing Gaussian beams with different NA that propagate through air (isotropic medium of $n \approx 1$) and a 1-mm-thick calcite with $\theta_{OA} = 45°$ (walk-off crystal).

We decided to perform the simulations from a monochromatic point of view because the spectral dependence has already been studied in Section 10.1 and, also, due to the computational requirements of the simulation and complexity of the full problem to extract conclusions.

In these simulations the beams under test are Laguerre-Gauss modes [144], whose electric field analytical definition is well known:

$$E_{\ell p}(x,y,z) = \frac{A_{\ell p}}{w(z)} \left(\frac{\sqrt{2(x^2+y^2)}}{w(z)} \right)^{|\ell|} L_p^{|\ell|} \left\{ \frac{2(x^2+y^2)}{w(z)^2} \right\} e^{-\frac{(x^2+y^2)}{w(z)^2}} \cdot$$

$$\cdot\, e^{i\left[\ell \arctan \frac{y}{x} + \frac{kr^2}{2R(z)} + \Phi_{\ell p}(z) + kz\right]} \quad \mathbf{(10.1)}$$

where $L_p^{|\ell|}$ represents the corresponding generalized Laguerre polynomial of index p and ℓ, also known as associated Laguerre polynomial [145]. The variables $w(z)$, $R(z)$ and $\phi_{\ell p}(z)$ correspond to the beam width, the curvature radius and a phase term along the propagation position, respectively. These parameters depend on the beam waist (w_0), the wavelength (λ) and the propagation position with respect to the focus (z), and they are given by the following equations:

$$
\begin{aligned}
w(z) &= w_0\left[1+\left(\frac{\lambda z}{\pi w_0^2}\right)^2\right]^{1/2}\\
R(z) &= z\left[1+\left(\frac{\pi w_0^2}{\lambda z}\right)^2\right]^{1/2}\\
\phi_{\ell p}(z) &= -(2p+|\ell|+1)\arctan\left(\frac{\lambda z}{\pi w_0^2}\right)
\end{aligned}
\qquad \mathbf{(10.2)}
$$

In particular, we want to study Laguerre-Gauss modes of $\ell = p = 0$ (LG_{00}) with a 5-mm waist (w_0') and λ =800 nm, which have been focused by thin lenses with different focal lengths (F). In order to calculate the electric field just after being focused, including the focusing term, it can be used Eqs. **10.1** and **10.2**, knowing that the waist has changed due to the focusing:

$$w_0 = \frac{\lambda F}{\pi w_0'}\frac{1}{\sqrt{1+\left(\frac{F\lambda}{\pi w_0'^2}\right)^2}} \qquad \mathbf{(10.3)}$$

In addition, it will also change the propagation reference because the waist will be at a different position. For simplicity, we are going to assume that each lens is placed in the waist of the initial beam ($z = 0$), so, if we calculate the electric field just after going through the lens, it should be calculated at the propagation distance $z = z_{ini}$, being z_{ini} the new waist position, which can be calculated as in [146]:

$$z_{ini} = -F\left(1-\frac{w_0^2}{w_0'^2}\right) \qquad \mathbf{(10.4)}$$

Furthermore, if different focal lengths are simulated for the same initial beam, essentially each focused beam can be associated to a certain NA:

$$NA = \frac{n\lambda}{\pi w_0} \qquad \mathbf{(10.5)}$$

where w_0 corresponds to the waist after being focused, which will be given by Eq. **10.3** and different for each focal length.

10.2.2 Results and Discussion

We have simulated the propagation at various distances for a set of four different focal lengths whose values and corresponding NA are collected in

Table 10.2. The range of focal lengths goes from a soft focusing situation (NA= 0.005) to a moderate focusing situation like the typical numerical aperture of a single-mode optical fiber (around 0.10-0.15).

Beam pre-focus **LG$_{00}$, $w_0 = 5$ mm and $\lambda = 800$ nm**				
F **(cm)**	100	50	10	5
NA	0.005	0.01	0.05	0.1

Table 10.2: Summary of focal lengths and corresponding NA.

In order to evaluate the differences between ordinary and walk-off non-collimated beams, we decided to decompose the wavefronts in a Zernike basis up to $n = 4$ order (Appendix B), which is commonly used in wavefront sensing. Since the Zernike basis is defined for a pupil of radius unity, and in order to follow the same criteria for each measurement, we defined the pupil normalizing by the radius at the 25% of the maximum ordinary intensity value.

We decided to study different propagation distances before ($z_F < 0$) and after ($z_F > 0$) the focus of each lens. The three Zernike terms (excluding the piston or offset term) that present non-null values for either the ordinary or walk-off beams are depicted in Fig. 10.4.

Notice that in the convergent part ($z_F < 0$) there is no simulation for absolute values of propagation greater than each focal length, since physically it makes no sense to calculate the focused beam at a position before the focusing lens. Regarding the propagation distances after the focus ($z_F > 0$), in principle, it should be possible to study the divergent behavior in propagation distances longer than the focal length. Nevertheless, this will expand the beam size in the XY coordinate space, reaching the edges of the grid and introducing artifacts. Thus, we decided to study for each NA only the values contained in the range given by its focal length $(-F, +F)$, since the physics is the same and the computational demanding is reasonable.

In Fig. 10.4 it can be observed that, at each propagation distance, all the Zernike coefficients are the same for each ordinary and walk-off beam, respectively, regardless of the NA value. This implies that the wavefront of both beams is the same for each propagation distance.

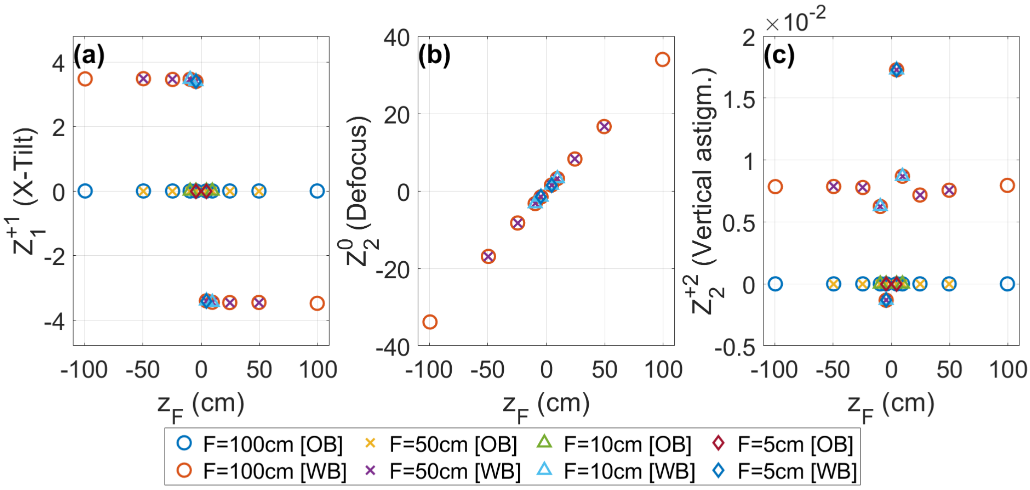

Fig. 10.4. *Non-null Zernike contributions obtained for the ordinary (OB) and walk-off (WB) beams focused by different focal length (F) lenses for various propagation distances relative to the focus of each lens (z_F). (a) X-Tilt, (b) defocus and (c) vertical astigmatism.*

The nearly constant value of X-Tilt, observed in Fig. 10.4(a), encodes the lateral shearing introduced due to the walk-off property. Moreover, in Fig. 10.4(c) it can be observed that, for all distances, the walk-off beams present a very small and nearly constant vertical astigmatism distortion. Nevertheless, the distortion is negligible in the range studied since the biggest vertical astigmatism contribution is 0.017.

The defocus contribution, represented in Fig. 10.4(b), is roughly the same for the ordinary and walk-off beams for each propagation distance (notice that they are overlapping). Actually, there is a small difference between the ordinary and walk-off beams whose relative value (i.e., $(C_w - C_o)/|C_o|$ being C_o and C_w the ordinary and walk-off contributions) becomes bigger close to the focus, Fig. 10.5. In addition, close to focus there is a slight asymmetry in the relative defocus.

Although the relative difference between ordinary and walk-off defocus increases when the beam is closer to focus, in the majority of situations it is negligible (biggest absolute value lower than 0.52%).

In conclusion, the spatiotemporal technique can be used without further

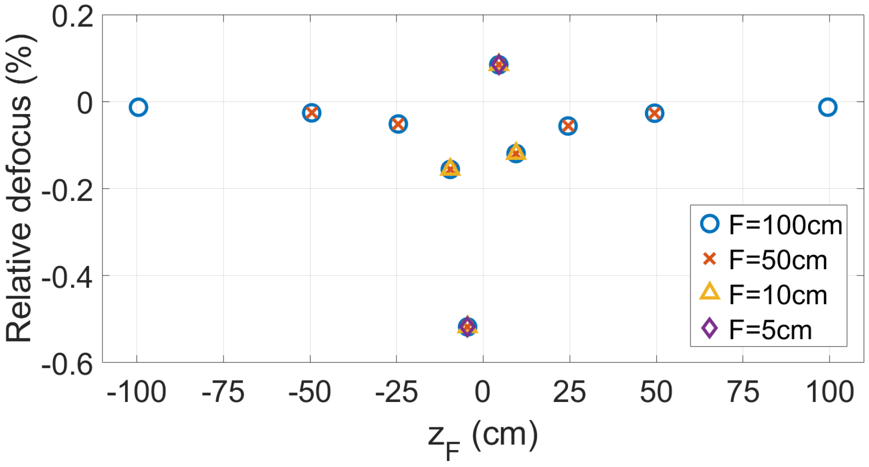

Fig. 10.5. *Evaluation of the relative defocus between the walk-off and ordinary wavefronts* ($(C_w - C_o)/|C_o|$ *being* C_o *and* C_w *the ordinary and walk-off contributions), which have been focused by different focal length (F) lenses for various propagation distances relative to the focus* (z_F)*.*

considerations for propagation distances far from focus, provided a good spatial resolution of the signal collection element and good overlapping of both replicas. If the measurement needs to be done in focus or very close to it, there could be distortions in the spatiospectral gradient or even no combination due to lack of overlap. A possible solution may be to measure the beam before the focus and then propagate the retrieval to the focus numerically.

10.3 Other limitations

In addition to the walk-off spectral and numerical aperture dependences, which have been analyzed previously, there are other additional considerations that should be known concerning the operation of the technique.

Firstly, since the technique is based on SI, the spatiospectral phase gradient from point to point cannot change more than 2π rad to correctly retrieve the phase. This can be easily solved using thinner walk-off crystal or, if not possible, using oversampling strategies.

Regarding the temporal duration, the shortest limit is given by the spectral dependence of the technique that can be improved using the achromatization strategy. On the other hand, the longest duration is limited by the spectral resolution required for the FTSI algorithm, which can be adapted using the appropriate spectrometer.

Moreover, as we will show in Chapter 11, in this Thesis we have usually characterized beams with a mm-scale size (2-3 mm), but larger or smaller beams can also be studied. On one hand, to analyze larger beams, it can be used bigger uniaxial elements or implement an aberration-free imaging system to reduce the beam to a suitable size for our set-up. On the other hand, to characterize smaller beams, it should be verified that the spatial resolution is enough to correctly measure the spatiospectral gradient. In the version used in the Thesis, the spatial resolution is given by the walk-off distance, since we are directly scanning in walk-off steps, but this can be reduced using thinner elements or uniaxial materials with lower birefringence. Although there are thinner walk-off crystals commercially available, other interesting strategies can solve this point, for example expanding the beam with an aberration-free system or maybe using oversampling strategies. Furthermore, it is essential to verify that the spatial resolution of the collection is much smaller than the detection step. In the fiber spectrometer prototype this will be approximately the fiber core. Thus, 4 μm for the experiments presented in Chapter 11.

Another point to take into account is the time required to measure the spatial grid. In the spatial scan prototype with a fiber spectrometer used in this Thesis, each spatial grid is composed by N^2 dots that should be scanned one by one. Thus, it is interesting to adapt the walk-off in order to have the best balance between spatial resolution and measurement time. One possibility to reduce the acquisition time is to use an imaging spectrometer 1-D spatial, so the N^2 grids could be reduced to N measurements at different lateral or vertical positions. Furthermore, another promising possibility is to use a hyperspectral camera [147–149] to measure each spatial grid in one acquisition/shot.

Computationally, the current version of the retrieval algorithm is simple, fast and straightforward because it is only based on Fourier Transforms and the integration of the gradient. The only critical point is to follow an integration path avoiding null signal points (exclusively in case of existing) that could introduce noise in the retrieval, as discussed in Section 8.1. Moreover, if the beam presents strong spectral bandwidth changes across the spatial profile, it is necessary to follow an integration path from the points showing broader spectra to the points with narrower ones.

Chapter 11

Application of bulk lateral shearing interferometry

Previously, in Chapters 8 and 10, we have studied the concept and operation range of the spatiotemporal technique implemented in this Thesis. In the current Chapter, we present the experimental proof of concept of the technique and we focus on its application to study various complex spatiotemporal structures generated with ultrashort lasers, like constant and time-varying optical vortices or astigmatic beams, using the spatial scan prototype introduced in Section 8.2.

11.1 Optical vortices in collimated beams

Optical vortices are a type of complex spatiotemporal structures that have gained great interest in the last decades due to their multiple applications, such as optical communications, optical tweezers for particle trapping or laser machining, among others [150].

Essentially, an optical vortex is a beam with an azimuthal variation of the phase associated with an Orbital Angular Momentum (OAM) or ℓ defined as $\exp(-i\ell\Phi)$, being Φ the azimuthal angle, which presents a singularity at the center. For example, the Laguerre-Gauss modes with $p = 0$ and different values of ℓ are optical vortices.

In particular, Fig. 11.1 presents the simulation of the intensity and phase profiles of some optical vortices with different OAMs.

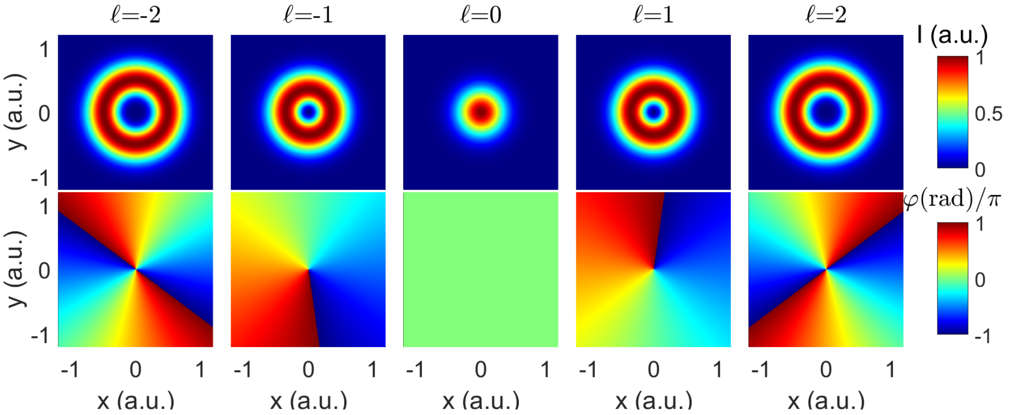

Fig. 11.1. *Intensity (first row) and phase (second row) profiles of optical vortices with different OAMs.*

During the last decades, different ways have been proposed to create and characterize optical vortices. For example, in [151] the authors used a spatial light modulator to generate them and a Shack-Hartmann wavefront detector with a FROG system for the characterization. Alternatively, a multi-pinhole plate can be used for the generation, as in [152], where the characterization was done analyzing the common fork interference pattern with a plane wave. Another example is [153], where the authors generated few-cycle optical vortices with a spiral phase plate (i.e., a glass plate with thickness depending linearly on the azimuthal angle) and studied them with spatially-resolved Fourier Transform spectrometry.

In this Thesis, we have used a type of nanostructured plates [154], called s-waveplates, which depending the incident polarization can generate radially polarized vortices $\left(R_m^{\ell_0}\right)$ with m polarization azimuthal index and ℓ_0 input OAM.

$$R_m^{\ell_0} = e^{-i\ell_0\Phi}\begin{pmatrix}\cos(-m\Phi)\\ \sin(-m\Phi)\end{pmatrix} \quad \textbf{(11.1)}$$

where Φ corresponds to the azimuthal angle.

In [154] it was demonstrated that the generated radially polarized vortex $\left(R_m^{\ell_0}\right)$ can be expressed as a combination of two vortices of $\ell_1 = \ell_0 + m$

and $\ell_2 = \ell_0 - m$ with right-circular polarization (RCP) and left-circular polarization (LCP), respectively:

$$R_m^{\ell_0} = \frac{e^{-i\ell_1\Phi}}{\sqrt{2}}\text{RCP} + \frac{e^{-i\ell_2\Phi}}{\sqrt{2}}\text{LCP} \tag{11.2}$$

Therefore, using a zero-order QWP, we can turn the circular polarizations into linear polarizations and select the desired OAM (ℓ_1 or ℓ_2) with a linear polarizer. We measured the resulting scalar beams with our technique.

In the laboratory we used two different s-waveplates: SP1 and SP2. On one hand, SP1 operates as a HWP with spatially varying fast axis ($\Phi_{\text{fast}} = \Phi/2$, being Φ the azimuthal angle), which turns incident linear polarization into radial polarization R_1^0. Thus, with SP1 we can generate $\ell = \pm 1$ optical vortices.

On the other hand, SP2 acts as a QWP with spatially varying fast axis ($\Phi_{\text{fast}} = \Phi$, being Φ the azimuthal angle), which converts incident circular polarization in radial polarization vortex of R_1^1. So, with SP2 we can generate $\ell = +2$ and $\ell = 0$ optical vortices.

Figs. 11.2(a,b) represent the spatial distribution of the fast axis orientation for the vortex plates SP1 and SP2, respectively.

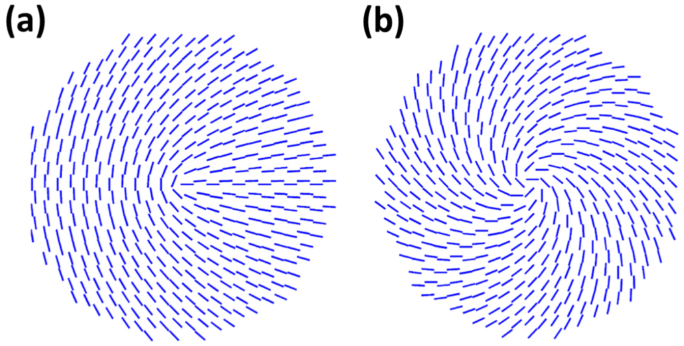

Fig. 11.2. *Representation of the fast axis spatial orientation in (a) SP1 and (b) SP2. Image adapted from [155].*

In addition, if we combine SP1 and SP2 with an achromatic HWP between them, we can generate radial polarization vortex of R_1^2 that can be decomposed into $\ell = +3$ and $\ell = +1$ optical vortices. In this case, it is necessary a HWP between both plates to change the helicity sign of the circular polarization, thus avoiding the cancellation of OAM and the generation of a R_1^0 state instead of the desired R_1^2 [154].

11.1.1 Proof of concept of the spatiotemporal technique

The first experiment that we performed with the new spatiotemporal technique was a proof of concept consisting on characterizing a constant optical vortex of $\ell = +2$, generated using the SP2, with two configurations of the technique [136]. The scheme of the experiment is shown in Fig. 11.3.

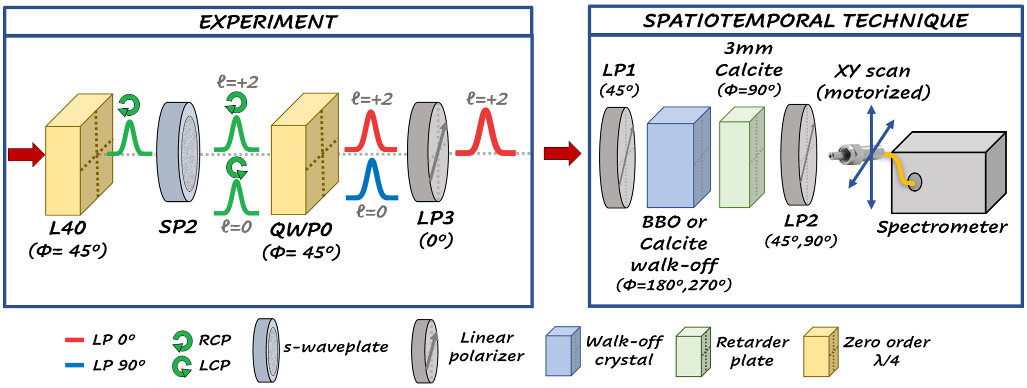

Fig. 11.3. *Scheme of the experimental set-up used to generate an $\ell = +2$ vortex for the proof of concept and the two variants of the characterization set-ups with BBO and calcite as walk-off crystals.*

Both configurations used two polarizing beamsplitter cubes (from Thorlabs), LP1 and LP2, a 3-mm-thick calcite with its fast axis in the Y-axis as retarder plate, which introduced a 1.8-ps delay at 798 nm, and a spectrometer (AvaSpec 2048-USB1, from Avantes Inc.) with an optical fiber coupler placed on a motorized XY-stage.

The difference between both configurations was the used walk-off crystal. On one set-up, we used a 1.12-mm-thick BBO cut with its O.A. at $\theta_{OA} = 29.2°$, which introduces a 71-μm walk-off and 120-fs delay at 798 nm. The other system used a 1.06-mm-thick calcite cut with $\theta_{OA} = 45°$, which introduces a 113-μm walk-off and 350-fs delay at 798 nm.

Moreover, in this experiment the temporal reference was measured deviating the beam before LP1 with a flip mirror to an amplitude swing system, and characterizing the beam in the lateral of the vortex at position $(x, y) = (0, -0.5)$ mm. In particular, we used the same system with the 2.1-mm-thick quartz rotating MWP utilized in Chapter 5. The measured amplitude swing trace with its retrieval are shown in Fig. 11.4. In this case, the retrieval was obtained using the Levenberg-Marquardt algorithm of [31], which has been mentioned in Chapter 3.

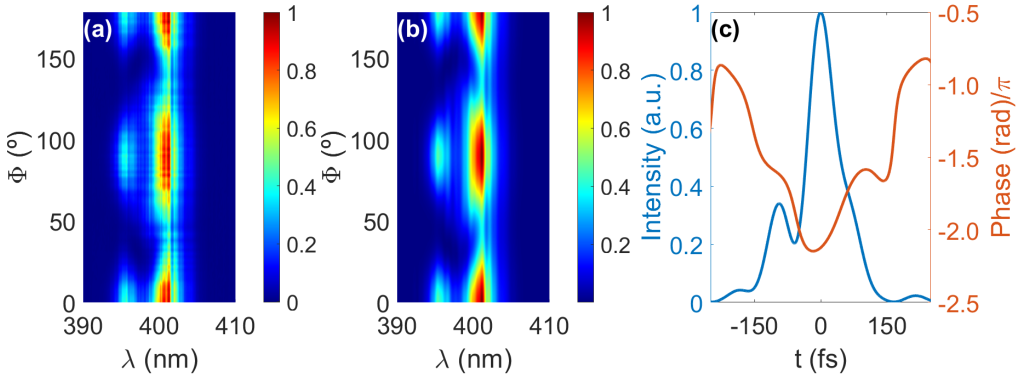

Fig. 11.4. *Characterization of the temporal reference with amplitude swing at position $(x, y) = (0, -0.5)$ mm. (a) Experimental trace, (b) retrieved trace, and (c) retrieved pulse. Temporal FWHM of 77.8 fs and a rms difference between experimental and retrieved traces of 0.024.*

In order to characterize a grid of similar size ($\geq$ 2 mm) but with the walk-off steps corresponding to each walk-off crystal, we performed a 29 x 29 grid scan with a spatial step of 71 μm with the BBO, and a 19 x 19 grid scan with spatial step of 113 μm with the calcite crystal.

In Fig. 11.5 it is shown the intensity (first row) and phase (second row) for the central wavelength of the pulse ($\lambda = 798$ nm) using the two characterization systems: BBO (first column) and calcite (second column). The complete spatiospectral retrieval is depicted in Appendix C.1.1. Notice that the graphics have been interpolated in a common grid with a 10-μm step to smooth the retrieval and ease the visualization.

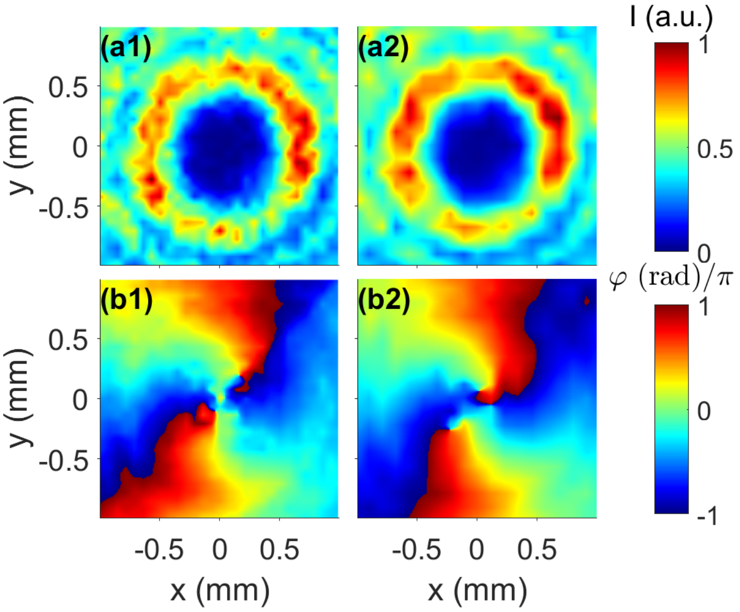

Fig. 11.5. *Intensity (a) and phase (b) profiles of the spatiospectral characterization for the central wavelength ($\lambda = 798$ nm) of the same optical vortex using the 2D4Quad approach and measuring the spatial spectrum of the ordinary beam with two walk-off crystal: BBO (first column) and calcite (second column). Note: the retrievals are shown interpolated with a spatial step of 10 μm.*

As it is observed in Fig. 11.5, both retrievals agree and correctly retrieve the $\ell = +2$ optical vortex (as seen in the phase and the intensity singularity). This is also observed in Fig 11.6, in which it is shown the azimuthal phase dependence for a ring of 600-μm radius, that has been calculated by splining the measured XY-maps in polar coordinates and comparing it with the theoretical phase of an $\ell = +2$ optical vortex.

The small discrepancies between theory and experiment could be associated to a non-perfect generation of the vortex in the s-waveplate and/or the spatial resolution before interpolating into polar coordinates. Despite the small differences, the agreement is very good between experiments and the theory. Besides, the measurements are done with two different set-ups, so we corroborate the validation of the spatiotemporal technique.

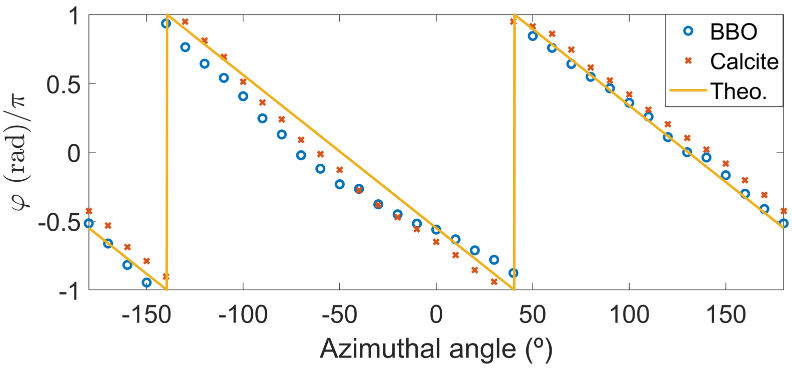

Fig. 11.6. *Comparison of the azimuthal phase retrieved for a 600-μm radius for each walk-off crystal (BBO and calcite) with the theoretical azimuthal phase of an $\ell = +2$ optical vortex (Theo.).*

Notice that the optical vortex is generated with an achromatic set-up. We have chosen to depict the results for the central wavelength, but the same results are found if representing them for a different wavelength (or for a particular time of the pulse). In Section 11.2 we will show time-dependent vortices and how the technique can resolve them both, in time and frequency.

11.1.2 Vortices in the visible and near-infrared

Once the technique was demonstrated, we used one configuration to characterize optical vortices of different OAM, thus observing how the technique operates with different complex beams. Taking into account that both configurations (BBO and calcite walk-off crystals) work properly, we decided to use the 1.06-mm-thick calcite walk-off crystal because the walk-off step (113 μm) is bigger than the one of the BBO (71 μm), so less points are needed to properly scan the full spatial profile of the beam implying faster measurements.

At the beginning of Section 11.1, it was shown how to generate optical vortices with different OAMs depending on the incident polarization and what s-waveplate is used. Taking this into account, we used the SP1 and the combination of SP1+SP2 to generate vortices with $\ell = \pm 1$ and $\ell = +3$. These vortices were measured in walk-off steps (113 μm) and the retrievals for the central wavelength ($\lambda = 798$ nm) are summarized in Fig. 11.7.

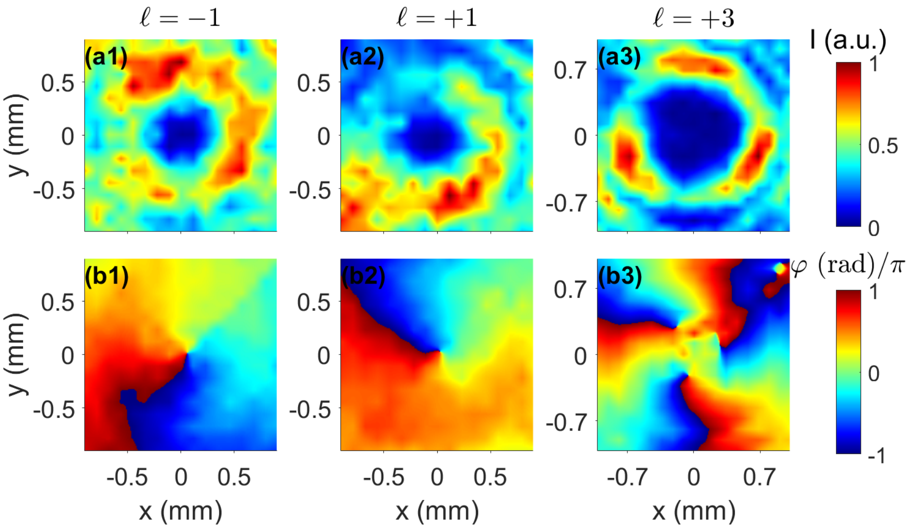

Fig. 11.7. *Intensity (a) and phase (b) profiles of the spatiospectral characterization for the central wavelength ($\lambda = 798$ nm) of three optical vortices with different topological charges: $\ell = -1$ (first column), $\ell = +1$ (second column) and $\ell = +3$ (third column). Note: the retrievals are shown interpolated with a spatial step of 10 μm.*

The complete spatiospectral retrieval of each optical vortex is depicted in Appendix C.1, corresponding the videos of C.1.2, C.1.3 and C.1.4 to the $\ell = -1$, $\ell = +1$ and $\ell = +3$ near-infrared optical vortices, respectively.

For each case, we used the amplitude swing technique to retrieve the spectral reference measured at position $(x, y) = (0, -0.5)$ mm, but in these situations we have used the Differential Evolution algorithm described in Chapter 4 for the retrievals.

As it can be observed in Fig. 11.7, the spatial intensity profiles of these vortices are somehow distorted due to a non-perfect generation. This spatial distortion is not observed in the proof of concept with the $\ell = +2$ vortex shown in Fig. 11.5, so it may be associated with the SP1. Despite this intensity distortion, the phase profiles are not affected, showing clearly each vortex OAM. In fact, these intensity distortions were also observed using the same s-waveplates in [154].

Furthermore, apart from its compactness and high stability, another interesting advantage of the spatiotemporal technique is that it can operate in all the transparency range of the uniaxial birefringent crystal. The only requirement to operate in a different spectral range is to calculate the walk-off in the new region. This estimation can be done using the theoretical model shown in Chapter 9 and the Sellmeier coefficients of the walk-off crystal material. For example, for the 1.06-mm-thick calcite walk-off crystal with $\theta_{OA} = 45°$ the walk-off around 400 nm is 123 μm, 10 μm bigger than the value at $\lambda = 800$ nm.

Although our s-waveplates are made to operate around 800 nm, we can generate optical vortices in the visible by doubling the frequency of the 800-nm vortices using a SHG crystal. Taking this into account, we used a SHG BBO in order to transform the $\ell = \pm 1, +2$ IR-vortices into visible vortices.

Moreover, in order to obtain the complete spatiospectral or spatiotemporal characterization, it is required to characterize a temporal reference of the visible vortices in a single spatial position. However, if we use a conventional temporal technique based on SHG, the nonlinear trace will be in the ultraviolet spectral range (around 200 nm) and up to now we do not have a spectrometer to measure it in the laboratory. Besides, in this case it will even reach the vacuum ultraviolet (i.e., ultraviolet region from 100 nm to 200 nm in which is necessary to work in vacuum).

Despite not being able to directly characterize the visible vortex spectral phase reference, we can calculate it. In particular, we can measure the IR generating vortex and obtain the SHG pulse as the square of the fundamental pulse in the temporal domain, as done for the spectral references of Fig. 11.8.

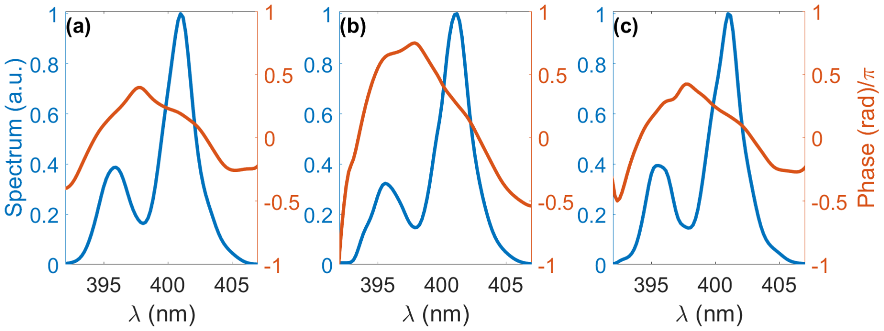

Fig. 11.8. Spectral reference of the visible vortices simulated from the optical vortices in the IR range: (a) $\ell = -2$, (b) $\ell = +2$, and (c) $\ell = +4$.

Knowing the spectral references and measuring the spatiospectral gradients with the technique, the complete characterization for the visible vortices can be obtained. The spatiospectral retrieval for the central wavelength ($\lambda = 396.7$ nm) for each vortex is shown in Fig. 11.9. The complete spatiospectral retrievals are depicted in Appendix C.1, being C.1.5, C.1.6 and C.1.7 the characterizations of the $\ell = -2$, $\ell = 2$ and $\ell = 4$ optical vortices in the visible range.

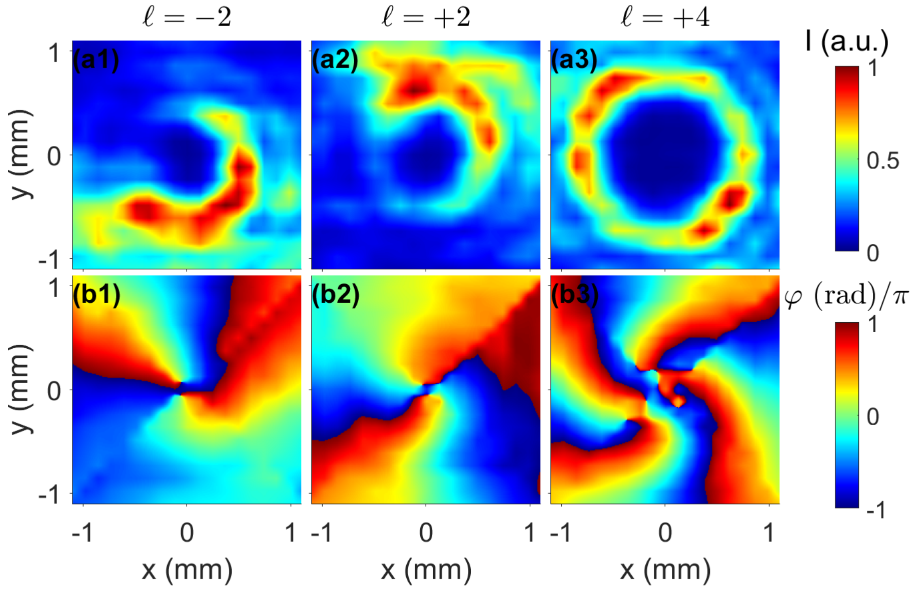

Fig. 11.9. *Intensity (a) and phase (b) profiles of the spatiospectral characterization for the central wavelength ($\lambda = 396.7$ nm) of three optical vortices in the visible spectral range with different topological charges: $\ell = -2$ (first column), $\ell = +2$ (second column) and $\ell = +4$ (third column). Note: the retrievals are shown interpolated with a spatial step of 10 μm.*

On one hand, according to the spatiospectral phase profiles (second row of Fig. 11.9), the OAM has been doubled, in agreement with the angular momentum conservation rule [156]. This rule indicates that OAM of the q-th order of the harmonic generation nonlinear process is $\ell_q = q\ell_0$, with ℓ_0 the OAM of the fundamental frequency. In our case we observe doubled OAMs because the nonlinear order is $q = 2$.

On the other hand, according to the spatiospectral intensity profile (first row of Fig. 11.9), the $\ell = \pm 2$ vortices are asymmetric and highly distorted compared to the $\ell = +4$ vortex. In the case of $\ell = -2$ the distortion is even embodied in the phase profile.

Comparing the visible and IR vortices, we observe that those generated with SP1 are more distorted in the visible range, but this makes sense, since the SHG magnifies the intensity distortions because it scales quadratically with the fundamental intensity. Thus, we can conclude that the SP2 imprints a better spatial distribution than SP1.

In conclusion, our spatiotemporal technique is able to characterize complex spatiotemporal couplings, like optical vortices with different topological charges, in different spectral regions just by changing the step size to the walk-off value in the spectral range. Please notice that the spectral reference is only required to link all the wavefronts or measure the spatiotemporal profile, but each individual wavefront (and amplitude) can be measured without it.

11.2 Time-varying optical vortices in collimated beams

In the previous Section, we have demonstrated that our spatiotemporal technique is able to accurately measure the spectrally-resolved wavefronts of beams with complex STCs, like the constant optical vortices. In this Section, we want to increase the complexity and to characterize time-varying optical vortices [136].

In fact, what we characterized is the spatiotemporal profile of the combination of two delayed optical vortices of different OAM. As it was explained in Section 11.1, when a circular polarized beam crosses the SP2, two circularly polarized optical vortices are generated with different topological charges ($\ell = +2$ and $\ell = 0$) and opposite helicity (RCP and LCP, respectively). Thus, as shown in the experimental set-up of Fig. 11.10, we can turn the RCP and LCP into horizontal and vertical polarization using a zero-order QWP with the appropriate orientation. Then, we introduce between them a small delay (∼65 fs) of the order of the pulse duration (∼75 fs) using a 2-mm-thick quartz plate. Thus, if we project both components into a common polarization state (e.g., linearly polarized at 45°), we will observe the superposition of both optical vortices using our spatiotemporal technique.

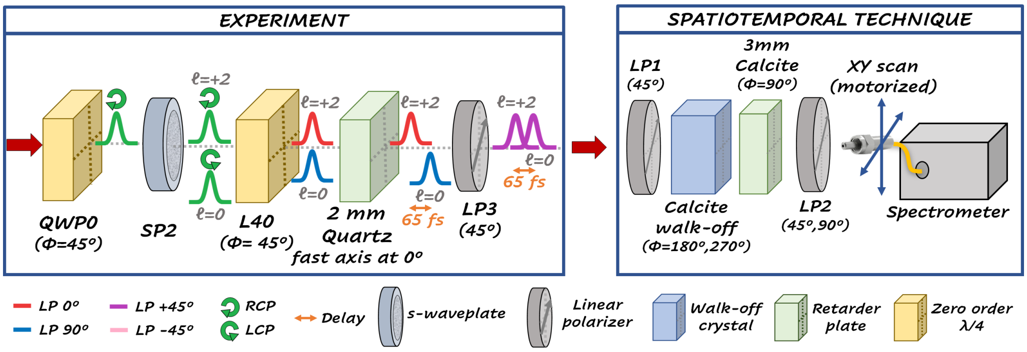

Fig. 11.10. *Scheme of the experimental set-up used to generate two delayed optical vortices of* $\ell = +2$ *and* $\ell = 0$ *with a temporal delay of ∼65 fs and the spatiotemporal technique used for the characterization.*

Firstly, we characterized the temporal reference of the beam under test at position $(0, -0.5)$ mm using the amplitude swing technique with the 2.1-mm-thick quartz rotating MWP mentioned in previous Sections. In Fig. 11.11 it is shown the retrieval obtained using the Levenberg-Marquardt retrieval algorithm developed in [31].

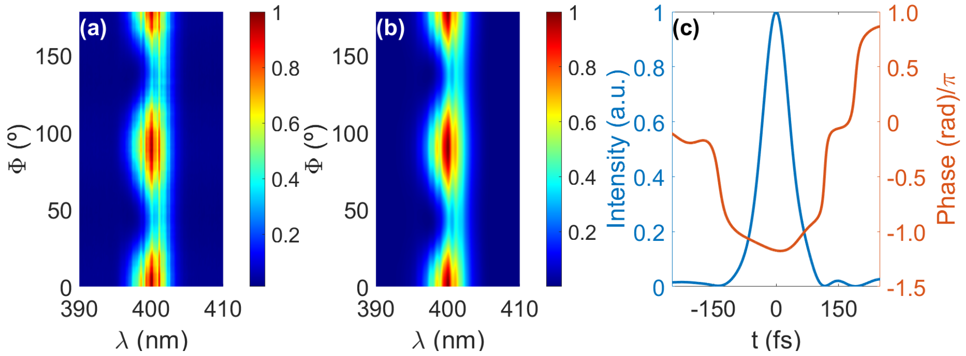

Fig. 11.11. *Characterization of the temporal reference using amplitude swing at position* $(x, y) = (0, -0.5)$ *mm. (a) Experimental trace, (b) retrieved trace, and (c) retrieved temporal pulse intensity and phase. Temporal duration FWHM of 78.4 fs and rms of 0.027.*

In this experiment we used the spatiotemporal technique with the 1.06-mm-thick calcite walk-off crystal performing a spatial scan grid of 19x19 with a spatial step of 113 μm (walk-off size around 800 nm). Moreover, taking into account the complexity of the spatiospectral profile, the retrieval was done using the *2D2Quad* approach, explained in Section 8.1. The spatiotemporal characterization for three different temporal snapshots, which correspond to the center ($t_2 = 0$ fs) and the tails of the average pulse ($t_1 = -45$ fs and $t_3 = +45$ fs), is shown in Fig. 11.12. The complete spatiotemporal characterization is depicted in Appendix C.2.1.

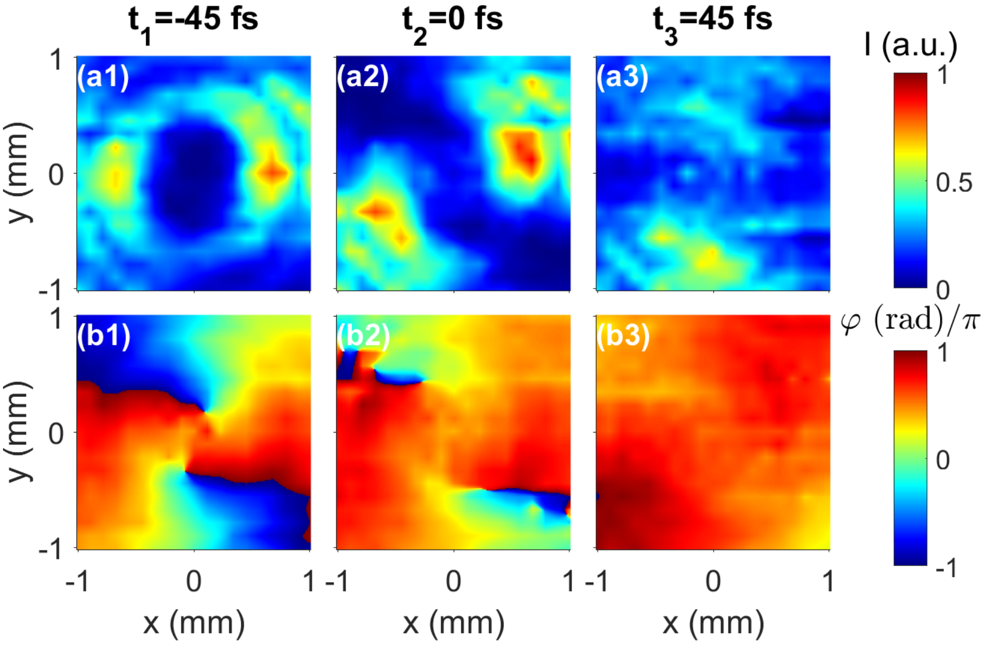

Fig. 11.12. *Retrieved spatiotemporal intensity (a) and phase (b) of the combinations of two optical vortices of $\ell = +2$ and $\ell = 0$, delayed 65 fs, analyzed using the 2D2Quad approach and measuring the spatial spectrum of the ordinary beam for three temporal snapshots: $t_1 = -45$ fs (first column), $t_2 = 0$ fs (second column), and $t_3 = +45$ fs (third column). Note: the retrievals are shown interpolated with a spatial step of 10 μm.*

Observing the spatiotemporal phase Fig. 11.12(b), we can distinguish different structures along the pulse. On one hand, in the leading edge (t_1) and the trailing edge (t_3) of the pulse we can observe the contribution of only one optical vortex of $\ell = +2$ and $\ell = 0$, respectively. On the other hand, at the pulse center (t_2) it is shown the interference of both vortices. There, the phase and intensity distributions depend on the relative amplitude and the relative phase of the delayed vortices.

In order to evaluate the results obtained in the experiment, we have simulated the two optical vortices superposition, obtaining the temporal evolution shown in Fig. 11.13. The full spatiotemporal dependence is depicted in Appendix C.2.2. We have assumed that each beam corresponds to a Laguerre-Gauss spatial mode (LG_{20} and LG_{00} for the $\ell = +2$ and $\ell = 0$ optical vortices), with the temporal profile retrieved in Fig. 11.11, and adding the calibrated phase introduced by the 2-mm-thick quartz retarder plate used for delaying the vortices. In addition, we have imposed that the energy of each spatial mode is similar, and the waist of the LG_{00} mode is defined as $\sqrt{2}$ the waist of the LG_{20} mode to have a good spatial overlapping like in the experiment.

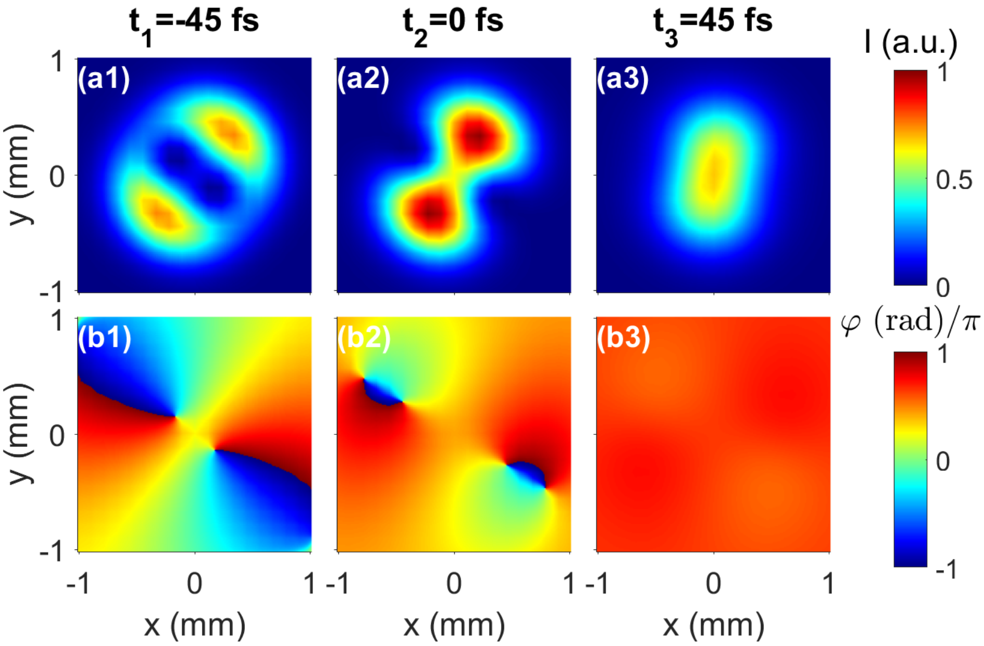

Fig. 11.13. *Simulated spatiotemporal intensity (a) and phase (b) of the combinations of two optical vortices of $\ell = +2$ and $\ell = 0$ delayed 65 fs for three temporal snapshots: $t_1 = -45$ fs (first column), $t_2 = 0$ fs (second column), and $t_3 = +45$ fs (third column).*

The experimental spatiotemporal retrieval, Fig. 11.12, and the numerical simulation, Fig. 11.13, show a good agreement. According to the phase profile, we observe the same OAM evolution, specially at the central time (Fig. 11.12(b2) and Fig. 11.13(b2)). The small deviations can be originated due to imperfections on the vortex generation using the s-waveplates or the lack of homogeneity of the input laser beam. Another source of discrepancy is the fact that the experimental $\ell = 0$ vortex is not a perfect LG_{00} spatial mode, since it has a minimum of transmittance at the center due to the design and manufacturing constraints of the s-waveplate.

Despite the small discrepancies, the good agreement of the experiment with the numerical simulation demonstrates that our spatiotemporal technique is able to characterize complex ultrashort laser beams.

Moreover, from this experiment it can be calculated the average temporal intensity profile obtained by spatial integration of the spatiotemporal intensity profile, Fig. 11.14.

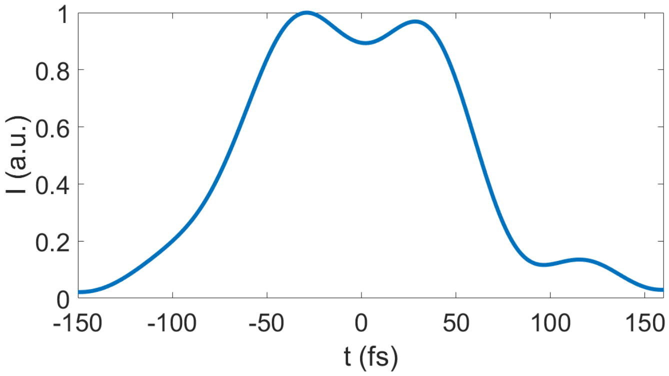

Fig. 11.14. *Temporal intensity obtained from the spatial integration of the experimental spatiotemporal intensity of Fig. 11.12. Temporal duration of 133 fs FWHM.*

It is observed that the average temporal intensity is completely different from the measured at the reference spatial point, shown in Fig. 11.11, and the FWHM is much bigger (133 fs for the whole beam and 78.4 fs in the reference point). Thus, with this experiment it is highlighted the importance of spatiotemporal characterization when having STCs, because using only a temporal characterization could give unreal values of the whole temporal duration. In fact, the temporal pulse profile varies spatially, hence the temporal duration at each spatial position is different.

11.3 Non-collimated astigmatic beams

In previous Sections, we have experimentally demonstrated that the spatiotemporal technique developed in this Thesis can characterize collimated beams with complex STCs. Specifically, in Section 10.2 we demonstrated theoretically that it is also able to analyze non-collimated beams, provided that the characterization is not performed close to focus.

Taking this into account, in this Section we want to experimentally measure the spatiospectral distribution of an ultrashort laser beam after being focused with an astigmatic lens. We decided to use astigmatic lenses instead of a spherical lens because they present a more complex spatiospectral distribution since they have two different focal lengths for two orthogonal axes.

As done in previous Sections, we used a Ti:sapphire laser spectrally centered at 800 nm as the ultrashort light source and the bulk lateral shearing interferometer as the spatiotemporal technique to analyze them. According to the spatiotemporal technique, as a walk-off crystal we used the 1.06-mm-thick calcite cut with $\theta_{OA} = 45°$ (113-μm walk-off and 350-fs delay around 800 nm) and, to adjust the delay, a 3-mm-thick calcite retarder plate (1.8 ps delay at 800 nm) with its fast axis in vertical direction.

In order to test the spatiotemporal system with a non-collimated beam, we used an astigmatic lens with 100-cm and 197-cm focal lengths, represented in Fig. 11.15. Furthermore, we measured the spatiospectral profile at two different propagation planes, 49 cm and 137 cm from the lens, represented in Fig. 11.15 as d_a and d_b respectively. Please notice that the spatiotemporal technique has a certain longitudinal size due to the elements required to implement it, but the measurement plane is the scanned by the fiber spectrometer placed over the XY-stage.

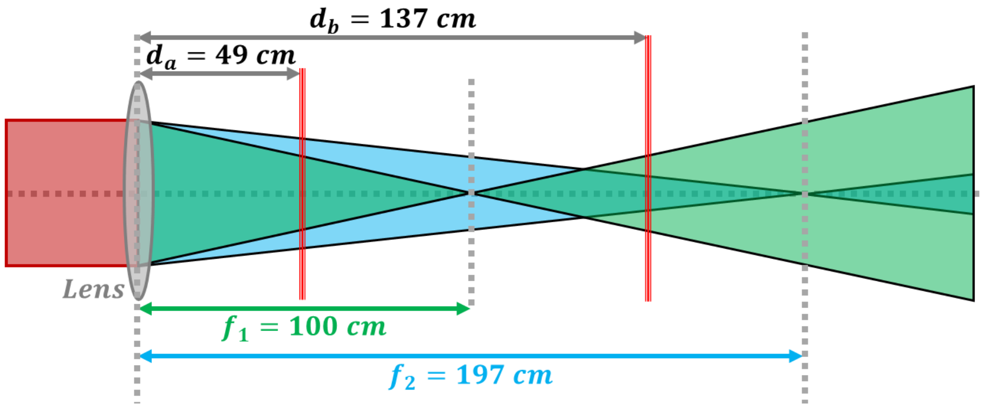

Fig. 11.15. *Representation of the experiment visualizing the focal lengths of the astigmatic lens (f_1 and f_2) and the two analyzed planes shown in red at distances d_a and d_b after the lens.*

Fig. 11.16 shows the spatiospectral characterization for the central wavelength (799.6 nm) for both propagation distances, Figs. 11.16(a1,b1) for d_a and Figs. 11.16(a2,b2) for d_b. Considering the experimental parameters (e.g., spectral bandwidth and NA), there is not any important chromatic effect, so here we only represent the central wavelength and later we will do the spectral analysis of the wavefront curvature. The full spatiospectral intensity and phase profiles for each measurement are depicted in Appendix C.3.

Figs. 11.16(a1,a2) show the spatial intensity distribution for the central wavelength for the measurements at $d_a = 49$ cm and $d_b = 137$ cm, respectively. From here, it can be observed that the beam at d_b is more spatially concentrated than at position d_a, in which the technique scans only part of the beam.

The spatial phase profiles, represented for the central wavelength in Figs. 11.16(b1,b2), have been obtained using the 2DMx strategy for each case. On one hand, in Fig. 11.16(b1) it can be observed that the beam at $d_a = 49$ cm corresponds to a bi-convergent (in two orthogonal axes) wavefront, since the used lens presents two different lens powers in two orthogonal directions and the observation plane is before both focal planes. On the other hand, the beam wavefront at $d_b = 137$ cm, Fig. 11.16(b2), is converging in one plane and diverging in the orthogonal one. This behavior can be corroborated taking into account the position of each measurement plane, since the first distance (d_a) is placed before both focal planes and the second distance (d_b) is place between both focal planes.

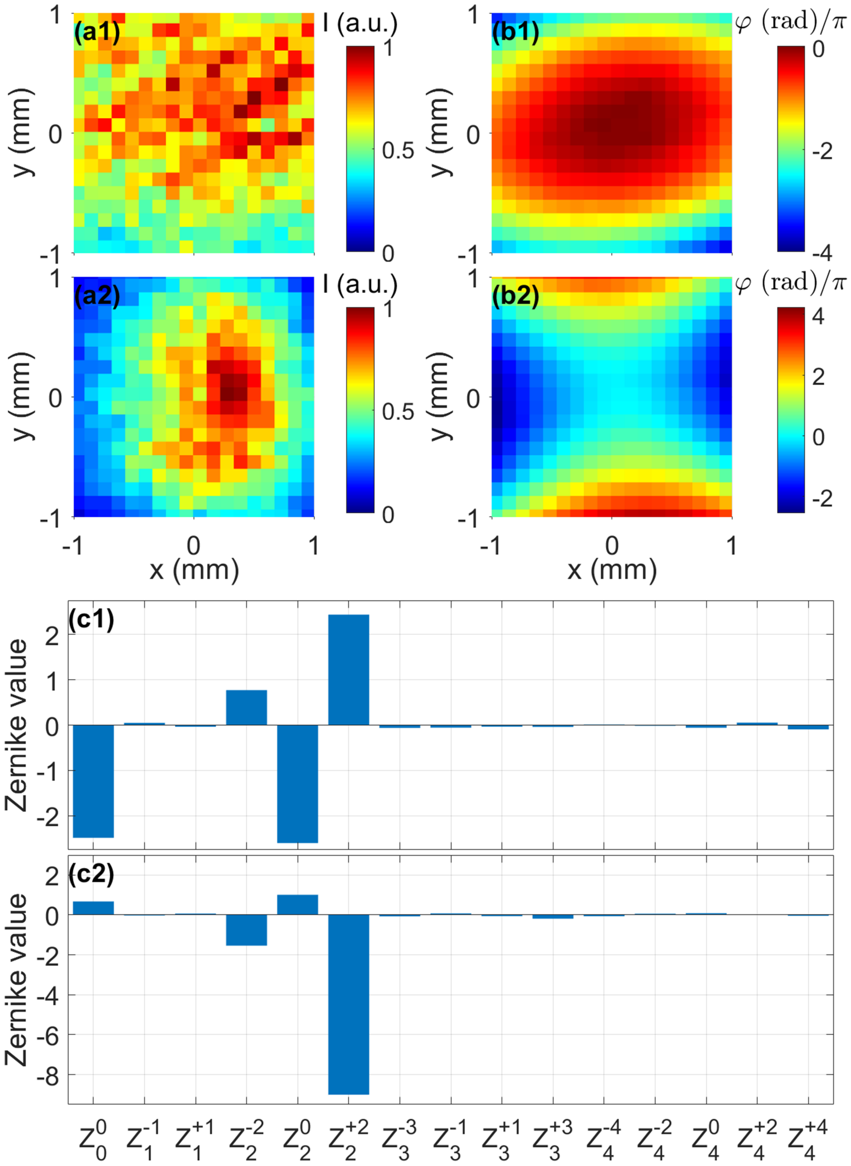

Fig. 11.16. *Spatial intensity (a) and phase (b) profiles and Zernike wavefront decomposition (c) for the central wavelength ($\lambda = 799.6$ nm) of the spatiospectral characterization at two propagation distances after the astigmatic lens: (a1,b1,c1) $d_a = 49$ cm and (a2,b2,c2) $d_b = 137$ cm.*

Moreover, the rotation of the phase distributions from the XY directions at Figs. 11.16(b1,b2) points out a possible rotation of the astigmatic lens.

To further analyze the STCs of the beams, the Zernike decomposition was performed up to $n = 4$ for each case (following the formalism explained in Appendix B), obtaining the contributions shown in Figs. 11.16(c1,c2) for d_a =49 cm and $d_b = 137$ cm, respectively. According to the Zernike analysis, the beams only present STCs up to order $n = 2$, and the main contributions (excluding the piston or offset term) correspond to the defocus (Z_2^0), vertical astigmatism (Z_2^{+2}) and oblique astigmatism (Z_2^{-2}). The presence of both types of astigmatism could be associated to an out of axis propagation, which naturally introduces oblique astigmatism even with spherical lenses, or also due to a small azimuthal rotation of the lens respect to the XY-axes, as suggested by the rotation of the phase distribution at Figs. 11.16(a2,b2) from the XY directions.

The Zernike analysis can be used to find out what kind of STCs the lens introduces but, in order to estimate the real physical values, like the radius of curvature, further analyses are required. For this purpose, we decided to model each wavefront using:

$$\varphi(X,Y) = C_0+2C_1X+2C_2Y+\frac{\pi(X\cos\phi+Y\sin\phi)^2}{\lambda R_1}+\frac{\pi(-X\sin\phi+Y\cos\phi)^2}{\lambda R_2} \tag{11.3}$$

where, R_1 and R_2 represent the two orthogonal radii of curvature of the wavefront and ϕ the azimuthal angle between the R_1 axis and the horizontal axis. Moreover, C_0 corresponds to the wavefront offset, whereas C_1 and C_2 represent the horizontal and vertical tilts respectively.

In order to fit each wavefront using the parameters shown in Eq. **11.3**, we have used a nonlinear optimization algorithm (Levenberg-Marquardt algorithm), that compares the fitted wavefront with the experimental one. Moreover, we have applied it along the bandwidth of the laser source for each measurement plane, obtaining the spectrally resolved radii of curvature distribution shown in Fig. 11.17.

In that figure, the fitted radii of curvature are also compared with the theoretical values taking into account the distance of the measurement plane from the lens and the calibrated focal lengths. Furthermore, the iterative

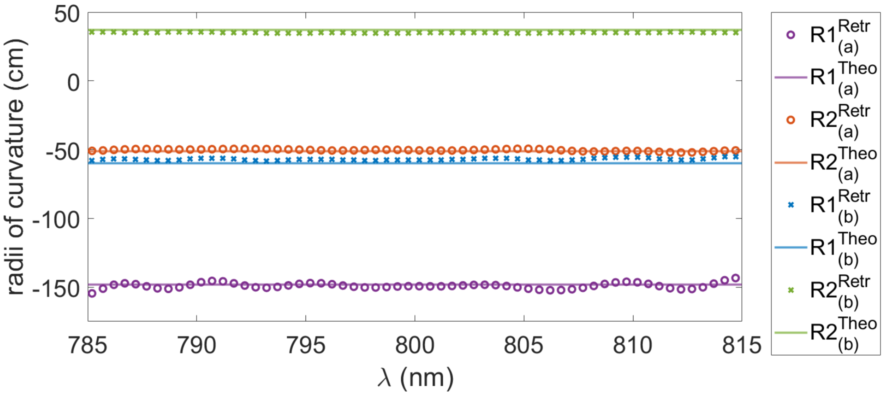

Fig. 11.17. *Spectral analysis of the radii of curvature for the two measurement planes (d_a and d_b referred in the legend as (a) and (b)), modeling the wavefronts using Eq.* **11.3** *(dots) and theoretical value (lines).*

optimization process has been done 10 times per wavelength. The statistical study shows that the standard deviation of all the fitted radii of curvature (for each wavelength) is lower that 0.01 mm and the rms difference of the fitted and experimental wavefronts lower than 10^{-4}.

The spectral mean and deviation of the radii of curvature shown in Fig. 11.17 are summarized in Table 11.1.

	Measurement plane: d_a = 49 cm		**Measurement plane: d_b = 137 cm**	
	Theo. (cm)	**Exp. (cm)**	**Theo. (cm)**	**Exp. (cm)**
R_1	-148	-149 ± 2	-60.0	-57.0 ± 0.8
R_2	-51	-50.4 ± 0.7	37	35.1 ± 0.2

Table 11.1: Summary of the theoretical (Theo.) and the experimental (Exp.) spectral dependences of the radii of curvature obtained by fitting the wavefronts using Eq. **11.3**.

There is a good agreement between the theoretical and the experimental values, with slight deviation for the measurement at d_b. This small deviation can be associated with an error in the determination of the experimental distance of the lens, since it is large and highly curved. Another possibility could be a small tilt or lateral positioning (i.e., being not perfectly centered) of the lens.

From the fit to Eq. **11.3**, it can also be extracted that the astigmatic wavefronts are azimuthally rotated respect to the XY-axes an angle 9.1° and 4.7° for the measurements at d_a and d_b, respectively. The difference in angle could be introduced due to small rotations during the change in lens position from one measurement to the other, or because the lens is not perfectly centered at the same transversal position.

In conclusion, the bulk lateral shearing interferometry technique can characterize convergent and divergent beams, even with more complex dependences. Therefore, the theoretical study of Section 10.2, which explained the possibility to measure these type of beam, provided the characterization is done far from focus, has been here experimentally demonstrated.

Part IV

CONCLUSIONS

Chapter 12

Conclusions and Perspectives

We have studied temporal and spatiotemporal compact ultrashort laser beam characterization techniques, which can analyze pulses of different temporal durations at various spectral regions, being able to operate under less controlled conditions because of their robust configuration. In particular, we have extended the applications of the recently introduced amplitude swing technique and we have developed and applied a new spatiotemporal technique called bulk lateral shearing interferometry. Both techniques rely on uniaxial birefringent crystals to implement bulk interferometers, which can be used in different spectral regions easily and with high stability due to their in-line configurations.

Regarding the temporal characterization, we have analyzed the extension of different capabilities of the amplitude swing technique, and, in addition, we have implemented a Differential Evolution retrieval algorithm to analyze the amplitude swing traces. On one hand, we have experimentally demonstrated that amplitude swing can operate at different spectral regions over more than an octave spectral range from visible to near-infrared without a significant modification of the set-up. This is possible because the amplitude swing only relies on the birefringence of its elements, without any spectral limitation due to, for example, beam splitters, chirped mirrors or grating compressors. In addition, we expect that this operation range can be extended to the entire visible and mid-infrared spectral regions.

On the other hand, we have experimentally proved that amplitude swing can analyze pulses in the few-cycle regime, regardless of whether they are perfectly compressed or moderately chirped. The advance over other techniques is that its less restrictive spectral limitation enables an easy adaptation to ultra-broadband pulses.

Furthermore, we have theoretically studied and experimentally demonstrated different ways of amplitude modulation, thus extending the amplitude swing concept to other configurations. Different implementations have been compared between them, as well as with the original configuration, subjected to different measurement conditions to study their capabilities, showing all of them similar results.

Regarding the spatiotemporal characterization, we have proposed a new technique based on the combination of spectral and spatial interferometry using birefringent uniaxial crystals, as well as a temporal measurement at a single spatial position used as a reference. The bulk implementation of the technique using birefringent media gives it robustness and simplicity. We have presented the concept of the bulk lateral shearing spectral interferometry explaining how the spatiospectral phase information is encoded and different strategies that can be used to extract it.

Moreover, we have studied the operation of the technique using numerical models, taking into account the light propagation theory within uniaxial media in order to study the operability of the system. Using these models, we have analyzed the potential limitations of the technique, due to the aberrations and chromatic effects that could be introduced by the light propagation in the birefringent media, for beams with different numerical apertures and spectral content. The introduced aberrations seem to be negligible except in the near focus region. In the experimental cases studied in this Thesis there is no relevant chromatic limitations affecting the measurements. However, since it could be important in broader spectral bandwidth cases (i.e., few-cycle pulse regime), we have also proposed a strategy to achromatize the spectral response of the technique in case it were necessary.

Furthermore, we have used the bulk lateral shearing interferometer to analyze beams with complex spatiotemporal dependences. On one hand, we have characterized optical vortices in the visible and infrared spectral regions with diverse orbital angular momenta (from -2 to +4), both constant and variable in time, showing very good agreement with the expected results. On the other hand, we have analyzed different propagation planes of astigmatic beams presenting good agreement with the expected evolution.

In sum, amplitude swing and bulk lateral shearing interferometry are compact, robust, and versatile characterization techniques, which can be easily applied in different scenarios due to their in-line and simple configuration, as well as their adaptability.

In the future, we expect that both techniques will ease the temporal and spatiotemporal characterization at different applications (e.g., characterization of materials at different spectral regions, bio-systems or nonlinear optical processes). Possible future works with both techniques may extend their capabilities, for example, improving the acquisition time and proposing single-shot configurations (especially interesting for the PW laser facilities), exploring different spectral ranges or enabling the analysis of vector beams.

12.1 Conclusiones y perspectivas futuras

Hemos estudiado técnicas de caracterización temporales y espaciotemporales compactas para el análisis de haces láser ultracortos, las cuales pueden medir pulsos de diferentes duraciones temporales en varias regiones espectrales, pudiendo incluso operar en condiciones menos controladas debido a su configuración robusta. En particular, hemos ampliado las aplicaciones de la técnica *amplitude swing*, y hemos desarrollado y aplicado una nueva técnica espaciotemporal denominada *bulk lateral shearing interferometry*. Ambas se basan en el uso de cristales birrefringentes uniáxicos para implementar interferómetros compactos, que se pueden usar en diferentes regiones espectrales fácilmente y con alta estabilidad debido a sus configuraciones en línea y en volumen.

Respecto a la caracterización temporal, hemos analizado la extensión de diferentes capacidades de la técnica *amplitude swing* y, además, hemos implementado un algoritmo de reconstrucción de tipo *Differential Evolution* para analizar las trazas. También hemos demostrado experimentalmente que la técnica puede operar en diferentes regiones espectrales, en un rango espectral de más de una octava desde el visible hasta el infrarrojo cercano, sin ninguna modificación significativa de la configuración. Esto es posible porque *amplitude swing* solo se basa en la birrefringencia de sus elementos y, por tanto, no presenta limitaciones espectrales asociadas a, por ejemplo, divisores de haz, *chirped mirrors* o compresores de redes. Además, esperamos que este rango de operación pueda extenderse a todas las regiones espectrales desde el visible hasta el infrarrojo medio.

Asimismo, hemos demostrado experimentalmente que *amplitude swing* puede analizar pulsos láser en el régimen de pocos ciclos, independientemente de si están perfectamente comprimidos o presentan un *chirp* moderado. Esto supone un avance respecto a otras técnicas, puesto que *amplitude swing* puede adaptarse fácilmente al estudio de pulsos con anchos de banda muy grandes debido a su menor limitación espectral.

Además, hemos estudiado tanto teóricamente como experimentalmente la extensión del concepto de *amplitude swing* demostrando diferentes estrategias para modular la amplitud. Las diferentes configuraciones analizadas han sido comparadas entre sí, así como con la configuración original, bajo diferentes condiciones de medida demostrando que todas ellas obtienen resultados similares.

Respecto a la caracterización espaciotemporal, hemos propuesto una nueva técnica basada en la combinación de interferometría espectral y espacial usando cristales uniáxicos, así como la medida de una referencia temporal en un punto espacial. La configuración en volumen, gracias al uso de medios birrefringentes, le confiere una gran robustez y simplicidad. Hemos presentado el concepto de *bulk lateral shearing interferometry* explicando como se codifica la fase y las diferentes estrategias que pueden emplearse para extraerla.

Asimismo, hemos empleado modelos numéricos para considerar la propagación de los haces láser a través de los medios uniáxicos, y así poder estudiar el rango de operatividad de la técnica. Gracias a estos modelos hemos analizado posibles limitaciones asociadas a aberraciones o efectos cromáticos, los cuales pueden introducirse cuando haces de diferentes aperturas numéricas o contenidos espectrales atraviesan medios birrefringentes. A partir de este estudio, hemos comprobado que las distorsiones introducidas en los casos estudiados, en general, son despreciables, excepto si la medida se realiza muy cerca del foco. En los experimentos realizados en la Tesis no se ha observado ningún efecto cromático limitante. A pesar de ello, se ha propuesto una estrategia para acromatizar el sistema en caso de ser necesario, ya que el efecto cromático podría ser significativo para anchuras espectrales mayores (por ejemplo, en el régimen de pocos ciclos).

Hemos usado la técnica *bulk lateral shearing interferometry* para analizar haces láser con complejas dependencias espaciotemporales. Por un lado, se han caracterizado vórtices ópticos en el visible e infrarrojo cercano con diversos momentos angulares orbitales (desde -2 hasta +4) constantes o variables en el tiempo. Los resultados se han comparado con simulaciones teóricas mostrando una gran similitud. Por otro lado, hemos analizado la propagación de haces astigmáticos en diferentes planos de propagación verificando que presentan gran concordancia con la evolución esperada.

En resumen, *amplitude swing* y *bulk lateral shearing interferometry* son técnicas compactas, robustas y versátiles que pueden ser fácilmente empleadas en diferentes condiciones debido a su configuración simple y en línea, así como su gran adaptabilidad.

Esperamos que en un futuro ambas técnicas faciliten la caracterización temporal y espaciotemporal en diferentes aplicaciones (por ejemplo, caracterización de materiales en diferentes rangos espectrales, bio-sistemas o procesos no lineales). Futuras líneas de trabajo con ambas técnicas pueden ampliar sus capacidades, por ejemplo, mejorando el tiempo de adquisición y proponiendo configuraciones mono-tiro (especialmente interesantes para las instalaciones de láser petavatio), explorando diferentes rangos espectrales o permitiendo el análisis de haces vectoriales.

Part V

BIBLIOGRAPHY

Chapter 13

References

[1] T. H. Maiman, “Stimulated Optical Radiation in Ruby,” *Nature*, vol. 187, pp. 493–494, 8 1960.

[2] W. H. Knox, “Ultrafast technology in telecommunications,” *IEEE Journal on Selected Topics in Quantum Electronics*, vol. 6, pp. 1273–1278, 11 2000.

[3] K. Sugioka, “Progress in ultrafast laser processing and future prospects,” *Nanophotonics*, vol. 6, pp. 393–413, 3 2017.

[4] C. L. Hoy, O. Ferhanoglu, M. Yildirim, Ki Hyun Kim, S. S. Karajanagi, K. M. C. Chan, J. B. Kobler, S. M. Zeitels, and A. Ben-Yakar, “Clinical Ultrafast Laser Surgery: Recent Advances and Future Directions,” *IEEE Journal of Selected Topics in Quantum Electronics*, vol. 20, pp. 242–255, 3 2014.

[5] M. Maiuri, M. Garavelli, and G. Cerullo, “Ultrafast Spectroscopy: State of the Art and Open Challenges,” *Journal of the American Chemical Society*, vol. 142, pp. 3–15, 1 2020.

[6] E. Garmire, “Nonlinear optics in daily life,” *Optics Express*, vol. 21, pp. 30532–30544, 12 2013.

[7] A. Pukhov, “Strong field interaction of laser radiation,” *Reports on Progress in Physics*, vol. 66, pp. 47–101, 1 2003.

[8] Y. He, P. Wang, R. T. White, and B. J. Orr, “Spectroscopic Applications of Optical Parametric Oscillators,” *Optics and Photonics News*, vol. 13, pp. 56–60, 5 2002.

[9] U. Keller, “Recent developments in compact ultrafast lasers,” *Nature*, vol. 424, pp. 831–838, 8 2003.

[10] D. Choudhury, J. R. Macdonald, and A. K. Kar, “Ultrafast laser inscription: perspectives on future integrated applications,” *Laser & Photonics Reviews*, vol. 8, pp. 827–846, 11 2014.

[11] M. Malinauskas, A. Žukauskas, S. Hasegawa, Y. Hayasaki, V. Mizeikis, R. Buividas, and S. Juodkazis, “Ultrafast laser processing of materials: from science to industry,” *Light: Science & Applications*, vol. 5, p. e16133, 3 2016.

[12] F. J. McClung and R. W. Hellwarth, “Giant Optical Pulsations from Ruby,” *Journal of Applied Physics*, vol. 33, pp. 828–829, 3 1962.

[13] E. Molva, “Microchip lasers and their applications in optical microsystems,” *Optical Materials*, vol. 11, pp. 289–299, 1 1999.

[14] W. E. Lamb, “Theory of an Optical Maser,” *Physical Review*, vol. 134, pp. A1429–A1450, 6 1964.

[15] A. H. Zewail, “Femtochemistry: Atomic-Scale Dynamics of the Chemical Bond Using Ultrafast Lasers (Nobel Lecture),” *Angewandte Chemie International Edition*, vol. 39, pp. 2586–2631, 8 2000.

[16] V. V. Lozovoy and M. Dantus, “Systematic Control of Nonlinear Optical Processes Using Optimally Shaped Femtosecond Pulses,” *ChemPhysChem*, vol. 6, pp. 1970–2000, 10 2005.

[17] C. Winterfeldt, C. Spielmann, and G. Gerber, “Colloquium : Optimal control of high-harmonic generation,” *Reviews of Modern Physics*, vol. 80, pp. 117–140, 1 2008.

[18] K. Sugioka and Y. Cheng, "Ultrafast lasers—reliable tools for advanced materials processing," *Light: Science & Applications*, vol. 3, p. e149, 4 2014.

[19] D. Strickland and G. Mourou, "Compression of amplified chirped optical pulses," *Optics Communications*, vol. 55, pp. 447–449, 10 1985.

[20] M. C. Asplund, J. A. Johnson, and J. E. Patterson, "The 2018 Nobel Prize in Physics: optical tweezers and chirped pulse amplification," *Analytical and Bioanalytical Chemistry*, vol. 411, pp. 5001–5005, 8 2019.

[21] F. Chen and J. R. V. de Aldana, "Optical waveguides in crystalline dielectric materials produced by femtosecond-laser micromachining," *Laser & Photonics Reviews*, vol. 8, pp. 251–275, 3 2014.

[22] R. R. Gattass and E. Mazur, "Femtosecond laser micromachining in transparent materials," *Nature Photonics*, vol. 2, pp. 219–225, 4 2008.

[23] B. K. McFarland, J. P. Farrell, P. H. Bucksbaum, and M. Gühr, "High Harmonic Generation from Multiple Orbitals in N 2," *Science*, vol. 322, pp. 1232–1235, 11 2008.

[24] E. Goulielmakis and T. Brabec, "High harmonic generation in condensed matter," *Nature Photonics*, vol. 16, pp. 411–421, 6 2022.

[25] M. Nisoli and G. Sansone, "New frontiers in attosecond science," *Progress in Quantum Electronics*, vol. 33, pp. 17–59, 1 2009.

[26] L. Gallmann, C. Cirelli, and U. Keller, "Attosecond Science: Recent Highlights and Future Trends," *Annual Review of Physical Chemistry*, vol. 63, pp. 447–469, 5 2012.

[27] D. Umstadter, "Relativistic laser plasma interactions," *Journal of Physics D: Applied Physics*, vol. 36, pp. R151–R165, 4 2003.

[28] P. K. Kaw, "Nonlinear laser–plasma interactions," *Reviews of Modern Plasma Physics*, vol. 1, p. 2, 12 2017.

[29] E. Esarey, C. B. Schroeder, and W. P. Leemans, “Physics of laser-driven plasma-based electron accelerators,” *Reviews of Modern Physics*, vol. 81, pp. 1229–1285, 8 2009.

[30] H. Daido, M. Nishiuchi, and A. S. Pirozhkov, “Review of laser-driven ion sources and their applications,” *Reports on Progress in Physics*, vol. 75, p. 056401, 5 2012.

[31] B. Alonso, W. Holgado, and I. J. Sola, “Compact in-line temporal measurement of laser pulses with amplitude swing,” *Optics Express*, vol. 28, pp. 15625–15640, 5 2020.

[32] I. A. Walmsley and C. Dorrer, “Characterization of ultrashort electromagnetic pulses,” *Advances in Optics and Photonics*, vol. 1, pp. 308–437, 4 2009.

[33] C. Dorrer, “Spatiotemporal Metrology of Broadband Optical Pulses,” *IEEE Journal of Selected Topics in Quantum Electronics*, vol. 25, p. 3100216, 7 2019.

[34] S. W. Jolly, O. Gobert, and F. Quéré, “Spatio-temporal characterization of ultrashort laser beams: A tutorial,” *Journal of Optics*, vol. 22, p. 103501, 10 2020.

[35] R. Trebino, “Ultrafast Optics Group: Prof. Rick Trebino webpage (www.frog.gatech.edu),” 2023.

[36] S. Akturk, X. Gu, P. Bowlan, and R. Trebino, “Spatio-temporal couplings in ultrashort laser pulses,” *Journal of Optics*, vol. 12, p. 093001, 9 2010.

[37] Y. Shen, Q. Zhan, L. G. Wright, D. N. Christodoulides, F. W. Wise, A. E. Willner, Z. Zhao, K.-h. Zou, C.-T. Liao, C. Hernández-García, M. Murnane, M. A. Porras, A. Chong, C. Wan, K. Y. Bliokh, M. Yessenov, A. F. Abouraddy, L. J. Wong, M. Go, S. Kumar, C. Guo, S. Fan, N. Papasimakis, N. I. Zheludev, L. Chen, W. Zhu, A. Agrawal, S. W. Jolly, C. Dorrer, B. Alonso, I. Lopez-Quintas, M. López-Ripa, I. J. Sola, Y. Fang, Q. Gong, Y. Liu, J. Huang, H. Zhang, Z. Ruan,

M. Mounaix, N. K. Fontaine, J. Carpenter, A. H. Dorrah, F. Capasso, and A. Forbes, “Roadmap on spatiotemporal light fields,” *Journal of Optics (Under Review, available on arXiv)*.

[38] C. Froehly, A. Lacourt, and J. C. Viénot, “Time impulse response and time frequency response of optical pupils.:Experimental confirmations and applications,” *Nouvelle Revue d’Optique*, vol. 4, pp. 183–196, 7 1973.

[39] J. Piasecki, B. Colombeau, M. Vampouille, C. Froehly, and J. A. Arnaud, “Nouvelle méthode de mesure de la réponse impulsionnelle des fibres optiques,” *Applied Optics*, vol. 19, pp. 3749–3755, 11 1980.

[40] Thorlabs-Inc., “Thorlabs webpage (www.thorlabs.com),” 2023.

[41] R. W. Boyd, *Nonlinear Optics, Third Edition.* USA: Academic Press, Inc., 3rd ed., 2008.

[42] P. A. Franken, A. E. Hill, C. W. Peters, and G. Weinreich, “Generation of Optical Harmonics,” *Physical Review Letters*, vol. 7, pp. 118–119, 8 1961.

[43] A. Baltuska, M. Pshenichnikov, and D. Wiersma, “Second-harmonic generation frequency-resolved optical gating in the single-cycle regime,” *IEEE Journal of Quantum Electronics*, vol. 35, pp. 459–478, 4 1999.

[44] G. D. Love, T. J. D. Oag, and A. K. Kirby, “Common path interferometric wavefront sensor for extreme adaptive optics,” *Optics Express*, vol. 13, no. 9, pp. 3491–3499, 2005.

[45] P. Beyersdorf and M. Cordier, “Measurement of thermo-elastic deformation of an optic using a polarization-based shearing interferometer,” *Applied Optics*, vol. 51, pp. 7426–7433, 11 2012.

[46] W. Boucher, S. Velghe, B. Wattellier, and D. Gatinel, “Intraocular lens characterization using a quadric-wave lateral shearing interferometer wave front sensor,” in *Optical Fabrication, Testing, and Metrology III*, p. 71020Q, 9 2008.

[47] F. Roddier, "Curvature sensing and compensation: a new concept in adaptive optics," *Applied Optics*, vol. 27, pp. 1223–1225, 4 1988.

[48] D. R. Neal, J. Copland, and D. A. Neal, "Shack-Hartmann wavefront sensor precision and accuracy," *Advanced Characterization Techniques for Optical, Semiconductor, and Data Storage Components*, vol. 4779, pp. 148–160, 2002.

[49] EdmunOptics, "Edmund optics webpage (www.edmundoptics.com)," 2023.

[50] C. Zhang, B. Zhao, and B. Xiangli, "Wide-field-of-view polarization interference imaging spectrometer," *Applied Optics*, vol. 43, pp. 6090–6094, 11 2004.

[51] H. P. Weber, "Method for Pulsewidth Measurement of Ultrashort Light Pulses Generated by Phase-Locked Lasers using Nonlinear Optics," *Journal of Applied Physics*, vol. 38, pp. 2231–2234, 4 1967.

[52] R. Trebino and D. J. Kane, "Using phase retrieval to measure the intensity and phase of ultrashort pulses: frequency-resolved optical gating," *Journal of the Optical Society of America A*, vol. 10, pp. 1101–1111, 5 1993.

[53] T. Tsang, M. A. Krumbügel, K. W. DeLong, D. N. Fittinghoff, and R. Trebino, "Frequency-resolved optical-gating measurements of ultrashort pulses using surface third-harmonic generation," *Optics Letters*, vol. 21, pp. 1381–1383, 9 1996.

[54] D. Kane and R. Trebino, "Characterization of arbitrary femtosecond pulses using frequency-resolved optical gating," *IEEE Journal of Quantum Electronics*, vol. 29, pp. 571–579, 2 1993.

[55] J. N. Sweetser, D. N. Fittinghoff, and R. Trebino, "Transient-grating frequency-resolved optical gating," *Optics Letters*, vol. 22, pp. 519–521, 4 1997.

[56] P. O'Shea, M. Kimmel, X. Gu, and R. Trebino, "Highly simplified device for ultrashort-pulse measurement," *Optics Letters*, vol. 26, pp. 932–934, 6 2001.

[57] T. Oksenhendler, S. Coudreau, N. Forget, V. Crozatier, S. Grabielle, R. Herzog, O. Gobert, and D. Kaplan, "Self-referenced spectral interferometry," *Applied Physics B*, vol. 99, pp. 7–12, 4 2010.

[58] C. Iaconis and I. A. Walmsley, "Spectral phase interferometry for direct electric-field reconstruction of ultrashort optical pulses," *Optics Letters*, vol. 23, pp. 792–794, 5 1998.

[59] V. V. Lozovoy, I. Pastirk, and M. Dantus, "Multiphoton intrapulse interference IV Ultrashort laser pulse spectral phase characterization and compensation," *Optics Letters*, vol. 29, pp. 775–777, 4 2004.

[60] M. Miranda, C. L. Arnold, T. Fordell, F. Silva, B. Alonso, R. Weigand, A. L'Huillier, and H. Crespo, "Characterization of broadband few-cycle laser pulses with the d-scan technique," *Optics Express*, vol. 20, pp. 18732–18743, 8 2012.

[61] B. Alonso, I. J. Sola, and H. Crespo, "Self-calibrating d-scan: measuring ultrashort laser pulses on-target using an arbitrary pulse compressor," *Scientific Reports*, vol. 8, p. 3264, 2 2018.

[62] V. Loriot, G. Gitzinger, and N. Forget, "Self-referenced characterization of femtosecond laser pulses by chirp scan," *Optics Express*, vol. 21, pp. 24879–24893, 10 2013.

[63] M. Miranda, J. Penedones, C. Guo, A. Harth, M. Louisy, L. Neoričić, A. L'Huillier, and C. L. Arnold, "Fast iterative retrieval algorithm for ultrashort pulse characterization using dispersion scans," *Journal of the Optical Society of America B*, vol. 34, pp. 190–197, 1 2017.

[64] D. Spangenberg, P. Neethling, E. Rohwer, M. H. Brügmann, and T. Feurer, "Time-domain ptychography," *Physical Review A*, vol. 91, p. 021803, 2 2015.

[65] S. B. Park, K. Kim, W. Cho, S. I. Hwang, I. Ivanov, C. H. Nam, and K. T. Kim, “Direct sampling of a light wave in air,” *Optica*, vol. 5, no. 4, pp. 402–408, 2018.

[66] A. Leblanc, P. Lassonde, S. Petit, J.-C. Delagnes, E. Haddad, G. Ernotte, M. R. Bionta, V. Gruson, B. E. Schmidt, H. Ibrahim, E. Cormier, and F. Légaré, “Phase-matching-free pulse retrieval based on transient absorption in solids,” *Optics Express*, vol. 27, pp. 28998–29015, 9 2019.

[67] E. Escoto, R. Jafari, R. Trebino, and G. Steinmeyer, “Retrieving the coherent artifact in frequency-resolved optical gating,” *Optics Letters*, vol. 44, no. 12, pp. 3142–3145, 2019.

[68] M. López-Ripa, B. Alonso, S. Jarabo, F. J. Salgado-Remacha, J. C. Aguado, and I. J. Sola, “Coherent artifact and time-dependent polarization in amplified ultrafast erbium-doped fibre lasers,” *Optics & Laser Technology*, vol. 140, p. 107018, 8 2021.

[69] V. V. Lozovoy, G. Rasskazov, D. Pestov, and M. Dantus, “Quantifying noise in ultrafast laser sources and its effect on nonlinear applications,” *Optics Express*, vol. 23, pp. 12037–12044, 5 2015.

[70] G. Rasskazov, V. V. Lozovoy, and M. Dantus, “Spectral amplitude and phase noise characterization of titanium-sapphire lasers,” *Optics Express*, vol. 23, pp. 23597–23602, 9 2015.

[71] E. Escoto, D. Gerth, B. Hofmann, and G. Steinmeyer, “Strategies for the characterization of partially coherent ultrashort pulses with dispersion scan,” *Journal of the Optical Society of America B*, vol. 36, pp. 2092–2098, 8 2019.

[72] B. Alonso, S. Torres-Peiró, R. Romero, P. T. Guerreiro, A. Almagro-Ruiz, H. Muñoz-Marco, P. Pérez-Millán, and H. Crespo, “Detection and elimination of pulse train instabilities in broadband fibre lasers using dispersion scan,” *Scientific Reports*, vol. 10, p. 7242, 4 2020.

[73] S. Akturk, M. Kimmel, P. O'Shea, and R. Trebino, "Measuring pulse-front tilt in ultrashort pulses using GRENOUILLE," *Optics Express*, vol. 11, pp. 491–501, 3 2003.

[74] S. Akturk, M. Kimmel, P. O'Shea, and R. Trebino, "Measuring spatial chirp in ultrashort pulses using single-shot Frequency-Resolved Optical Gating," *Optics Express*, vol. 11, pp. 68–78, 1 2003.

[75] A. S. Wyatt, I. A. Walmsley, G. Stibenz, and G. Steinmeyer, "Sub-10 fs pulse characterization using spatially encoded arrangement for spectral phase interferometry for direct electric field reconstruction," *Optics Letters*, vol. 31, pp. 1914–1916, 6 2006.

[76] P. Bowlan, P. Gabolde, A. Shreenath, K. McGresham, R. Trebino, and S. Akturk, "Crossed-beam spectral interferometry: a simple, high-spectral-resolution method for completely characterizing complex ultrashort pulses in real time," *Optics Express*, vol. 14, pp. 11892–11900, 11 2006.

[77] B. Alonso, I. J. Sola, O. Varela, J. Hernández-Toro, C. Méndez, J. San Román, A. Zaïr, and L. Roso, "Spatiotemporal amplitude-and-phase reconstruction by Fourier-transform of interference spectra of high-complex-beams," *Journal of the Optical Society of America B*, vol. 27, pp. 933–940, 5 2010.

[78] P. Bowlan, P. Gabolde, and R. Trebino, "Directly measuring the spatio-temporal electric field of focusing ultrashort pulses," *Optics Express*, vol. 15, pp. 10219–10230, 8 2007.

[79] M. Miranda, M. Kotur, P. Rudawski, C. Guo, A. Harth, A. L'Huillier, and C. L. Arnold, "Spatiotemporal characterization of ultrashort laser pulses using spatially resolved Fourier transform spectrometry," *Optics Letters*, vol. 39, pp. 5142–5145, 9 2014.

[80] G. Pariente, V. Gallet, A. Borot, O. Gobert, and F. Quéré, "Space-time characterization of ultra-intense femtosecond laser beams," *Nature Photonics*, vol. 10, pp. 547–553, 8 2016.

[81] A. Borot and F. Quéré, "Spatio-spectral metrology at focus of ultrashort lasers: a phase-retrieval approach," *Optics Express*, vol. 26, pp. 26444–26461, 10 2018.

[82] I. V. Il'ina, T. Y. Cherezova, and A. V. Kudryashov, "Gerchberg—Saxton algorithm: experimental realisation and modification for the problem of formation of multimode laser beams," *Quantum Electronics*, vol. 39, pp. 521–527, 6 2009.

[83] F. Bonaretti, D. Faccio, M. Clerici, J. Biegert, and P. Di Trapani, "Spatiotemporal Amplitude and Phase Retrieval of Bessel-X pulses using a Hartmann-Shack Sensor," *Optics Express*, vol. 17, pp. 9804–9809, 6 2009.

[84] S. L. Cousin, J. M. Bueno, N. Forget, D. R. Austin, and J. Biegert, "Three-dimensional spatiotemporal pulse characterization with an acousto-optic pulse shaper and a Hartmann–Shack wavefront sensor," *Optics Letters*, vol. 37, pp. 3291–3293, 8 2012.

[85] N. Weiße, J. Esslinger, S. Howard, F. M. Foerster, F. Haberstroh, L. Doyle, P. Norreys, J. Schreiber, S. Karsch, and A. Doepp, "Measuring spatio-temporal couplings using modal spatio-spectral wavefront retrieval," *arXiv*.

[86] P. Gabolde and R. Trebino, "Single-shot measurement of the full spatio-temporal field of ultrashort pulses with multi-spectral digital holography," *Optics Express*, vol. 14, pp. 11460–11467, 11 2006.

[87] B. Alonso, W. Holgado, and I. J. Sola, "Ultrashort laser pulse characterization by means of amplitude swing," in *2021 Conference on Lasers and Electro-Optics Europe and European Quantum Electronics Conference*, p. cf_8_1, Optica Publishing Group, 2021.

[88] B. Alonso and I. Sola, "Measurement of Ultrashort Vector Pulses from Polarization Gates by In-Line, Single-Channel Spectral Interferometry," *IEEE Journal of Selected Topics in Quantum Electronics*, vol. 25, p. 8900307, 7 2019.

[89] E. Escoto, A. Tajalli, T. Nagy, and G. Steinmeyer, “Advanced phase retrieval for dispersion scan: a comparative study,” *Journal of the Optical Society of America B*, vol. 35, pp. 8–19, 1 2018.

[90] N. C. Geib, M. Zilk, T. Pertsch, and F. Eilenberger, “Common pulse retrieval algorithm: a fast and universal method to retrieve ultrashort pulses,” *Optica*, vol. 6, pp. 495–505, 4 2019.

[91] I. J. Sola and B. Alonso, “Robustness and capabilities of ultrashort laser pulses characterization with amplitude swing,” *Scientific Reports*, vol. 10, p. 18364, 10 2020.

[92] K. W. DeLong, B. Kohler, K. Wilson, D. N. Fittinghoff, and R. Trebino, “Pulse retrieval in frequency-resolved optical gating based on the method of generalized projections,” *Optics Letters*, vol. 19, pp. 2152–2154, 12 1994.

[93] D. J. Kane, G. Rodriguez, A. J. Taylor, and T. S. Clement, “Simultaneous measurement of two ultrashort laser pulses from a single spectrogram in a single shot,” *Journal of the Optical Society of America B*, vol. 14, pp. 935–943, 4 1997.

[94] M. Miranda, T. Fordell, C. Arnold, A. L’Huillier, and H. Crespo, “Simultaneous compression and characterization of ultrashort laser pulses using chirped mirrors and glass wedges,” *Optics Express*, vol. 20, pp. 688–697, 1 2012.

[95] E. Escoto, A. Tajalli, T. Nagy, and G. Steinmeyer, “Advanced phase retrieval for dispersion scan: a comparative study,” *Journal of the Optical Society of America B*, vol. 35, pp. 8–19, 1 2018.

[96] P. Rocca, G. Oliveri, and A. Massa, “Differential evolution as applied to electromagnetics,” *IEEE Antennas and Propagation Magazine*, vol. 53, pp. 38–49, 1 2011.

[97] P. Sidorenko, O. Lahav, Z. Avnat, and O. Cohen, “Ptychographic reconstruction algorithm for frequency-resolved optical gating: super-

resolution and supreme robustness," *Optica*, vol. 3, pp. 1320–1330, 12 2016.

[98] T. Zahavy, A. Dikopoltsev, D. Moss, G. I. Haham, O. Cohen, S. Mannor, and M. Segev, "Deep learning reconstruction of ultrashort pulses," *Optica*, vol. 5, pp. 666–673, 5 2018.

[99] S. Kleinert, A. Tajalli, T. Nagy, and U. Morgner, "Rapid phase retrieval of ultrashort pulses from dispersion scan traces using deep neural networks," *Optics Letters*, vol. 44, pp. 979–982, 2 2019.

[100] R. Storn and K. Price, "Differential Evolution - A Simple and Efficient Heuristic for Global Optimization over Continuous Spaces," *Journal of Global Optimization*, vol. 11, pp. 341–359, 4 1997.

[101] M. F. Ahmad, N. A. M. Isa, W. H. Lim, and K. M. Ang, "Differential evolution: A recent review based on state-of-the-art works," *Alexandria Engineering Journal*, vol. 61, pp. 3831–3872, 5 2022.

[102] G. Cerullo and S. De Silvestri, "Ultrafast optical parametric amplifiers," *Review of Scientific Instruments*, vol. 74, pp. 1–18, 1 2003.

[103] D. Reid, J. Sun, T. Lamour, and T. Ferreiro, "Advances in ultrafast optical parametric oscillators," *Laser Physics Letters*, vol. 8, pp. 8–15, 1 2011.

[104] M. López-Ripa, I. J. Sola, and B. Alonso, "Amplitude swing ultrashort pulse characterization across visible to near-infrared," *Optics & Laser Technology*, vol. 164, p. 109492, 9 2023.

[105] S. Byrnes, "Frequency-resolved optical gating (FROG) (https://www.mathworks.com/matlabcentral/fileexchange/34986-frequency-resolved-optical-gating-frog)," 2020.

[106] R. Trebino, *Frequency-Resolved Optical Gating: The Measurement of Ultrashort Laser Pulses.* Boston, MA: Springer US, 2000.

[107] M. J. Shapiro, C. C. Chow, P. A. Karth, D. F. Kiernan, and M. P. Blair, "Effects of Green Diode Laser in the Treatment of Pediatric Coats

Disease," *American Journal of Ophthalmology*, vol. 151, pp. 725–731, 4 2011.

[108] H. M. Oubei, J. R. Duran, B. Janjua, H.-Y. Wang, C.-T. Tsai, Y.-C. Chi, T. K. Ng, H.-C. Kuo, J.-H. He, M.-S. Alouini, G.-R. Lin, and B. S. Ooi, "4.8 Gbit/s 16-QAM-OFDM transmission based on compact 450-nm laser for underwater wireless optical communication," *Optics Express*, vol. 23, pp. 23302–23309, 9 2015.

[109] D. A. Zayarny, A. A. Ionin, S. I. Kudryashov, S. V. Makarov, A. A. Kuchmizhak, O. B. Vitrik, and Y. N. Kulchin, "Pulse-width-dependent surface ablation of copper and silver by ultrashort laser pulses," *Laser Physics Letters*, vol. 13, p. 076101, 6 2016.

[110] J. Sun, J. P. Longtin, and P. M. Norris, "Ultrafast laser micromachining of silica aerogels," *Journal of Non-Crystalline Solids*, vol. 281, pp. 39–47, 3 2001.

[111] Y. Shao, W. Qin, H. Liu, J. Qu, X. Peng, H. Niu, and B. Z. Gao, "Ultrafast, large-field multiphoton microscopy based on an acousto-optic deflector and a spatial light modulator," *Optics Letters*, vol. 37, pp. 2532–2534, 7 2012.

[112] C. Spielmann, E. Seres, and J. Seres, "Extreme ultraviolet light source based on intracavity high harmonic generation in a mode locked Ti:sapphire oscillator with 9.4 MHz repetition rate," *Optics Express*, vol. 20, pp. 6185–6190, 3 2012.

[113] M. N. Zervas, M. Durkin, F. Ghiringhelli, K. Vysniauskas, L. Hickey, A. Gillooly, P. Turner, and B. Kao, "High peak power, high rep-rate pulsed fiber laser for marking applications," in *Fiber Lasers III: Technology, Systems, and Applications*, vol. 6102, p. 61020Q, SPIE, 2 2006.

[114] G. H. Kim, J. Yang, B. Lee, J. W. Kim, D. C. Heo, S. A. Chizhov, E. G. Sall', and V. E. Yashin, "High-power repetitively pulsed ytterbium lasers with supershort pulse width and direct diode pumping for technological and biomedical applications," *Journal of Optical Technology*, vol. 85, pp. 679–686, 11 2018.

[115] T. Dennis, E. A. Curtis, C. W. Oates, L. Hollberg, and S. L. Gilbert, “Wavelength references for 1300-nm wavelength-division multiplexing,” *Journal of Lightwave Technology*, vol. 20, pp. 804–810, 5 2002.

[116] Y. W. Song, S. Y. Set, S. Yamashita, C. S. Goh, and T. Kotake, “1300-nm pulsed fiber lasers mode-locked by purified carbon nanotubes,” *IEEE Photonics Technology Letters*, vol. 17, pp. 1623–1625, 8 2005.

[117] E. Poem, A. Golenchenko, O. Davidson, O. Arenfrid, R. Finkelstein, and O. Firstenberg, “Pulsed-pump phosphorus-doped fiber Raman amplifier around 1260 nm for applications in quantum non-linear optics,” *Optics Express*, vol. 28, pp. 32738–32749, 10 2020.

[118] N. Nishizawa, Y. Chen, P. Hsiung, E. P. Ippen, and J. G. Fujimoto, “Real-time, ultrahigh-resolution, optical coherence tomography with an all-fiber, femtosecond fiber laser continuum at 15 µm,” *Optics Letters*, vol. 29, pp. 2846–2848, 12 2004.

[119] T. Tamaki, W. Watanabe, and K. Itoh, “Laser micro-welding of transparent materials by a localized heat accumulation effect using a femtosecond fiber laser at 1558 nm,” *Optics Express*, vol. 14, pp. 10460–10468, 10 2006.

[120] L. Myers, “Review of quasi-phasematching and periodically poled lithium niobate,” in *Proceedings of the IEEE 1996 National Aerospace and Electronics Conference NAECON 1996*, vol. 2, pp. 733–739, IEEE, 1996.

[121] B. Davis, T. Saule, and C. A. Trallero-Herrero, “Random quasi-phase-matching for pulse characterization from the near to the long wavelength infrared,” *Optics Express*, vol. 30, pp. 44283–44289, 11 2022.

[122] O. Pérez-Benito and R. Weigand, “Nano dispersion scan: measurement of sub-7-fs laser pulses using second-harmonic nanoparticles,” *Optics Letters*, vol. 44, pp. 4921–4924, 10 2019.

[123] J. J. Carrera, X. M. Tong, and S.-I. Chu, "Creation and control of a single coherent attosecond xuv pulse by few-cycle intense laser pulses," *Physical Review A*, vol. 74, p. 023404, 2 2006.

[124] A. V. Mitrofanov, A. J. Verhoef, E. E. Serebryannikov, J. Lumeau, L. Glebov, A. M. Zheltikov, and A. Baltuška, "Optical Detection of Attosecond Ionization Induced by a Few-Cycle Laser Field in a Transparent Dielectric Material," *Physical Review Letters*, vol. 106, p. 147401, 4 2011.

[125] G. Ma, W. Dallari, A. Borot, F. Krausz, W. Yu, G. D. Tsakiris, and L. Veisz, "Intense isolated attosecond pulse generation from relativistic laser plasmas using few-cycle laser pulses," *Physics of Plasmas*, vol. 22, p. 033105, 3 2015.

[126] C. Hernández-García, W. Holgado, L. Plaja, B. Alonso, F. Silva, M. Miranda, H. Crespo, and I. J. Sola, "Carrier-envelope-phase insensitivity in high-order harmonic generation driven by few-cycle laser pulses," *Optics Express*, vol. 23, pp. 21497–21508, 8 2015.

[127] P. Rácz, S. E. Irvine, M. Lenner, A. Mitrofanov, A. Baltuška, A. Y. Elezzabi, and P. Dombi, "Strong-field plasmonic electron acceleration with few-cycle, phase-stabilized laser pulses," *Applied Physics Letters*, vol. 98, p. 111116, 3 2011.

[128] J. McKenna, F. Anis, A. M. Sayler, B. Gaire, N. G. Johnson, E. Parke, K. D. Carnes, B. D. Esry, and I. Ben-Itzhak, "Controlling strong-field fragmentation of H2+ by temporal effects with few-cycle laser pulses," *Physical Review A*, vol. 85, p. 023405, 2 2012.

[129] T. Brabec and F. Krausz, "Intense few-cycle laser fields: Frontiers of nonlinear optics," *Reviews of Modern Physics*, vol. 72, pp. 545–591, 4 2000.

[130] M. Zavelani-Rossi, D. Polli, G. Cerullo, S. De Silvestri, L. Gallmann, G. Steinmeyer, and U. Keller, "Few-optical-cycle laser pulses by OPA: broadband chirped mirror compression and SPIDER characterization," *Applied Physics B*, vol. 74, pp. s245–s251, 6 2002.

[131] A. Baltuška, M. S. Pshenichnikov, and D. A. Wiersma, "Amplitude and phase characterization of 4.5-fs pulses by frequency-resolved optical gating," *Optics Letters*, vol. 23, pp. 1474–1476, 9 1998.

[132] A. Trabattoni, T. Oksenhendler, H. Jousselin, G. Tempea, S. De Silvestri, G. Sansone, F. Calegari, and M. Nisoli, "Self-referenced spectral interferometry for single-shot measurement of sub-5-fs pulses," *Review of Scientific Instruments*, vol. 86, p. 113106, 11 2015.

[133] F. J. Salgado-Remacha, B. Alonso, H. Crespo, C. Cojocaru, J. Trull, R. Romero, M. Lopez, P. Guerreiro, F. Silva, M. Miranda, A. L'Huillier, C. Arnold, and I. Sola, "Single-shot d-scan technique for ultrashort laser pulse characterization using transverse second-harmonic generation in random nonlinear crystals," *Optics Letters*, vol. 45, pp. 3925–3928, 6 2020.

[134] F. Silva, B. Alonso, W. Holgado, R. Romero, J. S. Román, E. C. Jarque, H. Koop, V. Pervak, H. Crespo, and I. J. Sola, "Strategies for achieving intense single-cycle pulses with in-line post-compression setups," *Optics Letters*, vol. 43, pp. 337–340, 1 2018.

[135] G. Tamošauskas, G. Beresnevičius, D. Gadonas, and A. Dubietis, "Transmittance and phase matching of BBO crystal in the 3-5 μm range and its application for the characterization of mid-infrared laser pulses," *Optical Materials Express*, vol. 8, pp. 1410–1418, 6 2018.

[136] M. López-Ripa, I. J. Sola, and B. Alonso, "Bulk lateral shearing interferometry for spatiotemporal study of time-varying ultrashort optical vortices," *Photonics Research*, vol. 10, pp. 922–931, 4 2022.

[137] C. Dorrer and I. A. Walmsley, "Simple linear technique for the measurement of space–time coupling in ultrashort optical pulses," *Optics Letters*, vol. 27, pp. 1947–1949, 11 2002.

[138] F. E. Veiras, L. I. Perez, and M. T. Garea, "Phase shift formulas in uniaxial media: An application to waveplates," *Applied Optics*, vol. 49, pp. 2769–2777, 5 2010.

[139] M. C. Simon and K. V. Gottschalk, “Waves and rays in uniaxial birefringent crystals,” *Optik*, vol. 118, pp. 457–470, 10 2007.

[140] V. V. Fisanov, “Vector Formulations of the Laws of Reflection and Refraction of Forward and Backward Waves,” *Russian Physics Journal*, vol. 58, pp. 1074–1079, 12 2015.

[141] G. Ghosh, “Dispersion-equation coefficients for the refractive index and birefringence of calcite and quartz crystals,” *Optics Communications*, vol. 163, pp. 95–102, 5 1999.

[142] T. Mu, C. Zhang, Q. Li, L. Zhang, Y. Wei, and Q. Chen, “Achromatic Savart polariscope: choice of materials,” *Optics Express*, vol. 22, pp. 5043–5051, 3 2014.

[143] N. Quan, C. Zhang, and T. Mu, “Modified Savart polariscope with wide field of view and achromatic lateral displacement,” *Optics Communications*, vol. 382, pp. 392–398, 1 2017.

[144] A. E. Siegman, *Lasers.* University Science Books, Sausalito, CA: University Science Books, 1986.

[145] George B. Arfken, Hans J. Weber, and Frank E. Harris, *Mathematical Methods for Physicists.* Elsevier, 7th ed., 2012.

[146] D. C. O. Shea, *Elements of Modern Optical Design.* Wiley series in pure and applied optics, Chichester, England: Wiley-Blackwell, 1985.

[147] L. Wang, Z. Xiong, D. Gao, G. Shi, and F. Wu, “Dual-camera design for coded aperture snapshot spectral imaging,” *Applied Optics*, vol. 54, pp. 848–858, 2 2015.

[148] H. Tang, T. Men, X. Liu, Y. Hu, J. Su, Y. Zuo, P. Li, J. Liang, M. C. Downer, and Z. Li, “Single-shot compressed optical field topography,” *Light: Science & Applications*, vol. 11, p. 244, 8 2022.

[149] S. Howard, J. Esslinger, R. H. W. Wang, P. Norreys, and A. Döpp, “Hyperspectral Compressive Wavefront Sensing,” *High Power Laser Science and Engineering*, p. 1–8, 2023.

[150] Y. Shen, X. Wang, Z. Xie, C. Min, X. Fu, Q. Liu, M. Gong, and X. Yuan, "Optical vortices 30 years on: OAM manipulation from topological charge to multiple singularities," *Light: Science & Applications*, vol. 8, p. 90, 12 2019.

[151] R. Grunwald, T. Elsaesser, and M. Bock, "Spatio-temporal coherence mapping of few-cycle vortex pulses," *Scientific Reports*, vol. 4, p. 7148, 11 2014.

[152] L. Ma, P. Zhang, Z. Li, C. Liu, X. Li, Y. Zhang, R. Zhang, and C. Cheng, "Spatiotemporal evolutions of ultrashort vortex pulses generated by spiral multi-pinhole plate," *Optics Express*, vol. 25, pp. 29864–29873, 11 2017.

[153] M. Miranda, M. Kotur, P. Rudawski, C. Guo, A. Harth, A. L'Huillier, and C. L. Arnold, "Spatiotemporal characterization of ultrashort optical vortex pulses," *Journal of Modern Optics*, vol. 64, pp. S1–S6, 12 2017.

[154] I. Lopez-Quintas, W. Holgado, R. Drevinskas, P. G. Kazansky, I. J. Sola, and B. Alonso, "Optical vortex production mediated by azimuthal index of radial polarization," *Journal of Optics*, vol. 22, p. 095402, 9 2020.

[155] M. Beresna, M. Gecevičius, and P. G. Kazansky, "Polarization sensitive elements fabricated by femtosecond laser nanostructuring of glass [Invited]," *Optical Materials Express*, vol. 1, pp. 783–795, 8 2011.

[156] C. Hernández-García, A. Picón, J. San Román, and L. Plaja, "Attosecond extreme ultraviolet vortices from high-order harmonic generation," *Physical Review Letters*, vol. 111, p. 083602, 8 2013.

[157] V. Lakshminarayanan and A. Fleck, "Zernike polynomials: a guide," *Journal of Modern Optics*, vol. 58, p. 1678, 10 2011.

Part VI

APPENDICES

Appendix A

Noise study for generalizing amplitude swing

In Chapter 7, different configurations of the amplitude swing technique have been studied. In particular, in Section 7.2, it was simulated the effect of noise to the retrievals and it was presented an example of the complete study for a noise level of 4.3% rms. Here it is depicted the complete evolution of the example pulse with the noise. We present a link to Drive in order to ease the visualization of the video, but it is also available in the institutional repository of the Universidad de Salamanca, Gestión del Repositorio Documental de la Universidad de Salamanca (GREDOS).

Noise analysis video

- **Contextualization:** the current study analyzes the effect of noise in the range from 0% to ∼15% added to the ideal traces of four different amplitude swing configurations (rotating MWP, HWP, QWP and ZWP). The simulated pulse presents Gaussian spectrum centered at $\lambda = 800$ nm with 50-fs FTL duration FWHM and a spectral phase that combines GDD=1000 fs^2, TOD=2000 fs^3 and an oscillatory term $(0.3\pi \cdot \cos[50(\omega - \omega_0) + 0.25\pi])$.

- **Thumbnail:**

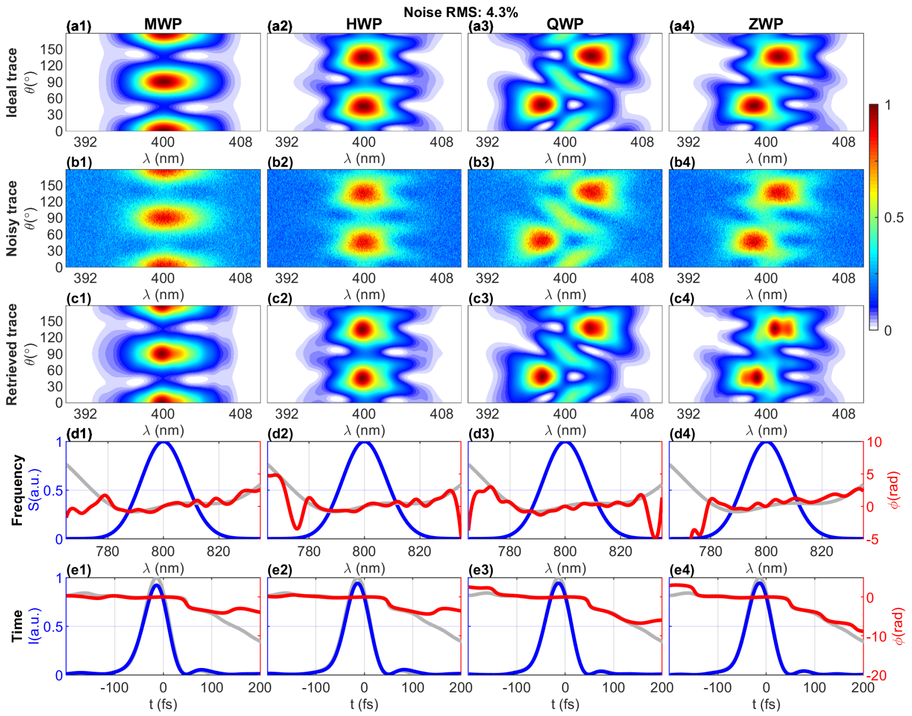

- **Caption:** Comparison of amplitude swing configurations analyzing traces with different levels of numerical white Gaussian noise added. (a) Ideal, (b) noisy and (c) retrieved amplitude swing traces. (d) Spectral and (e) temporal comparison of the retrieved (blue and red) and theoretical (gray) pulses. The configurations studied are: (column 1) rotating MWP, (column 2) rotating HWP, (column 3) rotating QWP, and (column 4) rotating ZWP with $\Phi_r = 0.75\pi$ rad.

- **External link:** `VideoThesis_GeneralizingAswing_Noise.avi` [1]

---

[1] `https://drive.google.com/file/d/1tOZlPKeZyIZvIYdSTMZtaifZYOKIytBX/view?usp=sharing`

Appendix B

Zernike Polynomials

Zernike polynomials is a mathematical polynomial series widely used in different fields like optometry, astronomy or photonics to evaluate distortions in the optical wavefronts [157].

These polynomials are associated with two indices called azimuthal degree (m) and radial degree (n), being the Zernike polynomial of order (n, m) defined as:

$$Z_n^m = \begin{cases} R_n^{|m|} \cdot \sin(m\Phi) & \text{for } m < 0 \\ R_n^{|m|} \cdot \cos(m\Phi) & \text{for } m \geq 0 \end{cases} \tag{B.1}$$

where Φ is the azimuthal angle dimension, n is an integer with $n \geq 0$ and m is an integer in the range $m \in [-n, n]$ defined in steps of 2. R_n^m is the radial polynomial calculated as:

$$R_n^m(\rho) = \sum_{k=0}^{\frac{n-m}{2}} \frac{(-1)^k (n-k)!}{k! \left(\frac{n+m}{2} - k\right)! \left(\frac{n-m}{2} - k\right)!} \rho^{n-2k} \tag{B.2}$$

being ρ the radial dimension.

The components of the Zernike basis are orthogonal over the unit disk, so they satisfy the following relation:

$$\iint\limits_{\text{circle}} Z_n^m(r, \Phi) Z_{n'}^{m'}(r, \Phi) r \mathrm{d}r \mathrm{d}\Phi = \frac{1}{2n+1} \delta_{n,n'} \delta_{m,m'} \tag{B.3}$$

Usually a characterization up to $n = 4$ gives enough information of the principal wavefront distortions. The expressions of each Zernike polynomial and the classical names used to designate them are depicted in Table B.1. In addition, Fig. B.1 qualitatively represents each Zernike polynomial of the series up to $n = 4$.

Z_n^m	**Math. expression**	**Classical name**
Z_0^0	1	Piston or offset
Z_1^{-1}	$\rho \sin \Phi$	Y-Tilt
Z_1^{+1}	$\rho \cos \Phi$	X-Tilt
Z_2^{-2}	$\rho^2 \sin(2\Phi)$	Oblique astigmatism
Z_2^0	$2\rho^2 - 1$	Defocus
Z_2^{+2}	$\rho^2 \cos(2\Phi)$	Vertical astigmatism
Z_3^{-3}	$\rho^3 \sin(3\Phi)$	Vertical trefoil
Z_3^{-1}	$(3\rho^3 - 2\rho) \sin \Phi$	Vertical coma
Z_3^{+1}	$(3\rho^3 - 2\rho) \cos \Phi$	Horizontal coma
Z_3^{+3}	$\rho^3 \cos(3\Phi)$	Oblique trefoil
Z_4^{-4}	$\rho^4 \sin(4\Phi)$	Oblique quadrafoil
Z_4^{-2}	$(4\rho^4 - 3\rho^2) \sin(2\Phi)$	Oblique secondary astigmatism
Z_4^0	$(6\rho^4 - 6\rho^2 + 1)$	Primary spherical
Z_4^{+2}	$(4\rho^4 - 3\rho^2) \cos(2\Phi)$	Vertical secondary astigmatism
Z_4^{+4}	$\rho^4 \cos(4\Phi)$	Vertical quadrafoil

Table B.1: Mathematical expressions and classical names of Zernike polynomials up to $n = 4$.

A general wavefront over the unit circle pupil ($\varphi(\rho, \Phi)$) can be decomposed in the Zernike polynomials basis, and the coefficient (a_n^m) of each polynomial (Z_n^m) will give information of the presence and relevance of aberrations.

$$\varphi(\rho, \Phi) = \sum_{n,m} a_n^m Z_n^m(r, \Phi) \qquad \textbf{(B.4)}$$

Notice that the Zernike polynomial basis only is orthogonal over the unit circle, Eq. **B.3**, so to do the wavefront decomposition above mentioned it is necessary to normalize the spatial dimensions.

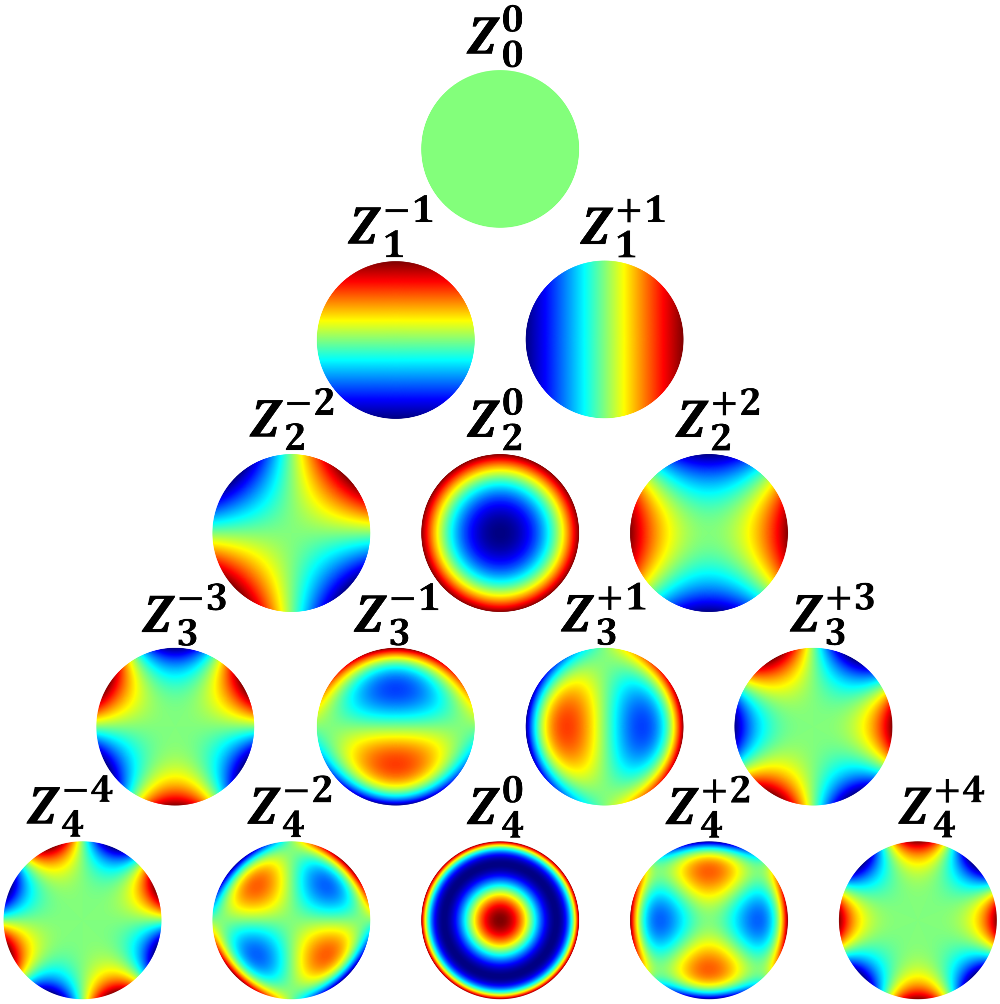

Fig. B.1. *Representation of the Zernike polynomials (*Z_n^m*) up to n=4.*

Appendix C

Spatiotemporal and spatiospectral complete retrievals

The spatiotemporal characterization technique proposed in this Thesis is able to retrieve the temporally and spectrally resolved wavefronts. In each corresponding application of Chapter 11, we have presented either the retrievals for a specific wavelength of the spatiospectral characterization or some temporal snapshots of the spatiotemporal characterization. In this Appendix, the links to the videos of the complete characterization obtained with the bulk lateral shearing interferometer are collected. Here, we present links to Drive in order to ease the visualization of the videos, but they are also available in the institutional repository GREDOS.

C.1 Optical vortices

Here we present the spatiospectral intensity (a) and phase (b) profiles obtained for the full spatiospectral characterization of optical vortices shown in Section 11.1.

C.1.1 Proof of concept video

- **Contextualization:** spatiospectral characterization of a known optical vortex of $\ell = +2$ using two configurations with different walk-off crystals, 1.12-mm-thick BBO cut with $\theta_{OA} = 29.2°$ and 1.06-mm-thick calcite cut with $\theta_{OA} = 45°$.

- **Thumbnail:**

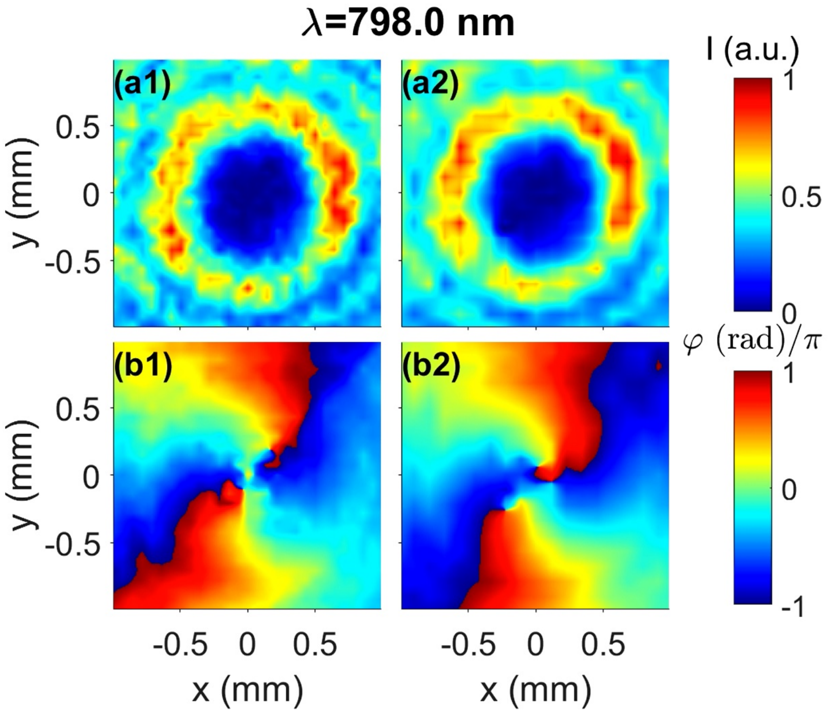

- **Caption:** Intensity (a) and phase (b) profiles of the spatiospectral characterization. (a1,b1) and (a2,b2) corresponds to the spatiospectral retrievals obtained with the calcite and BBO walk-off crystals, respectively.

- **External link:** `VideoThesis_Vortices_ProofOfConcept.avi` [1]

---

[1] `https://drive.google.com/file/d/19FwLrLxVrCqbLtvslfDcKVKjynUNjcMA/view?usp=sharing`

C.1.2 Near-infrared vortex video: $\ell = -1$

- **Contextualization:** spatiospectral characterization of an optical vortex of $\ell = -1$ in the near-infrared spectral range characterized using a 1.06-mm-thick calcite cut with $\theta_{OA} = 45°$.
- **Thumbnail:**

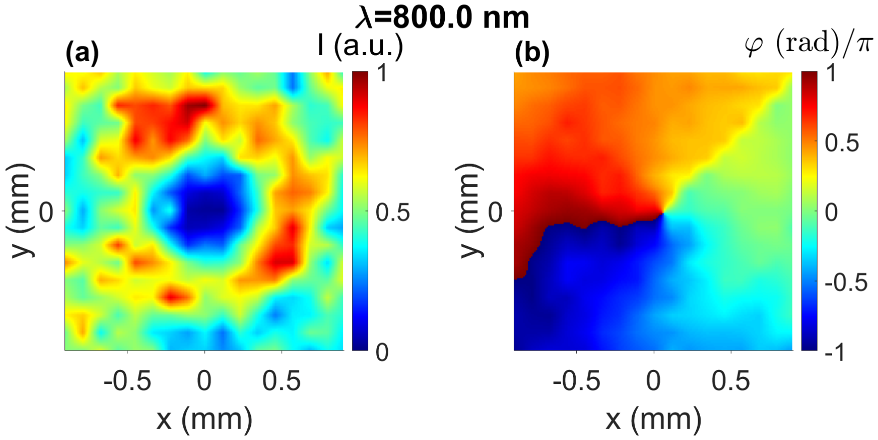

- **Caption:** Spatiospectral intensity (a) and phase (b) profiles evolution.
- **External link:** `VideoThesis_Vortex_NIR_Lneg1.avi` [2]

---

[2] `https://drive.google.com/file/d/1r1ehJe2nlje1rUBA0tGjqQeyRAqS--Af/view?usp=share_link`

C.1.3 Near-infrared vortex video: $\ell = +1$

- **Contextualization:** spatiospectral characterization of an optical vortex of $\ell = +1$ in the near-infrared spectral range characterized using a 1.06-mm-thick calcite cut with $\theta_{OA} = 45°$.

- **Thumbnail:**

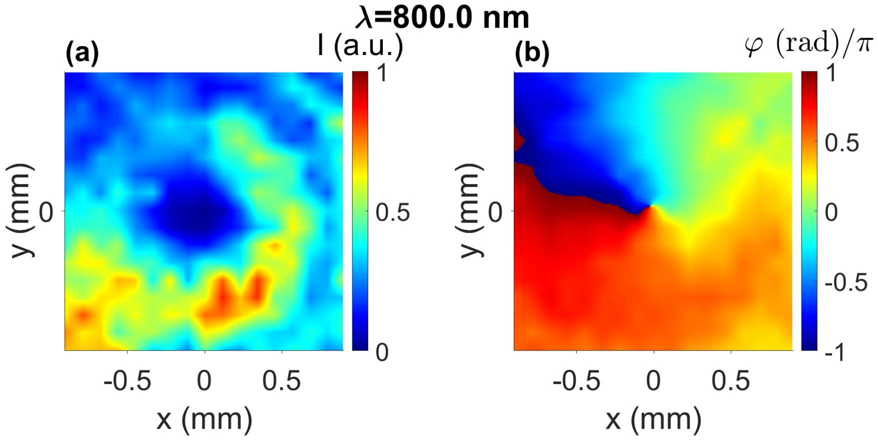

- **Caption:** Spatiospectral intensity (a) and phase (b) profiles evolution.

- **External link:** `VideoThesis_Vortex_NIR_L1.avi` [3]

---

[3] `https://drive.google.com/file/d/1F3136doAxMoX_yPBOeanup3UYee9qzAN/view?usp=share_link`

C.1.4 Near-infrared vortex video: $\ell = +3$

- **Contextualization:** spatiospectral characterization of an optical vortex of $\ell = +3$ in the near-infrared spectral range characterized using a 1.06-mm-thick calcite cut with $\theta_{OA} = 45°$.

- **Thumbnail:**

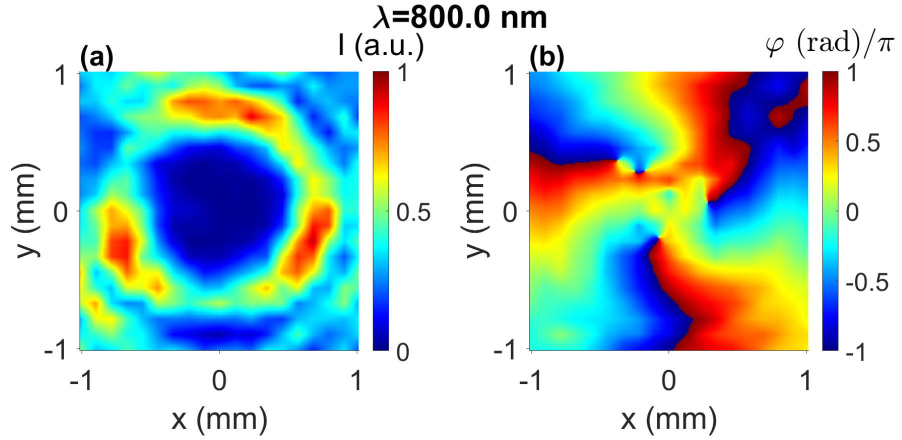

- **Caption:** Spatiospectral intensity (a) and phase (b) profiles evolution.

- **External link:** `VideoThesis_Vortex_NIR_L3.avi` [4]

---

[4] `https://drive.google.com/file/d/1ZLG57pQPRR9ugPmoTf_A0OGM7y2SIpF6/view?usp=share_link`

C.1.5 Visible vortex video: $\ell = -2$

- **Contextualization:** spatiospectral characterization of an optical vortex of $\ell = -2$ in the visible spectral range characterized using a 1.06-mm-thick calcite cut with $\theta_{OA} = 45°$.

- **Thumbnail:**

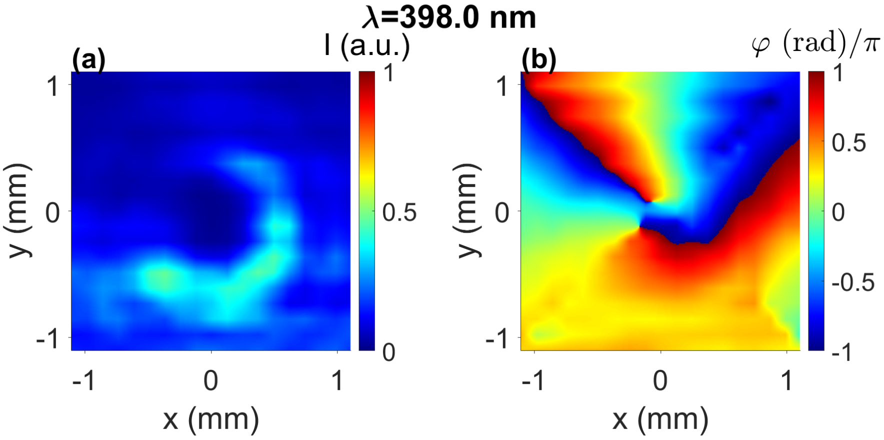

- **Caption:** Spatiospectral intensity (a) and phase (b) profiles evolution.

- **External link:** `VideoThesis_Vortex_VIS_Lneg2.avi` [5]

---

[5] `https://drive.google.com/file/d/1eQIQRwuxv-DG1cI7pNha4UHEZo62-3dN/view?usp=share_link`

C.1.6 Visible vortex video: $\ell = +2$

- **Contextualization:** spatiospectral characterization of an optical vortex of $\ell = +2$ in the visible spectral range characterized using a 1.06-mm-thick calcite cut with $\theta_{OA} = 45°$.

- **Thumbnail:**

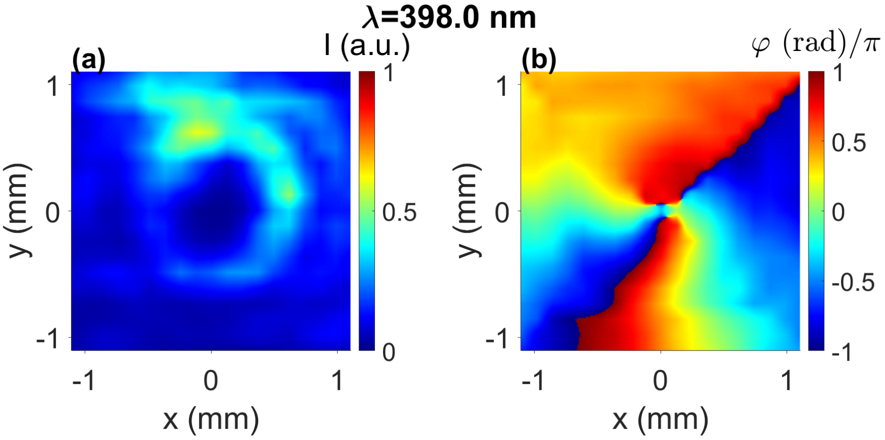

- **Caption:** Spatiospectral intensity (a) and phase (b) profiles evolution.

- **External link:** `VideoThesis_Vortex_VIS_L2.avi` [6]

---

[6] `https://drive.google.com/file/d/1PQx5CRm0crsGXb-b4xfo4UcxkwJy1w8c/view?usp=share_link`

C.1.7 Visible vortex video: $\ell = +4$

- **Contextualization:** spatiospectral characterization of an optical vortex of $\ell = +4$ in the visible spectral range characterized using a 1.06-mm-thick calcite cut with $\theta_{OA} = 45°$.

- **Thumbnail:**

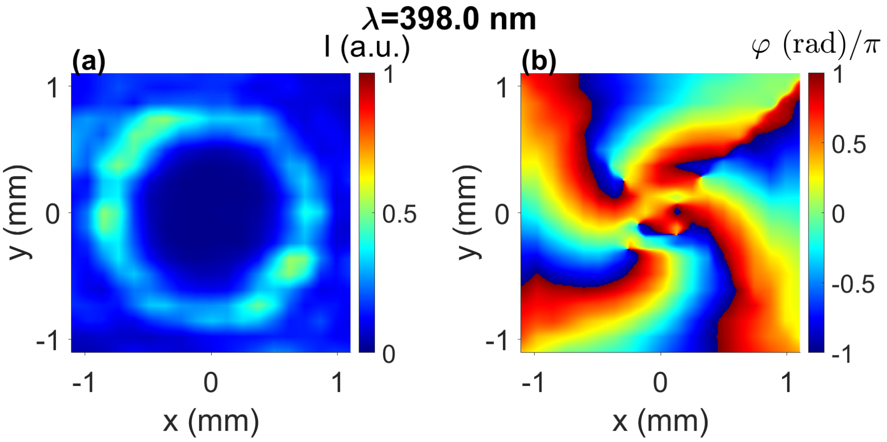

- **Caption:** Spatiospectral intensity (a) and phase (b) profiles evolution.

- **External link:** `VideoThesis_Vortex_VIS_L4.avi` [7]

---

[7] `https://drive.google.com/file/d/1enBrPf10RB6ze8j8hfLADXpjR7KKbw_M/view?usp=share_link`

C.2 Time-varying optical vortices

Here we present the complete spatiotemporal characterizations of the interference of two delayed vortices explained in Section 11.2.

C.2.1 Time varying vortex video: Experiment

- **Contextualization:** experimental spatiotemporal characterization of the interference pattern generated by combining two optical vortices of $\ell = +2$ and $\ell = 0$ with a 65-fs delay. Characterization done using a 1.06-mm-thick calcite cut with $\theta_{OA} = 45°$.

- **Thumbnail:**

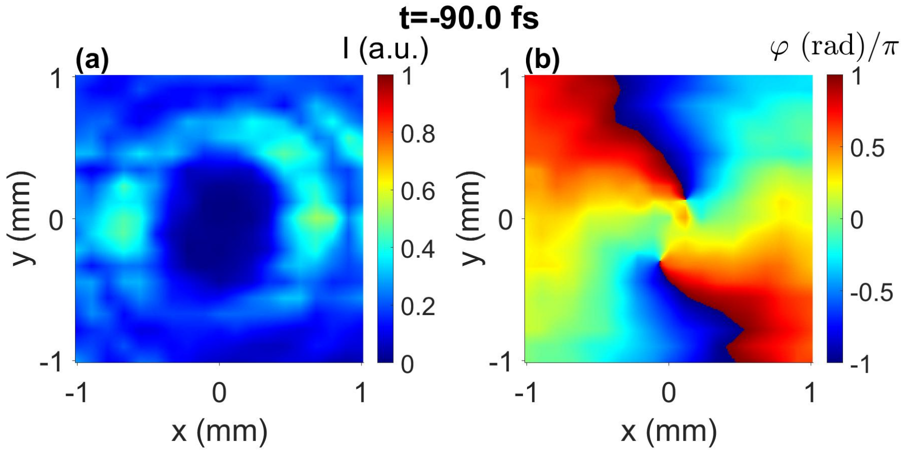

- **Caption:** Spatiotemporal intensity (a) and phase (b) profiles evolution.

- **External link:** `VideoThesis_TimeVarying_Vortex_Exp.avi` [8]

---

[8] `https://drive.google.com/file/d/1BmwQHe7q3Di7rDdGzdK3wwrGq28oo-hg/view?usp=share_link`

C.2.2 Time varying vortex video: Simulation

- **Contextualization:** simulation of spatiotemporal dependence of the interference pattern generated by combining two Laguerre-Gauss modes ($\ell_1 = +2$ and $\ell_2 = 0$ for each beam and $p = 0$ for both) with a 65-fs delay.

- **Thumbnail:**

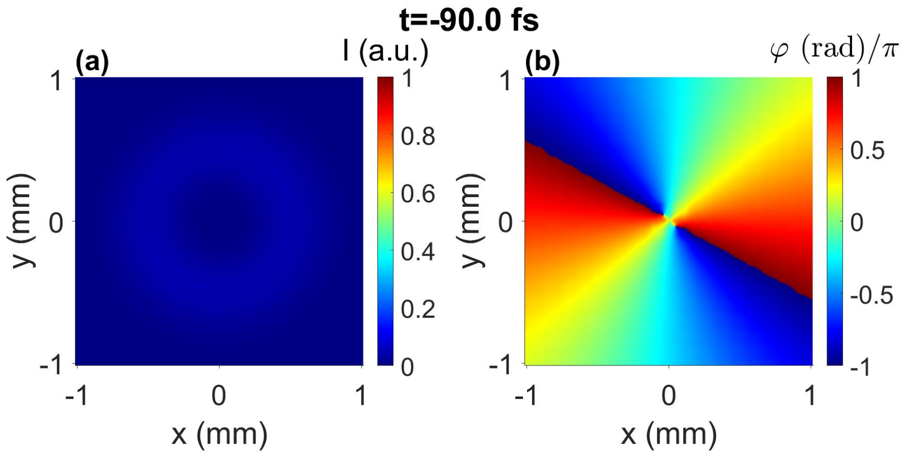

- **Caption:** Spatiotemporal intensity (a) and phase (b) profiles evolution.

- **External link:** `VideoThesis_TimeVarying_Vortex_Sim.avi` [9]

---

[9] `https://drive.google.com/file/d/1KfMUsOOfXLpYyDwnVAbmKC-mPA_RZ5MH/view?usp=share_link`

C.3 Non-collimated astigmatic beams

Here we present the spatiospectral characterization of the focusing beams of Section 10.2.

C.3.1 Astigmatic beam video: $z = d_a = 49$ cm

- **Contextualization:** spatiospectral characterization of a beam focused with an astigmatic lens (100-cm and 197-cm focal lengths). Measurement done after 49 cm of propagation from the lens and characterized with a 1.06-mm-thick calcite cut with $\theta_{OA} = 45°$.

- **Thumbnail:**

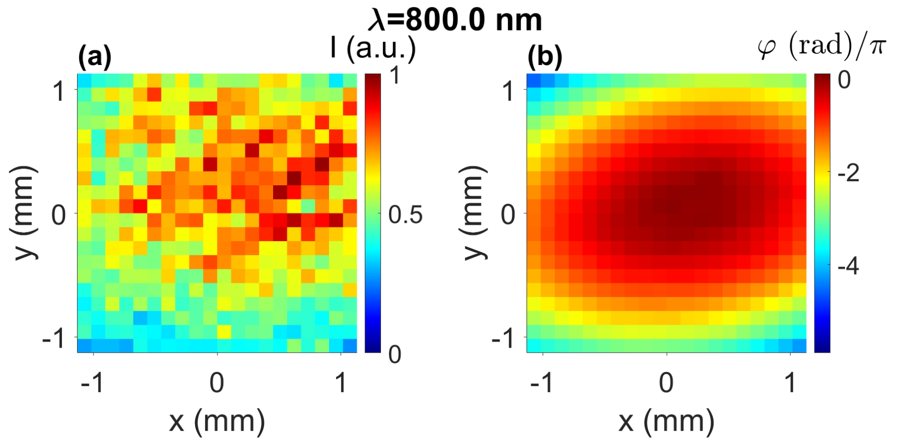

- **Caption:** Spatiospectral intensity (a) and phase (b) profiles evolution.

- **External link:** `VideoThesis_Astigmatic_Biconvergent.avi` [10]

---

[10] `https://drive.google.com/file/d/1xOR1rqQobXkwQFUTkG2JQIUzfV92lFsE/view?usp=share_link`

C.3.2 Astigmatic beam video: $z = d_b = 137$ cm

- **Contextualization:** spatiospectral characterization of a beam focused with an astigmatic lens (100-cm and 197-cm focal lengths). Measurement done after 137 cm of propagation from the lens and characterized with a 1.06-mm-thick calcite cut with $\theta_{OA} = 45°$.

- **Thumbnail:**

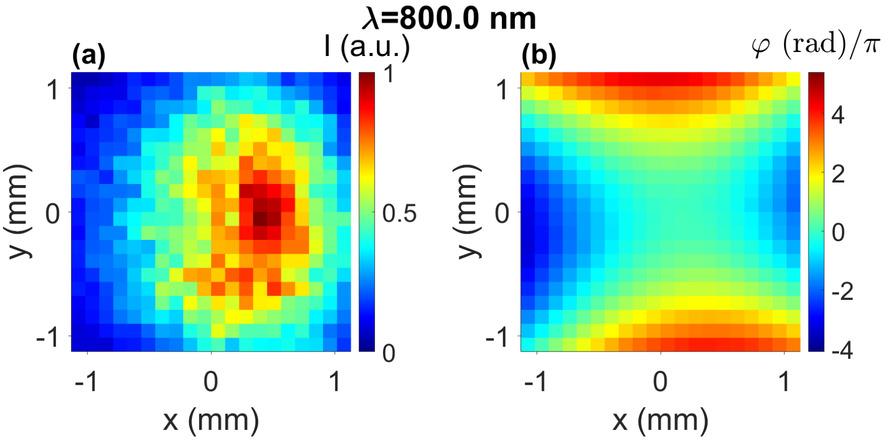

- **Caption:** Spatiospectral intensity (a) and phase (b) profiles evolution.

- **External link:** `VideoThesis_Astigmatic_ConvDiv.avi` [11]

---

[11] `https://drive.google.com/file/d/1uleDhW7OlC1l9d3YOAMj_zHdHUvKzGFc/view?usp=share_link`

Appendix D

List of Publications

Up to the time of depositing the Thesis, the articles published from the work presented here are:

- **M. López-Ripa**, I. J. Sola, and B. Alonso, "Bulk lateral shearing interferometry for spatiotemporal study of time-varying ultrashort optical vortices," *Photonics Research*, vol. 10, pp. 922-931, 4 2022.
- **M. López-Ripa**, I. J. Sola, and B. Alonso, "Amplitude swing ultrashort pulse characterization across Visible to Near-Infrared", *Optics and Laser Technology*, vol. 164, p. 109492, 9 2023.

During the Thesis, the author has also worked in the following articles:

- **M. López-Ripa**, B. Alonso, S. Jarabo, F. J. Salgado-Remacha, J. C. Aguado and I. J. Sola, "Coherent artifact and time-dependent polarization in amplified ultrafast erbium-doped fibre lasers", *Optics and Laser Technology*, vol. 140, p. 107018, 8 2021.
- F. J. Salgado-Remacha, B. Alonso, H. Crespo, C. Cojocaru, J. Trull, R. Romero, **M. López-Ripa**, P. T. Guerreiro, F. Silva, M. Miranda, A. L'Huillier, C. L. Arnold, and I. J. Sola, "Single-shot d-scan technique for ultrashort laser pulse characterization using transverse second-harmonic generation in random nonlinear crystals", *Optics Letters*, vol. 45, pp. 3925-3928, 14 2020.

- Y. Shen, Q. Zhan, L. G. Wright, D. N. Christodoulides, F. W. Wise, A. E. Willner, Z. Zhao, K.-h. Zou, C.-T. Liao, C. Hernández-García, M. Murnane, M. A. Porras, A. Chong, C. Wan, K. Y. Bliokh, M. Yessenov, A. F. Abouraddy, L. J. Wong, M. Go, S. Kumar, C. Guo, S. Fan, N. Papasimakis, N. I. Zheludev, L. Chen, W. Zhu, A. Agrawal, S. W. Jolly, C. Dorrer, B. Alonso, I. Lopez-Quintas, **M. López-Ripa**, I. J. Sola, Y. Fang, Q. Gong, Y. Liu, J. Huang, H. Zhang, Z. Ruan, M. Mounaix, N. K. Fontaine, J. Carpenter, A. H. Dorrah, F. Capasso, and A. Forbes, “Roadmap on spatiotemporal light fields,” *Journal of Optics*, (Under Review).

The results of this Thesis are part of the project *PID2020-119818GB-I00* funded by *MCIN/AEI/10.13039/501100011033/*; the projects *PC_TCUE18-20_0050*, *SA136-P20* and *SA287-P18* funded by *Junta de Castilla y León* and *European Regional Development Fund*; the projects *EQC2018-004117-P* and *FIS2017-87970-R* funded by *Ministerio de Economía y Competitividad*; the project *851201* funded by *H2020 European Research Council.*

MINISTERIO DE CIENCIA E INNOVACIÓN
AGENCIA ESTATAL DE INVESTIGACIÓN
Junta de Castilla y León
Consejería de Educación
GOBIERNO DE ESPAÑA
MINISTERIO DE ECONOMÍA Y COMPETITIVIDAD

Europa impulsa nuestro crecimiento
FONDO EUROPEO DE DESARROLLO REGIONAL
UNIÓN EUROPEA
erc
European Research Council
Established by the European Commission